

Efficiency Potential of Solar Thermochemical Reactor
Concepts with Ecological and Economic Performance
Analysis of Solar Fuel Production

Wirkungsgradpotenzial solar-thermochemischer Reaktor-
konzepte mit einer Analyse der ökologischen und
ökonomischen Leistungsfähigkeit solarer Kraftstoffherstellung

Von der Fakultät für Maschinenwesen der Rheinisch-Westfälischen Technischen Hochschule
Aachen zur Erlangung des akademischen Grades eines Doktors der Ingenieurwissenschaften
genehmigte Dissertation

vorgelegt von

CHRISTOPH FALTER

Berichter: Univ.-Prof. Dr.-Ing. Robert Pitz-Paal
Privatdozent Dr. rer. nat. habil. Andreas Sizmann

Tag der mündlichen Prüfung: 02.06.2017

Diese Dissertation ist auf den Internetseiten der Universitätsbibliothek online verfügbar.

Acknowledgments

This thesis was accomplished in the context of the two EU-funded research projects of the seventh framework program SOLAR-JET (grant agreement number 285098) and of the Horizon 2020 program SUN-to-LIQUID (grant agreement number 654408).

I would like to thank Univ.-Prof. Dr.-Ing. Robert Pitz-Paal who gave me the opportunity to continue my scientific work in this fascinating field by accepting me as a PhD student and who guided my work with very helpful and constructive support. I am also grateful to PD Dr. Andreas Sizmann who co-supervised my thesis and was always available for detailed discussions with deep scientific fascination and knowledge.

The team of the SOLAR-JET and SUN-to-LIQUID projects provided an interesting and very pleasant working environment including Prof. Dr. Steinfeld, Prof. Dr. Jonathan Scheffe, Dr. Philipp Furler, Dr. Daniel Marxer, Prof. Dr. Donald Reinalda, Dr. Joanna Bauldreay, Prof. Dr. Hans Geerlings, Dr. Patrick Le Clercq, Dr. Parthasarathy Pandi, Dr. Stephan Brendelberger, Dr. Martin Dietz, Justine Curtit, Prof. Dr. Manuel Romero, and Dr. Ellart De Wit.

My modeling efforts were supported by Dr. Patrick Le Clercq through helpful discussions and by Dr. Parthasarathy Pandi by providing a reference for my Monte Carlo analysis and valuable input through his modeling experience. Prof. Dr. Donald Reinalda and Prof. Dr. Hans Geerlings gave me input for my economic model of the solar fuels production plant and were available for discussions about the important parameters.

I am grateful to Dr. Valentin Batteiger, Dr. Arne Roth and PD Dr. Andreas Sizmann for their critical feedback on manuscripts and the development of my thesis, as well as for many important discussions about my research. I would like to extend my thanks to Univ.-Prof. Dr. Mirko Hornung who provided a very supportive working environment at Bauhaus Luftfahrt.

Jan Felinks was very helpful in the context of data for vacuum pumping from a manufacturer and with giving me the feeling of belonging to the group of PhD students at DLR, even when I could not be there.

Many thanks to Dr. Philipp Furler, Christian Endres, Dr. Daniel Marxer, Oliver Boegler, and all the PhD students at DLR and ETH for sharing many memories and for creating a memorable atmosphere at our gatherings. Special thanks to Philipp and Daniel at ETH for their hospitality whenever I came to visit.

Thanks to all my colleagues at Bauhaus Luftfahrt who created a productive and supportive environment during all my time which was very helpful for my work and my personal development.

I am deeply grateful for the unconditional and loving support of my family, their encouragement, motivation, and patience. Thank you.

Abstract

The alternative fuel production pathway of solar thermochemical splitting of water and carbon dioxide into hydrogen and carbon monoxide by redox reactions of a metal oxide, and their subsequent conversion into liquid fuels by Fischer-Tropsch synthesis, is investigated.

A generic model is developed for the description of solar thermochemical reactors including heat exchangers, where elements of redox material move in counter-flow through heat exchanger chambers, in which they transfer energy by radiation. In a first implementation of the model, infinitely fast thermal diffusion within the material is assumed and the influence on heat exchange of the wall separating the hot from the cold elements is neglected. A heat exchanger efficiency potential of over 80% is determined.

In a second implementation of the model, the effect of the separating wall is considered and heat diffusion in the porous redox material is simulated. Heat exchanger efficiency is found to have a potential of about 70%, where heat diffusion in the redox material is identified to be a limiting factor for heat exchange. Through an efficient design of the heat exchanger, efficiencies close to the optimal case of infinitely fast heat diffusion can be reached.

The model is adapted for the description of heat exchange between two unmixed particle beds moving in counter-flow in a cylindrical enclosure. Heat exchanger efficiency is found to have a potential of close to 60% and to be limited by heat transfer within the particle beds which can be enhanced e.g. by optimizing the bed diameters, heat exchanger length, particle size, and the velocity of the beds.

The analysis is complemented by an assessment of ecological and economic performance of a baseline case fuel production plant with an output of 1000 barrels per day (bpd) of jet fuel and 865 bpd of naphtha, using water from seawater desalination and carbon dioxide by capture from the atmosphere, having a thermochemical efficiency of 20%, and using heat and electricity provided by conversion of solar primary energy and combustion of the gaseous Fischer-Tropsch products. The energy conversion efficiency from incident sunlight to lower heating value of the produced fuels is determined to be 5.0%. A life cycle analysis shows greenhouse gas (GHG) emissions of 0.49 kg_{CO₂-eq.} per liter of jet fuel, which is a reduction of over 80% compared to conventional jet fuel. The main drivers of the GHG emissions are identified to be the origins of carbon dioxide and electricity, the combustion of gaseous Fischer-Tropsch products, and the construction of the solar concentration infrastructure.

The water consumption is 7.4 liters per liter jet fuel for on-site processes and 40.2 liters for off-site processes, which is orders of magnitude lower than that of biofuels and about equal to that of fossil fuels. The area-specific productivity is 3.3×10^4 liters of jet fuel equivalents per hectare and year, which is lower than the best power-to-liquid pathways but about an order of magnitude higher than that of biofuels.

An economic model based on the annuity method shows production costs of 2.23 € per liter of jet fuel for the baseline case. The economic drivers are the construction and operation of the solar concentration facility, the provision of electricity by an on-site concentrated solar power plant, carbon dioxide capture, and the lifetime of the fuel production plant.

Zusammenfassung

In der vorliegenden Arbeit wird der Produktionspfad alternativer Kraftstoffe, beruhend auf der solaren thermochemischen Spaltung von Wasser und Kohlendioxid in Wasserstoff und Kohlenmonoxid durch Redoxreaktionen eines Metalloxids, und deren Konversion zu flüssigen Kraftstoffen durch die Fischer-Tropsch-Synthese, untersucht.

Es wurde ein generisches Modell zur Beschreibung solarer thermochemischer Reaktoren mit Wärmeübertragern entwickelt, in dem Redox-Material im Gegenstrom Wärmeübertragerkammern durchläuft, in denen Wärme durch Strahlung übertragen wird. In einer ersten Evolutionsstufe des Modells wird unendlich schnelle Wärmeausbreitung im Material angenommen und der Einfluss der Trennwand zwischen heißem und kaltem Material vernachlässigt. Das Wirkungsgradpotential liegt über 80%.

In einer zweiten Evolutionsstufe des Modells wird der Einfluss der Trennwand berücksichtigt und die Wärmeausbreitung im Material simuliert. Der Wärmeübertragerwirkungsgrad hat ein Potential von etwa 70%, wobei die Wärmediffusion im Redox-Material der limitierende Faktor ist. Durch einen vorteilhaften Entwurf des Wärmeübertragers können Wirkungsgrade nahe dem optimalen Falle unendlich schneller Wärmediffusion realisiert werden.

Das Modell wurde angepasst zur Beschreibung des Wärmetausches zwischen gegenläufig bewegten undurchmischten Partikel-Festbetten in einer zylindrischen Geometrie. Der Wärmeübertragerwirkungsgrad weist ein Potential nahe 60% auf, welches durch den Wärmetransport im Partikelbett limitiert ist. Der Wirkungsgrad kann z.B. durch die optimale Wahl der Betticken, der Länge des Wärmeübertragers, der Partikelgröße und der Geschwindigkeit der Betten verbessert werden.

Die Untersuchung wird durch eine ökologische und ökonomische Analyse einer Produktionsanlage für Kraftstoff mit einer Kapazität von 1000 Barrel Kerosin pro Tag (bpd) und 865 bpd Naphtha ergänzt. Wasser wird aus Meerwasserentsalzung gewonnen, Kohlendioxid aus der Luft eingefangen, der thermochemische Wirkungsgrad liegt bei 20% und Prozesswärme und Elektrizität werden durch die Umwandlung solarer Primärenergie und Verbrennung des gasförmigen Anteils der Fischer-Tropsch-Produkte gewonnen. Der Umwandlungswirkungsgrad einfallenden Sonnenlichts zum Heizwert der produzierten Kraftstoffe beträgt 5,0%. Die Ökobilanz des Prozesses ergibt Treibhausgasemissionen von 0,49 kg_{CO₂-eq.} pro Liter Kerosin, was einer Reduktion von über 80% gegenüber konventionellem Kraftstoff entspricht. Die Treiber der Emissionen sind die Herkunft des Kohlendioxids und Stroms, die Verbrennung der gasförmigen Fischer-Tropsch-Produkte und die Errichtung der Anlage zur Konzentration des Sonnenlichts.

Der Wasserverbrauch beträgt 7,4 Liter pro Liter Kerosin am Ort der Anlage und 40,2 Liter für externe Prozesse und liegt damit um Größenordnungen unter dem von Biokraftstoffen und ist in etwa gleich dem von fossilen Kraftstoffen. Die flächenbezogene Produktivität ist $3,3 \times 10^4$ Liter Kerosinäquivalent pro Hektar und Jahr, was niedriger ist als die der besten Power-to-Liquid-Pfade, jedoch etwa eine Größenordnung über der von Biokraftstoffen liegt.

Die ökonomische Untersuchung mit der Annuitätenmethode ergibt Kosten von 2,23 € pro Liter Kerosin für die betrachtete Produktionsanlage. Die Treiber der Produktionskosten sind die Errichtung und der Betrieb der solaren Konzentrationsanlage, die Erzeugung von CSP-Strom am Standort, der Kohlendioxideinfang und die Lebenszeit der Anlage.

Contents

Acknowledgments.....	III
Abstract	V
Zusammenfassung.....	VII
Contents.....	XI
Nomenclature.....	XV
1 Motivation, scope and structure of work	1
2 Background and prior research.....	5
2.1 Production pathway	6
2.1.1 Water desalination.....	6
2.1.2 Carbon dioxide provision	7
2.1.3 Solar concentration.....	10
2.1.4 Thermochemistry	13
2.1.5 Syngas storage.....	18
2.1.6 Fischer-Tropsch conversion	20
2.2 Prior research.....	22
3 Reactor modeling.....	25
3.1 Modeling of reduction and oxidation reactions.....	25
3.1.1 Reduction reaction.....	25
3.1.2 Oxidation chamber	26
3.1.3 Governing equations	26
3.2 Generic chamber model - Idealized internal heat transfer.....	33
3.2.1 Introduction	33
3.2.2 Prior research.....	33
3.2.3 Model description.....	35
3.2.4 Boundary conditions	39

3.2.5	Material properties	39
3.2.6	Numerical solution	40
3.2.7	Model validation	40
3.2.8	Results	42
3.3	Generic chamber model - Modeled internal heat transfer	55
3.3.1	Introduction	55
3.3.2	Prior research.....	56
3.3.3	Model description.....	57
3.3.4	Governing equations	60
3.3.5	Boundary conditions	64
3.3.6	Material properties	65
3.3.7	Numerical solution	65
3.3.8	Model validation	67
3.3.9	Results	70
3.3.10	Conclusions for heat exchanger design	83
3.4	Particle reactor concept	85
3.4.1	Introduction	85
3.4.2	Prior research.....	86
3.4.3	Model description.....	87
3.4.4	Governing equations	90
3.4.5	Boundary conditions	95
3.4.6	Material properties	96
3.4.7	Numerical solution algorithm.....	97
3.4.8	Model validation	99
3.4.9	Results	104
3.4.10	Conclusions for heat exchanger design	119
3.5	Potential of thermodynamic cycle efficiency	120

4	Ecological and economic analysis	123
4.1	Introduction	123
4.2	Prior research.....	124
4.3	Baseline plant configuration.....	125
4.3.1	Energy and mass balance	126
4.3.2	Energy conversion efficiency.....	130
4.4	Ecological assessment	131
4.4.1	Goal and scope definition.....	133
4.4.2	Functional unit.....	134
4.4.3	Inventory analysis	134
4.4.4	Allocation method.....	134
4.4.5	Data sources and further assumptions.....	135
4.4.6	Impact assessment and interpretation.....	137
4.5	Assessment of economic performance	161
4.5.1	Annuity method for estimation of production costs.....	162
4.5.2	Boundary conditions for baseline case.....	164
4.5.3	Investment costs	165
4.5.4	Operation and maintenance costs.....	170
4.5.5	Results for baseline case	175
4.5.6	Sensitivity analysis	176
4.6	Ecological and economic performance of further operation scenarios	178
4.6.1	Private financing of production plant.....	178
4.6.2	CO ₂ capture from NGCC plant	180
4.6.3	Use of grid electricity	183
4.6.4	Sale of oxygen.....	185
4.6.5	Comparison of dish and tower systems for solar concentration.....	185
4.6.6	Comparison to Power-to-Liquid fuel production pathway	187

4.6.7	Possibilities for cost reductions and emission reductions	189
5	Conclusions and outlook.....	191
	References	197
	List of Figures	213
	List of Tables.....	220
A	Annex.....	222
A.1	Derivation of realistic pump efficiency	222
A.2	Rosseland extinction coefficient as a function of porosity	223
A.3	Thermal conductivity of RPC.....	224
A.4	Overall thermal conductivity of RPC including radiation term	225
A.5	Technical assumptions for baseline case of fuel production plant	226
A.6	Assumptions for derivation of greenhouse gas emissions.....	227
A.7	Fuel properties	228
A.8	Assumptions for calculation of economic performance	228
A.9	Assumptions for generic reactor models	230

Nomenclature

Latin letters

A	Surface area [m^2], annuity factor [-]
a	Diameter of contact surface area particle-wall [m]
B	Deformation parameter [-]
C	Concentration ratio [-], cash flow [€]
C_f	Form factor of particles [-]
c	Concentration [-]
c_p	Specific heat capacity at constant pressure [$\text{J kg}^{-1} \text{K}^{-1}$]
c_v	Specific heat capacity at constant volume [$\text{J kg}^{-1} \text{K}^{-1}$]
\bar{c}	Mean velocity of translation of gas molecules [m s^{-1}]
d	Diameter, thickness [m]
f_{CO_2}	Molar flow rate of CO_2 into oxidation chamber as a multiple of δ_{red} [-]
ΔG_{O_2}	Oxygen molar free energy [J mol^{-1}]
ΔH	Enthalpy of reaction [J mol^{-1}]
ΔH_{O}	Partial molar enthalpy of oxygen [J mol^{-1}]
h	Height of particle reactor [m]
I	Radiative intensity [$\text{W m}^{-2} \text{sr}^{-1}$]
I	Investment costs [€]
i	Chamber in heat exchanger, interest rate [-]
K	Thermodynamic equilibrium constant [-], permeability [m^{-2}]
k	Thermal conductivity relative to thermal conductivity of fluid [-]
L	Length [m]
l	Modified mean free path of gas molecules [m]
M	Molecular mass [kg mol^{-1}]
m	Mass [kg]
\dot{m}	Mass flow rate [kg s^{-1}]
n	Project lifetime [years], number of computational layers [-], integer [-]
\dot{n}	Molar flow rate [mol s^{-1}]
P	Power [W]
p	Pressure relative to standard state [-]
Q	Annually produced amount of fuel [L]
\dot{Q}	Heat flux [W]
\dot{q}	Heat flux [W m^{-2}]
R	Thermal resistance [K W^{-1}]
\mathcal{R}	Universal gas constant [$\text{J mol}^{-1} \text{K}^{-1}$]
r	Radius [m]
S	Direction of radiation [-]

ΔS_{O}	Partial molar entropy of oxygen [$\text{J mol}^{-1} \text{K}^{-1}$]
T	Temperature [K]
T	Tax rate [-]
\bar{T}	Arithmetic mean temperature [K]
t	Time [s]
$t_{CI,\nu}$	t-value of the student t function for confidence interval CI
Δt	Residence time in heat exchanger chamber [s]
Δt^{num}	Numerical time step [s]
u	Fluid flux at average pressure [m s^{-1}]
V	Volume [m^3]
v	Velocity [m s^{-1}]
x	Local variable in heat exchanger [m]
z	Real gas compressibility factor [-], local variable in heat exchanger [m]

Greek letters

α	Heat transfer coefficient [$\text{W m}^{-2} \text{K}^{-1}$]
α_a	Absorption coefficient [-]
β	Extinction coefficient [-]
γ	Accommodation coefficient [-]
δ	Oxygen nonstoichiometry of ceria [-], roughness factor of particles [-]
ε	Emissivity [-]
η	Thermodynamic cycle efficiency [-], dynamic viscosity [Pa s]
λ	Thermal conductivity [$\text{W m}^{-1} \text{K}^{-1}$]
ν	Degrees of freedom [-]
ρ	Density [kg m^{-3}]
σ	Stefan-Boltzmann constant [$\text{W m}^{-2} \text{K}^{-4}$]
σ_s	Scattering coefficient [m^{-1}]
Λ	Mean free path of gas molecules [m]
Φ_A	Plate surface coverage factor by particles [-]
φ	Porosity of particle bed [-]
ψ	Flatness coefficient of particles [-]
ω	Solid angle [sr]

Subscripts

0	Surroundings
abs	Absorption
Aux	Auxiliary
b	Blackbody
c	Core, conduction

CeO ₂	Ceria
chamber	Heat exchanger chamber
CO	Carbon monoxide
CO ₂	Carbon dioxide
CO _{2,i}	CO ₂ entering the oxidation chamber
dir	Direct contact of particle and wall
f	Fluid, form factor
G	Gas
gasrec	Gas heat recuperation
H	High, reduction
H ₂	Hydrogen
H ₂ O	Water
he	Heat exchanger
he,cold	Cold side of heat exchanger
he,int	Interface between chamber halves in heat exchanger
he,end	Hot end of heat exchanger
he,ext	External side of heat exchanger facing the surroundings
he,ext,total	Total external area of heat exchanger facing the surroundings
he,hot	Hot side of heat exchanger
he,int,total	Total interface between chamber halves in heat exchanger
he,wall	Wall of heat exchanger facing surroundings
heat	Heating
heat-to-electricity	Conversion of heat to electricity
hot bed→sw	Between hot bed and separating wall
i,j	Coordinates
k,l	Lower k-th chamber
k,u	Upper k-th chamber
l	Lower chamber half
L	Low, oxidation
loss,conv	Convective losses
loss,rad	Radiative losses
O&M	Operation and maintenance
O ₂	Oxygen
ox	Oxidation
p	Particle
products	Gaseous products
Pump,vacuum	Vacuum pump
R	Radial direction
rad	Radiation
red	Reduction
red,CeO ₂	Reduction of CeO ₂

rerad	Reradiation
s	Solid
sb	In particle bed
sc	Standard conditions
sep.CO/CO ₂	Separation of gas mixture of CO and CO ₂
sw	Separating wall
sw,in	Inside of separating wall facing hot bed
sw,out	Outside of separating wall facing cold bed
sw→cold bed	Between separating wall and cold bed
total	Sum of individual shares
u	Upper chamber half
V	Volume
W	Wall
wall-bed	Between wall and particle bed
wp	Between wall and single particle
ws	Between wall and particle bed
Z	Axial direction

Superscripts

<i>n</i>	Time step
num	Numerical

Abbreviations

TLCC	Total life cycle costs [€]
PV	Present value [€]

1 Motivation, scope and structure of work

The transportation sector today relies almost exclusively on liquid fuels derived from the refinement of fossil crude oil [1]. Besides historic reasons, this is due to their superior energy density, handling and storage properties. Among the different means of transport, especially aviation and heavy-duty road and sea traffic rely heavily on hydrocarbon fuels because of their inherent high restrictions with respect to the energy and power density of the fuel. For these applications, a change towards electrification is not as easy to implement as for light-duty road transport, where first electro-mobility solutions have started to appear on the market already. Additionally, rising concerns about climate change, partly due to emissions from the transportation sector, and regional supply security, due to limitation of the resources, drive the search for alternatives for vehicle propulsion. As the demand for personal travel is very likely to increase [2], the production of a sustainable energy-dense fuel is a key enabler for GHG reductions in the transportation sector of the future. Especially the conversion of solar energy, the most abundant renewable energy source on earth, to liquid fuels appears to be an attractive path due to the very large geographical production potential [3–6].

Compared to other approaches of producing solar fuels, based on photochemistry or electrochemistry, thermochemical processes promise thermodynamic advantages that could enable higher energy conversion efficiencies [7]. Using concentrated solar energy, chemical reactions are driven to split carbon dioxide and water into syngas, a mixture of hydrogen and carbon monoxide, which is converted in the Fischer-Tropsch process into liquid hydrocarbon fuels. For the implementation of thermochemical cycles, different solar reactor concepts exist that use redox cycles of metal oxides, e.g. ceria, to produce syngas or its constituents. In a first step, the metal oxide is reduced at high temperature and reduced oxygen partial pressure, releasing oxygen. In a second step, the material is oxidized with water and carbon dioxide at reduced temperature, producing syngas and returning to its initial state. Depending on the chemistry of the process, i.e. whether or not the redox material undergoes a phase change from solid to gaseous state, different requirements have to be met. In the former case, high-temperature separation of the gaseous products is required to avoid their recombination [8], while these processes show a high theoretical efficiency potential due to the stoichiometric reaction of the metal oxide. In the latter case, cycles where the material remains in its solid state throughout the reactions offer significant technical advantages.

In the past couple of years, the development of solar reactors has included redox reactions of ceria that do not fully reduce the metal oxide but rather stop at an earlier stage to retain the reactive material in a solid phase [9–13]. This does not allow achieving the same level of reduction and therefore yield per mass of oxide per cycle. However, contrary to the Zn/ZnO-cycle, for example, gaseous products are not prone to recombine which allows a simpler reactor and process design, as now principally only a single vessel is required. First experiments show promising results with respect to technical viability and achieved cycle efficiency [10,11,14,15].

Among the reactor concepts working with redox reactions of metal oxides not undergoing phase changes, three different approaches may be distinguished. Firstly, a continuously rotating and heat recuperating concept was presented in 2008 [16], where rings of reactive material are heated and reduced on one side and oxidized on the other. Through the counter-rotation of adjacent rings, heat recuperation is achieved. A similar concept was introduced in [17]. Secondly, in 2009, a batch reactor concept was developed at ETH Zurich that uses ceria for syngas production [10]. Inert gases are used for the reduction of the oxygen partial pressure which limits the efficiency potential due to energy penalties which are proportional to the inverse of the pressure, as shown in [18]. Thirdly, reactor concepts based on the movement of particles have been presented in [18] and [19]. Besides these three concepts, recently, an isothermal reactor concept has been proposed that tries to alleviate the necessity for solid heat recuperation through a pressure swing process operating at constant temperature throughout reduction and oxidation [12,13]. However, the operation at a constant high temperature makes very high gas recuperation efficiencies necessary to achieve high overall cycle efficiency. In fact, it is concluded that the introduction of an additional temperature swing will increase the cycle efficiency over the isothermal concept [13]. From the different concepts shown above, prerequisites for a highly efficient reactor concept can be deduced, e.g. heat recuperation and gas separation, as also shown and analyzed in previous studies on reactor concepts [13,17,18,20–22]. It also becomes clear that the approaches of the different concepts vary considerably, underlining that a single most efficient reactor concept has not been found so far. For non-stoichiometric cycles, the amount of fuel produced per cycle and mass of redox material is small, which makes the thermal energy input for the temperature swing between oxidation and reduction temperatures a major energy requirement of the cycle. Heat recuperation from the solid phase is therefore a crucial concept for the achievement of high efficiencies and is consequently modeled in this work.

From techno-economic analyses of the whole process pathway of producing solar thermochemical fuels, it is known that the efficiency of the thermochemical conversion step is decisive for the overall pathway efficiency [23–25] and through its influence on the required solar collector area it has a strong influence also on the process economics and environmental performance [3,5,24]. It is therefore of high importance to gain insight into the realistic efficiency potentials of different reactor concepts for the thermochemical production of syngas and to investigate its influence on the overall pathway economics and environmental performance.

To the best knowledge of the author, the comprehensive approach of this work, i.e. the evaluation of parametric reactor concepts and the ecological and economic feasibility of the whole solar fuel production path, goes beyond the analyses found in the literature. Existing analyses of the thermochemical conversion step have focused either on general thermodynamic considerations of the redox mechanisms of the chosen material or on specific reactor concepts and their detailed description. With these approaches however, it is not possible to analyze the realistic efficiency potentials of a large number of reactor concepts, which is required at the current stage of development. The generic reactor models presented in this work close the gap between fundamental thermodynamic analyses and specific reactor concepts by introducing a means to estimate the performance of many reactor designs. Important parameters such as material thickness, heat exchanger length, residence time, or material porosity can be varied to investigate their influence on efficiency. Furthermore, the discussion of economic and ecological feasibility of the whole fuel production pathway adds crucial information about the other process steps and enables a comprehensive analysis of the solar thermochemical fuel production using a common set of assumptions. The chosen approach of this work therefore represents a novelty with respect to the state of the art of research on solar thermochemical fuels and contributes new insights to the discussion on solar reactor concepts and the general feasibility of the fuel production pathway.

In the following, the structure of the work is described. In Chapter 2 the single process steps of the fuel production pathway are explained, prior research of solar thermochemical fuel production is discussed and the novelty of the approach of this work with respect to the state of the art of research is indicated.

In Chapter 3, a generic reactor model is introduced and for the three different cases of idealized internal heat transfer (Section 3.2), modeled internal heat transfer (Section 3.3), and

the particle reactor concept (Section 3.4), the prior research is discussed, the model is described with governing equations and boundary conditions. The models are validated with selected results from the literature or by standard solution techniques. Different parameters are varied and conclusions are drawn for heat exchanger and reactor design.

In Chapter 4, the ecological and economic performance of a baseline case plant design is investigated. The ecological analysis is founded on a life cycle analysis including the derivation of greenhouse gas emissions, water footprint and land requirement of solar thermochemical jet fuel production. The economic analysis determines the production cost of the fuel. A sensitivity study is performed to investigate the influence of important parameters on both economic and ecological indicators.

In Chapter 5, conclusions and recommendations from the thermochemical reactor modeling and the economic and ecological analyses are given.

2 Background and prior research

In the transportation sector, especially aviation is dependent on hydrocarbon fuels, which is due to their high specific energy and favorable handling properties. Hydrogen can be directly combusted or used in a fuel cell to power electric motors, however, its comparably low energy density (H_2 at 700 bar: 4.2 MJ L^{-1} [26], liquid H_2 : 8.5 MJ L^{-1} [27], jet fuel: 34.6 MJ L^{-1} lower heating value [28]) requires a significantly larger storage volume for the same mission length. Reduced storage space inside of the airplane or its deteriorated aerodynamics for an external storage design may lead to an economic disadvantage over the conventionally powered option, while the development of a global hydrogen infrastructure is required additionally to the redesign of the aircraft powertrain and storage system.

As a second option, the electrification of the powertrain achieves significantly higher energy conversion efficiencies. The specific exergy of batteries is however below that of jet fuel (batteries: currently $0.7\text{-}1.8 \text{ MJ kg}^{-1}$ for lithium ion batteries, jet fuel: 17.3 MJ kg^{-1} [29]), and thus the energy storage of an electric airplane has to be considerably heavier than that of the conventional airplane. Further development of the battery technology is not expected to change this fundamental relationship [30]. Considering a maximum take-off weight of an airplane, the heavier electrically-powered option has a decreased mission length. This can be shown by adjusting the Breguet range equation to describe electric airplanes: comparing a fully electric airplane (in the year 2035, 190 passengers, batteries with a high specific energy of 5.4 MJ kg^{-1}) with a conventional airplane at the same maximum take-off weight of 109.3 t, shows that the range of the conventional option is higher by a factor of six [31]. Even when using favorable assumptions for the development of batteries and electric components, it is questionable whether fully electric long-range air travel will become an option in the future.

Due to the challenges associated to the implementation of hydrogen fuel cells and batteries, long-range air travel is likely to depend also in the future on hydrocarbon fuels. To provide supply security and to reduce greenhouse gas emissions it is therefore desirable to produce synthetic hydrocarbon fuels that can be used with the current fuel infrastructure and aircraft powertrain.

In this chapter, fundamental information about the fuel pathway analyzed in this work is given and a link to prior research is made.

2.1 Production pathway

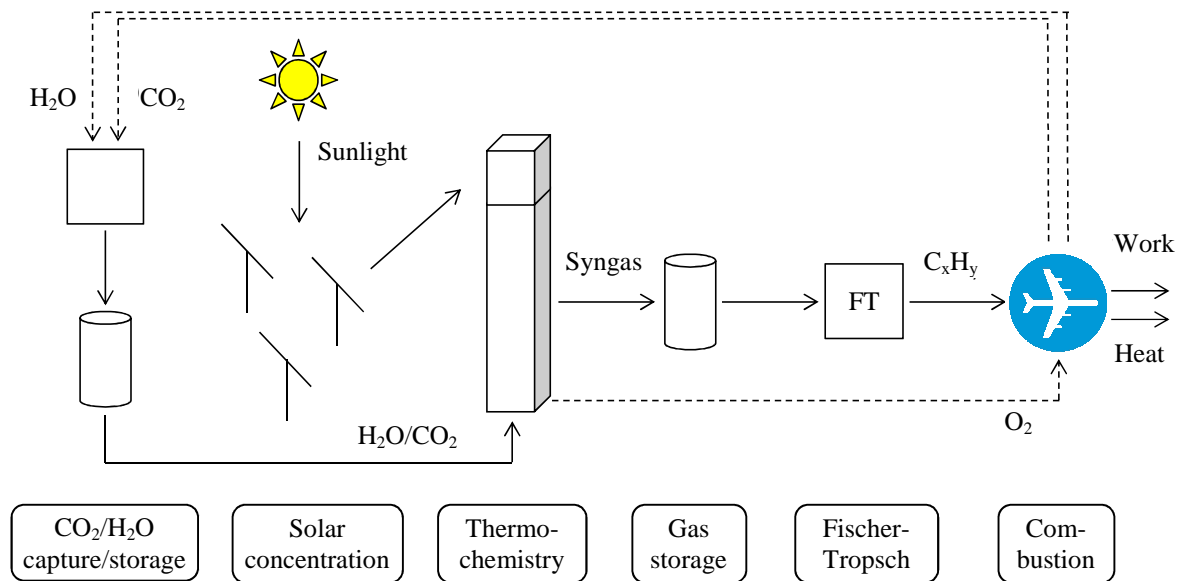


Figure 2.1 Schematic of solar thermochemical jet fuel production pathway.

An overview of the fuel production pathway is shown in Figure 2.1. The resources water and carbon dioxide have to be provided to the thermochemical reactor which is heated with concentrated solar energy using a tower or dish concentrator. Inside of the reactor, a two-step redox reaction of a metal oxide takes place, splitting water and carbon dioxide into oxygen and a mixture of hydrogen and carbon monoxide, also referred to as synthesis gas or syngas. The syngas is then converted in the Fischer-Tropsch process into liquid hydrocarbons such as jet fuel, diesel, or gasoline. In the following, the individual process steps are explained in more detail.

2.1.1 Water desalination

For the provision of water, natural fresh water reservoirs are not taken into account because they may be required as drinking water or for plant irrigation and are not replenished on a short time scale. On the other hand, several technologies for the desalination of seawater exist that are able to provide fresh water, e.g. distillation and membrane separation. The former evaporates the fresh water which then separates from the salt remaining in the solution, and which has a relatively high energy consumption of about $2 \text{ kWh}_{\text{el}}/\text{m}^3$ of electricity and $40 \text{ kWh}/\text{m}^3$ of heat, or an equivalent of $14.5\text{-}21.4 \text{ kWh}_{\text{el}}/\text{m}^3$ [32] (corresponds to less than 1%

of the higher heating value of the hydrogen molecules in 1 m^3), making this technology viable only in a place where cheap energy is available.

A common way to desalinate seawater today is by membrane separation using reverse osmosis, as used for example in the US, Spain, or the Middle East [33]. When two solutions of saltwater with different salt concentrations are separated by a membrane which allows only water molecules to pass but holds back salt ions, water molecules will move from the diluted side to the concentrated side to alleviate the gradient in salt concentration. By applying pressure on the concentrated side, this process can be controlled and even reversed, so that seawater is desalinated. Recent development has reduced the practical energy requirements to about $3 \text{ kWh}_{\text{el}} \text{ m}^{-3}$ which is close to the thermodynamic limit of $1.06 \text{ kWh}_{\text{el}} \text{ m}^{-3}$ for the desalination of seawater with a salt concentration of 35000 ppm at a recovery rate of 50% [34]. Compared to the amount of energy which is stored in the hydrogen molecules of 1 m^3 water, the corresponding desalination energy is smaller by about four orders of magnitude (at a higher heating value of hydrogen of 286 kJ mol^{-1}).

2.1.2 Carbon dioxide provision

Different capture technologies exist which are based on chemical absorption, chemisorption, physical absorption, physical adsorption, membrane technology, or cryogenic separation. Individual options are explained in the following.

Chemical absorption is a common method of CO_2 capture from combustion processes or the atmosphere, where the gas is chemically bound to an alkaline sorbent, such as monoethanolamine. Its desorption requires the input of heat at elevated temperatures. Several demonstration plants for capture from flue gases exist today which have proven the technology to be viable [35].

Besides chemical absorption, physical absorption by Van-der-Waals or electrostatic forces to sorbents such as methanol, N-methyl-2-pyrrolidone, polyethylene, and others is possible. However, the binding forces are lower and absorption is proportional to the gas partial pressure. Desorption is carried out through a swing in temperature or pressure [36,37].

Physical adsorption occurs when the CO_2 molecules are bound to the surface of the sorbent rather than in the bulk. Potential sorbents include activated carbon, zeolite, aluminum oxide, and silica gel. For desorption, pressure or temperature swings are used, as for physical

absorption. As the adsorption is a surface-controlled process, the capacity of the sorbent depends on its surface area rather than its volume. Also, the selectivity of the adsorbent may present a limit for the binding of CO₂ [37].

Chemisorption is similar but involves a chemical reaction on the surface of the adsorbent. Temperature-vacuum swings may be used for the adsorption-desorption cycle. Promising results have been presented in the literature for air capture of CO₂ [38–40].

Membranes are molecular sieves that selectively allow the passage of different gas species while others are held back. Materials for the membrane are similar to those for physical adsorbents and share their porous structure. Gases are separated based on a difference in species concentration and hydrostatic pressure on both sides of the membrane. Gas separation membranes use hydrostatic pressure differences together with different gas permeabilities to separate gases, while gas absorption membranes do not use a pressure gradient but sweep away the gas diffusing through the membrane by a liquid sorbent. Flooding, foaming and channeling of liquid sorbent in the membrane is minimized [37].

Cryogenic separation uses the different boiling points of gases in a gas mixture. By reducing the temperature, the gases liquefy separately which is the principle of the Linde process. However, as CO₂ is only present in a comparably low concentration in the atmosphere, a relatively large amount of gas has to be cooled for its separation which leads to an unfavorable energy requirement [37].

In the solar thermochemical pathway, contrary to processes based on photosynthesis, CO₂ has to be actively supplied to the reactor which requires a source and a capture process. Today, many different point sources of CO₂ exist such as fossil power plants or industrial processes, e.g. cement production, natural gas sweetening, or ethanol and biogas plants. If CO₂ is captured from a fossil process, some of the emissions should be allocated to the fuel production process. A larger use of fossil based energy will then deteriorate the life cycle greenhouse gas emissions. Other industrial processes may not be easily accessible from a geographical and technical point of view, or may not be scalable to the desired production volumes. In the long-term, CO₂ capture from the atmosphere may therefore become interesting as it represents a sustainable source of CO₂ which can be accessed anywhere and which obviates the problem of long-distance CO₂ transport. As its concentration is two orders of magnitude lower than in the exhaust of a fossil power plant, the energy requirement for its separation is necessarily higher which can be seen from equation (2.1) which describes the

minimum thermodynamic work required for the separation of a gas species from a gas mixture [41].

$$W_{\text{separation}} = \frac{1}{x} \cdot \mathfrak{R} \cdot T \cdot \left(x \cdot \ln \frac{1}{x} + (1-x) \cdot \ln \frac{1}{(1-x)} \right) \quad (2.1)$$

x is the concentration of the gas to be separated, \mathfrak{R} is the ideal gas constant, and T is the temperature. The theoretical minimum separation work is shown with the black line in Figure 2.2 together with experimental values from the literature.

The thermodynamic work needed to separate a mixture of two gases increases with decreasing concentration of the gas to be extracted, however, the increase follows a logarithmic function. The separation work of CO₂ from the atmosphere is therefore higher only by a factor of two to four with respect to capture from a point source. State-of-the-art experimental values of CO₂ capture energy are on the order of the higher heating value of the equivalent amount of CO (e.g. capture energy: 269.3 kJ mol_{CO₂}⁻¹ [42], HHV CO: 283.4 kJ mol⁻¹).

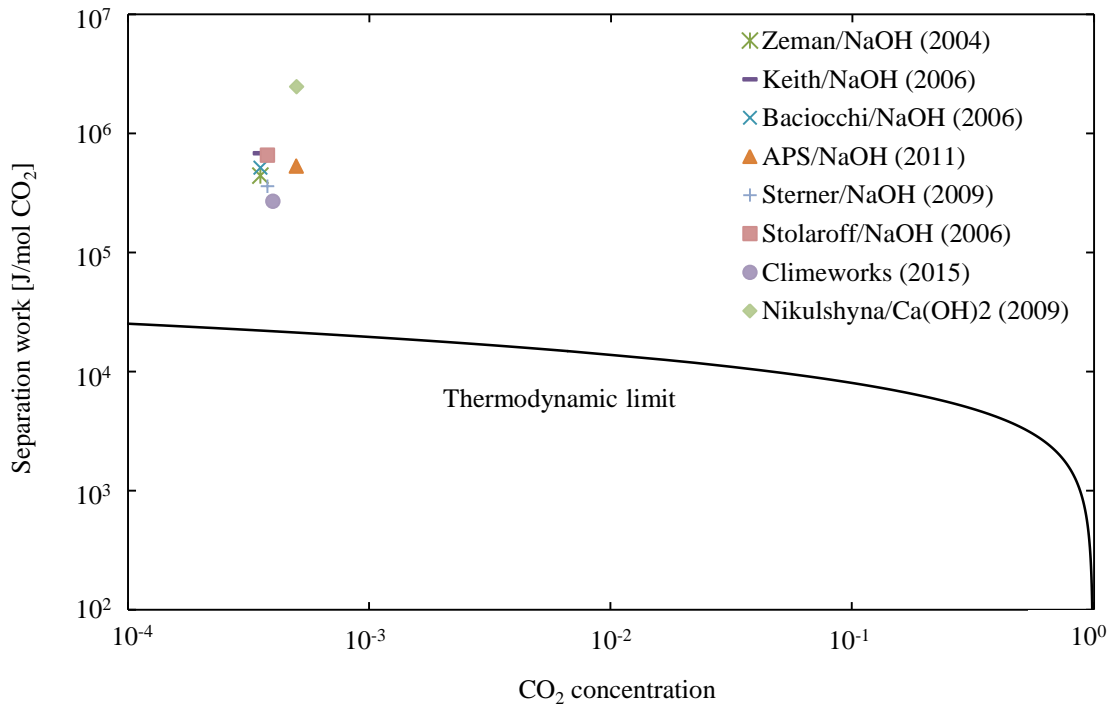


Figure 2.2 Theoretical separation work for a mixture of two gases and experimental values from the literature (Zeman et al. [43], Keith et al. [44], Baciocchi et al. [45], APS [46], Sterner [47], Stolaroff [48], Climeworks [42], Nikulshyna [36]). For comparison, the higher heating value of one mol of CO is 283.4 kJ mol⁻¹.

2.1.3 Solar concentration

For the thermochemical cycle to operate, temperatures in the range of 1800 K are required for the reduction of the redox material. This is achieved through the absorption of concentrated solar radiation in a cavity receiver. Depending on the losses from the reactor to the environment, a certain level of input power is required which for a defined geometry corresponds to a level of solar concentration. To reach a temperature of 1773 K, for example, a concentration of 560 suns is required for an ideal black-body absorber. Losses increase the level of concentration needed in a realistic system.

Concentration of solar energy appears today in many concentrated solar power plants around the world for the production of electricity and has thus reached industrial maturity. However, among the different options, only point focus devices are able to supply the required level of concentration ratio to the thermochemical reactor. Concentration ratios of solar towers are in the range of 1000-1500 suns [49], while solar dish systems reach even higher values but are much more limited with respect to the achievable power level per unit due to reasons of structural stability. As the unit size differs considerably between tower and dish systems, a fuel production plant requires a completely different plant layout including different reactor unit sizes and gas distribution, depending on the concentrator.

The choice of the concentration device has therefore a direct influence on the scalability, efficiency, and cost of the overall fuel production plant. In the following, the two possible options of tower and dish systems are discussed.

Solar towers

Solar tower concentrators use an array of heliostats tracking the sun to reflect the sunlight on top of the tower where an absorber converts the radiation into high-temperature heat (Figure 2.3). Major loss mechanisms are shading and blocking, a decreasing reflectivity of the mirror surfaces, errors in the tracking of the sun, deviations of the mirrors from their ideal shape, and cosine losses.

Table 2.1 Annual average efficiency of solar tower concentration at the Gemasolar CSP plant [50]. Field optical efficiency includes cosine losses, and losses due to blocking and shading, heliostat tracking, and focal length and shape deviations.

Loss mechanisms	Efficiency
Heliostat reflectivity	93.5%
Field optical efficiency	64.6%
Field availability	98.5%
Mirror corrosion avoidance	100.0%
Mirror cleanliness	95.0%
Field high wind outage	99.0%
Annual heliostat field efficiency	56.0%

Minor losses are atmospheric attenuation, defocus, initial startup of the plant, or passing of clouds. Typical values for the loss mechanisms are shown in Table 2.1 for the Gemasolar plant [50]. The main losses occur in the optical properties of the heliostat field which includes the major loss mechanisms cited above. A total annual heliostat field efficiency of 56.0% is derived which is in good agreement with other values in the literature [51,52].



Figure 2.3 Two CSP tower plants in Spain (PS10 and PS20) [53].

Solar dishes

Dish concentrators have a three-dimensional parabolic shape to reflect the incoming rays onto the receiver which is held above the dish surface (Figure 2.4). The concentrator is always pointing directly at the sun which avoids cosine losses, a major loss mechanism of solar towers. Furthermore, the distance between the reflector and the receiver is on the order of meters, which reduces atmospheric attenuation of the radiation. Losses occur due to the mirror reflectivity being below unity, mirror misalignment, tracking errors, deviations of the slope from the ideal parabolic shape, and shading of the mirror surface by the receiver. In Table 2.2, representative values of the loss mechanisms and the total concentration efficiency are shown.

The optical concentration efficiency of a solar dish surpasses that of a solar tower. However, the unit size is limited to tens of kilowatt due to constructional constraints, while solar towers can achieve power levels higher by three orders of magnitude.

Today, several tower CSP plants exist [54] and more are planned for the coming years, while solar dish systems are not seen in large industrial production, even though their solar-to-electrical conversion efficiency has been shown to reach over 30% [55] which surpasses by far that of solar towers.

Table 2.2 Annual average efficiency of solar dish concentration [56]. Intercept includes losses due to slope errors and misalignment of mirror and receiver.

Loss mechanisms	Efficiency
Mirror reflectivity	93.5%
Average mirror cleanliness	93.1%
Intercept	98.0%
Total concentration efficiency	85.3%



Figure 2.4 The Big Dish prototype at the campus of the Australian National University [56].

2.1.4 Thermochemistry

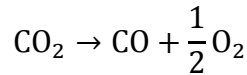
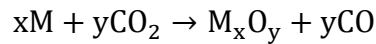
The solar thermochemical conversion of water and carbon dioxide into syngas stores solar energy in the chemical potential of hydrogen and carbon monoxide. In the following, direct thermolysis is distinguished from three different two-step cycles.

2.1.4.1 Direct thermolysis

The conceptually simplest way to thermally split H_2O and CO_2 into H_2 , CO , and O_2 , is their direct decomposition which is a one-step process that requires very high temperatures of 2500 K and above [57–59]. This high-temperature requirement makes both reactor design fairly difficult and high-temperature gas separation necessary to prevent recombination of the gases. This may be done by quenching the gas mixture which introduces a large energy penalty due to the excessive use of inert gases. Due to these challenges two-step processes have been more in the center of attention in the past years.

2.1.4.2 Two-step thermochemical cycles

To alleviate the challenges associated with thermolysis, additional steps can be introduced into the thermodynamic cycle that reduce the required upper process temperature to below 2000 K and inherently separate H₂ and CO from O₂ so that high-temperature gas separation is not required. The basis for these processes is redox reactions of a metal oxide.



The first reaction (Equation (2.2)) is the reduction of the metal oxide which is thermodynamically favored at high temperatures and low oxygen partial pressures: oxygen is removed from the metal oxide. The second reaction (Equations (2.3)) is the oxidation which brings the metal oxide back into its original state by splitting water and carbon dioxide and incorporating the oxygen back into the metal oxide lattice. The overall reaction is then the splitting of water and carbon dioxide into hydrogen, carbon monoxide and oxygen.

Many different thermochemical cycles have been investigated in the past decades, both theoretically and experimentally. The ones which have received most attention are the cycles based on ferrites, zinc oxide, and, most recently, ceria [6]. These three cycles are explained in more detail below.

Definition of energy conversion efficiency

Thermochemical energy conversion efficiency is defined as

$$\eta = \frac{n_{\text{syngas}}\Delta H_{\text{syngas}}}{Q_{\text{solar}} + Q_{\text{aux}}}, \quad (2.5)$$

where n_{syngas} is the amount of syngas produced, ΔH_{syngas} is its higher heating value, Q_{solar} is the solar energy input to the thermochemical reactor, and Q_{aux} are the thermal energy requirements of auxiliary processes such as inert gas production, vacuum pumping, or gas separation processes.

Ferrite cycle

In an early study of the two-step thermochemical cycles, Nakamura [60] suggested the ferrite cycle which encompasses the thermal dissociation of magnetite into ferrous oxide and oxygen, and the regeneration of the magnetite in the reaction of the iron oxide with water steam, producing hydrogen.



The temperatures of the reduction and oxidation reactions are approximately 2500 K and 450 K, respectively, where the high temperature required in the reduction step leads to fusing, sintering, and vaporization of the material, and eventually to an abatement of the amount of reactive material available [57,61,62]. Consequently, the reduction temperature is sought to be lowered by the introduction of mixed-metal oxides, i.e. use of $(\text{Fe}_{1-x}\text{M}_x)_3\text{O}_4$ with $\text{M} = \text{Zn}, \text{Mn}, \text{Ni}, \text{Co}$ and stabilizing it on an inert support structure made from ZrO_2 , SiO_2 or Yttria-stabilized zirconia [57,62–65].

Reactor concepts for the ferrite cycle include cavity reactors [16,66,67], fluidized bed reactors [68], packed bed reactors [69], and a multi-channel honeycomb reactor [67].

Theoretical energy conversion efficiencies of the ferrite cycle may reach 29% and above at complete material conversion without heat recovery [57,70], and above 70% for complete heat recuperation [16]. If a cycle conversion rate of 35% of magnetite to wustite is assumed, the efficiency drops to about 16% [16].

ZnO-cycle

The zinc oxide cycle is based on the reduction of ZnO at high temperatures of about 2000 K. ZnO is thermally decomposed to its constituents zinc and oxygen which consequently have to be separated at high temperatures to avoid their recombination.



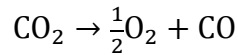
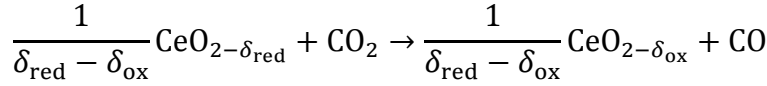
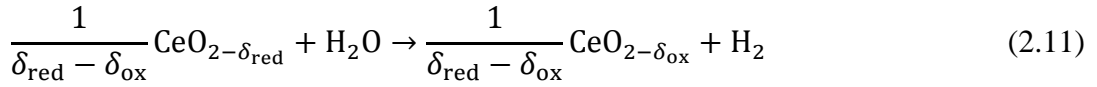
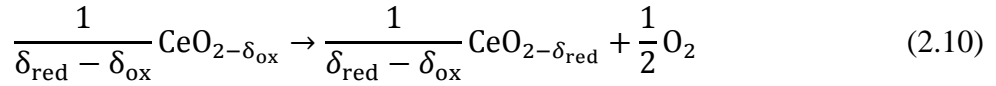
This can be done by quenching the gases in an inert gas or by electrothermal methods [71]. Oxidation of zinc has to be performed above the melting point of the material because of the reaction kinetics [61]. Further, the formation of a passivating ZnO-layer may hinder oxidation of the zinc through a limitation of mass transfer [61,72].

Several reactor concepts have been discussed and tested, such as particles entrained in a flow [72–74], stagnant particles in a tubular reactor [75], sliding particles in a cavity reactor [76], and particles in a moving cavity reactor [77–79].

The theoretical energy conversion efficiency of the ZnO-cycle is 39% without heat recovery [70] and over 80% with complete heat recovery [71]. However, experiments have reached lower values of 0.16% with a 10 kW reactor at the PSI in Switzerland [80].

Ceria cycle

Ceria has been used in both stoichiometric and nonstoichiometric cycles, where the former have shown difficulties due to vaporization of CeO₂ at the required elevated temperatures of about 2300 K [81]. The nonstoichiometric ceria cycle has received more attention in recent years and can be described with the following equations. Reduction of the material (equation (2.10)) occurs at elevated temperatures and reduced oxygen partial pressures as described by Panlener et al. [82] and shown in Figure 2.5. At lower temperatures, the material is reoxidized (equations (2.11)) by splitting water and/or carbon dioxide, thereby producing hydrogen and/or carbon monoxide. The overall reaction of the two-step process is then the splitting of water and/or carbon dioxide (equation (2.12)).



The ceria cycle has gained attention in recent years due to the high oxygen conductivity of the material [83], as well as its structural stability over large ranges of temperature and oxygen nonstoichiometry [82,84]. With these properties, fast reaction kinetics during both, reduction and oxidation, as well as a comparably simple reactor design are possible because the reactive material remains in its solid state throughout the thermochemical cycle. This obviates phase changes and high-temperature gas separation steps. A single reactor chamber can be used in a temperature-pressure swing cycle using concentrated solar energy as the source of high-temperature heat, as shown in [10].

While Chueh et al. used pure CeO_2 for their experiments, doping of the material with other elements such as Gd, Y, Sm, Ca, Sr, Fe, Ni, Mn, ZrO_2 , or CrO_2 has been analyzed theoretically and experimentally to lower the reduction temperature and to increase the oxygen nonstoichiometry [85–91].

Several different reactor concepts have been suggested in the literature, comprising a simple cavity design [10], counter-rotating rings inside a cavity [13,16,17,21,92], moving particle beds [18], and an aerosol reactor [19].

Thermodynamic analyses encompass [13,20,81,86,93] and calculated efficiencies range from below 10% without heat recovery [20] to over 30% with heat recovery [20,93].

These analyses are however either of a fundamental thermodynamic quality without a discussion of practical implementation or show detailed information on specific reactor concepts which are not easily transferrable to other concepts.

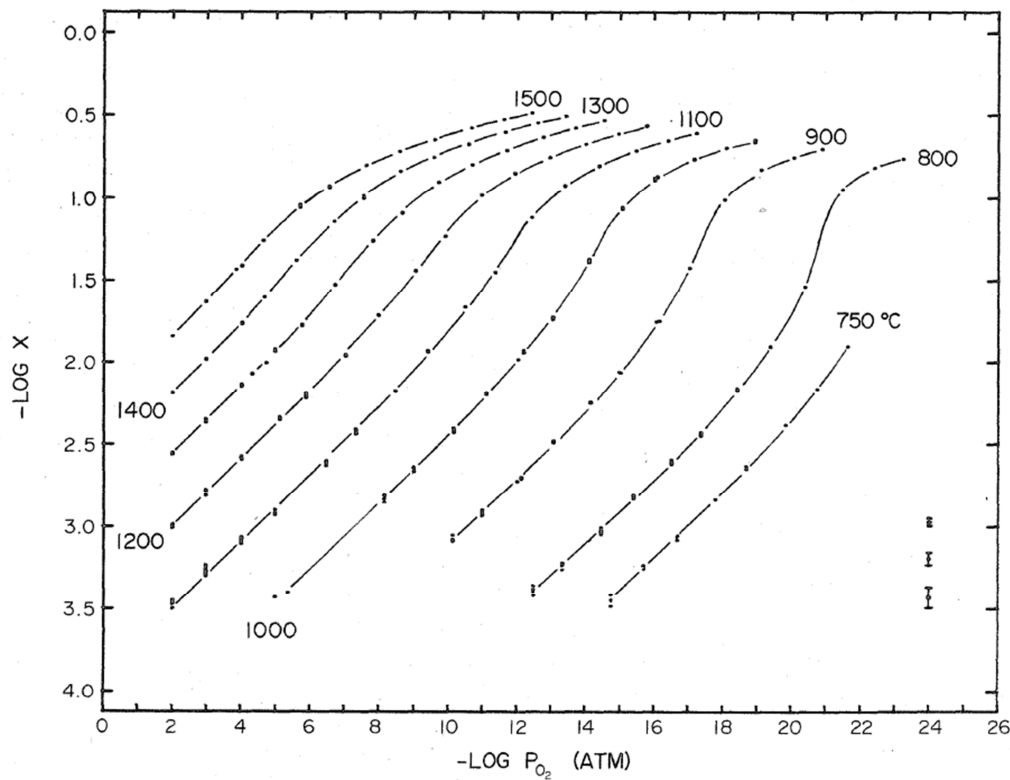


Figure 2.5 Oxygen nonstoichiometry of pure CeO_2 as a function of temperature and oxygen partial pressure (reprinted from [82] with permission from Elsevier).

To close the gap between the existing studies and to open the discussion towards the determination of efficiency potentials of many different technically relevant reactor concepts, a generic approach is required as it is suggested in this work.

2.1.5 Syngas storage

Syngas produced in the thermochemical conversion step is stored and supplied to the Fischer-Tropsch reaction where liquid fuels are produced. The storage unit provides therefore a buffer which allows the FT conversion to be run continuously day and night, which is currently a technical requirement. Furthermore, short-term drops in solar irradiation, that may deteriorate the syngas production rate, can be balanced.

Today, different syngas storage technologies exist, i.e. compressed gas, solid carriers (metal hydrides) or liquid carriers (methanol, ammonia), or cryogenic storage. Syngas being a mixture of two gases, solid and liquid carriers would need to be designed to be able to store either the gas mixture or the gases separately. For the former, it may be technically

challenging to store two gases with different properties, while for the latter, gas separation after the thermochemical reactors would be required in case of co-current syngas production. As a large storage capacity is likely to be required for an industrial size facility, a material intensive storage option such as those involving liquid or solid carriers may be too expensive or complex to handle.

Cryogenic storage involves the liquefaction of gases which requires cooling to their boiling point. In case of syngas, the boiling points of carbon monoxide (82 K) and hydrogen (20.3 K) are not the same which may necessitate two separate storage vessels that each has to be cooled and insulated to reduce heat losses to the environment. As both, the output from the thermochemical reactors and the input to the FT conversion, are gaseous, two phase changes would be necessary, introducing thermodynamic irreversibilities into the system. Furthermore, the cost of cryogenic syngas storage is estimated to be six to nine times higher than other storage options [94].

Besides liquefaction of the gases, they may also be stored at elevated pressure either in specially designed vessels above ground or in salt caverns and depleted oil fields underground. The latter may, in case of availability, reduce the storage costs, but requires special geological prerequisites that may not be present in many locations. Therefore, above-ground storage is assumed as the method of choice.

For storage of gases on a large scale, low-pressure tanks (gasometers) can be employed that operate slightly above atmospheric pressure and at volumes up to 340000 m³ [94]. Gasometers can reach life-times of 100 years for the building and about 10 years for their sealings [94].

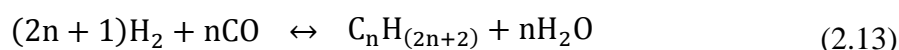
To increase the storage capacity, the syngas may be compressed to higher pressures and stored in spherical or cylindrical vessels that work at up to 550 bars and at volumes up to roughly 250 m³ per vessel [94]. In general, the storage design is modular and has a relatively low degree of economy of scale [94].

Syngas storage has reached a technology readiness level which makes it suitable for operation in an industrial environment. It is therefore not seen as a critical limiting process step in the realization of a first commercial solar fuel production facility.

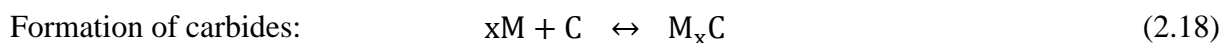
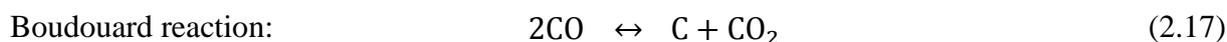
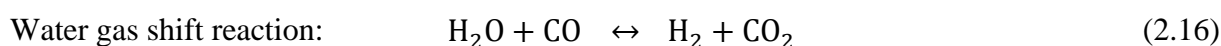
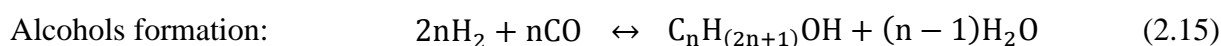
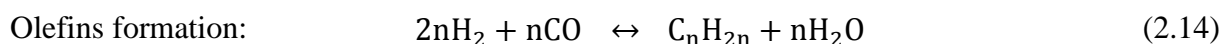
2.1.6 Fischer-Tropsch conversion

In the 1920s, at the Kaiser-Wilhelm-Institute in Berlin, Franz Fischer and Hans Tropsch developed a process to convert syngas into liquid hydrocarbons. With this technology, it is possible to convert biomass, coal, or natural gas into transportation fuels, which is especially interesting for countries with large supplies of these resources and no access to the global fuel market, as was the case for Germany during the Second World War. Today, FT conversion is used on an industrial scale to produce liquid hydrocarbons from natural gas, for example, in the Shell Pearl Gas-to-Liquids (GtL) facility in Qatar, where 140000 barrels of liquids are produced per day [95]. On the other end of the industrial scale, small companies such as Velocys or CompactGTL operate facilities on the order of a few barrels per day (bpd) [96,97].

The main reaction producing olefins can be described as follows [98]:



Other reactions are involved, such as the water gas shift reaction and others that lead to the production of alkenes, alcohols and the destruction of the catalyst through the formation of carbides [98]:



Two types of catalyst are common, either based on iron or on cobalt. The iron-based catalysts operate at temperatures of 320-350°C and produce mainly light hydrocarbons such as gasoline, while cobalt-based catalysts operate at lower temperatures of about 200-250°C and produce longer hydrocarbons, such as diesel or jet fuel [99].

Different reactor concepts have been used in the past for FT synthesis, comprising circulating fluidized beds and fixed fluidized beds for gasoline and light olefin production at 350°C and 25 bar [98]. For the production of diesel and jet fuel, as the products of main interest in the present work, two other types of reactors are interesting. The fixed-bed tubular design (see

Figure 2.6), as for example used by Shell in their Pearl GtL plant in Qatar, uses tubes filled with catalyst that are surrounded by cooling water for temperature control. The syngas enters the tubes from the top and the products exit the tubes at the bottom. Another reactor design is the slurry reactor, where the catalyst is dispersed in a liquid with a high thermal capacity such as the FT wax. Syngas is bubbled from the bottom through the slurry, achieving effective contact with the catalyst.

Temperature control is efficient because the cooling water contacts a large body of liquid. Slurry reactors can be 75% cheaper than the more complex tubular fixed bed reactors [98].

The energy efficiency of the Fischer-Tropsch conversion from syngas to gaseous and liquid hydrocarbons is close to 60% based on a rigorous analysis assuming an Anderson-Schulz-Flory distribution of the gaseous FT products with a growth factor of 0.9 and a total product distribution of 50% jet fuel, 40% naphtha, and 10% gaseous products [25].

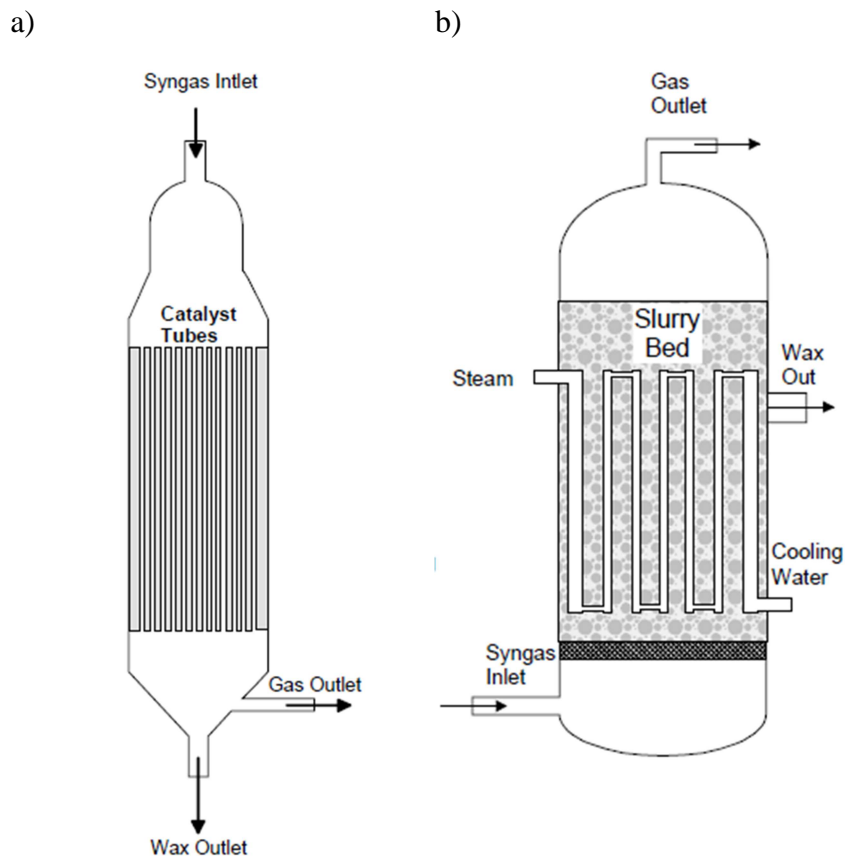


Figure 2.6 Schematic of two Fischer-Tropsch reactors: (a) Tubular fixed bed reactor, (b) slurry bed reactor for the production of long-chained hydrocarbons such as jet fuel (figure taken from [100]).

2.2 Prior research

Regarding the thermochemical conversion of ceria, several theoretical analyses have been published in recent years. A comprehensive study of ceria as a thermochemical reaction medium includes a thermodynamic and a kinetic analysis [83]. The authors indicate an efficiency potential of more than 20% without heat recovery, however, at very high reduction temperatures and not accounting for the energy required to establish the low oxygen partial pressure of 10^{-5} atm. A parametric analysis investigates the effects of solid phase and gas phase heat recovery from the ceria cycle [20]. The authors point out that improvements in both the material development as well as solid phase heat recovery are required to increase the energy conversion efficiency above 10%. The effects of doping ceria with Gd, Y, Sm, Ca, and Sr in the compound $M_x\text{Ce}_{1-x}\text{O}_2$ are analyzed in [93]. As the authors describe, even though doping reduces the reduction enthalpy, energy conversion efficiency is negatively affected, leaving pure ceria as the most efficient material in the analysis except towards very high heat recovery values. An isothermal reactor concept is viable and provides the possibility of simplified reactor design due to the fact that solid phase heat recovery is not required [13]. However, the introduction of a mild temperature swing increases the energy conversion efficiency.

More detailed concepts of thermochemical reactors based on ceria redox reactions have been published at the same time, presenting studies of reactors including heat recovery concepts. A particle reactor concept with a cylindrical cavity exchanges heat through the wall of the cavity between the reduced and oxidized particles to enable solid phase heat transfer [18]. Another reactor concept exchanges solid phase heat between two rotating cylinders. Both cylinders rotate in opposite direction in a cavity open to concentrated solar radiation on one side and insulated on the others. The authors claim that a heat recovery effectiveness of over 80% is possible with their system [17,21]. A detailed concept of an isothermally operated reactor is presented in [92]. A reactor concept that consists of reducing ceria particles falling through the heated section of a tube is shown in [19]. Through the counter-flow of inert gases from the bottom of the tube, the particles and the resulting oxygen are inherently separated.

Economic analyses of solar fuels in the literature comprise methanol production [23], hydrogen generation [101,102], and fuels based on solar thermochemistry [3,5]. However, concerning the fuel production path shown in Figure 2.1, the number of publications is small.

Kim et al. assume CO₂ capture from a fossil power plant, where the emissions are allocated to the plant and not the fuel production, a conversion efficiency of 20% from incident sunlight to syngas which is converted to liquid fuels via Fischer Tropsch conversion, and arrive at a minimum selling price of about 1.50 € L⁻¹ of gasoline equivalent [5]. For the same fuel production pathway, Kim et al. [24] investigate the environmental impact of the fuels and indicate well-to-tank emissions for gasoline of -1.58 kg_{CO₂-equiv.} L⁻¹ which corresponds to well-to-wake emissions of 0.74 kg_{CO₂-equiv.} L⁻¹, about 30% of the CO₂ emissions from conventional gasoline [103].

3 Reactor modeling

This chapter comprises three modular and generic models for the description of a large number of solar thermochemical reactor concepts. The models have a common approach for the calculation of thermal heat transfer and chemical reactions in the reduction and oxidation chambers but differ in their description of energy transfer in the heat exchanger. In the following Section 3.1, the common modeling of the reaction chambers along with assumptions are described. In Sections 3.2-3.4, three heat exchanger models are presented that allow the description of solar thermochemical reactors using solid elements and particles of reactive material.

3.1 Modeling of reduction and oxidation reactions

Reduction and oxidation are modeled on a fundamental thermodynamic level by formulating the energy balance of both reaction chambers which are assumed to be closed systems at constant temperature and pressure. The extent of reaction is derived based on known values of enthalpy and entropy in the literature assuming thermodynamic equilibrium (see Section 3.1.3.1). The accommodation of multiple elements in each of the reaction chambers enables the decoupling of residence times in the heat exchanger from those of the chemical reactions. By choosing a specific number of elements for each of the chambers, the residence times are chosen such that reduction and oxidation proceed to completion. Modeling of the kinetics of the chemical reactions, which requires a detailed knowledge of gas concentrations and therefore fluid dynamics in the reaction chambers, is not part of the research performed in this thesis. The specific properties of the reduction and oxidation chamber are explained in the following.

3.1.1 Reduction reaction

Concentrated solar radiation is directly incident on the reactive material in the reduction chamber which is assumed to be a well-insulated cavity and thus to lose heat by reradiation

only. Losses to the surroundings due to convection and due to active cooling of the reactor are neglected. The cavity design of the reduction chamber allows concentrated solar radiation to enter through a small opening and to be effectively absorbed through multiple reflections on the inside. Direct impingement of the radiation on the reactive material provides effective heat transfer as shown in the literature [10,15,16,78], where the specific design of the chamber is not part of this study. A vacuum pump keeps the pressure at the prescribed level by removing oxygen that evolves from the material during reduction (see Figure 3.1).

3.1.2 Oxidation chamber

Oxidation is performed in a chamber with constant temperature and pressure which is insulated towards the surroundings to reduce heat losses. As the solar radiation input is limited to the reduction chamber, the constant temperature is kept by the energy of the exothermal reaction which is assumed to balance the heat losses towards the environment. In the literature, it has been shown that oxidation can be performed with a reticulated porous ceramic made from ceria even in a cavity with an opening to the surroundings without the input of solar radiation to maintain the temperature [15]. Operation in a closed chamber without a constant opening therefore reduces heat losses during oxidation and is thus considered to be feasible.

3.1.3 Governing equations

3.1.3.1 Calculation of nonstoichiometry

Without loss of generality of the approach, we consider nonstoichiometric ceria as the reactive material. Application to other materials is straightforward if the respective material properties are known. Solid pieces of ceria are reduced at an elevated temperature T_H and a reduced oxygen partial pressure p_{O_2} . The level of oxygen nonstoichiometry is increased from δ_{ox} after oxidation to δ_{red} after reduction, see Equation (2.10).

When the reduction reaction is completed, the ceria pieces are passed to the oxidation chamber through the heat exchanger, where heat is exchanged through radiation with oxidized pieces moving in the lower half of chambers in the opposite direction. In each heat exchanger

chamber, the pieces have a residence time Δt before they pass on to the next one. As the reaction kinetics may require different times, the residence times in the reaction chambers and the heat exchanger are decoupled by allowing a different number of pieces in the reduction and oxidation chamber (Figure 3.1). Following the argument of Tsotsas and Martin, convection within each chamber half is assumed to be small and is therefore neglected [104].

Heat between the ceria pieces is solely exchanged through radiation. The upper half of the chambers is assumed to be separated from the lower one through a barrier in order to ensure separation of gases, to prevent recombination and thus enabling high efficiencies in the reactor. In the first model, the separating wall is assumed not to hinder heat exchange between the reduced and oxidized ceria pieces, which should be fulfilled for the separating wall having high thermal conductivity and emissivity, and being in direct contact with either piece in steady state operation: the separating wall will then immediately assume the temperature of the element being in direct contact and emit radiation with high emissivity. The separating wall then acts like a coating on the ceria surface rather than a radiation shield.

In the oxidation chamber, the reduced ceria is contacted with carbon dioxide to reoxidize the material (see Equations (2.11)). Carbon dioxide is split into oxygen and carbon monoxide, where the oxygen enters the ceria lattice and carbon monoxide is captured. Oxidation can also be achieved with water steam to produce hydrogen or with a mixture of both oxidants to produce syngas directly [105]. In the following, CO_2 shall be used as an oxidant without loss of generality. In theory, the stoichiometric amount of oxidant could be supplied to the reactor to produce pure carbon monoxide. For reasons of thermodynamic driving force and kinetics, however, an excess amount of oxidant is supplied, resulting in a mixture of CO and CO_2 at the exit of the oxidation chamber. As the Fischer-Tropsch (FT) reactor works best with only small amounts of CO_2 contamination in the syngas and in order to recycle excess oxidant, separation of the CO/CO_2 gas is performed.

For the reduction of oxygen partial pressure, a pump is assumed to evacuate the reduction chamber to a defined value of p_{O_2} . As the heat exchanger connects the reaction chambers which are at different total pressure levels, the pressure in the heat exchanger would rise linearly from the low pressure of the reduction chamber to the high pressure in the oxidation chamber. To prevent the oxidant from entering the heat exchanger and from reaching the reduction chamber, the heat exchanger is kept at the reduction pressure by evacuating the second-to-last chamber next to the oxidation chamber (labeled “ $n-1$ ” in Figure 3.1). Were this

additional evacuation not implemented, the reduced ceria pieces in the intermediate heat exchanger chambers would be partially oxidized before the oxidation chamber and oxygen and oxidant would mix in the reduction chamber. To prevent a possible recombination and therefore loss of product, the additional evacuation is performed.

The oxygen nonstoichiometry δ_{ox} of the reduction reaction has been experimentally analyzed by Panlener et al. [82] as a function of oxygen partial pressure and temperature. A function fitted to the experimental data is used to calculate δ_{red} in the reduction chamber [18]. The oxidation reaction is the sum of the reverse reduction reaction Equation (2.10) and carbon dioxide splitting Equation (2.11). The former can be described by

$$\Delta G_{\text{O}_2}(T_L, \delta_{\text{ox}}) = \mathcal{R}T_L \ln K = \mathcal{R}T_L \ln p_{\text{O}_2}, \quad (3.1)$$

where $\Delta G_{\text{O}_2}(T_L, \delta_f)$ is the oxygen molar free energy, T_L the oxidation temperature, K the thermodynamic equilibrium constant of the overall reaction and p_{O_2} the oxygen partial pressure relative to the standard state of 1 atm. The oxygen partial pressure can be derived from

$$K_{\text{CO}_2} = \frac{p_{\text{CO}} p_{\text{O}_2}^{\frac{1}{2}}}{p_{\text{CO}_2}}. \quad (3.2)$$

The equilibrium partial pressure of CO_2 is calculated from a mass balance of the closed system

$$p_{\text{CO}_2} = \frac{\dot{n}_{\text{CO}_2,i} - (\delta_{\text{red}} - \delta_{\text{ox}})\dot{n}_{\text{CeO}_2}}{\dot{n}_{\text{total}}} = \frac{(f_{\text{CO}_2} \delta_{\text{red}} - (\delta_{\text{red}} - \delta_{\text{ox}}))\dot{n}_{\text{CeO}_2}}{\dot{n}_{\text{total}}}. \quad (3.3)$$

$\dot{n}_{\text{CO}_2,i}$ is the molar flow rate of CO_2 entering the oxidation chamber, $(\delta_{\text{red}} - \delta_{\text{ox}})\dot{n}_{\text{CeO}_2}$ is the molar flow rate of CO produced (and CO_2 consumed) and \dot{n}_{total} the total molar flow rate of gases. The partial pressure of CO is

$$p_{\text{CO}} = \frac{(\delta_{\text{red}} - \delta_{\text{ox}})\dot{n}_{\text{CeO}_2}}{\dot{n}_{\text{total}}}. \quad (3.4)$$

Solving Equation (3.2) for the oxygen partial pressure gives

$$p_{O_2} = \left(\frac{K_{CO_2} p_{CO_2}}{p_{CO}} \right)^2. \quad (3.5)$$

Putting Equation (3.5) into Equation (3.1), inserting Equations (3.3)-(3.4) and rewriting the partial molar free energy of lattice oxygen as a sum of enthalpy and entropy gives

$$\Delta H_O(T_L, \delta_{ox}) - T_L \Delta S_O(T_L, \delta_{ox}) = \mathcal{R} T_L \ln \left(\frac{K_{CO_2} p_{CO_2}}{p_{CO}} \right) \quad (3.6)$$

$$= \mathcal{R} T_L \ln \left(\frac{K_{CO_2} (f_{CO_2} \delta_{red} - (\delta_{red} - \delta_{ox}))}{(\delta_{red} - \delta_{ox})} \right), \quad (3.7)$$

where ΔH_O , ΔS_O and K_{CO_2} are known functions of temperature and nonstoichiometry.

By specifying the amount of CO_2 supply f_{CO_2} and δ_{red} (through a fitted function to experimental values), the above equation can then be solved for δ_{ox} .

3.1.3.2 Energy balance

Energy that is required to move ceria is neglected, as in [18] it has been shown to be a negligible amount for the case of ceria particles. Energy available from the exothermic oxidation reaction is assumed to stabilize the ceria temperature in the oxidation chamber where there is no solar energy input and any additional energy to be lost.

The overall energy balance of the system is

$$\begin{aligned} \dot{Q}_{solar} + P_{aux} - \dot{Q}_{heat,CeO_2} - \dot{Q}_{red,CeO_2} - \dot{Q}_{heat,CO_2} \\ + \dot{Q}_{products} - \dot{Q}_{rerad} - P_{pump,vacuum} - P_{sep,CO_2} = 0, \end{aligned} \quad (3.8)$$

where \dot{Q} denotes the flow of thermal energy and P the flow of mechanical or electrical energy. In the derivation of the thermodynamic cycle efficiency η , P is converted to \dot{Q} to establish a common form of energy (Equation (3.17)).

The solar radiative power input to the reactor is

$$\dot{Q}_{solar} = \frac{1}{\eta_{abs}} (\dot{Q}_{heat,CeO_2} + \dot{Q}_{red,CeO_2} + \dot{Q}_{heat,CO_2} - \dot{Q}_{products}), \quad (3.9)$$

where η_{abs} is the absorption efficiency of the solar reduction chamber and is calculated with the assumption of a well-insulated blackbody cavity, leading to reradiation losses of $\dot{Q}_{\text{rerad}} = (1 - \eta_{\text{abs}})\dot{Q}_{\text{solar}}$.

$\dot{Q}_{\text{heat,CeO}_2}$ is the rate of heat required to increase the temperature of the oxidized ceria piece from the temperature at the exit of the heat exchanger $T_{2,1}$ to the reduction temperature T_{H} ,

$$\dot{Q}_{\text{heat,CeO}_2} = (1 - \eta_{\text{he}})\dot{n}_{\text{CeO}_2} \int_{T_{\text{L}}}^{T_{\text{H}}} c_{p,\text{CeO}_2}(T) dT. \quad (3.10)$$

The required thermal power input to heat ceria is reduced by the amount of heat recovered from the solid phase in the heat exchanger with an efficiency of η_{he} which is defined as

$$\eta_{\text{he}} = \frac{\int_{T_{\text{L}}}^{T_{2,1}} c_{p,\text{CeO}_2}(T) dT}{\int_{T_{\text{L}}}^{T_{\text{H}}} c_{p,\text{CeO}_2}(T) dT}, \quad (3.11)$$

where $T_{2,1}$ is the temperature of the ceria piece at the end of the heat exchanger before entering the reduction chamber.

$\dot{Q}_{\text{red,CeO}_2}$ is the rate of energy required to reduce the material from δ_{ox} to δ_{red}

$$\dot{Q}_{\text{red,CeO}_2} = \dot{n}_{\text{CeO}_2} \Delta H_{\text{red}} = \dot{n}_{\text{CeO}_2} \int_{\delta_{\text{ox}}}^{\delta_{\text{red}}} \Delta H_{\text{CeO}_2}(\delta) d\delta. \quad (3.12)$$

ΔH_{CeO_2} is only weakly dependent on temperature and pressure and is thus taken to be a function of the nonstoichiometry only. Values for the reduction enthalpy as a function of oxygen nonstoichiometry are taken from Panlener et al. [82].

$\dot{Q}_{\text{heat,CO}_2}$ is the thermal power to heat CO_2 from ambient conditions to the oxidation temperature

$$\dot{Q}_{\text{heat,CO}_2} = \dot{n}_{\text{CO}_2} \int_{T_0}^{T_{\text{L}}} c_{p,\text{CO}_2}(T) dT. \quad (3.13)$$

$\dot{Q}_{\text{products}}$ is the thermal power that can be recovered from the gases leaving the reduction and oxidation zones (O_2 , CO , CO_2) with an efficiency of η_{gasrec} .

$$\dot{Q}_{\text{Products}} = \eta_{\text{gasrec}} \left(\dot{n}_{\text{CO}} \int_{T_0}^{T_L} c_{p,\text{CO}}(T) dT + \dot{n}_{\text{CO}_2} \int_{T_0}^{T_L} c_{p,\text{CO}_2}(T) dT + \dot{n}_{\text{O}_2} \int_{T_0}^{T_L} c_{p,\text{O}_2}(T) dT \right). \quad (3.14)$$

A distinction is made in the calculation of the pumping power between the idealized case of isothermal pumping and a more practically relevant case based on data from a pump manufacturer [106,107]. In both cases, the released oxygen in the reduction chamber and the oxidant lost through the opening of the oxidation chamber has to be removed.

The isothermal pumping power for the idealized case is [41]

$$P_{\text{pump,idealized}} = \dot{n}_{\text{O}_2} \mathcal{R} T_{\text{pump}} \ln(p_{\text{O}_2}^{-1}) \quad (3.15)$$

The molar flow rate of oxygen \dot{n}_{O_2} is calculated from stoichiometry of the overall reaction as half of the flow rate of evolving carbon monoxide, the temperature T_{pump} of the vacuum pump is assumed to be the ambient temperature and p_{O_2} is the partial pressure of oxygen in the reduction chamber. The realistic pumping work is calculated through fitting a function to actual vacuum pump electrical power consumption data provided by a manufacturer [106,107], where the derivation is shown in the annex. The realistic pump efficiency thus is $\eta_{\text{pump,realistic}} = 0.8437 p_{\text{O}_2}^{0.3662}$, where the realistic pump power $P_{\text{pump,realistic}}$ is calculated by dividing the thermodynamic power by the realistic pump efficiency at the chosen oxygen partial pressure.

Especially towards lower pressures, the required power for pressure reduction shows a strong deviation from the theoretical limit as the parasitic power consumption of a realistic vacuum pump becomes dominant. Also for the CO/CO₂ separation a theoretical and a practically relevant description of the required power input is chosen. For the idealized case, the rate of thermodynamic separation work is [41]

$$P_{\text{sep,CO/CO}_2,\text{idealized}} = (\dot{n}_{\text{CO}} + \dot{n}_{\text{CO}_2}) \mathcal{R} T_0 \left(c_{\text{CO}} \ln \frac{1}{c_{\text{CO}}} + (1 - c_{\text{CO}}) \ln \frac{1}{(1 - c_{\text{CO}})} \right). \quad (3.16)$$

\dot{n} is the flow rate of gas and c is the gas concentration. The separation is assumed to be complete, i.e. pure streams of CO and CO₂ are produced. This level of purity may not be

required for the syngas conversion but represents the ideal case of complete oxidant recycling and undisturbed FT reaction and is therefore assumed here. For the case of the practically relevant separation work, literature data for the capture of CO₂ from a flue gas stream from a fossil power plant have been chosen as a reference. 132 kJ of heat and 9 kJ of electricity are thus required for the capture of one mol of CO₂ [108].

The required auxiliary power input $P_{\text{aux}} = P_{\text{pump}} + P_{\text{sep,CO/CO}_2}$ is divided by the efficiency of the conversion of heat to electricity $\eta_{\text{heat-to-electricity}}$ to arrive at the auxiliary heat input $\dot{Q}_{\text{aux}} = P_{\text{aux}}/\eta_{\text{heat-to-electricity}}$. This conversion to heat is performed to establish a common energy basis in the following definition of thermodynamic cycle efficiency. As however different ways exist to convert heat to electricity with different efficiencies, the distinction between parasitic power and heat is nevertheless important.

The efficiency of the reactor is defined as

$$\eta = \frac{\text{chemical energy stored in product}}{\text{solar power into reactor} + \text{auxiliary power}} = \frac{\dot{n}_{\text{CO}} \text{HHV}_{\text{CO}}}{\dot{Q}_{\text{solar}} + \dot{Q}_{\text{aux}}}. \quad (3.17)$$

This definition assumes the energy input to the reactor to be accounted at the system boundary of the reactor, i.e. the concentration efficiency and the primary energy conversion efficiency for auxiliary power can be included depending on the chosen technologies.

3.2 Generic chamber model - Idealized internal heat transfer

3.2.1 Introduction

The presented model in this analysis is a generic approach to parametrically describe the most important aspects of solar reactors working with solid elements of reactive material and enables to investigate very different concepts from the batch-operated processes to quasi-continuous counter-flow arrangements. So far analyses have either focused on a specific reactor concept or on basic considerations without conceptual implementation. Therefore it is worth investigating a reactor model that is able to explore upper-bound performance limits and specific concepts in a wide design space, in order to gain further insight into crucial aspects for achieving high efficiencies.

Parts of this chapter were published in: Falter, C. P., Sizmann, A., and Pitz-Paal, R., 2015, "Modular reactor model for the solar thermochemical production of syngas incorporating counter-flow solid heat exchange," *Solar Energy*, 122, pp. 1296–1308 [109].

3.2.2 Prior research

In the past couple of years, the development of solar reactors has included non-volatile redox reactions of ceria that do not fully reduce the metal oxide but rather stop at an earlier stage to retain the reactive material in the solid phase [9–13]. Consequently, this does not allow achieving the same level of reduction and therefore yield per mass of oxide per cycle. However, contrary to the Zn/ZnO-cycle, for example, gaseous products are not prone to recombine which allows a simpler reactor and process design, as now only a single vessel is minimally required. First experiments show promising results with respect to technical viability and achieved cycle efficiency [10,11,14].

Theoretical analyses of the ceria cycle comprise the following publications. In [83], a thermodynamic analysis of solar syngas production based on a two-step thermochemical ceria cycle is presented. The thorough analysis includes thermodynamics and kinetics, as well as an experimental demonstration of stable hydrogen production over 500 cycles on a ceria sample with the mass of one gram. In their theoretical efficiency calculations, the authors include reradiation losses and equilibrium thermodynamics of both the reduction and oxidation

reaction but do not take into account the energy necessary to establish the oxygen partial pressure of 10^{-5} atm. Over 20% efficiency without heat recovery is shown to be achievable given the assumptions made.

In [20], the effects of solid phase and gas phase heat recovery from a two-step solar thermochemical cycle based on ceria are investigated in a parametric analysis. The authors point out that improvements in both the material development as well as solid phase heat recovery are required to increase the energy conversion efficiency above 10%. Solid phase heat recovery also allows reducing the reduction temperature and thus a simpler reactor design.

The effects of doping ceria with Gd, Y, Sm, Ca, and Sr in the compound $M_x\text{Ce}_{1-x}\text{O}_2$ are analyzed by using the assumption of an ideal solution mixture in combination with a defect interaction model in [93]. As the authors describe, even though doping reduces the reduction enthalpy, energy conversion efficiency is negatively affected, leaving pure ceria as the most efficient material in the analysis except towards very high heat recovery values.

Among the reactor concepts working with non-volatile redox reactions of metal oxides, three different approaches may be distinguished. Firstly, a continuously rotating and heat recuperating concept was presented by Diver et al. [16] where rings of reactive material are heated and reduced on one side and oxidized on the other. Through the counter-rotation of adjacent rings, heat recuperation is achieved. A similar concept was recently presented in [17,21]. Secondly, in 2009, a batch reactor concept was developed at ETH Zurich that uses ceria for syngas production [10] and which has been further progressed in recent years [11,14,15,105,110]. Inert gases are used for the reduction of the oxygen partial pressure which also limits the efficiency potential, as shown by Ermanoski et al. [18]. Thirdly, reactor concepts based on the movement of particles have been presented that use i) a continuous feeding process, counter-flow heat exchange and gas separation through packed beds of particles [18] or ii) a downward movement of particles in counter-flow with an inert gas [19]. Besides these three concepts, recently, an isothermal reactor concept has been proposed that tries to alleviate the necessity for solid heat recuperation through a pressure swing process operating at constant temperature throughout reduction and oxidation [12,13,92]. A parametric analysis is performed in [13] to investigate the influence of different variables on the energy conversion efficiency. The authors conclude that the general concept of isothermal cycling is viable and provides the possibility of simplified reactor design due to the fact that

solid phase heat recovery is not required. However, the authors also state that the introduction of a temperature swing on the order of 100 K is going to increase the energy conversion efficiency over the isothermal concept. The operation at a constant high temperature makes very high gas recuperation efficiencies necessary to achieve high overall cycle efficiency. The development of solid heat recuperation concepts as modeled in this paper is therefore seen to be crucial for highly efficient reactors.

From the different concepts and their analyses shown above, prerequisites for a highly efficient reactor concept can be deduced, i.e. heat recuperation and gas separation, besides others, as also shown and analyzed in previous studies on reactor concepts [13,17,18,20–22].

As analyses so far have either focused on a specific reactor concept or on basic considerations without conceptual implementation, it is worth investigating a reactor model that is able to explore upper-bound performance limits and specific concepts in a wide design space, in order to gain further insight into crucial aspects for achieving high efficiencies. With respect to a related analysis that focuses on a particle reactor concept [18] which is used for the validation of the presented model, further generalization and development is sought through the use of a realistic pump efficiency and modeling of the oxidation reaction and the heat exchange. The presented model in this analysis is therefore a generic approach to parametrically describe the most important aspects of solar reactors and enables to investigate very different concepts from the batch-operated processes to quasi-continuous counter-flow arrangements. In the following, the model is presented and demonstrated with an example. This will be the basis to gain more insight into favorable reactor design in the future through a variation of the parameters, e.g. the number of heat exchanger chambers or residence time.

3.2.3 Model description

A generic reactor concept for a two-step thermochemical process is described consisting of a reduction chamber, intermediate chambers for heat exchange and an oxidation chamber (Figure 3.1).

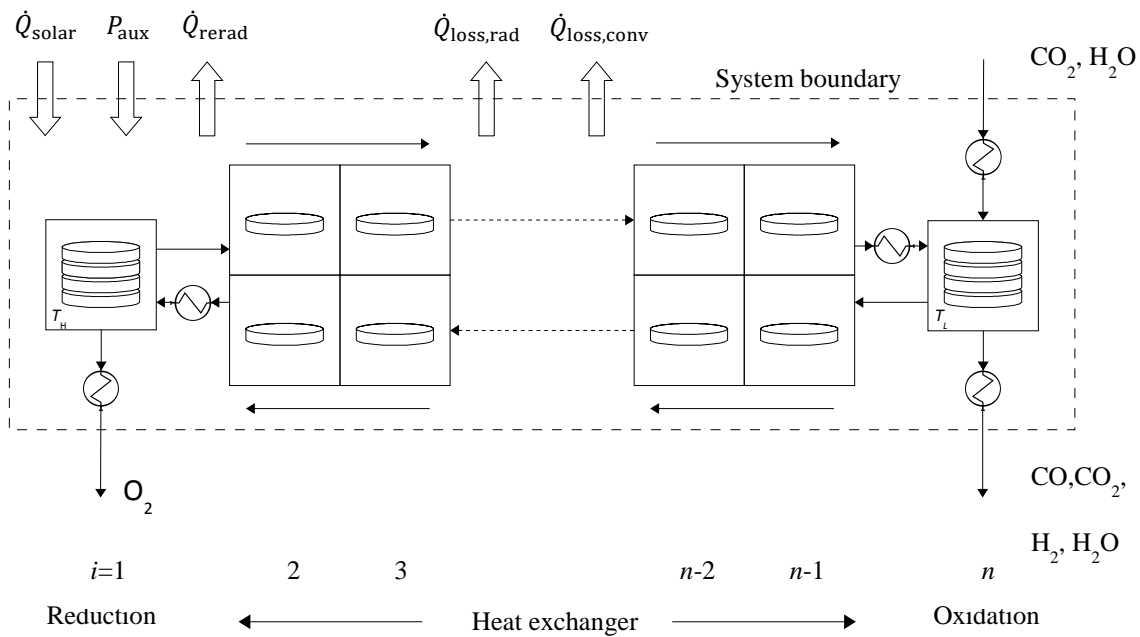


Figure 3.1 Schematic of generic reactor model including n chambers, one each for reduction ($i=1$) and oxidation ($i = n$), and $n-2$ physical heat exchanger chambers ($i = 2 \dots n-1$), each containing the mass m of reactive material. Each heat exchanger chamber is subdivided in an upper and a lower half-chamber by a gas-tight separating wall.

With initial species concentrations and constant temperatures in the reaction chambers, equilibrium thermodynamics and species conservation are used to calculate the nonstoichiometry and the amount of fuel produced. The evolving temperatures in the heat exchanger are calculated with a lumped parameter model that applies conservation of energy between the thermal energy stored in the ceria elements, internal radiative heat exchange and energy lost to the surroundings by radiation and convection.

The reactor concept consists of $(n-2)$ heat exchanger chambers in order to allow the description of technically feasible heat exchanger concepts working with experimentally proven sizes of elements of reactive material. For example, the batch-reactor concept [10,11,14,15] could be improved through the introduction of a small number of heat exchanger chambers operating between a reduction and oxidation chamber. In the analysis of the example system below, ceria elements of 1 kg are used as is roughly the case in [14].

Heat exchanger

The temperature of the ceria pieces in the heat exchanger is calculated with an energy balance of the single chambers (sample chamber shown in Figure 3.2), where a transient lumped

parameter model with $(n-2)$ control volumes, each subdivided into upper and lower chamber halves, is used to calculate the steady state. Heat is transferred between the upper and lower chamber half through radiation and heat is lost to the environment through convection and radiation, where the outer wall temperature of the heat exchanger is assumed to have a constant value of 373 K and the wall emissivity to be 0.5.

The energy balance of the element in one chamber half of the heat exchanger is

$$\frac{dE}{dt} = mc_{p,\text{CeO}_2} \frac{dT}{dt} = \mp \dot{Q}_{\text{heat exchange}} - \dot{Q}_{\text{loss,rad}} - \dot{Q}_{\text{loss,conv}}, \quad (3.18)$$

where the negative sign in front of the net heat exchange rate $\dot{Q}_{\text{heat exchange}}$ is for the upper chamber and the positive sign is for the lower chamber half. $\dot{Q}_{\text{loss,rad}}$ and $\dot{Q}_{\text{loss,conv}}$ are the losses due to radiation and convection, respectively.

The radiation heat transfer to the adjacent half of the chamber is modeled with

$$\dot{Q}_{\text{heat exchange}} = \frac{A_{\text{he,int}} \sigma (T_{k,u}^4 - T_{k,l}^4)}{\frac{1}{\varepsilon_u} + \frac{1}{\varepsilon_l} - 1}, \quad (3.19)$$

i.e. the formula for heat exchange between parallel flat plates with a view factor of 1 due to the close proximity [16,111]. σ is the Stephan-Boltzmann constant, $T_{k,u}$ and $T_{k,l}$ are the temperatures of the upper and lower half of the k -th chamber, respectively. The heat propagation into the material is assumed to proceed at a large rate compared to the rate of radiative heat exchange.

This is approximately the case e.g. for materials with a high thermal conductivity, a low thermal mass, a favorable geometry or intra-chamber intermixing particles. In a concrete technical realization, the propagation of heat in the material depends on the geometry, the porosity and density of the material, besides others, and can, depending on its value, significantly influence the heat exchanger efficiency, as will be shown in an example below.

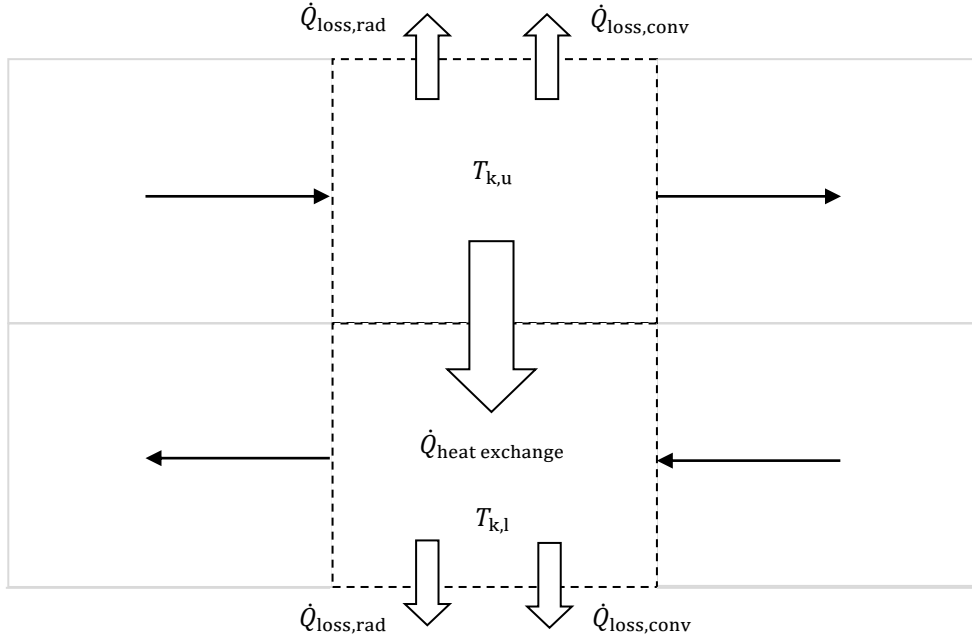


Figure 3.2 Schematic of upper and lower heat exchanger control volumes in the k -th chamber between two chamber openings, i.e. for $t \in [n\Delta t; (n+1)\Delta t]$. Heat is transferred by radiation from the upper chamber at $T_{k,u}$ to the lower chamber at $T_{k,l}$ and energy is lost to the surroundings by radiation and convection.

Firstly, however, to gain fundamental insight into the upper bound of efficiency and in order not to limit the model to the analysis of specific system realizations, the assumptions above are chosen.

From basic geometry, the total length of the heat exchanger is $L_{\text{he,total}} = (n - 2) \times L_{\text{chamber}}$, where $L_{\text{chamber}} = \sqrt{A}$ for the assumed quadratic heat exchange area of a single chamber, the total internal area is $A_{\text{he,int,total}} = (n - 2) \times A$, the total area facing the environment is $A_{\text{he,ext,total}} = 6 \times A_{\text{he,int,total}}$. For a single chamber half, the external area $A_{\text{he,ext}}$ is thus three times the internal area $A_{\text{he,int}} = A$. Radiation heat transfer from the reactor wall to the environment is

$$\dot{Q}_{\text{loss,rad}} = \varepsilon_{\text{wall}} A_{\text{he,ext}} \sigma (T_{\text{he,wall}}^4 - T_0^4). \quad (3.20)$$

Heat loss to the environment by convection is

$$\dot{Q}_{\text{loss,conv}} = \alpha A_{\text{he,ext}} \Delta T = \alpha A_{\text{he,ext}} (T_{\text{he,wall}} - T_0), \quad (3.21)$$

where $T_{\text{he,wall}}$ is the temperature of the heat exchanger wall facing the surroundings which is assumed to be 373 K, and the convective heat transfer coefficient α is taken to be $15 \text{ W m}^{-2} \text{ K}^{-1}$ [112].

3.2.4 Boundary conditions

Heat transfer through the insulation and reactor walls is not modeled here but rather a fixed temperature of the outside of the reactor walls is assumed. In general, the insulation is designed to reduce heat losses to the surroundings by bringing the temperature of the reactor wall close to the temperature of the environment. This requires the limitation of heat transfer by radiation and conduction: a large extinction coefficient to resist radiation heat transfer at high temperatures, and a low thermal conductivity to resist conduction at lower temperatures. This can either be achieved by using a single material which combines these features, e.g. highly porous alumina [113], or by adding different materials with specific properties that resist heat transfer in a defined temperature range. Heat is then lost to the surroundings by convection and radiation from the reactor walls which are assumed to have a temperature of 373 K and an emissivity of 0.5, while the surroundings are at a temperature of 300 K.

3.2.5 Material properties

Values for the reduction enthalpy as a function of oxygen nonstoichiometry are taken from [82]. The properties of CO_2 and all other gases have been calculated with tables from [114]. The emissivities ε_u and ε_l are both functions of temperature [115]. The emissivity of the CeO_2 -RPC is taken from [116] and the specific heat capacity of solid CeO_2 from [117].

An overview of the material properties used for the calculations is shown in Table A.5 and Table A.6 in the Annex.

3.2.6 Numerical solution

Through the formulation of energy conservation equations for each chamber, a non-linear system of equations is defined which are discretized in time with the explicit Euler scheme. The system of equations is then solved for each time step in Matlab. Starting from a first guess of the temperature distribution in the heat exchanger, the parallel calculation of temperature evolution in all heat exchanger chambers is continued until a steady state is reached, i.e. until the maximum change in temperature of the control volumes after two consecutive time steps is smaller than 0.001 K.

3.2.7 Model validation

To give credibility to the developed model, its results are compared with data from the recent literature. As comparable models have been introduced recently that describe reactor concepts using also a more generic approach, a validation by comparison with these data is sought. For this purpose, the presented model is adapted to describe the respective literature model to allow for a comparison of results. Two models are chosen for the comparison. The first literature model is a particle reactor concept which is approached with fundamental thermodynamic modeling in [18].

For the comparison, the generic model is adjusted to match the assumptions made in the literature: the changes comprise an adjustment of chamber number and residence time to match the recuperation efficiency, the adoption of a similar formulation of thermodynamic cycle efficiency, the assumption of complete reoxidation of the material at the prescribed oxidation temperature, the assumption of the thermodynamic minimum for the vacuum pumping work, and the choice of identical system parameters such as temperatures, pressures and component efficiencies, besides others. At $p_{\text{O}_2} = 10^{-3}$, the model in [18] and the generic model predict efficiencies of 35.3% and 34.9%, respectively. For a variation of the oxygen partial pressure between 1 and 10^5 Pa and otherwise constant parameters, the average deviation between the calculated efficiency and the literature values is 1.5% (Figure 3.3).

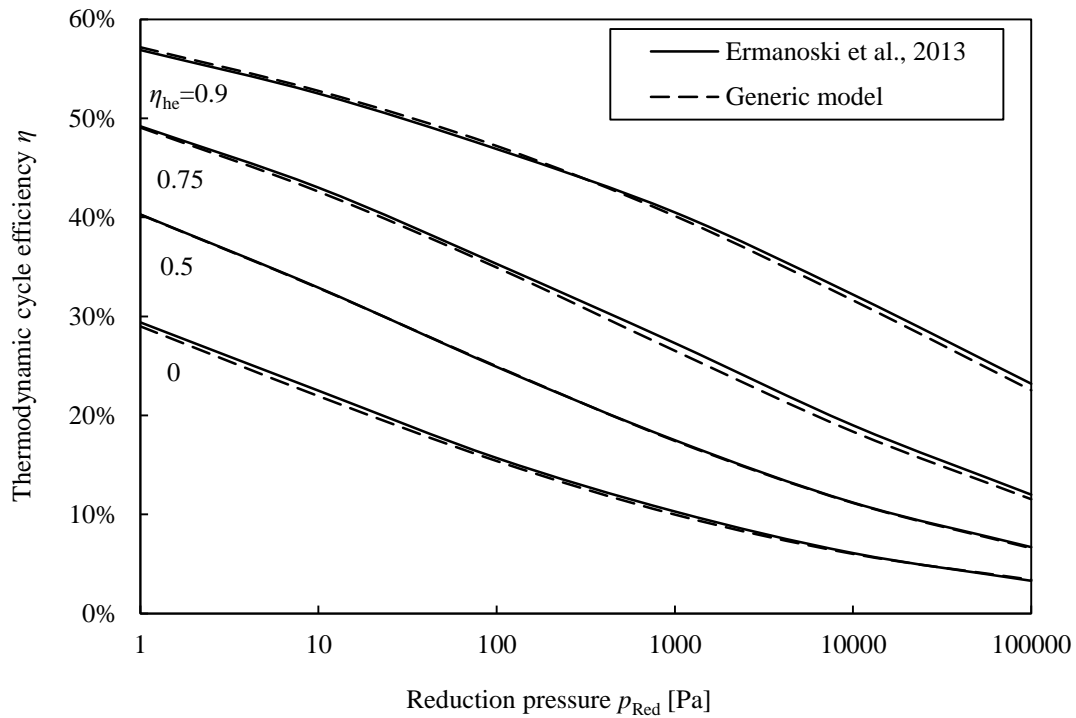


Figure 3.3 Comparison of results of the generic model and of the model by Ermanoski et al. in [18]. Shown are values of thermodynamic cycle efficiency η as a function of reduction pressure p_{red} and heat exchanger efficiency η_{he} .

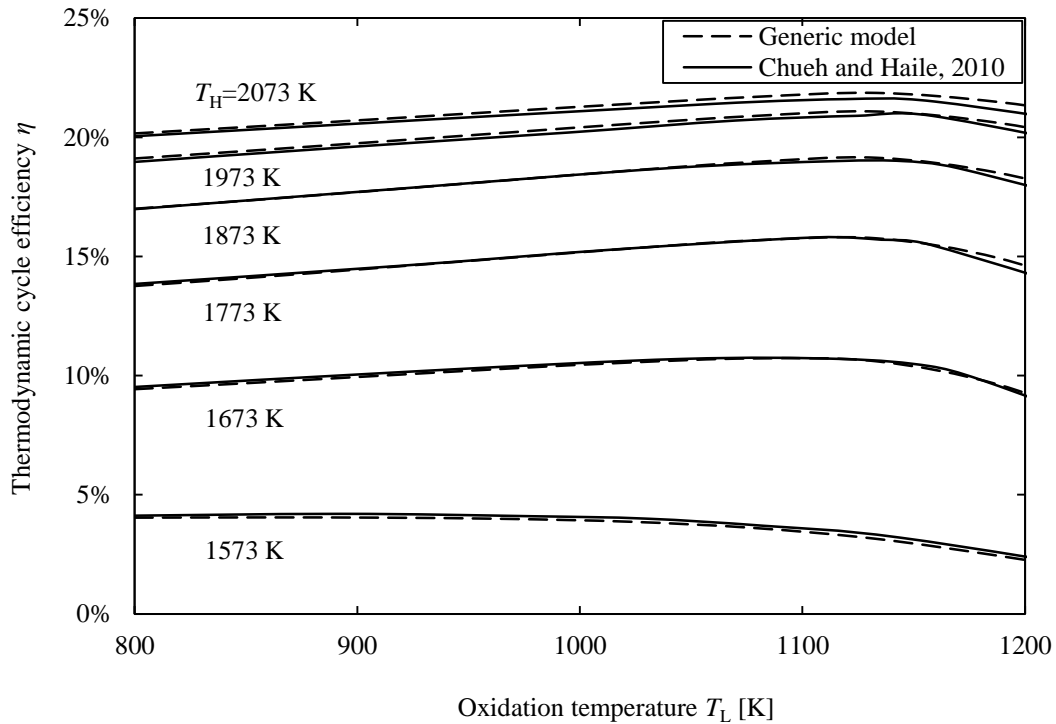


Figure 3.4 Comparison of results of the generic model and of the model by Chueh and Haile in [86]. Shown are values of thermodynamic cycle efficiency η as a function of reduction temperature T_H and oxidation temperature T_L . Heat recuperation efficiency from the gaseous and solid phase is zero.

Deviations between the two models are explained by small deviations of the heat exchanger efficiency and by inaccuracies of the literature data acquisition, besides others.

The second literature model is described in [86], where a batch reactor concept without heat recuperation is assumed. Contrary to the first model discussed above, thermodynamics of both oxidation and reduction reaction are modeled. The generic model is adjusted in the following way: the chamber number is set to $n = 2$ to exclude internal heat recuperation, gas heat recuperation is set to zero, thermodynamics of the oxidation reaction are taken into account, system parameters are set equally and an identical formulation of thermodynamic cycle efficiency is chosen, excluding vacuum pumping work. At $p_{\text{O}_2} = 10^{-5}$, $T_{\text{L}} = 1157$ K, $T_{\text{H}} = 1773$ K, and a concentration ratio of 5000 suns, the model in [86] and the generic model predict efficiencies of 15.5% and 15.6%, respectively. For a variation of reduction and oxidation temperatures at a constant oxygen partial pressure of 10^{-5} atm, the average deviation between the calculated efficiency and the literature values is 1.2% (Figure 3.4). Discrepancies of the results are partly due to possible deviations in the calculation of oxygen nonstoichiometry and due to inaccuracies in the data acquisition process.

The comparison with two literature models thus shows a very good agreement, validates the chosen approach and demonstrates the wide range of applicability of the model in the description of very diverse solar reactor concepts.

3.2.8 Results

In the following, the applicability of the model shall be demonstrated with an example system. The system has a ceria mass of 1 kg per piece with an area of 0.01 m^2 facing the other chamber half, a concentration ratio of 3000 suns, a vacuum pump to reduce the oxygen partial pressure to 10^{-3} atm, an oxidation pressure of 1 atm and a gas heat recovery efficiency of 95%.

Preliminary calculations found that 80 chambers constitute a system close to the optimum which is why this number of chambers is chosen here. The total length of the heat exchanger is then $78 \times \sqrt{A} = 7.8$ m, its internal area is $78 \times A = 0.78 \text{ m}^2$ and its external area is $6 \times 78 \times A = 4.7 \text{ m}^2$. The other system parameters can be taken from Table 3.1. Mass loss of oxidant due to the opening of the oxidation chamber which is at a higher pressure than the

other chambers is accounted for. A value of $f_{\text{CO}_2} = 2$ has been chosen in order to increase efficiency [86].

Table 3.1 Parameter values for example system.

Parameter	Label	Value	Unit
Concentration ratio	C	3000	-
Oxidation temperature	T_L	1000	K
Reduction temperature	T_H	1800	K
Temperature of surroundings	T_0	300	K
Reduction pressure (relative to 1 atm)	p_{red}	10^{-3}	-
CO ₂ -flow (times $\text{min}=\delta_{\text{red}}$) in oxidation chamber	f_{CO_2}	2.0	-
Number of chambers	n	80	-
Residence time in heat exchanger	Δt	10	s
Mass of ceria piece	m	1.0	kg
Area of ceria piece facing other chamber	A	0.010	m ²
Efficiency of gas heat recovery	η_{gasrec}	0.95	-
Conversion efficiency of heat to electricity	$\eta_{\text{heat-to-electricity}}$	0.4	-
Convective heat transfer coefficient	α	15	W m ⁻² K ⁻¹

3.2.8.1 Temperature distribution in heat exchanger chambers

The temperature distribution in the chambers is as seen in Figure 3.5, with the temperature in the upper chambers (going from the reduction chamber to the oxidation chamber) falling from $T_H = 1800$ K to 1079 K and in the lower chambers (opposite direction) rising from $T_L = 1000$ K to 1601 K. The efficiency η_{he} of the heat exchanger thus is 73.9%.

In general, this efficiency is a function of number of chambers, residence time and the entry temperatures, besides others. Here, we assume one piece at a time in the reduction and one in the oxidation chamber only. However, the degrees of freedom of the model could be increased by allowing a larger number of pieces in the reaction chambers, decoupling the residence time in the heat exchanger from the residence times in the reaction chambers.

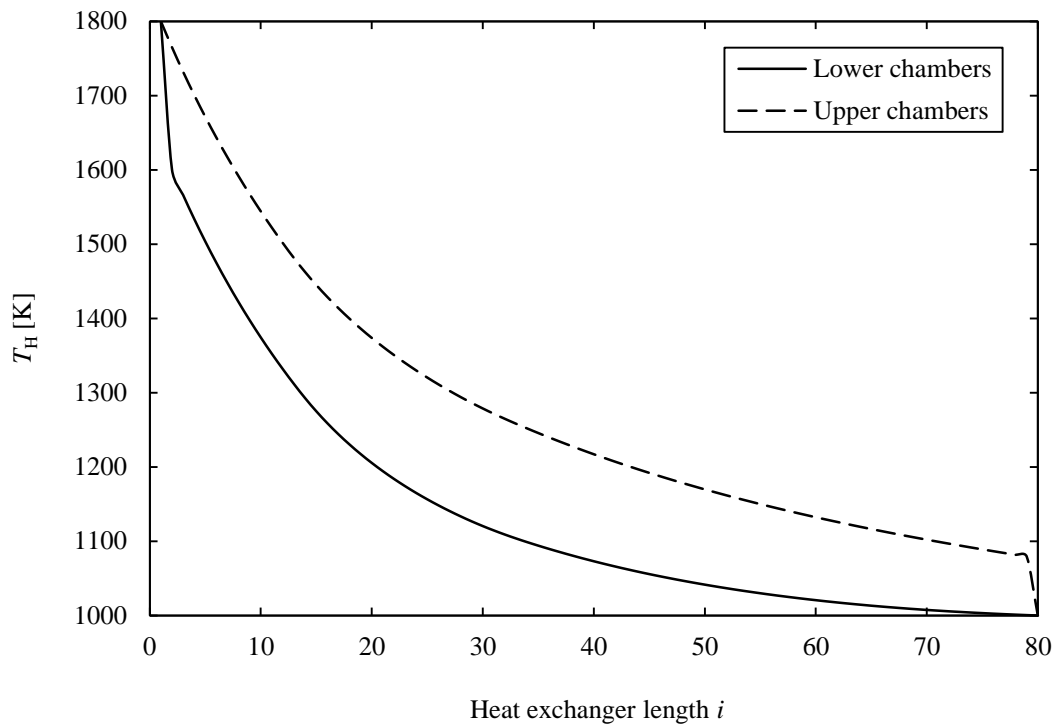


Figure 3.5 Temperature profile for generic reactor model with $n = 80$ chambers and a residence time Δt of 10 s and other parameters from Table 3.1.

3.2.8.2 Energy balance

The energy balance normalized to the amount of carbon monoxide produced is shown in Figure 3.6 and Table 3.2. The largest part of the energy input is required to heat ceria in spite of a heat recuperation efficiency of more than 70% in the heat exchanger. Effective heat recuperation is especially important in non-volatile cycles because compared to volatile cycles the mass of reactive material to be heated per mol of fuel produced is large. This was also discussed by Siegel et al. [118] with the introduction of a utilization factor of the reactive material consisting of the degree of reduction and heat recuperation. The next largest items in the energy budget are reduction enthalpy and energy lost due to reradiation. Absolute reradiation losses strongly increase with reduction temperature, however, the increased reduction temperature also leads to higher amounts of CO produced, decreasing the normalized reradiation losses. Due to these two adverse effects, the reradiation losses normalized to the amount of fuel produced are stabilized with respect to increasing reduction temperatures.

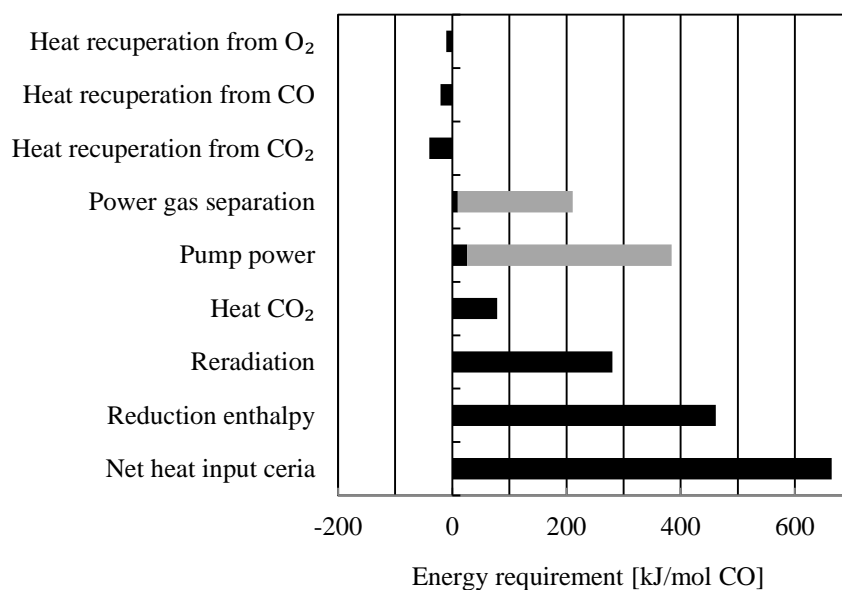


Figure 3.6 Energy balance of generic vacuum reactor with $n = 80$ chambers and a residence time Δt of 10 s. The two values shown for gas separation and pump power are based on the minimum thermodynamic work (black bars) and realistic efficiencies (grey bars). The oxidation temperature T_L is 1000 K and the reduction temperature T_H is 1800 K. Energy from gas heat recuperation is negative.

Table 3.2 Numerical energy requirements corresponding to Figure 3.6.

Energy requirement	[kJ/mol]
Heat recuperation from O ₂	-10.8
Heat recuperation from CO	-20.6
Heat recuperation from CO ₂	-40.0
Heat equivalent of gas separation (idealized/realistic)	9.7/201.4
Heat equivalent of vacuum pumping (idealized/realistic)	26.0/358.4
Heat CO ₂	79.0
Reradiation	280.6
Reduction enthalpy	461.3
Net heat input ceria	664.5

For the vacuum pump and the gas separation, the black bars show the ideal thermodynamic minimum and the grey bars show the realistic values as derived above. The assumed thermodynamic work only contributes insignificantly to the overall energy balance while the practically more relevant values increase the relative impact of vacuum pumping and gas separation considerably. The common assumption in literature of the thermodynamic

minimum work is therefore likely to underestimate actual values and thus their influence on the energy balance (see e.g. [18]). Heating of the oxidant carbon dioxide does not influence the energy balance significantly. Heat recuperated from the gases leaving the reactor reduces the required concentrated solar radiation input as the energy can be used to preheat incoming gases. However, due to the relatively small oxygen nonstoichiometry and as the oxidant flow rate is chosen proportional to the evolving oxygen, energy stored in the sensible heat of the gases presents only a minor contribution, even though the recovery rate has been chosen high with 95% efficiency (as in [13,18]). When reduction is performed at higher temperatures, the oxidation temperature should be increased as well. The reason for this is that two adverse effects occur: when the temperature swing is increased, a higher energy penalty for heating follows. On the other hand, a lower oxidation temperature favors reoxidation of the material and thus enhances productivity of the cycle. For the given system, a rise in reduction temperature thus leads to a higher oxidation temperature to maximize overall efficiency.

3.2.8.3 Efficiency as a function of temperature and oxygen partial pressure

In Figure 3.7, efficiency is shown as a function of reduction temperature T_H for oxygen partial pressures between 10^{-5} atm and 1 atm during reduction, where the ideal case assuming minimum thermodynamic work for vacuum generation and gas separation is shown with the dashed lines and the case based on more realistic efficiencies is shown with the solid lines. The pressure in the oxidation chamber is 1 atm and the oxidation temperature has been optimized on basis of the ideal case, as discussed above. All other parameter values can be taken from Table 3.1. Depending on the pressure in the reduction chamber, deviations are visible between the ideal and the realistic efficiencies: with decreasing pressure the actually required pumping work differs to a large degree from the theoretical value, becoming limiting for the lowest pressure shown. This is due to a rapid decline of the pump efficiency with decreasing pressure for the realistic case as opposed to the logarithmic progression of the thermodynamic minimum for the idealized case, resulting in large deviations in the reactor efficiency.

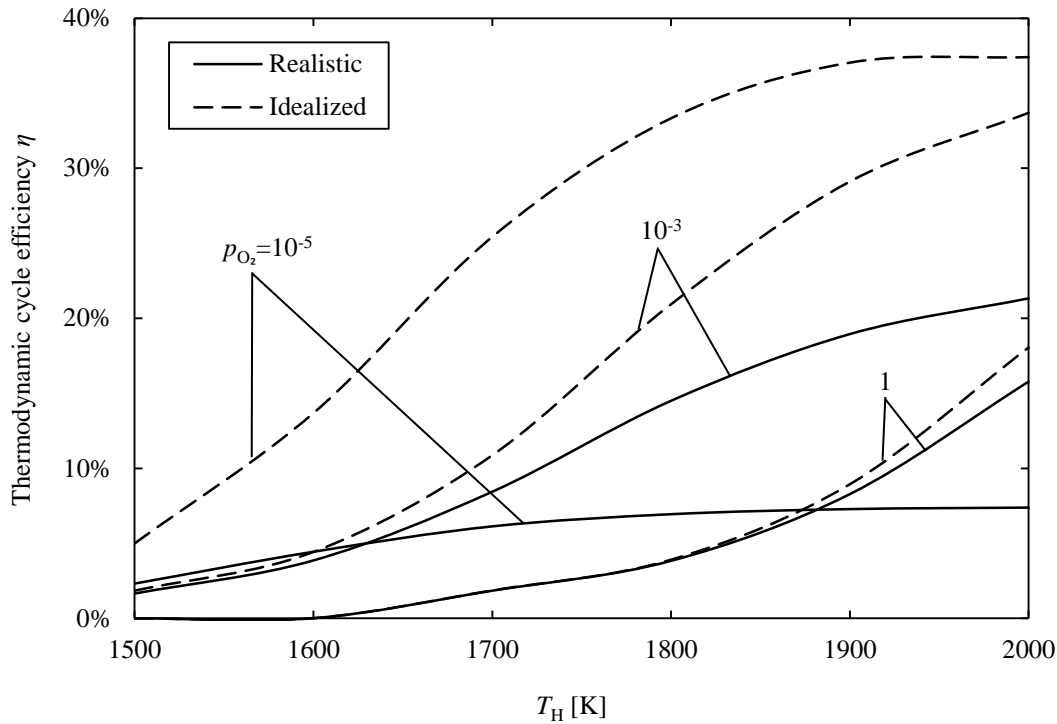


Figure 3.7 Idealized (thermodynamic work for vacuum pump and gas separation assumed) and realistic (realistic efficiencies for vacuum pump and gas separation assumed) efficiency of generic vacuum reactor with $n = 80$ chambers and a residence time $\Delta t = 10$ s as a function of reduction temperature T_H for different values of reduction oxygen partial pressure p_{O_2} (relative to standard state of 1 atm). Realistic pump efficiencies are 1.3%, 6.7% and 84.4% for the pressures of $p_{O_2}=10^{-5}$, 10^{-3} and 1, respectively. The oxidation temperature is chosen such as to maximize efficiency with values of T_L in the range 750-1250 K, depending on T_H and p_{O_2} .

In fact, the highest efficiency for the idealized case is reached for the lowest pressure as also shown in literature [18]. However, the realistic case reaches its highest efficiency at a pressure of about 1-10 mbar. Below this value the required energy input for the pressure reduction becomes excessive. Towards higher reduction temperatures, the deviation between the ideal and realistic cases increases due to the larger oxygen flow rate that has to be removed and the associated pumping work. This result shows clearly that much could be gained from the development of more efficient pumps. As vacuum pumping is a mature technology, it remains to be determined where the technical limit of efficiency is.

As expected, efficiency is enhanced with rising reduction temperatures. This is due to the exponential increase in oxygen nonstoichiometry with temperature at constant oxygen partial pressure, as can be seen in [82], which outweighs growing losses with temperature, such as reradiation losses or heating of the oxide and gases.

The largest efficiencies for the idealized case are reached at the highest reduction temperature and the lowest oxygen partial pressure: at $T_H = 2000$ K and $p_{O_2} = 10^{-5}$, $\eta = 0.38$, while the largest efficiency in the realistic case is $\eta = 0.23$ at $T_H = 2000$ K and $p_{O_2} = 10^{-2}$. From a practical point of view, however, such high temperatures may not be achievable due to maximum temperature constraints in reactor engineering and material use with respect to mechanical stability of the porous structure and sublimation, for example [11,119]. The effective limit of efficiency is therefore lower than the mathematical limit.

3.2.8.4 Efficiency as a function of operation temperatures

For a given number of chambers and residence time and otherwise constant parameters, the reduction and oxidation temperatures define the heat exchanger efficiency. The reason for this is that heat exchange is achieved through radiation between the hot and cold ceria pieces which is a function of the delta of the fourth power of their temperatures.

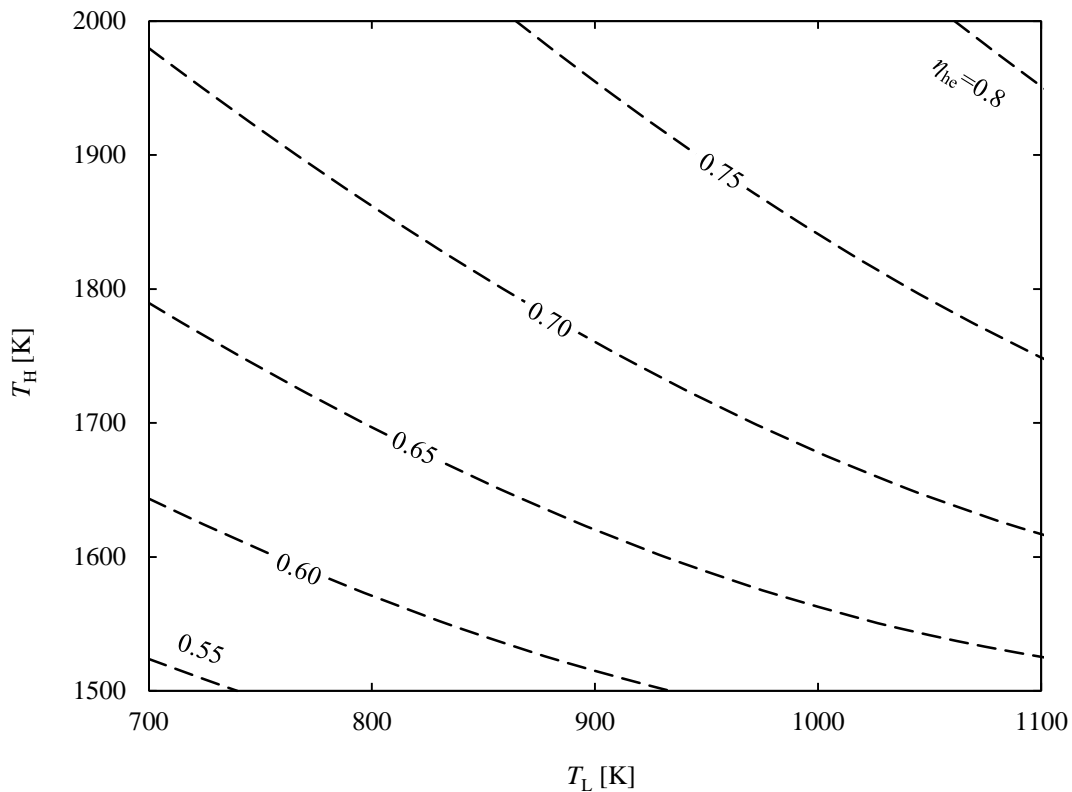


Figure 3.8 Contour plot of heat exchanger efficiency of generic vacuum reactor with $n = 80$ chambers and a residence time $\Delta t = 10$ s as a function of oxidation temperature T_L and reduction temperature T_H .

Also, the heat capacity of ceria is temperature dependent. In Figure 3.8, the heat exchanger efficiency η_{he} as defined in Equation (3.11) is shown as a function of reduction and oxidation temperatures. The other parameters can be taken from Table 3.1. In the analyzed temperature regime, higher oxidation temperatures increase heat exchanger efficiency. This is partly due to the temperature dependent emissivity of the material having higher values at elevated temperatures which enhances heat transfer [22,115]. Also with increasing reduction temperatures, the heat exchanger works more efficiently: at $T_H = 2000$ K, a value exceeding $\eta_{he} = 0.8$ can be reached. This is due to the fact that at higher temperatures, the emitted radiative power from a ceria piece increases proportional to the fourth power of temperature, enhancing overall heat transfer.

If the oxidation temperature is fixed, the heat exchanger efficiency can be increased simply by raising the reduction temperature. This is due to the bidirectional heat exchange between hot and cold pieces: there is no penalty in increasing the reduction temperature as the heat transfer from the hot to the cold piece will be enhanced due to increased radiative power from the former to the latter. High heat exchanger efficiencies substantially reduce the required energy input from solar energy and thus increase overall efficiency.

Thermodynamics of the fuel production cycle are critically dependent on the temperatures and oxygen partial pressures prevalent during oxidation and reduction. In order to increase the productivity of the cycle per unit mass of ceria, it may be required to reduce the temperature below the optimal value of the heat exchange process. The penalty that follows for the recuperation may be outweighed by the benefit of increased fuel productivity. The optimization of cycle efficiency is thus a trade-off between multiple mechanisms, which is also the reason why overall efficiency is maximized at different oxidation and reduction temperatures than which were calculated for maximum heat recuperation efficiency.

In Figure 3.9, overall cycle efficiency is calculated as a function of T_L and T_H for both the idealized and realistic assumptions for vacuum pump power and gas separation. Obviously, a higher reduction temperature increases efficiency, where penalties from increased energy requirements from the larger temperature swing and reradiation are compensated by enhanced fuel productivity.

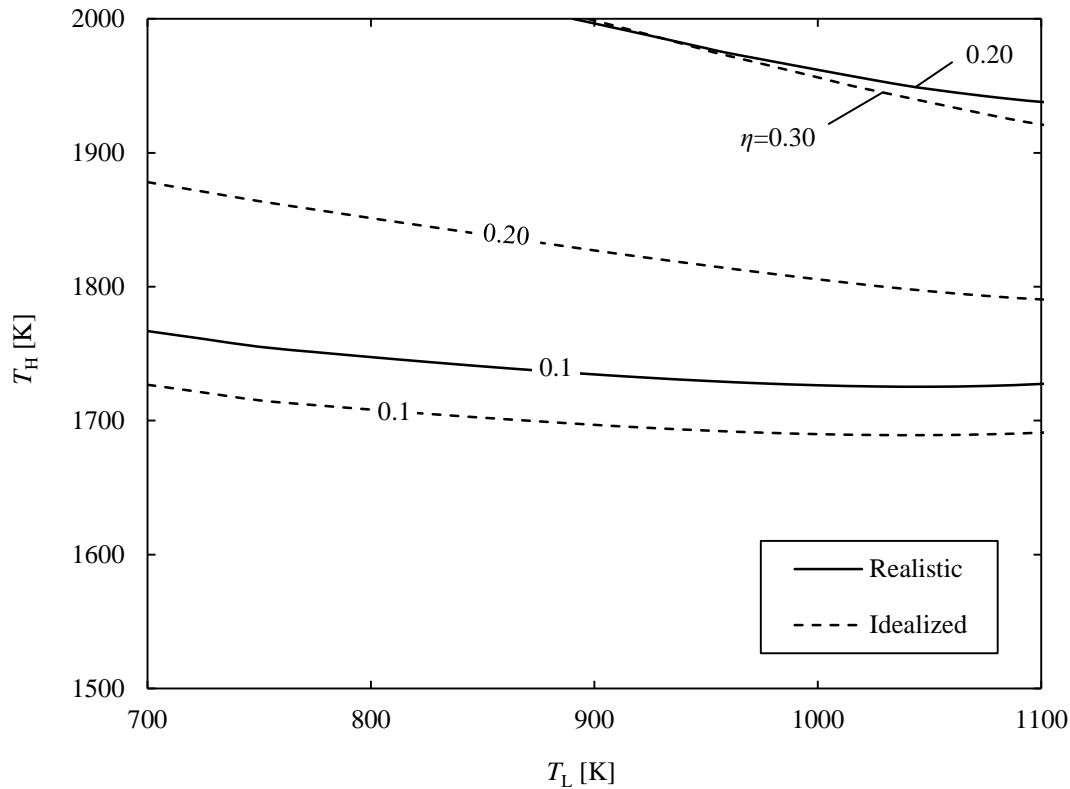


Figure 3.9 Contour plot of idealized (thermodynamic work for vacuum pump and gas separation assumed) and realistic (realistic efficiencies for vacuum pump and gas separation assumed) cycle efficiency of generic vacuum reactor with $n = 80$ chambers and a residence time $\Delta t = 10$ s as a function of oxidation temperature T_L and reduction temperature T_H for a reduction oxygen partial pressure of 10^{-3} atm.

The influence of the higher energy requirements for gas separation and vacuum generation for the realistic case are clearly visible: a higher reduction temperature of about 50 K is required to reach an efficiency of 10% while towards higher efficiencies, this required temperature increase over the ideal case becomes larger. Within the analyzed temperature regime, efficiencies of 30% and above can only be reached with the idealized assumptions.

3.2.8.5 Efficiency as a function of heat exchanger length and residence time

The number of heat exchanger chambers and the residence time of the elements per chamber are varied in Figure 3.10 to investigate the influence upon the efficiency of the thermodynamic cycle and of the heat exchanger. In the parameter region shown in the graph, efficiency can be enhanced through an increase of the residence time Δt or the number of heat exchanger chambers n_{he} : both will intensify the heat exchange between hot and cold elements.

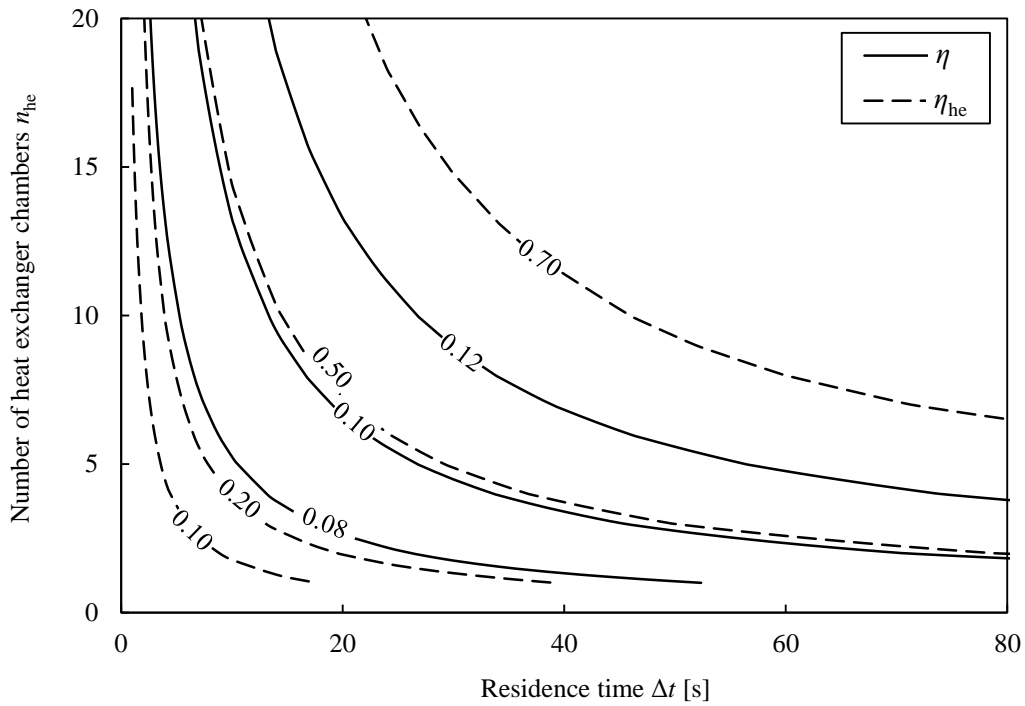


Figure 3.10 Efficiency of the thermodynamic cycle η and of the heat exchanger η_{he} as a function of the number of heat exchanger chambers n_{he} and the residence time per chamber Δt .

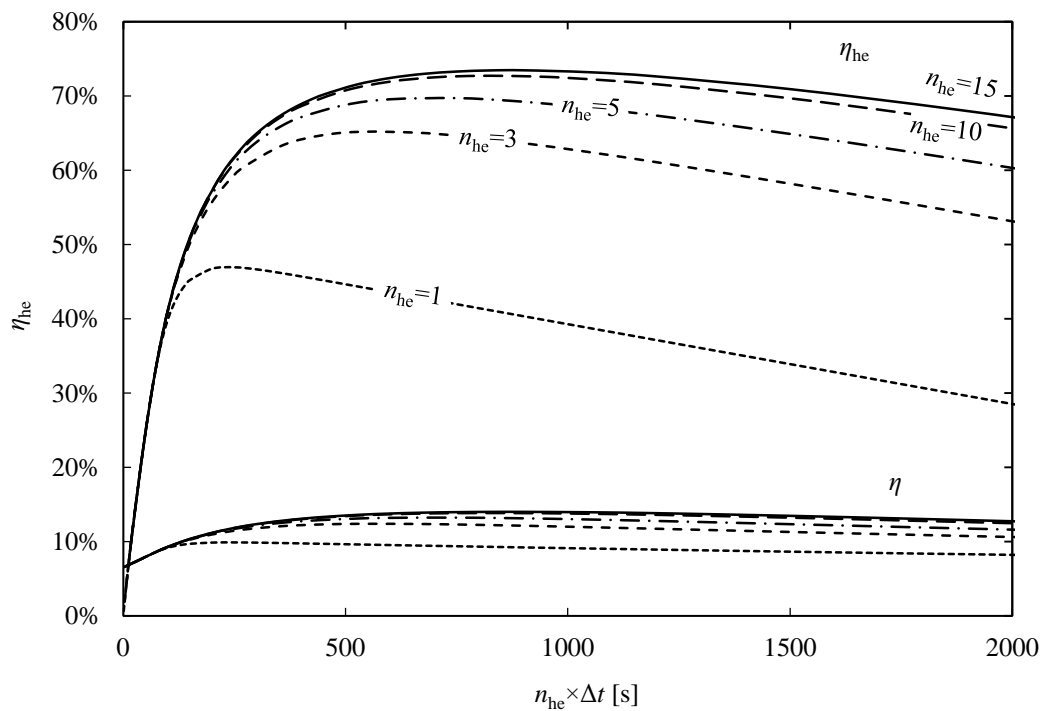


Figure 3.11 Efficiency of the thermodynamic cycle η and of the heat exchanger η_{he} as a function of the total residence time of the reactive material in the heat exchanger $n_{he} \times \Delta t$.

The highest efficiencies achievable are $\eta_{he} = 0.70$ and $\eta = 0.13$ for adequate parameter combinations in the region of $n_{he} \geq 7$ and $\Delta t \geq 18$ s, e.g. $n_{he} = 15$ and $\Delta t = 24$, or $n_{he} = 7$ and

$\Delta t = 60$. The fact that different parameter combinations may be used to achieve a given efficiency hints towards a direct functional dependence between heat exchanger length and residence time.

In the shown region, a longer heat exchanger (larger n_{he}) and residence time per chamber (larger Δt) both enhance efficiency, which is equivalent to a longer total residence time of the elements in the heat exchanger. Outside of the shown region, efficiency decreases if the heat exchanger length or the residence time is chosen too large because of heat losses to the environment.

In Figure 3.11, efficiency is shown as a function of the total residence time of the reactive material in the heat exchanger $n_{\text{he}} \times \Delta t$. In the graph, different heat exchanger lengths, represented by the number of heat exchanger chambers n_{he} , are highlighted.

In general, the heat exchanger efficiency shows a strong increase for $n_{\text{he}} \times \Delta t \leq 250$ s, reaches a maximum at $n_{\text{he}} \times \Delta t \approx 750$ s and decreases for $n_{\text{he}} \times \Delta t > 750$:

- The strong increase at small values of $n_{\text{he}} \times \Delta t$ shows that the introduction of a heat exchanger and the intensification of heat exchange, i.e. the prolongation of the total residence time, has a strong effect on both η_{he} and η .
- The maximum of $\eta_{\text{he}} > 70\%$ can be reached with about ten heat exchanger chambers or more, where the residence time has to be adjusted accordingly. Depending on n_{he} , a maximum of η_{he} is achievable, where the maxima are shifted towards longer total residence times for increasing heat exchanger lengths.
- At a given total residence time, η_{he} increases with the number of chambers. This behavior is expected because a heat exchanger with a larger number of chambers has more intermediate temperature levels for heat exchange and thus introduces less irreversibility. The limit of the chamber concept is an ideal counter-flow heat exchanger.
- Efficiency is limited by heat losses to the environment by convection and radiation for $n_{\text{he}} \times \Delta t > 750$ s.

3.2.8.6 Analysis of internal heat transfer limitations

In order to analyze the influence of heat transfer within the reacting medium in the heat exchanger and to give an example of the applicability of the generic model with respect to a practically relevant case, the model is modified in the following way. The reactive medium is assumed to have a thickness of 0.05 m at a porosity of 0.8, a mean pore diameter of 2.5×10^{-3} m [14,120], and a mass of 0.77 kg. The thermal diffusivity of the RPC is $0.0434 \text{ cm}^2 \text{ s}^{-1}$ at 1500 K. Alumina insulation thickness is 0.05 m and the thickness of the reactor wall made from Inconel 600 is 3×10^{-3} m. In the porous ceria and alumina insulation, heat is transferred by radiation and conduction, where the former is modeled with the Rosseland diffusion approximation as for example in [121–124] and the latter is modeled with a modified form of the three resistor model [120]. See Section 3.3.4 for equations and Figure 3.13 for an illustration of the approach for the calculations. In the Diffusion Approximation, the extinction coefficient of the material is $\beta = \Psi_1 \frac{\sqrt{1-\varphi}}{d_{\text{mean}}}$ with $\Psi_1 = 1.765$, $d_{\text{mean}} = 0.0022 \cdot \varphi + 7.59 \times 10^{-4}$ m and ε the porosity of the material, while in the three resistor model the model parameter f is approximated by $\sqrt{g_0 - g_1 \varphi}$ with $g_0 = 0.754$, $g_1 = 0.829$ [120]. Material properties are taken from [113,115,117,125,126]. The finite difference method is used for the discretization of the porous domains of ceria and insulation which are subdivided into a number of layers with constant properties. Ten layers both in the ceria and the insulation domain are chosen after a grid convergence study showed convergence of the results with increasing number of layers and the results deviate by less than 1.2% from the calculation with the two-fold number of layers at a ten times smaller time step. A one-dimensional transient heat transfer model is thus formulated that solves the system of coupled nonlinear equations with the explicit Euler method. A comparison of the generic model with the more complex model for a heat exchanger with ten chambers (see Figure 3.1), a residence time of 10 s per chamber, and a mass of 0.77 kg per ceria piece gives heat exchanger efficiencies of 0.422 and 0.194, respectively. The temperature profiles of the upper and lower chambers of the heat exchanger as calculated with both models can be seen in Figure 3.12. The more complex model predicts less efficient heat exchange and thus a flatter temperature profile in both chamber halves. This result indicates that heat propagation through the porous media may have a significant influence on overall heat transfer and hence heat exchanger efficiency and has to be evaluated in each specific reactor realization. In the following section, the model is extended to include heat transfer in the reactive material.

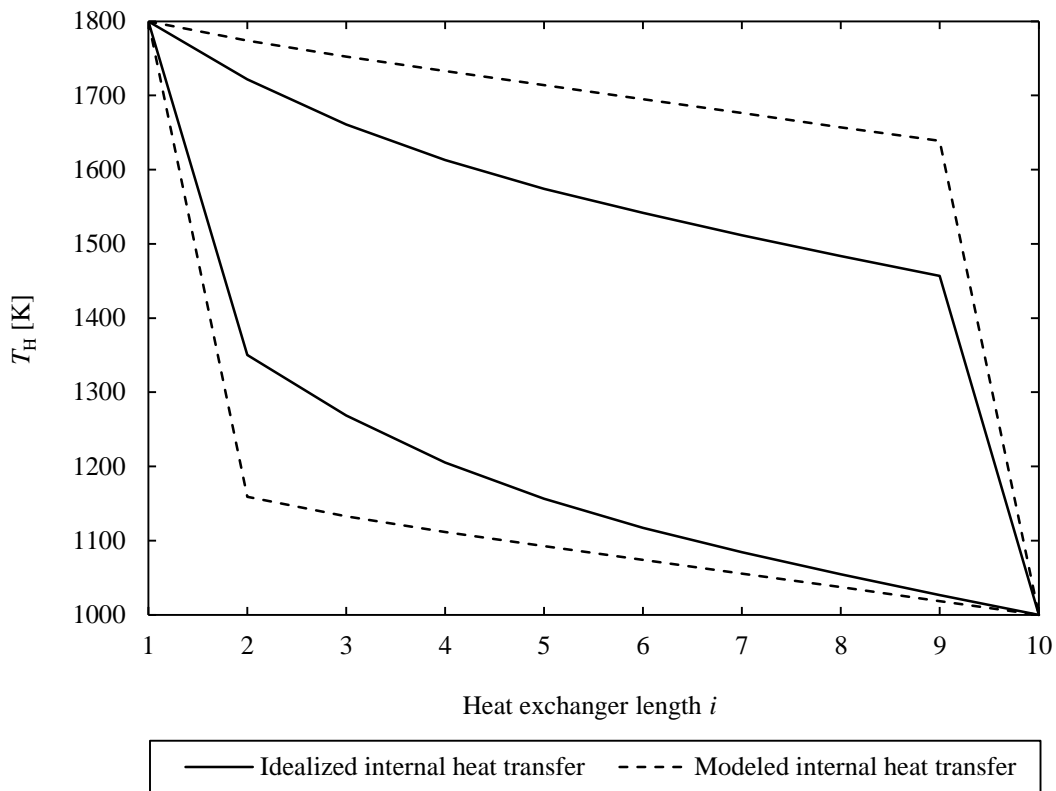


Figure 3.12 Comparison of temperature profiles in upper and lower chambers for idealized internal heat transfer within the reactive medium and modeled internal heat transfer using the Rosseland diffusion approximation and the three resistor model. See Section 3.3.4 for equations and Figure 3.13 for an illustration of the approach for the calculations. The heat exchanger has eight chambers with a residence time of 10 s each. This example shows that internal heat transfer may have a significant influence on the performance of the heat exchanger.

An increase of heat exchanger efficiency may be sought through the choice of an advantageous geometry that maximizes heat transfer between counter-flowing elements and minimizes heat losses towards co-flowing elements. Further, counter-flow heat transfer may be enhanced through the choice of thin elements with optimized porosity. The models presented in this work are suitable for the investigation of maximum theoretical efficiencies and those achievable under more realistic assumptions for a variety of parameters such as geometry and porosity.

3.3 Generic chamber model - Modeled internal heat transfer

In Chapter 3.2, a generic reactor model was presented that assigns a single temperature to the reactive material in each of the heat exchanger chambers, which is equal to immediate heat diffusion within the material. This represents the ideal limiting case of quick internal heat transfer which may not be achievable in practice. In order to extend the applicability of the model, it is further developed in this chapter to include the heat transfer within the reactive medium.

Parts of this chapter were published in: Falter, C. P. and Pitz-Paal, R., 2017, “A generic solar-thermochemical reactor model with internal heat diffusion for counter-flow solid heat exchange,” *Solar Energy*, 144, pp. 569–579 [127].

3.3.1 Introduction

Recent analyses have shown that in two-step thermochemical cycles, heat transfer is the rate limiting factor during reduction of solid non-volatile reactive material, while mass transfer limits the reaction rate during oxidation [10,11,14,15]. The implications for the material design are thus to allow for efficient radiation absorption during reduction and for rapid chemical conversion during oxidation. The material development for porous ceria has thus sought to improve both radiative absorption and chemical conversion by the introduction of porosity on two scales: the macroporous structure permits radiation to penetrate the structure and to be absorbed in the volume of the material rather than at the surface, which enables a more rapid and more equal heating process [14]. The introduction of an additional microporous structure in the material increases the specific surface area and thus decreases the reaction time of oxidation [14]. With this approach, a comparably large experimental efficiency was reached. From a practical standpoint, it is therefore interesting to investigate the potential of this porous material structure in the generic reactor model. Up to this point, an unobstructed heat exchange process in the material and between reactive material in the upper and lower heat exchanger chamber has been assumed. However, in reality, heat diffusion in the porous structure could deviate from this behavior, leading to a deteriorated heat exchange process. To investigate the potential for heat exchange by radiation and its implications on the cycle efficiency, heat diffusion in the porous material is included in the model.

For the modeling of radiation heat transfer in the porous material, different approaches are available, e.g. the P_N model, discrete ordinates, Rosseland diffusion approximation (RDA) or the Monte Carlo model (MC) [111]. The Monte Carlo model delivers accurate results and is oftentimes used as a reference for other methods, however it is computationally expensive [123,124,128]. The Rosseland diffusion approximation is inaccurate at solid-fluid boundaries because the assumption of isotropic radiation is not fulfilled. In the presented model, the fluid is assumed to be optically non-participating and radiation heat exchange between the chamber halves reduces the anisotropy at the boundary. The RDA model is therefore expected to deliver accurate results, which is confirmed by the model validation in Chapter 3.3.8. For the intended purpose of the calculation of many parameter combinations, a computationally quick method is required for the calculations. For these reasons, the Rosseland diffusion approximation is selected. As this method can only be used with optically thick media, the optical thickness of the porous element is chosen not to be smaller than three [111,112].

3.3.2 Prior research

A description of transient heat transfer in a heat exchanger as the one discussed in this section is not found in the literature. However, heat transfer in porous media using the Rosseland diffusion approximation is described in the following sources.

Three different approaches for the combined calculation of conduction and radiation in the fibrous insulation of the Space Shuttle entering the atmosphere of the Earth are compared in [124]. The approaches are approximations of the radiation transfer equation, an approximation of radiation thermal conductivity, and the radiation diffusion approximation. The author concludes that the diffusion approximation was suited best for the calculation of the transient temperature profile in the fibrous material.

In [112], different models for the description of heat transfer from a reticulated porous ceramic (RPC) heated by concentrated solar radiation to a gas flowing through its pores are compared, notably the Rosseland diffusion approximation, the P_1 -model, and a Monte Carlo model. The authors show that the diffusion approximation does not produce adequate results at the fluid-solid boundary at an optical thickness of three and choose the P_1 -model. This is a well-known characteristic of the diffusion approximation and should be treated with care in

the cases where a fluid-solid boundary exists. In the present case, this problem does not arise in the same manner because of the reduced anisotropy at the fluid-solid boundary.

Heat and mass transfer in different SiC-foam samples are analyzed with the diffusion approximation, the P_1 -model, the two-flux approximation, and the Monte Carlo model [123]. The authors conclude that the two-flux approximation reproduces the results of the Monte Carlo analysis best, while the diffusion approximation overpredicts the solid temperature at the inlet solid-fluid boundary. At the outlet, the fluid temperature is predicted with high accuracy.

The Monte Carlo model is used to derive the boundary condition of solar radiation impinging on a porous media receiver and the Rosseland diffusion approximation for the calculation of heat transfer for the solid and fluid domain inside of the receiver [122]. The authors justify their choice of the diffusion approximation with its ability to make fairly good predictions compared with experimental measurements in studying detailed radiative transfer mechanisms in porous media.

For the description of effective thermal conductivity of a porous medium, different models are compared with their data derived from direct pore level simulations which are based on tomography scans of a reticulated porous ceramic [120]. The authors find that the extended three resistor model which expresses the fitting parameter f as a function of porosity is able to describe with great accuracy the effective thermal conductivity of the sample.

The Rosseland diffusion approximation and the three resistor model for the description of radiation heat transfer and effective thermal conductivity in porous media are thus well-described in the literature and have been used for calculations of similar heat transfer processes. These models are thus selected for the description of heat transfer processes in the porous domain of the reactive material in the heat exchanger due to their accuracy and favorable computational expense.

3.3.3 Model description

In general, the proposed heat exchanger has the identical characteristics as described above in Chapter 3.2, i.e. a number of $n-2$ heat exchanger chambers, where elements of the reactive material exchange heat through radiation in a counter-flow arrangement between the reaction

chambers for reduction and oxidation (Figure 3.1). During reduction, an oxygen nonstoichiometry is created in the reactive material in an atmosphere of reduced oxygen partial pressure. Oxidation, on the other hand, is performed in an atmosphere under a large partial pressure of carbon dioxide and/or water. A physical gas-tight separation between the elements in their reduced and oxidized state is thus required to prevent premature reoxidation of the former in the heat exchanger. This separation is implemented with a separating wall in the proposed reactor model, where the separating wall is assumed to be made of a material with high emissivity and thermal conductivity in order to reduce its influence on the radiation heat exchange. The separating wall does not present a radiation shield in a classical sense because of the direct contact with the element in the upper chamber. Through its high thermal conductivity and low mass, the separating wall quickly assumes the temperature of the element in the upper chamber half and its high emissivity enables effective thermal radiation heat exchange with the element in the lower chamber half. The separating wall therefore acts as a “coating” on the elements in the upper chambers and not as a radiation shield. SiC/HfC was identified to possess the desired material properties for the separating wall. However, due to possible chemical reactions of SiC and CeO₂ at elevated temperatures, a direct contact is prevented through the introduction of an additional layer of solid Al₂O₃ which is commonly used as insulation material in its porous form. The non-porous Al₂O₃ (99.5% purity, 0% porosity) has a higher thermal conductivity of 35 W m⁻¹ K⁻¹ [129] (porous alumina: ≈0.2 W m⁻¹ K⁻¹ [113]) and is thus more suitable as a separating layer.

As the internal heat transfer within the reactive material in Chapter 3.2 was idealized, it shall be modeled in more detail here. For this purpose, the heat exchanger model is extended to include heat transfer inside of the material.

In Figure 3.13, one representative heat exchanger chamber of the model is shown including the computational domains. The reactive RPC material and the adjacent Al₂O₃-SiO₂ insulation are modeled as homogenous porous domains, in which energy is transferred by radiation and conduction. The separating wall between the chamber halves is modeled as a solid domain (composed of layers of Al₂O₃ and SiC/HfC, each of 1 mm thickness), while the gap is modeled as a fluid domain. The influence of the separating wall on heat transfer is analyzed in Section 3.3.9.2. The fluid in the gap is assumed to be oxygen.

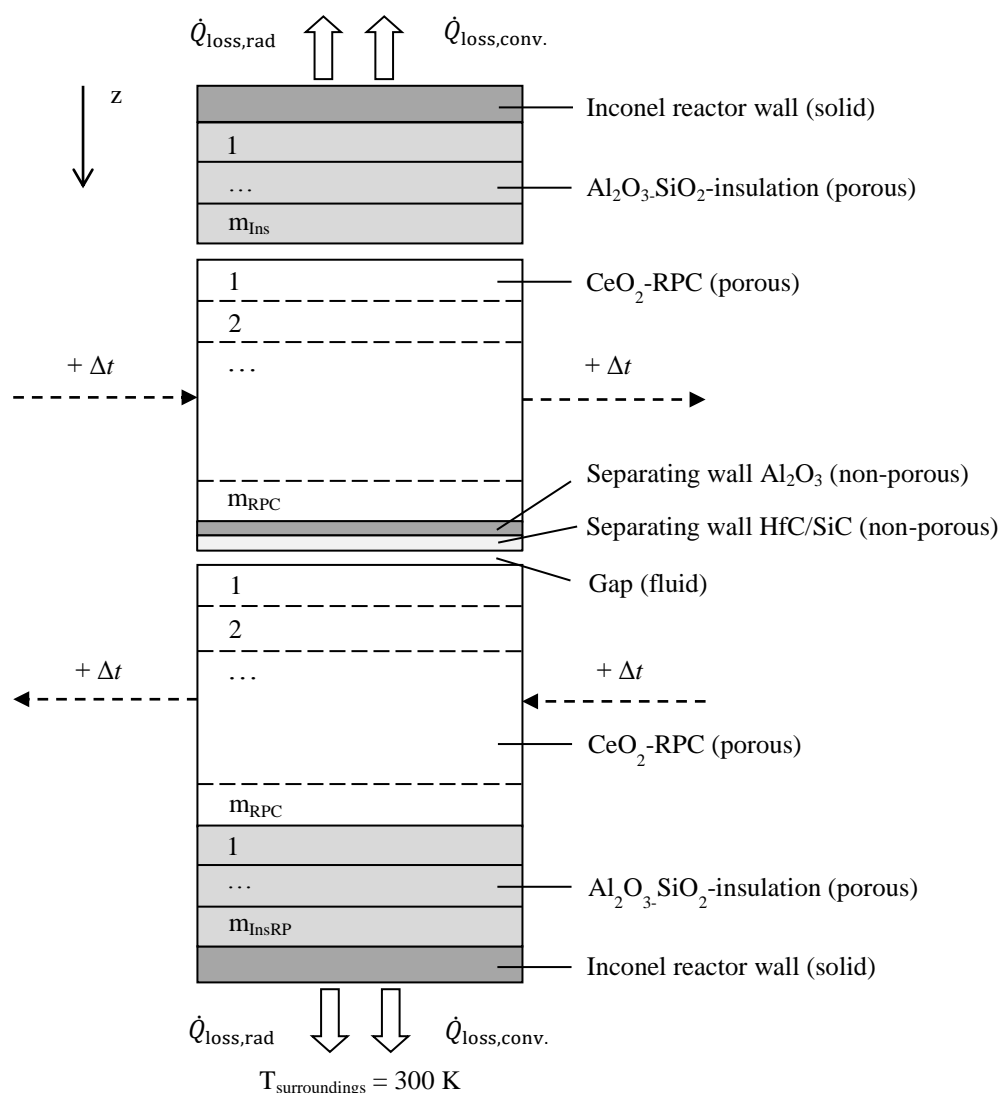


Figure 3.13 Schematic of one representative heat exchanger chamber for the modeling of radiation heat exchange between chamber halves and internal heat transfer in the reactive medium and adjacent insulation. Indicated are also the boundary conditions and the movement of the reactive material.

The reactor wall is made from Inconel 600 and has a thickness of 0.003 m. Due to the low temperature level behind the insulation, also regular steel would be appropriate for the reactor wall, however, Inconel 600 is chosen here analogous to recent experiments [10,14,15,105].

A porous insulation material made from $\text{Al}_2\text{O}_3\text{-SiO}_2$ is used [113] with a low thermal conductivity and emissivity to effectively reduce the heat transfer through the reactor walls to the surroundings. A computational study was performed to analyze heat exchanger efficiency as a function of insulation thickness. The thickness is chosen to be 0.1 m after the study showed that a further increase in thickness leads to only very small improvements in

efficiency. The thickness of the reactive material has a default value of 0.05 m but is varied in a parameter study to investigate its influence on heat exchanger efficiency.

Between the separating wall and the reactive material, a gap of 1 mm thickness is assumed.

All other system parameters are as described in Chapter 3.2.3.

3.3.4 Governing equations

Porous domains

In the porous domains of the RPCs and of the insulation, the transient energy conservation equation is used for the modeling of heat transfer.

$$\rho c_p \frac{\partial T}{\partial t} = -\frac{\partial \dot{q}}{\partial z} + \dot{q}_{\text{chem}} \quad (3.22)$$

ρ is the density of the RPC, c_p is the heat capacity of ceria, T is the temperature, t is the time, \dot{q} is the heat flux comprised of conduction and radiation and \dot{q}_{chem} is the volumetric heat of the chemical reactions. For heat conduction, the Fourier law is used with the thermal conductivity λ .

$$\dot{q} = \dot{q}_{\text{cond}} + \dot{q}_{\text{rad}} = -\lambda \frac{\partial T}{\partial z} + \dot{q}_{\text{rad}} \quad (3.23)$$

As the model does not solve the motion in the fluid domain, the local oxygen partial pressure is not known exactly. Thus, for convenience, the chemical heat source term is included in the energy balance of the reactor chambers (Equation (3.8)). Rewriting Equation (3.22) then gives

$$\rho c_p \frac{\partial T}{\partial t} = \frac{\partial}{\partial z} \cdot \left(\lambda \frac{\partial T}{\partial z} \right) - \frac{\partial}{\partial z} \dot{q}_{\text{rad}}. \quad (3.24)$$

The density and specific heat capacity of the porous domain are comprised of contributions from the solid and the fluid domain in the following way.

$$\rho = \rho_s \cdot (1 - \varphi) + \rho_f \cdot \varphi \quad (3.25)$$

$$c_p = \frac{c_{p,s} \cdot \rho_s \cdot (1 - \varphi) + c_{p,f} \cdot \rho_f \cdot \varphi}{\rho_s \cdot (1 - \varphi) + \rho_f \cdot \varphi} \quad (3.26)$$

The subscripts “s” and “f” denote the solid and fluid domain, respectively, and φ is the porosity of the RPC. For the chosen materials and for reduced pressure, $\rho_f \ll \rho_s$ and thus $\rho \rightarrow \rho_s \cdot (1 - \varphi)$ and $c_p \rightarrow c_{p,s}$. Due to the small influence of the fluid on both the density and specific heat capacity, the density is assumed to be the solid density reduced by the porosity of the RPC and the specific heat capacity is assumed to be that of the solid material.

For the calculation of heat propagation in the porous medium, conduction and radiation are considered, while convection through the gas phase is neglected. The omission of convection is based on its small influence on the overall heat transfer which was observed in the literature: Tsotsas and Martin concluded that appreciable free convection occurs for common temperature differences only in very large voids of the order of centimeters and that its contribution to the overall heat transfer is considered to be negligible [104]. The reduced pressure in the reactor further diminishes the convective heat transfer and the lack of space available due to the assumption of similar volumes of heat exchanger chamber halves and elements hinders the establishment of a convective flow within each chamber half.

Thermal conductivity of oxygen is assumed to be independent of pressure. This is predicted by kinetic gas theory, where Maxwell pointed out that in the formulation of thermal conductivity $\lambda = 1/3 c_v \rho \Lambda \bar{c}$ with c_v the specific heat capacity of the gas at constant volume, ρ its density, Λ the mean free path of the gas molecules, and \bar{c} their mean velocity of translation, the dependency of density and mean free path on pressure cancel each other [130]. However, there is experimental evidence that indicates that towards low pressures, this theory may not hold and that thermal conductivity of a gas can be expected to be zero at zero pressure [130]. Here, the gas in the pores of the reactive material is assumed to be oxygen as it evolves with rising temperatures. This gas has therefore an influence on the internal heat transfer within the reactive medium as it provides the possibility for conductive heat transfer. However, the influence on overall heat transfer is limited to about 1% as can be shown by setting the thermal conductivity of the gas to zero. Due to these reasons and in order to simplify the calculations, the pressure dependence of the thermal conductivity is neglected.

The temperatures in the porous domain require the inclusion of radiation heat transfer into the equations, where the fluid is assumed to be non-participating, i.e. radiation is modeled in the porous domain of the reactive media, in the gap between the media, and in the porous insulation. The RPC is modeled with effective radiative properties of absorption and scattering coefficients which have been determined from direct numerical pore-level

simulations [120]. In the modeling of the porous domains, therefore emission, absorption, and scattering are taken into account. The radiative transfer equation for a gray medium with emission, absorption, and isotropic scattering is considered.

$$\frac{dI}{dS} = \alpha_a I_b - (\alpha_a + \sigma_s)I + \frac{\sigma_s}{4\pi} \int_{4\pi} I d\omega \quad (3.27)$$

I is the radiation intensity at a given location, S is the direction, α_a is the absorption coefficient, I_b is the blackbody radiation intensity, σ_s is the scattering coefficient, and ω is the solid angle.

The radiation source term in Equation (3.23) is given by

$$\frac{\partial}{\partial z} \dot{q}_{\text{rad}} = \alpha_a \left(4\pi I_b - \int_{4\pi} I d\omega \right) \quad (3.28)$$

The radiation source term is modeled with the Rosseland diffusion approximation assuming an absorbing, emitting, and isotropically scattering optically thick medium [111].

$$\frac{\partial}{\partial z} \dot{q}_{\text{rad}} = -\frac{\partial}{\partial z} \left(\lambda_{\text{rad}} \frac{\partial T}{\partial z} \right), \quad (3.29)$$

where the thermal radiative conductivity λ_{rad} for a refractive index of one is given by

$$\lambda_{\text{rad}} = \frac{16\sigma T^3}{3\beta_R}, \quad (3.30)$$

and where β_R is the Rosseland mean attenuation coefficient and σ is the Stefan-Boltzmann constant.

RPC: For a gray medium, as assumed here, β_R is equal to the extinction coefficient β of the medium which is defined as a function of porosity [120]

$$\beta = \Psi_1 \cdot \frac{\sqrt{1-\phi}}{d_{\text{mean}}}, \quad (3.31)$$

with the parameter $\Psi_1 = 1.765$ and the mean pore diameter d_{mean} which is defined as [120]

$$d_{\text{mean}} = 2.20 \times 10^{-3} \cdot \phi + 4.59 \times 10^{-4} \text{ m}. \quad (3.32)$$

The pore diameter is therefore a function of porosity φ , i.e. an increase in porosity is directly linked to an increase in pore diameter and both variables cannot be chosen independently.

Conduction through the porous medium is described with the three-resistor model using a combination of serial and parallel resistances in the solid and fluid phases to derive an overall thermal conductivity of the porous medium [120].

$$\lambda = (1 - \sqrt{g_0 - g_1\varphi}) \frac{k_f}{\varphi + (1 - \varphi) \frac{k_f}{k_s}} + \sqrt{g_0 - g_1\varphi} (\varphi k_f + (1 - \varphi) k_s) \quad (3.33)$$

The values of the parameters g_0 and g_1 are 0.754 and 0.829 [120], k_f and k_s are the thermal conductivities of the fluid and solid material, and φ is the porosity of the porous domain. The effective thermal conductivity of the porous medium λ is then used in the energy conservation equation (Equation (3.24)).

Insulation: The porous insulation is comprised of fibers of Al_2O_3 and SiO_2 . As the mean pore diameter is not known, experimental values for the Rosseland mean attenuation coefficient and for the thermal conductivity are used to describe the thermal energy transfer across the insulation. The former are taken from Zhang et al. [121] and the latter from the manufacturer of the type M-35 buster insulation [113] which has also been used in experiments at ETH Zurich [14,15,83,105].

Inserting Equations (3.30) and (3.33) into Equation (3.24), the energy conservation equation for the porous domains can be written as

$$\rho c_p \frac{\partial T}{\partial t} = \frac{\partial}{\partial z} \left(\lambda \frac{\partial T}{\partial z} \right) - \frac{\partial}{\partial z} \dot{q}_{\text{rad}} \quad (3.34)$$

$$= \frac{\partial}{\partial z} \left((\lambda + \lambda_{\text{rad}}) \frac{\partial T}{\partial z} \right). \quad (3.35)$$

Solid and fluid domains

In the solid and fluid domains, heat conduction is modeled with the law after Fourier.

$$\rho c_p \frac{\partial T}{\partial t} = \frac{\partial}{\partial z} \left(\lambda \frac{\partial T}{\partial z} \right) \quad (3.36)$$

where λ is the thermal conductivity of either the fluid or solid material.

3.3.5 Boundary conditions

In the following, the boundary conditions for the computational domain are given.

Reactor wall facing surroundings

Energy is transferred by radiation and convection from the reactor wall to the surroundings which are assumed to have a temperature of 300 K.

$$k_c \frac{\partial}{\partial z} T|_{rw \rightarrow 0} = \dot{q}_{\text{rad}} + \dot{q}_{\text{conv}} \quad (3.37)$$

$$= \varepsilon_{\text{he,wall}} \sigma (T_{\text{he,wall}}^4 - T_0^4) + \alpha_{\text{conv}} (T_{\text{he,wall}} - T_0) \quad (3.38)$$

The subscripts “he,wall” and “0” denote the reactor wall and the surroundings, $\varepsilon_{\text{he,wall}}$ is the emissivity of the reactor wall, and α_{conv} is the convective heat transfer coefficient from the reactor wall to the surroundings.

Separating wall facing RPC in lower chamber

Radiation heat exchange between the separating wall and the RPC in the lower chamber is modeled with the view factor for infinite parallel flat plates. The boundary condition at the surface of the separating wall facing the RPC in the lower chamber is then

$$\lambda_{\text{sw}} \frac{\partial}{\partial z} T|_{\text{sw} \rightarrow \text{RPC,l}} = - \frac{\sigma (T_{\text{sw} \rightarrow \text{RPC,l}}^4 - T_{\text{RPC,l} \rightarrow \text{sw}}^4)}{\frac{1}{\varepsilon_{\text{sw}}} + \frac{1}{\varepsilon_{\text{RPC}}} - 1} - \lambda_f \frac{\partial}{\partial z} T. \quad (3.39)$$

λ_{sw} is the thermal conductivity of the separating wall, σ is the Stefan-Boltzmann constant, $T_{\text{sw} \rightarrow \text{RPC,l}}$ is the temperature of the separating wall facing the RPC in the lower chamber, $T_{\text{RPC,l} \rightarrow \text{sw}}$ is the temperature of the RPC in the lower chamber facing the separating wall, ε_{sw} and ε_{RPC} are the emissivities of the separating wall and the RPC in the lower chamber, and λ_f is the thermal conductivity of the fluid.

RPC in lower chamber facing separating wall

Analogous to above, the boundary condition for the top layer of the RPC in the lower chamber half facing the separating wall is

$$\lambda_{\text{RPC}} \frac{\partial T}{\partial z} \Big|_{\text{RPC,l} \rightarrow \text{sw}} = \frac{\sigma (T_{\text{sw} \rightarrow \text{RPC,l}}^4 - T_{\text{RPC,l} \rightarrow \text{sw}}^4)}{\frac{1}{\varepsilon_{\text{sw}}} + \frac{1}{\varepsilon_{\text{RPC}}} - 1} + \lambda_f \frac{\partial T}{\partial z}. \quad (3.40)$$

λ_{RPC} is the effective thermal conductivity due to radiation and thermal conduction of the RPC which is calculated with Equations (3.30) and (3.33).

3.3.6 Material properties

An overview of the material properties used for the calculations is shown in Table A.5 and Table A.6 in the Annex. The convective heat transfer coefficient from the reactor wall to the surroundings at 300 K is $15 \text{ W m}^{-1} \text{ K}^{-1}$ [112]. The emissivity, thermal conductivity, specific heat capacity, and density of the reactor wall made from Inconel 600 are taken from [126]. Its thickness is chosen to be 3 mm. The emissivity of the $\text{Al}_2\text{O}_3\text{-SiO}_2$ insulation is from [116], its radiative extinction coefficient from [121], its thermal conductivity and density from [113], and its specific heat capacity from [131]. Effective radiative properties and parameters for the modeling of combined conduction and radiation in the porous domains are taken from direct numerical pore-level simulations for the RPC material [120] and from [120,121] for the porous insulation. The emissivity of ceria is used from [116] and the properties for the three resistor model to calculate the effective thermal conductivity from [120]. The thermal conductivity of solid CeO_2 is taken from [115], its density from [132], and its specific heat capacity from [117]. The thermal conductivity of oxygen and the specific heat capacity of oxygen, carbon monoxide, and carbon dioxide are taken from [133].

3.3.7 Numerical solution

The finite volume method is used for the spatial discretization of the energy conservation equations (3.24) and (3.36), subdividing the computational domain into a number of layers

with constant properties at the cell centers. A representative cell in the porous RPC domain is shown in Figure 3.14. As the problem is one-dimensional, the area of all cells is equal to the area of the RPC perpendicular to the direction of the spatial variable x .

The implicit Euler scheme is used for the discretization of the energy conservation equation in time.

$$\rho A \Delta x c_p \frac{T^{n+1} - T^n}{\Delta t^{\text{num}}} = \sum \dot{Q} = \dot{Q}_{\text{cond}} + \dot{Q}_{\text{rad}} + \dot{Q}_{\text{conv}} \quad (3.41)$$

For the porous domains the discretization is written as follows.

$$\begin{aligned} \rho A \Delta x c_p \frac{T^{n+1} - T^n}{\Delta t^{\text{num}}} = & \lambda A \frac{T_{i-1,j}^{n+1} - T_{i,j}^{n+1}}{\Delta x} - \lambda A \frac{T_{i,j}^{n+1} - T_{i+1,j}^{n+1}}{\Delta x} \\ & + \lambda A \frac{T_{i-1,j}^{n+1} - T_{i,j}^{n+1}}{\Delta x} - \lambda A \frac{T_{i,j}^{n+1} - T_{i+1,j}^{n+1}}{\Delta x} \end{aligned} \quad (3.42)$$

The subscripts “ i ” and “ j ” indicate the location of the volume element, where the former denotes the i -th layer in x -direction, and the latter the j -th chamber of the heat exchanger. Linear interpolation is used to find the temperatures at cell interfaces necessary for the derivation of the thermal conductivity which is a function of temperature.

The energy conservation equations are then written for the whole computational domain giving a system of coupled non-linear equations. Using the boundary conditions shown in Section 3.3.5, the system of equations is solved for each time step in MATLAB [134].

A grid convergence study is performed to determine the number of computational layers in the insulation and the reactive material. Ten layers are chosen for both domains at a time step of one second after the convergence study showed a deviation of less than 1.1% compared to the solution using twice the amount of layers at a ten times smaller time step. Due to their low thickness, one layer is chosen for the reactor wall, and the separating walls.

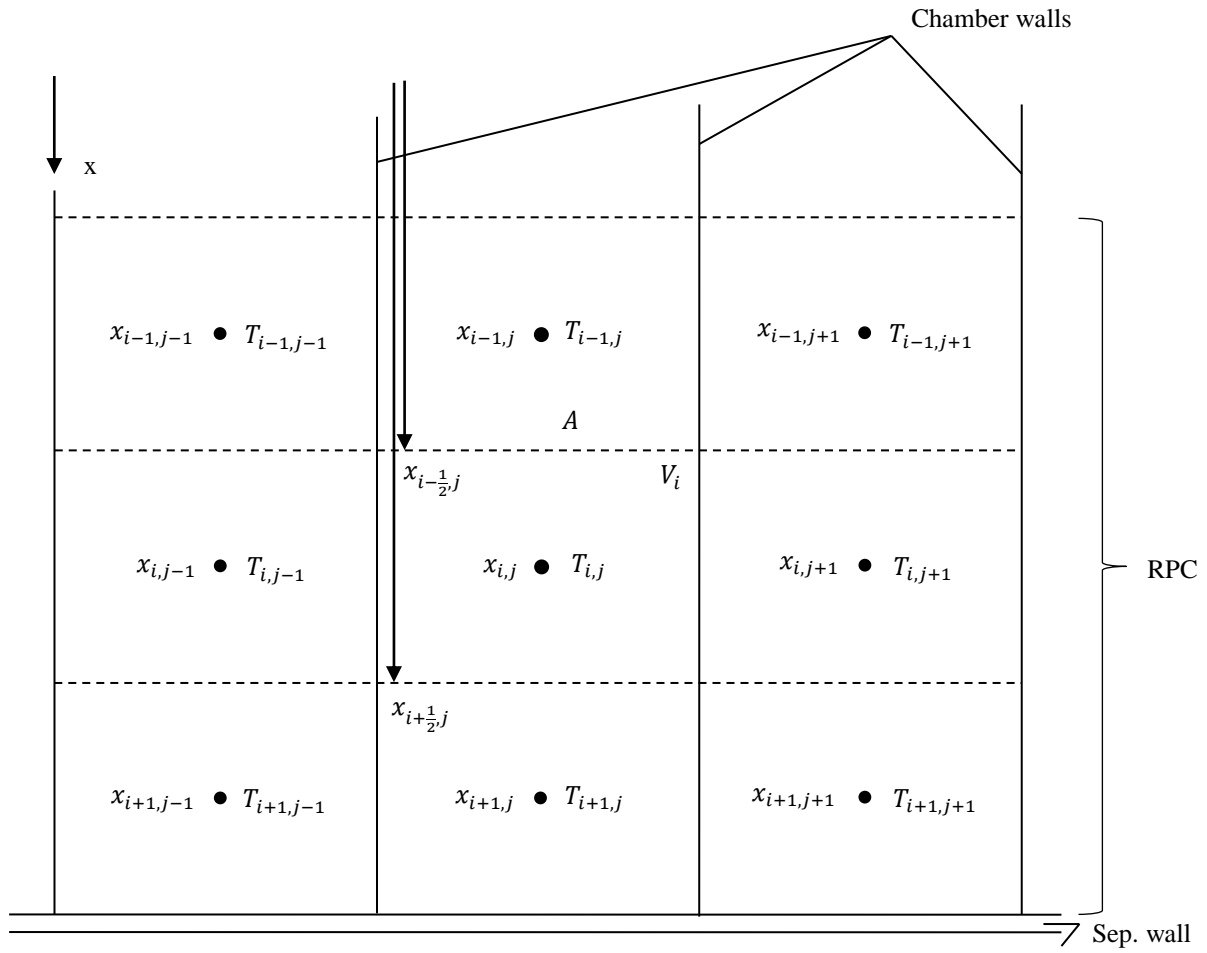


Figure 3.14 Schematic of representative porous media volume elements in finite volume discretization. Shown are the upper chamber halves of three adjacent chambers.

3.3.8 Model validation

In order to validate the reactor model, the single-chamber heat exchange between two RPCs separated by a thin wall is solved with the proposed reactor model and compared to a Monte Carlo analysis, where the result of the latter is taken as a reference.

The overall heat exchange of reactive material in counter-flow is comprised of a succession of identical heat exchange processes of RPCs at different temperatures in the single chambers of the heat exchanger. Therefore, the following test case used for model validation represents the overall heat exchange and is thus used for its assessment.

For the test case, a temperature of 1600 K is chosen as a uniform temperature for the RPC in the upper chamber and the adjacent separating wall which is made of two 1-mm layers of

Al_2O_3 and SiC/HfC , respectively. The former is used for the physical separation of SiC and CeO_2 which may undergo carbothermal reduction when brought into contact at high temperatures, and has an emissivity of about 0.4 [116] and a thermal conductivity of $35 \text{ W m}^{-1} \text{ K}^{-1}$ [129]. The latter is a material used for protective coatings with an emissivity of 0.85, a thermal conductivity of $80 \text{ W m}^{-1} \text{ K}^{-1}$, and a very high maximum operating temperature of over 2000 K [135]. The RPC in the lower chamber half has a starting temperature of 1200 K (see Figure 3.15). The simulation time is 40 s which represents a common residence time per chamber in the heat exchanger. In the Monte Carlo analysis, 2×10^5 rays are used per time step of 0.01 s and the resulting radiation heat term is inserted into the energy conservation equation which is then solved to obtain the temperature profile in the computational domain. Heat conduction is modeled in both models with the three resistor model, so that the difference between the models is derived from the description of the radiative source term.

The MC model is a statistical tool and uses random numbers to describe the radiation emitted from the computational domain. This causes the results to scatter statistically. In order to reduce the variability of the results, the MC model is run ten times and the results are averaged and compared with the RDA solution. 95%-confidence intervals are calculated from the MC data using the *student t function*.

$$\left[\bar{T}_i - \frac{t_{CI,\nu} \cdot s}{\sqrt{N}}; \bar{T}_i + \frac{t_{CI,\nu} \cdot s}{\sqrt{N}} \right] \quad (3.43)$$

\bar{T}_i is the arithmetic mean temperature of the $N = 10$ calculations at position i , $t_{CI,\nu}$ is the t -value of the *student t function* for the confidence interval CI and $\nu = N - 1$ degrees of freedom, and s is the sample standard deviation. All confidence intervals for the temperatures are below 1 K for a resolution of 100 layers per RPC.

In Figure 3.16, the temperature profiles for the test case are shown after 40 seconds of heat exchange, calculated with the Monte Carlo method for the radiation source term using 100 layers per RPC and the Rosseland diffusion approximation using 10 layers per RPC. The results of both models agree very well with an average deviation of 0.41%. The largest difference between the models of 1.61% or 23.3 K is seen at the separating wall because the RDA can give erroneous results at boundaries where the radiation is anisotropic.

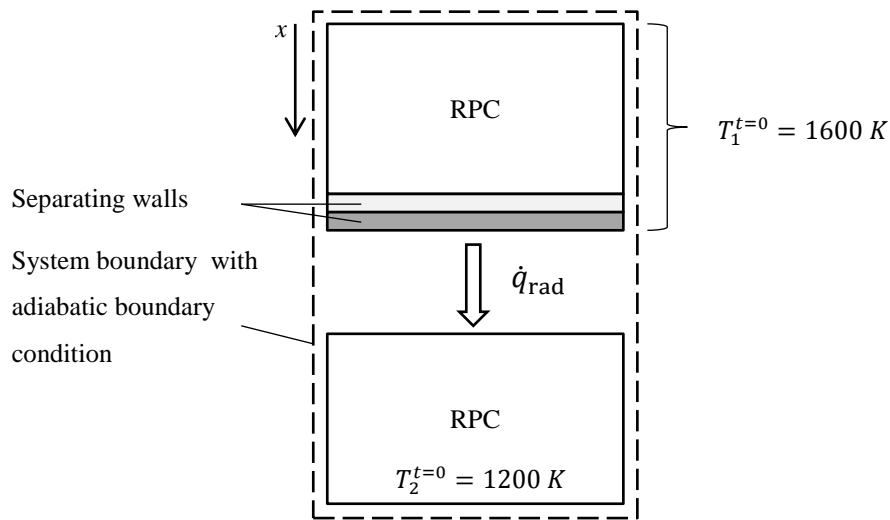


Figure 3.15 Schematic of test case used for validation of the Rosseland diffusion model with the Monte Carlo model. At the beginning of the simulation, two RPCs, separated by two layers of SiC/HfC and Al₂O₃ (1 mm thickness each) are at temperatures of 1600 K and 1200 K, respectively, with adiabatic boundary conditions towards the environment. In the transient simulation, the temperature profiles of the RPCs and the separating walls are calculated after 40 s with both models and compared.

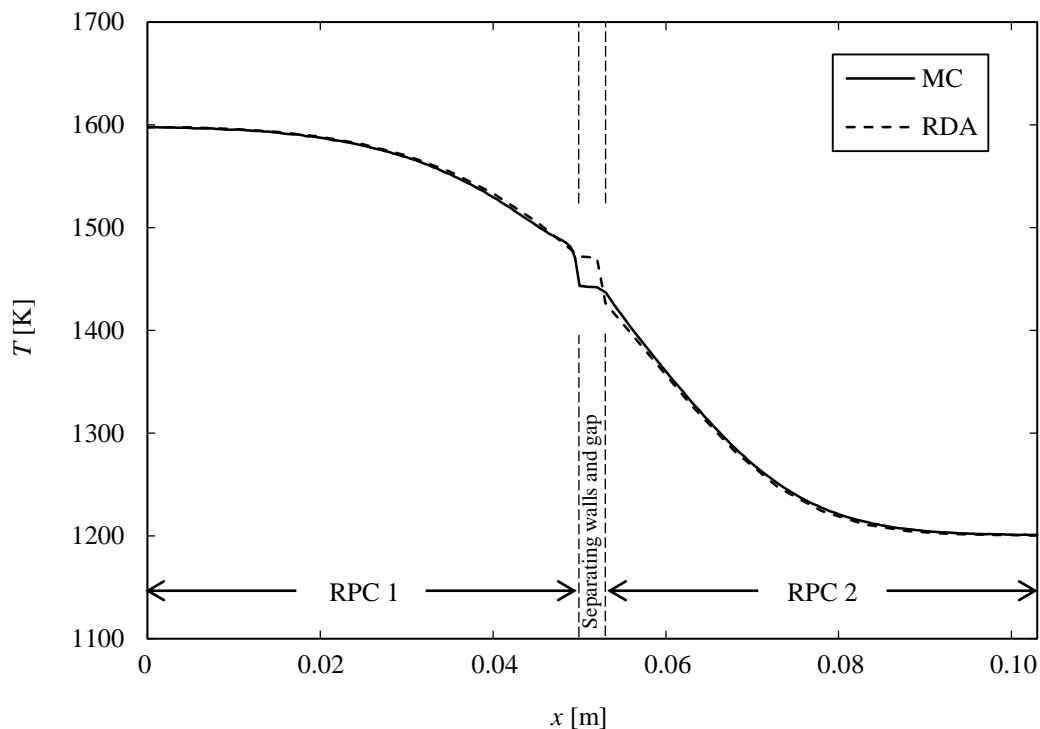


Figure 3.16 Temperature profiles obtained with the Monte Carlo model (MC) and the Rosseland diffusion approximation (RDA) for two RPCs separated by two layers of SiC/HfC and Al₂O₃ (1 mm thickness each), after 40 s of heat exchange. The starting temperatures are 1600 K for the first RPC ($0 \leq x \leq 50$ mm) and the walls ($50 < x \leq 52$ mm), and 1200 K for the second RPC ($53 \leq x \leq 103$ mm).

Due to its high accuracy and smaller computational expense of about two orders of magnitude, the RDA is chosen for the computations.

3.3.9 Results

3.3.9.1 Definition of heat exchanger efficiency

Analogous to the definition given in Equation (3.11), the efficiency of the heat exchanger is defined as the energy transferred to a reactive element in the heat exchanger divided by the thermal energy required for heating the element from the oxidation to the reduction temperature. The heat exchanger efficiency therefore describes the share of the required thermal energy for cycling between the temperature levels of the chemical reactions that is provided by the heat exchanger. In the model discussed in this section, the reactive elements are subdivided into a number n of computational layers. The total amount of transferred energy is then found by summing the energy transferred to each layer of the element at the end of the heat exchanger before entering the reduction chamber.

$$\eta_{\text{he}} = \frac{\sum_1^n m_j \int_{T_L}^{T_{\text{he, end}}} c_p dT}{m \int_{T_L}^{T_H} c_p dT} \quad (3.44)$$

n is the number of computational layers per element of reactive material, c_p is its specific heat capacity as a function of temperature, T_L and T_H are the temperatures of oxidation and reduction, respectively, and $T_{\text{he, end}}$ is the temperature of the element coming out of the heat exchanger at the end of the heating process.

In the results shown in the following analyses, also the cycle efficiency as defined in Equation (3.17) in its realistic definition, i.e. with realistic assumptions of vacuum pump power and gas separation energy, is used.

3.3.9.2 Influence of separating wall

Here, the influence of the separating walls on the heat exchange between the reduced and oxidized elements shall be analyzed. In general, an ideal separation would be achieved with a wall that has no temperature drop over its thickness and at least the same emissivity as ceria,

so as not to add resistance to the radiation heat exchange between the elements in the chamber halves.

This ideal separation is sought to be approached through the choice of a low thickness of 1 mm for each layer (Al_2O_3 and SiC/HfC) in combination with high thermal conductivities (Al_2O_3 : $35 \text{ W m}^{-1} \text{ K}^{-1}$ [129], SiC/HfC: $80 \text{ W m}^{-1} \text{ K}^{-1}$ [136]), so as to minimize the temperature drop over the walls. Furthermore, the emissivity of the SiC/HfC is comparably high with 0.85, even higher than ceria for temperatures up to 1300 K, so that also the second requirement is met. In Figure 3.17, the computational domains are shown. For the representative case of eight heat exchanger chambers with a residence time of 10 s and other parameters from Table 3.3, the heat exchanger efficiency with the separating walls is calculated to be 41.6%. Without the separating walls, i.e. assuming the reactive material to have direct radiative exchange with each other, a heat exchanger efficiency of 39.6% is calculated. The relative deviation is therefore 5.0%. Note that the efficiency in case of the separating walls is higher than without due to the low temperature drop over the walls and the excellent emissivity of the SiC/HfC which is in direct thermal contact with the RPC in the upper chamber half. At temperatures below 1100 K, the emissivity of ceria is 0.5 compared to 0.85 of the SiC/HfC which explains the better heat exchange in the colder regions of the heat exchanger in the case of the latter material.

In the following parameter studies, the calculations are performed with the separating wall, as shown in Figure 3.17 a).

Table 3.3 Chosen parameter values for the baseline case.

Parameter	Label	Value	Unit
Concentration ratio	C	3000	-
Oxidation temperature	T_L	1000	K
Reduction temperature	T_H	1800	K
Temperature of surroundings	T_0	300	K
Reduction pressure (relative to 1 atm)	p_{red}	10^{-3}	-
Oxidation pressure (relative to 1 atm)	p_{ox}	1.0	-
CO ₂ -flow (times $\text{min}=\delta_{\text{red}}$) in oxidation chamber	f_{CO_2}	2.0	-
Number of chambers (including reaction chambers)	n	10	-
Residence time per heat exchanger chamber	Δt	40	s
Mass of ceria piece	m	0.77	kg
Thickness of ceria piece	L	0.05	m
Porosity of reactive material	φ	0.8	-
Efficiency of gas heat recovery	η_{gasrec}	0.5	-
Conversion efficiency of heat to electricity	$\eta_{\text{heat-to-electricity}}$	0.4	-
Convective heat transfer coefficient	α_{conv}	15	$\text{W m}^{-2} \text{K}^{-1}$

3.3.9.4 Length of heat exchanger and residence time

An increased number of heat exchanger chambers at a constant chamber length, i.e. increased physical length of the heat exchanger, introduces heat exchange on more intermediate temperature levels and thus changes the characteristic towards a continuous counter-flow heat exchanger. A larger residence time, on the other hand, intensifies heat exchange in the existing number of chambers.

In the following, both the number of heat exchanger chambers and the residence time of the elements per chamber, are varied to analyze their influence on efficiency.

In Figure 3.18, heat exchanger efficiency is shown as a function of the number of heat exchanger chambers n_{he} (excluding the reaction chambers, i.e. $n_{\text{he}} = n-2$ in Figure 3.1) and residence time of the elements per heat exchanger chamber. The number of heat exchanger chambers is varied between zero and 20, and the residence time is varied between one second and 100 seconds.

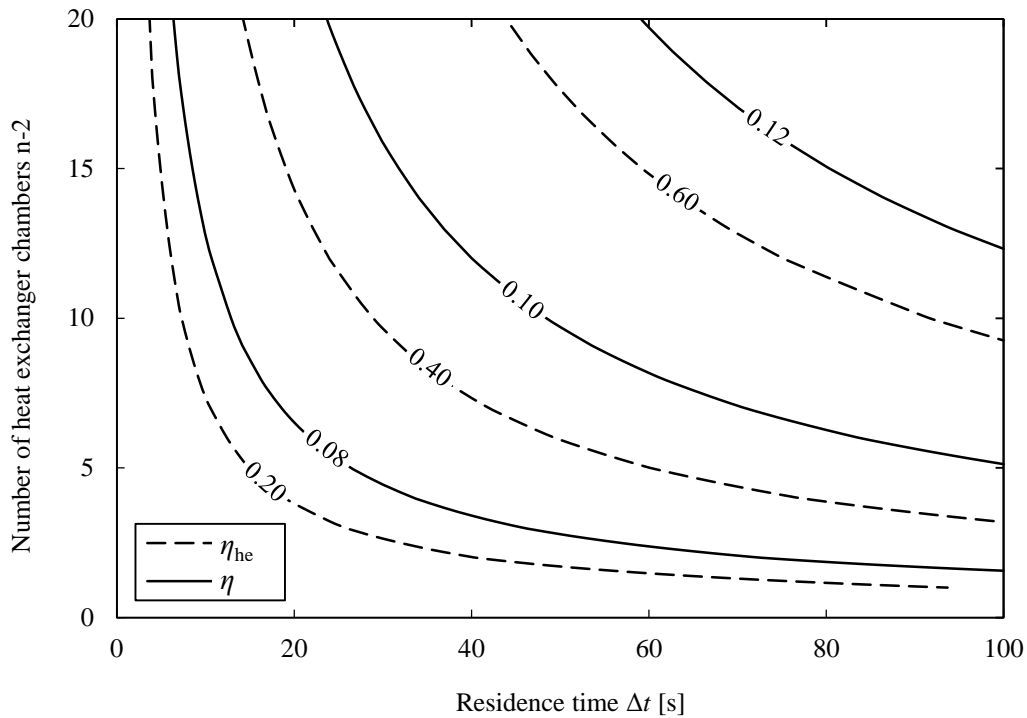


Figure 3.18 Cycle efficiency η and heat exchanger efficiency η_{he} as a function of the number of heat exchanger chambers $n_{he}=(n-2)$ and residence time per chamber Δt . Parameter values are defined according to Table 3.3.

In general, a direct correlation between the number of chambers and the residence time is visible which means that a certain level of efficiency can be reached with a number of parameter combinations. For example, $\eta_{he} = 0.4$ can be reached with $n_{he} = 20$ and $\Delta t = 14$ s, or $n_{he} = 5$ and $\Delta t = 60$ s. With interest in a compact heat exchanger, a low number of chambers can be chosen and the residence time can be adjusted accordingly.

The largest efficiency that can be reached in the chosen parameter space is over 60% which requires a heat exchanger with at least 11 chambers at a residence time of 80 seconds.

In Figure 3.18, both an increase in residence time and number of chambers increases efficiency, which indicates a dependency on the total residence time $n_{he} \times \Delta t$ of the elements in the heat exchanger. A given total residence time can be achieved with a combination of n_{he} and Δt , however, it should be expected that there are limitations to this principle regarding the chosen number of chambers: a smaller number of chambers forces the heat exchange to take place on fewer levels of temperature, while a larger number of chambers introduces more temperature levels and thus should approach the ideal counter-flow heat exchanger more closely.

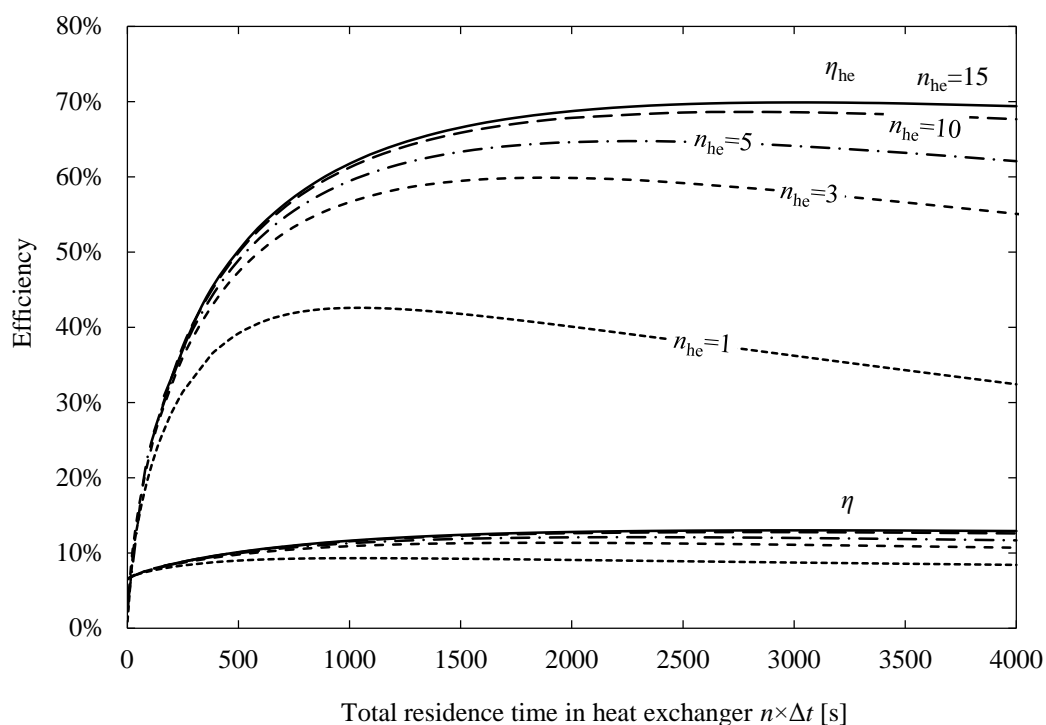


Figure 3.19 Cycle and heat exchanger efficiency as a function of the total residence time of the elements in the heat exchanger $n_{he} \times \Delta t$. At a given value of total residence time, a larger number of chambers reduces the irreversibilities of the heat exchange process by introduction of more intermediate temperature levels. Parameter values are defined according to Table 3.3.

The irreversibilities associated with the heat exchange process are thus higher for a smaller number of chambers. In Figure 3.19, efficiency is shown as a function of the total residence time of the elements in the heat exchanger. As expected, for a given value of total residence time, efficiency increases with the number of heat exchanger chambers up to about $n_{he} = 15$.

The highest efficiency is reached at $n_{he} \times \Delta t \approx 3000$ s for $n_{he} \geq 15$. At small values of $n_{he} \times \Delta t$, efficiency shows a strong increase which is not dependent on n_{he} . If the total residence time exceeds its optimum value, efficiency decreases due to the losses to the environment. With the information given about the dependency of efficiency on the number of chambers and residence time, it is possible to design the heat exchanger length to maximize efficiency.

3.3.9.5 Reduction and oxidation temperatures

The reduction and oxidation temperatures influence the syngas production rate through the thermodynamics of the redox reactions (see Section 2.1.4.2).

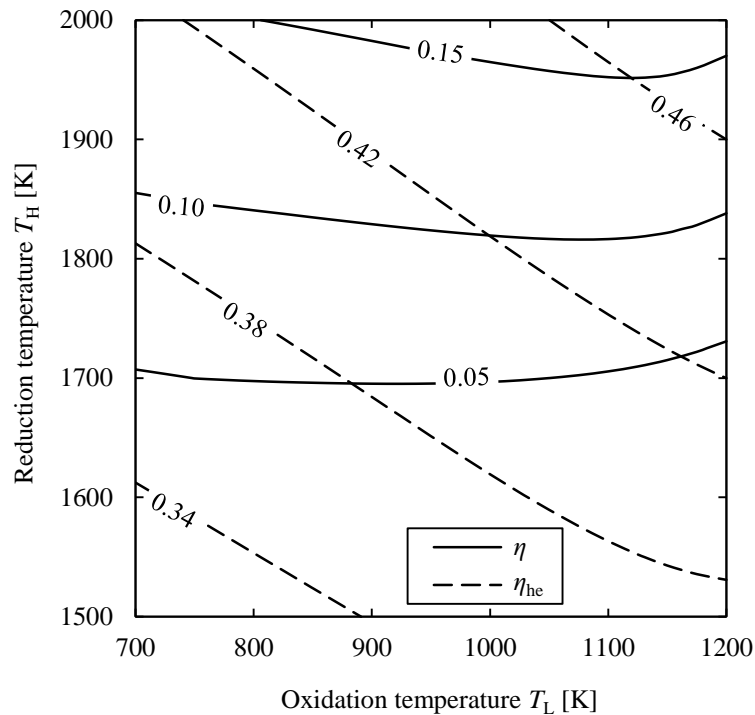


Figure 3.20 Cycle efficiency and heat exchanger efficiency as a function of reduction and oxidation temperatures for a heat exchanger with $n = 10$ chambers at a residence time of 40 s and a material thickness of 0.05 m. All other parameter values are defined according to Table 3.3.

Furthermore, the heat exchanger efficiency is affected as the inlet temperatures of the medium into the heat exchanger have been defined to be equal to the temperatures of the reaction chambers and because of the temperature dependency of the emissivity of the reactive material and of the radiation heat exchange.

In the following, the reduction temperature is varied between 1500 K and 2000 K and the oxidation temperature between 700 K and 1200 K to study the influence on efficiency. The number of chambers is ten at a residence time of 40 s and a material thickness of 0.05 m. In Figure 3.20, both the cycle efficiency η and the heat exchanger efficiency η_{he} are shown.

In the analyzed temperature regime, a heat exchanger efficiency of close to 50% can be reached towards higher reduction and oxidation temperatures. The material radiative emissivity is temperature dependent, rising from 0.5 at $T < 1100$ to 0.9 at $T \geq 1300$ K, which leads to a larger net thermal radiation term between the elements towards higher temperatures according to Equation (3.19): at an assumed fixed temperature difference of 400 K between the elements, the net radiation heat exchange is 760 W at temperatures of 1400 K and 1000 K, and 4400 W at temperatures of 1800 K and 1400 K. This behavior is expected since higher temperatures increase both the material emissivity and the ΔT^4 -term in Equation (3.19).

Regarding the cycle efficiency, values above 15% can be reached, where the ideal reduction and oxidation temperatures are also found towards higher values. The reason for the increased efficiency towards higher temperatures is the increased heat exchanger efficiency which has an important influence on cycle efficiency (Equation (3.10)), and an enhanced fuel production of the cycle due to an enlarged nonstoichiometry (Figure 2.5).

On the other hand, at constant oxidation temperature, an increase of reduction temperature increases the temperature swing of the reactive material and thus the energy required for the reactor operation. Therefore, a trade-off between fuel productivity and energy requirement is found, requiring an elevation of the oxidation temperatures when the reduction temperatures are increased to enhance efficiency.

3.3.9.6 Thickness of reactive material elements

The thickness of the elements of reactive material is varied to find its influence on heat exchanger efficiency and cycle efficiency.

Overall heat transfer between the reduced and oxidized elements is composed of i) radiation heat exchange between the top layer of the material in the lower chamber half and the separating wall, ii) heat conduction in the separating wall, and iii) the internal heat transfer within the reactive materials, as well as heat losses to the surroundings. The separating wall has a high thermal conductivity and is therefore not limiting the heat transfer. The former i) is limited by the emissivities of the materials and their temperatures, while the latter iii) is limited by the effective thermal conductivity of the material which is determined by the porosity of the material, the thermal conductivities of the solid and fluid, and the radiative properties of the porous material. An increase of material thickness does not change the thermal conductivity due to radiation or conduction, however, it increases the volume in which the heat has to be diffused and thus makes an equal temperature distribution within the material more difficult to achieve. With increasing thickness of the elements and at otherwise constant heat exchanger length and residence time, it is therefore expected that the temperature distribution within the elements will become more uneven, not allowing all of the material to participate to the same degree in the heat exchange process.

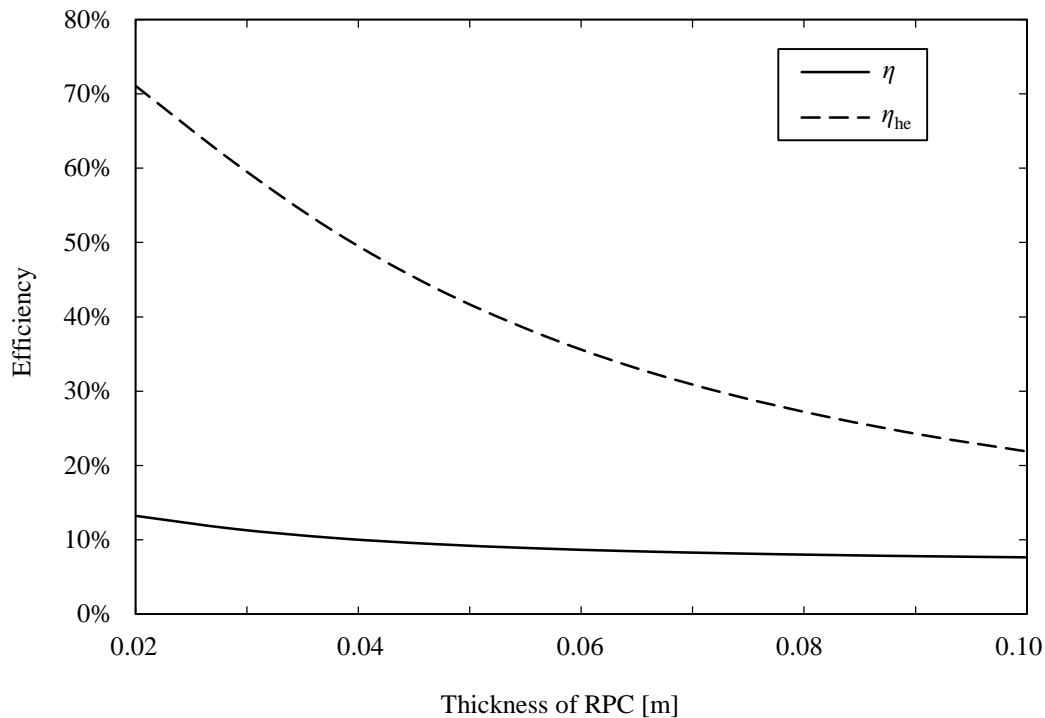


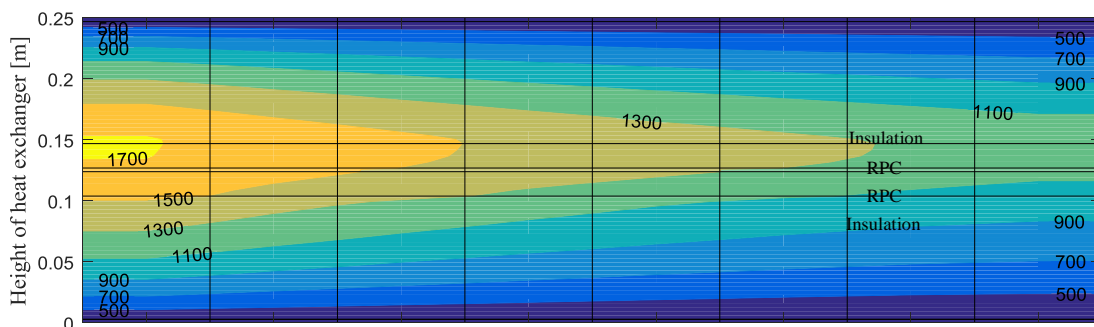
Figure 3.21 Heat exchanger efficiency η_{he} and cycle efficiency η as a function of RPC thickness for a heat exchanger with $n = 10$ chambers at a residence time of 40 s. All other parameter values are defined according to Table 3.3.

In Figure 3.21, the efficiencies of the heat exchanger and of the cycle are shown as a function of the RPC thickness which is varied between 0.02 m and 0.10 m. In general, the cycle efficiency η does not vary significantly due to the comparably low efficiency level at the chosen operating point which is limited especially by the reduction temperature and pressure.

Heat exchanger efficiency increases strongly for a decreasing material thickness: at 0.10 m $\eta_{he} = 22.1\%$ and at 0.02 m $\eta_{he} = 71.0\%$. This significant improvement is due to the fact that at a defined heat exchanger length and residence time of the elements, there is a finite time for the thermal energy to be diffused in the material. Thinner elements are therefore more likely to reach a uniform temperature distribution, while for larger thicknesses, parts of the material are participating poorly or not at all in the heat exchange between hot and cold elements which decreases heat exchanger efficiency.

In Figure 3.22, the temperature profiles of the heat exchanger are shown for a material thickness of 0.02 m and 0.10 m. The heat exchanger has eighth chambers, the temperatures of the reduction and oxidation chambers adjacent to the heat exchanger are 1800 K and 1000 K, respectively, and the residence time per chamber is 40 s.

a) Thickness: 0.02 m



b) Thickness: 0.10 m

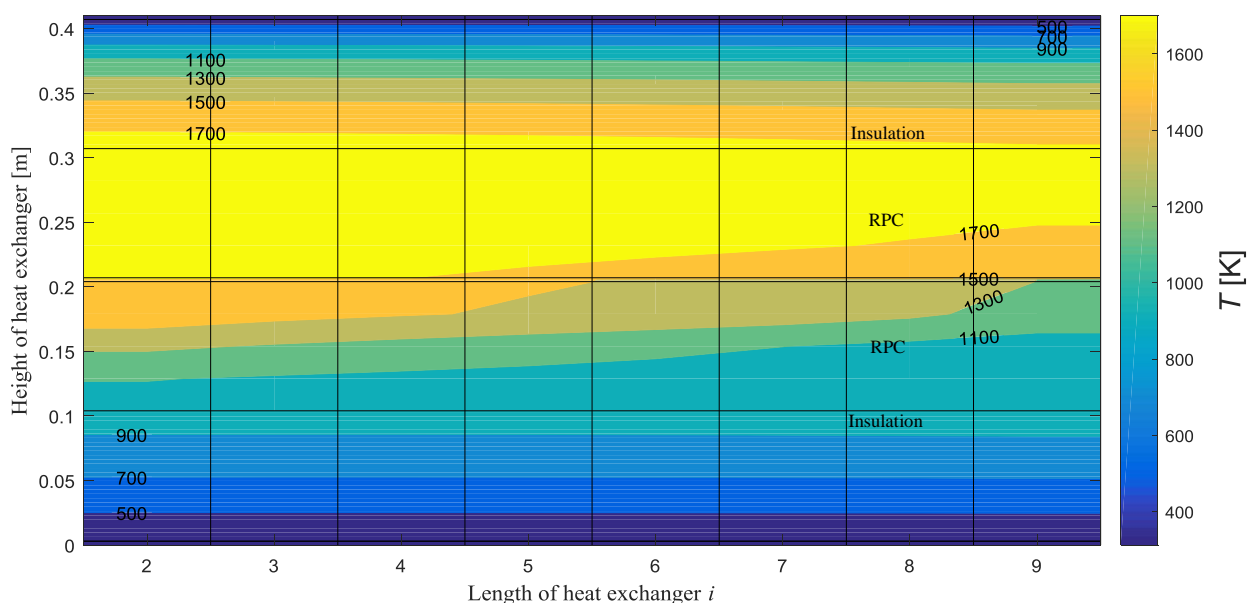


Figure 3.22 Comparison of heat exchanger temperature profiles for an RPC thickness of a) 0.02 m and b) 0.10 m. The heat exchanger has 8 chambers ($2 \leq i \leq 9$). Shown is the temperature profile of the heat exchanger including insulation and walls. The thinner material is heated more evenly to a higher temperature and thus allows for a higher heat exchanger efficiency (compare temperature profile in lower chamber half at $i = 2$). Parameter values are defined according to Table 3.3.

The profiles thus show the temperature changes of the reactive material inside of the heat exchanger (compare also Figure 3.1 for a general overview of the heat exchanger). Following the path of the colder elements ($i = 9 \rightarrow i = 2$), the heating process can be seen, where the final temperature in the heat exchanger is reached at $i = 2$. Comparing the final state of the two RPCs in a) and b) shows that the thinner material gets heated to temperatures above 1500 K with a maximum temperature difference of about 90 K (maximum temperature: 1630 K, minimum temperature: 1538 K).

The thicker material on the other hand shows a much larger maximum temperature difference of over 600 K (maximum temperature: 1610 K, minimum temperature: 990 K) since the heat diffusion process within the material is slower than the heat exchange process between the chambers with the assumed residence time.

Thus, for the larger material thickness and a total residence time of $8 \times 40 \text{ s} = 320 \text{ s}$, the internal heat diffusion process is limiting the heat exchange between hot and cold elements. Either a longer total residence time (through an increase of the residence time per chamber or an increase of the heat exchanger length) or a lower material thickness has thus to be chosen to increase the efficiency of the heat exchanger. The heating process thus becomes more efficient with a reduction of material thickness as already seen in Figure 3.21.

The influence of material thickness on heat exchanger efficiency is of course dependent on the specific properties of the heat exchanger and the reactant which were fixed here in the operating point of the baseline case (Table 3.3). For a different number of heat exchanger chambers and residence times, the efficiency curve is shifted, however, the general functional dependency between material thickness and efficiency remains the same, as it is defined by the relative magnitude of heat transfer between the chamber halves and within the materials.

The supposition of facilitated heat transfer in elements with a lower thickness is therefore confirmed which leads to a first recommendation for the design of heat exchangers, i.e. the consideration of both heat exchange processes i) between hot and cold material and ii) within the materials itself.

3.3.9.7 Porosity of reactive material

A change in porosity both influences radiation heat exchange through the extinction coefficient (Equation (3.31)) and conduction heat exchange through the effective thermal conductivity (Equation (3.33)). An increase in porosity therefore enhances radiation heat exchange through a reduction of the extinction coefficient and deteriorates conductive heat exchange within the material through a relative increase of the fluid volume which has a lower conductivity than the solid. Furthermore, the element mass is reduced. The effect of porosity on overall heat transfer is thus a trade-off between these mechanisms.

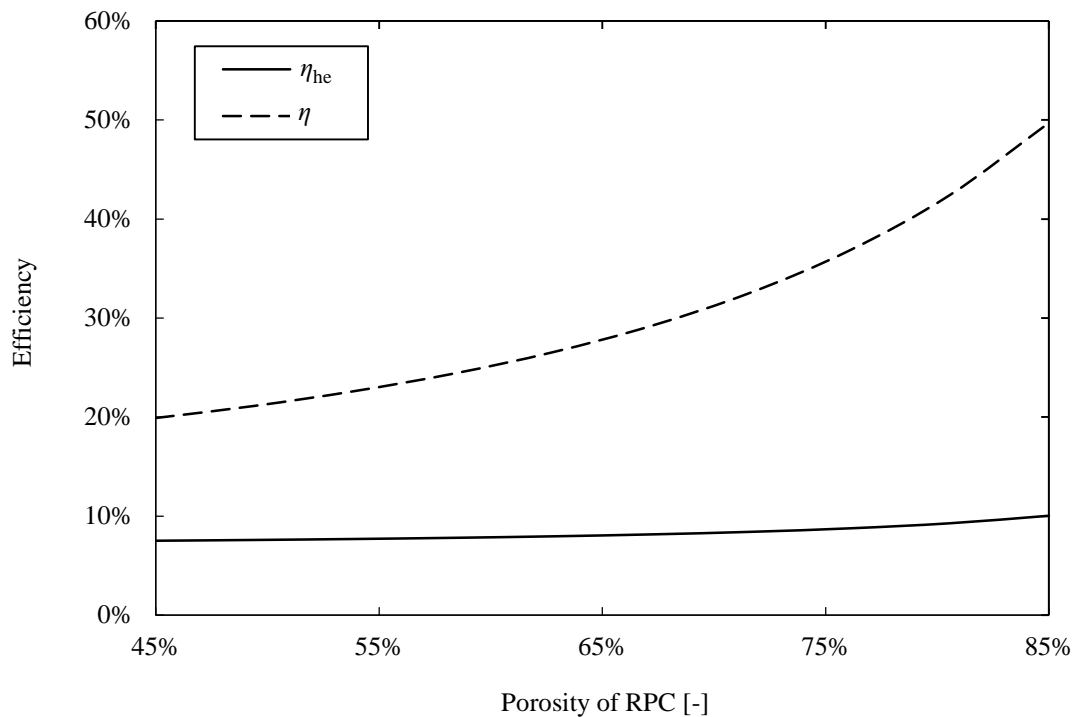


Figure 3.23 Heat exchanger efficiency η_{he} and cycle efficiency η as a function of porosity of the reactive elements for a heat exchanger with $n = 10$ chambers at a residence time of 40 s, and a material thickness of 0.05 m. All other parameter values are defined according to Table 3.3.

At high temperatures above about 1000 K, radiation heat exchange dominates the thermal energy transfer within the material. Consequently, when porosity is increased, heat can be diffused more easily within the lighter RPCs and an enhancement of heat exchange between the hot and cold elements is expected. A reduction of mass by a decrease of thickness was already seen to be advantageous in Section 3.3.9.6.

At a thickness of 0.05 m, the porosity of the reactive material is varied between a value of 45% and 85% in order to analyze its influence on efficiency which is shown in Figure 3.23. The heat exchanger efficiency increases monotonically with porosity from a value of 19.9% at 45% porosity to 49.7% at 85% porosity. Cycle efficiency rises from 7.6% to 9.9%.

This result confirms the enhancement of heat exchanger efficiency with an increase of porosity due to the reduction of the thermal mass of the elements and better radiative penetration of the element volume through a reduced extinction coefficient. The deteriorated thermal conductivity of the porous material has a smaller negative effect due to the high temperatures in the heat exchanger which leads to radiation as the dominating heat exchange mechanism.

This conclusion is valid for the porosity formulation used in the calculations which relies on a mean pore diameter. For a further evolution of the porous reactive material, a gradual change of porosity with large pores for the inlet of direct irradiation and a decrease of porosity inside the volume to increase the mass loading could be beneficial. However, the description of this gradual change in porosity requires an adaptation of the current model.

3.3.9.8 Reduction pressure

Thermodynamics predict an increase of oxygen nonstoichiometry of ceria for an increase of temperature or a reduction of oxygen partial pressure (see Figure 2.5) [82].

At a constant reduction temperature of $T_H = 1800$ K, a lower oxygen partial pressure will thus increase the amount of syngas produced. However, for the reduction of the pressure, a vacuum pump is required, the efficiency of which strongly decreases towards lower pressures, which counteracts the benefit of increased oxygen nonstoichiometry.

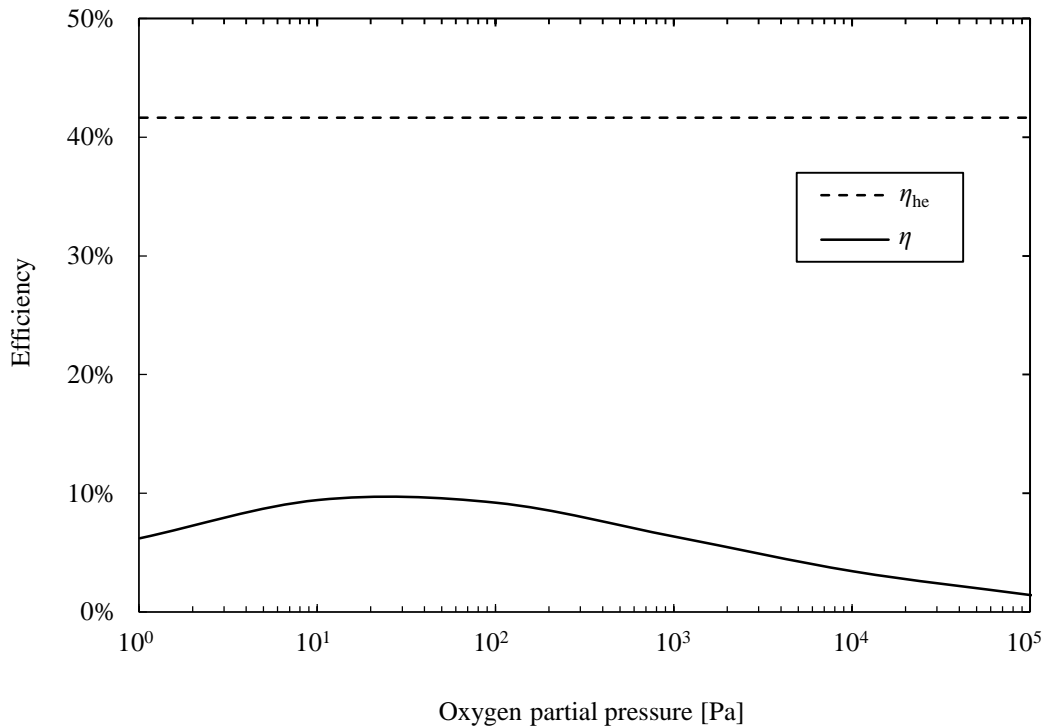


Figure 3.24 Heat exchanger efficiency and cycle efficiency as a function of oxygen partial pressure for a heat exchanger with $n = 10$ chambers at a residence time of 40 s. All other parameter values are defined according to Table 3.3.

Due to these two adverse effects, an optimum of reduction oxygen partial pressure can be found. In Figure 3.24, efficiency is shown as a function of the oxygen partial pressure. As can be seen in the graph, the optimum pressure lies between 10 and 100 Pa, while the heat exchanger efficiency is not affected by the change of reduction pressure. A trade-off has therefore to be made between increased syngas production and decreasing efficiency of vacuum pumping.

3.3.10 Conclusions for heat exchanger design

From the parameter study performed above, recommendations for the heat exchanger design using a counter-flow of solid pieces of ceria are deduced:

- A correlation exists between heat exchanger length and residence time, allowing different combinations of these two variables at constant heat exchanger efficiency. In general, η_{he} close to 70% is possible with an adequate combination of length and residence time. Above a certain limit and with respect to economics, it may therefore be advantageous to design the heat exchanger with a shorter length and a correspondingly longer residence time of the elements per chamber.
- Heat exchanger efficiency can be increased through the elevation of both reduction and oxidation temperatures (the entry temperatures into the heat exchanger are defined to be the reaction temperatures). The overall efficiency is less sensitive to the oxidation temperature and a high efficiency requires high reduction temperatures due to thermodynamics and the heat exchange process being based on thermal radiation.
- Both heat exchange processes between the elements as well as within the elements have to be considered for heat exchanger design. For a large material thickness and low porosity, internal heat diffusion can be slow compared to the residence time in the heat exchanger which leads to a challenge to dissipate the exchanged heat within the material. As only a part of the material is effectively participating in the heat exchange, this negatively influences the heat exchange process and therefore heat exchanger efficiency. A better performance can be achieved through a decrease of the material thickness, an increase of the residence time, or an increase of material porosity.

- An increase in material porosity (at a proportionally larger mean pore diameter) achieves a better penetration of the radiation into the material volume and at the same time decreases thermal conductivity and mass. The effects of higher volumetric radiation penetration and reduced thermal mass outweigh the reduced thermal conductivity and thus a higher porosity increases the heat exchanger efficiency.
- There exists an optimum reduction pressure between 10 and 100 Pa, as towards lower pressures the pump efficiency becomes limiting while towards higher pressures thermodynamics of ceria reduction are limiting.

3.4 Particle reactor concept

In Chapters 3.2 and 3.3, a computational model was presented that calculates the heat transfer between elements of porous redox material moving in counter-flow between reduction and oxidation chambers. In the first implementation, heat transfer within the redox material was assumed to be infinitely fast, while in the second case internal heat transfer was modeled. In this chapter, another fundamental idea of solar thermochemical reactor design is analyzed, i.e. the cycling of particles of reactive material between the reduction and oxidation chambers of the solar reactor.

3.4.1 Introduction

The use of redox particles for the two-step thermochemical reactions has several advantages. During reduction, the small mass enables high heat transfer rates with reaction times on the order of one second as shown in experiments at the University of Colorado at Boulder, USA, at the Swiss Federal Institute of Technology in Zurich and at the Paul-Scherrer-Institute in Villigen, Switzerland [19,137]. Furthermore, for ceria, the oxygen mobility reaches high values [86] and no passivation layer is formed at the surface of the material as may be the case for Zn-particles [138]. During oxidation, the large area-to-volume ratio of particles in connection with the short diffusion lengths therefore reduces the reaction time.

The small size of particles further has the advantage of a larger degree of freedom for reactor design because the reactive material can be moved in many ways between the reaction chambers. It is therefore possible to choose a counter-flow of particles with a large surface area to increase the solid-solid heat exchange. Compared to the solid porous structure used in the previous reactor models, particles promise to give more options for the reactor design and thus also to increase efficiency. As particles may be moved easily, the separation of the reaction chambers with separate atmospheres can possibly be achieved in a less complicated way than for larger bulk material. Furthermore, the use of particles enables a continuously operating reactor concept which is crucial for the achievement of high solar resource utilization. Resistance to thermal shocks is another advantage of reactive particles, as the particles are less prone to crack than large solid structures.

However, the deployment of reactive particles in the environment of a solar thermochemical reactor also introduces several challenges and disadvantages. For example, the feeding mechanism has to be reliable and it has to be ensured that the feeder does not react with the redox material. Also, parts of the feeder are likely to be subjected to the upper process temperature which limits the material choice considerably. Depending on the residence times and the size of the reactor volumes, the particles could possibly experience sintering which has to be avoided in a continuous reactor concept.

As of today, experimental experience with particle concepts has yet to prove its long-term operability and advantages over other concepts such as the batch-operated single-chamber reactor. However, the potential of the particle concept for highly efficient continuous solar syngas production justifies further research in this area.

3.4.2 Prior research

Particles in a heat transfer system in CSP power plants have been a topic for some time, where one of the advantages over molten salts is the increase of upper process temperature towards 1000°C. A cycle based on three types of particles for i) primary heat transfer from the sun, ii) heat exchange between reactive particles of different temperatures, and iii) reactive particles is discussed in [139], and thermochemical energy conversion efficiencies in the range of 30% in an optimistic estimate and about 15% in a more realistic estimate are given. Recent advances in receiver design, particle materials, and balance of plant for the falling particle technology for CSP power plants are presented in [140].

The thermochemical reduction of ceria particles falling through an indirectly heated tube is investigated in [19]. Through counter-flow with argon, the evolving oxygen and the reduced ceria are inherently separated. Very short reaction times of about one second are achieved and the influence of particle size on the extent of reduction is analyzed.

A particle-based reactor concept for the combined reduction and oxidation of ceria is presented in [18], where the oxidized particles are elevated in a spiral movement in the outer volume of a double-walled tube with a moving bed of hot reduced particles on the inside. Solar energy heats up the particles reaching the top of the elevator, when falling into the inner tube. Gas separation is claimed to be achieved through the moving bed of reduced particles

which represents an effective seal towards the oxidation chamber. So far only little experimental data is available regarding the feeder mechanism and the heat exchanger efficiency at low temperature [141], and the operability at high temperatures suitable for thermochemical splitting cycles has yet to be shown.

Researchers at the Niigata University investigate an internally circulating fluidized bed of $\text{NiFe}_2\text{O}_4/\text{m-ZrO}_2$ -particles in [64].

The state of the art of solar particle receivers for the production of hydrogen is reviewed and a conceptual design of Sandia National Laboratories is presented in [142].

The dissociation of ZnO -particles in a rotating cavity receiver is analyzed in [78] which represents the thermal reduction of the redox material. In a second step, zinc and oxygen have to be thermally quenched to low temperatures with an inert gas to prevent their recombination, which is investigated in [143]. Although having a large theoretical potential, the quenching is very energy intensive, limiting the overall energy conversion efficiency.

A methane flow laden with carbon black particles in the μm -range is converted to carbon and hydrogen in an experimental 5-kW particle-flow reactor directly irradiated by concentrated solar radiation in [144]. The authors reached a 16% solar energy-to-chemical conversion efficiency at a maximum theoretical value of 31%.

Fe_3O_4 on cubic yttria-stabilized zirconia is used for a two-step water splitting cycle and its adequacy for thermochemical splitting cycles analyzed with respect to cycle stability and reproducibility of the evolving amounts of gas in [64].

CO_2 is removed from a gas stream with a cyclic thermochemical process based on the consecutive CaO -carbonation and CaCO_3 -calcination in a solar irradiated reactor. The particles are held in a fluidized bed to expose the reacting material directly to the concentrated irradiation [36].

3.4.3 Model description

The proposed particle reactor model for the two-step thermochemical syngas production consists of a reduction area, an oxidation chamber, and a heat exchanger connecting both reaction zones (see Figure 3.25). The heat exchanger consists of a double-walled tube, where

the oxidized cold particles are elevated in a packed bed on the outside and the reduced hot particles are moving in a counter-flow packed bed on the inside. As was already observed for the bulk porous metal oxide used in the chamber model of the previous chapters, heat diffusion in the reactive material can be a limiting factor for heat exchange. Therefore, to improve the heat exchanger, an inert cylindrical centerpiece is added to force the reduced particles into an annular ring which reduces the bed thickness. In this way, the volume of particles far from the heat exchange surface is minimized and the required length of heat diffusion within the particle bed is reduced. The oxidized particles fall into the annular section of the inner tube when reaching the top and are directly irradiated by solar energy incident from the top. Reduced particles are removed from the bottom and inserted into the oxidation chamber, where they are contacted with H_2O , CO_2 , or a mixture thereof, to produce syngas. The packed bed of reduced particles thus moves downwards, while oxidized particles coming out of the oxidation chamber are fed to the bottom of the outer tube of the heat exchanger, inducing an upward movement of the packed bed of oxidized particles. The beds are assumed to be unmixed, i.e. there is no relative movement of the particles in the moving beds, which is a conservative estimation. Mixing of the beds can significantly enhance heat transfer but is outside of the scope of this analysis. Identically to the approach used in Chapters 3.2 and 3.3, the computational model focuses on the heat exchanger which is decoupled from the thermodynamic model in the reaction chambers. Heat exchanger efficiency is derived and inserted into the energy balance of the overall system.

A schematic of the reactor model including the computational domains is shown in Figure 3.25. The heat exchanger outside wall is a solid domain and made from Inconel 600 with a thickness of 0.003 m. The insulation between the outer reactor wall and the moving bed of oxidized particles is a porous domain made from (porous) Al_2O_3 with a thickness of 0.1 m. The separating wall between the moving beds of particles is a solid domain from (non-porous) Al_2O_3 at a thickness of 0.003 m. The separation between the beds provides sealing with respect to evolving gases and should otherwise have a high thermal conductivity for heat exchange. Non-porous Al_2O_3 is therefore chosen as it is suitable for the process temperatures, does not react with ceria and provides a seal for the gases. The inner tube at the center of the heat exchanger has a diameter of 0.04 m and is made from porous Al_2O_3 to provide insulation.

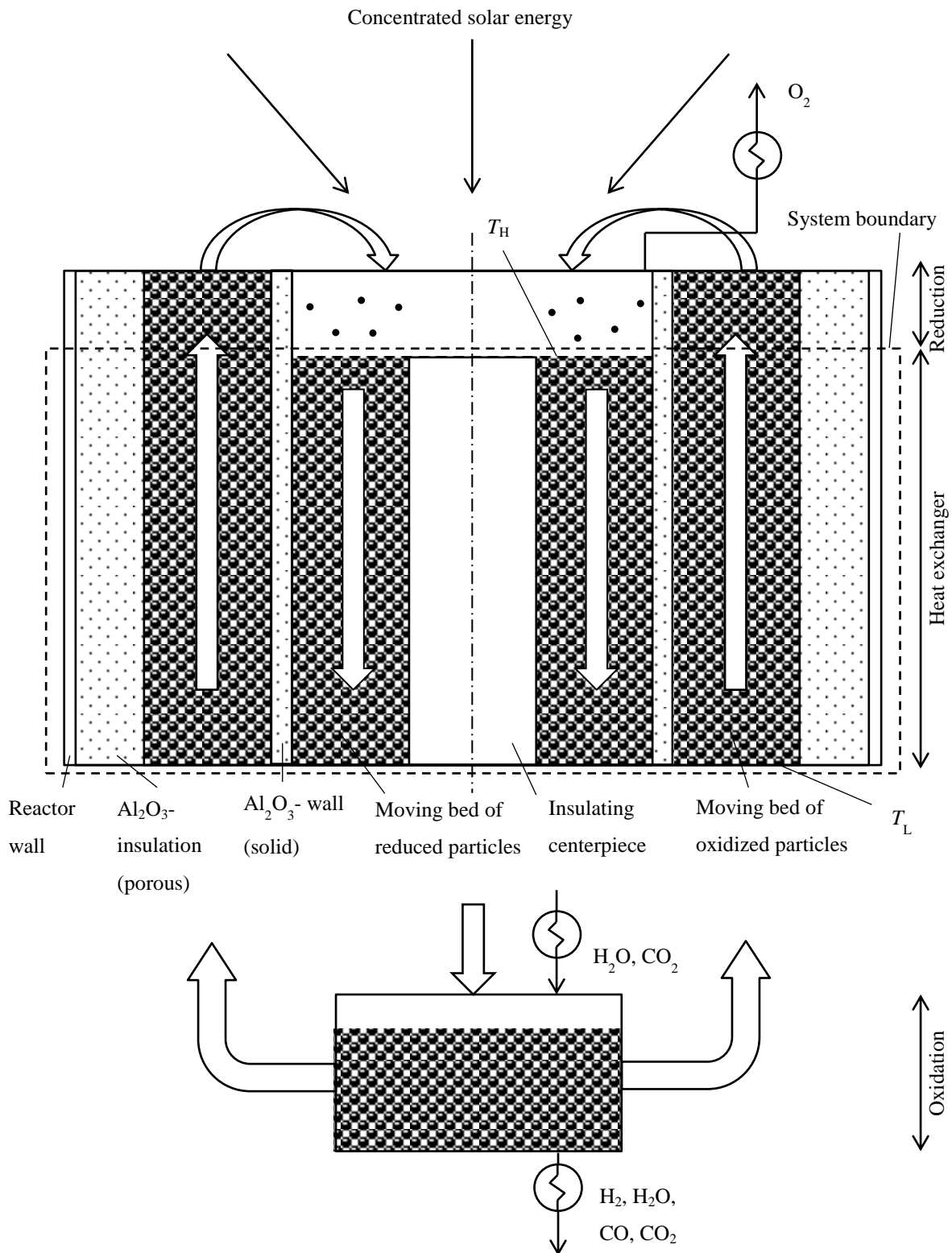


Figure 3.25 Schematic of particle heat exchanger model including computational domains.

The chosen diameter of the moving beds fulfills conservation of mass, i.e. the mass flow of oxidized particles is equal to the mass flow of reduced particles. The moving beds of particles

are modeled as porous domains. Heat is transferred by radiation and conduction inside of the moving beds, and between the beds and the adjacent domains. In the porous domain of the insulation, heat is transferred by radiation and conduction and in the solid domains only by conduction. Heat is lost from the reactor walls to the surroundings by convection and radiation.

At the top end of the heat exchanger where solar energy is incident on the particles, a fixed temperature is chosen for the reduced particles. Equally, the oxidation temperature is assumed to be the inlet temperature of oxidized particles into the heat exchanger. Reradiation losses are included in the energy balance of the solar reactor as in the two preceding models.

3.4.4 Governing equations

Solid domain

In the solid domain, heat conduction is modeled with the law after Fourier.

$$\rho c_p \frac{\partial T}{\partial t} = \nabla \cdot (\lambda \nabla T) \quad (3.45)$$

where λ is the thermal conductivity of the solid material.

Particle bed domains

Heat transfer between wall and particle bed:

For the description of thermal energy transfer between the walls and the bed of particles, the model after Schlünder is used [145] which is presented in the following. In the model, an expression for the heat transfer coefficient α is found which allows the derivation of the heat flow between the wall and the bed according to

$$\dot{Q}_{\text{wall-bed}} = \alpha A \Delta T. \quad (3.46)$$

A fundamental characteristic of the thermal energy transfer from a wall to an adjacent bed of particles is a large temperature step between the wall and the first particles in the bed, and a smaller temperature gradient inside of the bed of particles. The heat exchange is therefore

determined by i) heat transfer at the boundary of the wall and the particle bed (described by heat transfer coefficient α_{ws}) and ii) heat transfer in the particle bed (α_{sb}).

The overall resistance α for thermal energy transfer between the wall and the adjacent bed of particles is then related to the single resistances α_{ws} and α_{sb} in the following way.

$$\frac{1}{\alpha} = \frac{1}{\alpha_{ws}} + \frac{1}{\alpha_{sb}} \quad (3.47)$$

The heat transfer coefficient at the boundary of bed and particles α_{ws} is comprised of the contributions for heat transfer between wall and particles, wall and gas phase, by radiation, and by direct contact between the wall and the particles.

$$\alpha_{ws} = \Phi_A \alpha_{wp} + (1 - \Phi_A) \frac{2\lambda_G/d}{\sqrt{2} + (2l + 2\delta)/d} + \alpha_{rad} + \alpha_{dir} \quad (3.48)$$

Φ_A is the plate surface coverage factor by the particles, α_{wp} is the heat transfer coefficient between the wall and a particle, λ_G is the continuum heat conductivity of the gas, d is the particle diameter, l is the modified mean free path of the gas molecules, δ is the roughness factor of the particles, α_{rad} is the heat transfer coefficient for radiation, and α_{dir} is the heat transfer coefficient for direct contact of particle and wall.

α_{wp} is defined as

$$\alpha_{wp} = \frac{4\lambda_G}{d} \left[\left(1 + \frac{2l + 2\delta}{d} \right) \ln \left(1 + \frac{d}{2l + 2\delta} \right) - 1 \right], \quad (3.49)$$

where the modified mean free path l is

$$l = 2\Lambda \frac{2 - \gamma}{\gamma} \quad (3.50)$$

Λ is the mean free path and is derived from

$$\Lambda = \frac{16}{5} \sqrt{\frac{\mathcal{R}T}{2\pi M}} \frac{\eta}{p} \quad (3.51)$$

where \mathcal{R} is the universal gas constant, M is the molecular mass of the gas, η its dynamic viscosity, and p its pressure. γ is the accommodation coefficient which is derived by

$$\log\left(\frac{1}{\gamma} - 1\right) = 0.6 - \frac{\left(1000 \frac{\text{K}}{T}\right) + 1}{C}, \quad (3.52)$$

where C is 2.8 for air and this value is also chosen for oxygen due to lack of experimental data [146–148].

The radiative heat transfer coefficient is

$$\alpha_{\text{rad}} = 4\sigma \frac{1}{\frac{1}{\varepsilon_{\text{wall}}} + \frac{1}{\varepsilon_{\text{bed}}} - 1} T^3, \quad (3.53)$$

where σ is the Stefan-Boltzmann constant, $\varepsilon_{\text{wall}}$ is the emissivity of the wall, and ε_{bed} is the emissivity of the bed of particles.

The contribution of the direct contact of particles and wall is

$$\alpha_{\text{dir}} = 2 \frac{a \lambda_S}{d}, \quad (3.54)$$

where a is the diameter of the contact surface area of particle and wall in case the particles are not perfectly spherical, d is the particle diameter, and λ_S is the thermal conductivity of the particles. For the ratio $\frac{a}{d}$, a value of 3×10^{-4} is chosen [145].

Heat transfer from bed surface to bulk:

Assuming a constant wall temperature and a moving bed of particles, the time averaged heat transfer coefficient for the penetration of heat from the bed surface into the bulk is expressed after [145] with

$$\alpha_{\text{sb}} = \frac{2 \sqrt{(\rho c_p \lambda)_{\text{bed}}}}{\pi \sqrt{t}}, \quad (3.55)$$

with the porosity ρ , the heat capacity c_p and the thermal conductivity λ , each referring to the bed of particles and evaluated at the mean bed temperature, and the contact time t . Here, for simplicity, the arithmetic mean temperature of the bed is chosen instead of the calorific mean temperature. For a moving bed and an isothermal wall, the contact time is equal to the total residence time of the particles on the wall L/v , with the length of the wall L and the velocity of

the particles v . However, for the case of the double-walled heat exchanger, the wall cannot be assumed to be isothermal and a different contact time has to be used. When the cold bed enters the heat exchanger, the particles have a uniform temperature of T_L which increases while the particles rise, until it reaches its final temperature at the exit of the heat exchanger. When the bed is isothermal, $\alpha_{sb} \rightarrow \infty$ and the overall heat transfer coefficient is equal to α_{ws} (see equation (3.47)) [145]. When the temperature drops inside the bed, $\alpha_{sb} < \alpha_{ws}$, and the heat transfer is limited by the resistance from bed surface to the bulk material of the bed. For both hot and cold beds, the overall heat transfer coefficient α will therefore have a high value of α_{ws} at the entrance of the heat exchanger ($t \approx 0$) which drops to lower values along the axial length ($t > 0$). The contact time of hot and cold particles is therefore increased from entrance to exit in the following way:

- in the first layer, the contact time is $t = \Delta t^{\text{num}}$, and
- in the m -th layer $t = m \times \Delta t^{\text{num}}$,

where Δt^{num} is the residence time of the particles in each of the numerical axial layers.

Heat transfer within particle bed:

For the description of heat transfer in the particle bed, the model after Zehner, Bauer and Schlünder is used [149] which gives an expression for the thermal conductivity of the bed which can then be used in the law of Fourier.

$$\rho c_p \frac{\partial T}{\partial t} = \nabla \cdot (\lambda \nabla T) \quad (3.56)$$

$$\dot{Q}_{\text{bed}} = \lambda_{\text{bed}} A \Delta T \quad (3.57)$$

In this model, a representative unit cell of the particle bed is analyzed which is comprised of a cylindrical core with two opposing particle halves, and a fluid layer surrounding the core.

When using a unit cell, either parallel heat flow lines or parallel isotherms are assumed to facilitate the calculations, which is a simplification. In the present model, the incorrect assumption of parallel heat flow lines is sought to be corrected by simulating spherical particles with non-spherical particles [149]. The model is used in its more complicated form

including the effects of radiation, pressure dependency, and heat transfer through non-spherical particles.

The thermal conductivity of the particle bed is expressed with

$$k_{\text{bed}} = \frac{\lambda_{\text{bed}}}{\lambda_f} = (1 - \sqrt{1 - \varphi})\varphi[(\varphi - 1 + k_G^{-1})^{-1} + k_{\text{rad}}] + \sqrt{1 - \varphi}[\psi k_p + (1 - \psi)k_c]. \quad (3.58)$$

λ_{bed} is the thermal conductivity of the bed of particles, λ_f that of the fluid in between the particles, φ is the porosity of the bed, ψ is the flatness coefficient of the particles, and k_G , k_{rad} and k_c are the thermal conductivity of the gas including the effect of pressure dependence, the radiative conductivity, and the thermal conductivity of the core of the unit cell, each relative to the fluid thermal conductivity.

$$k_c = \frac{2}{N} \left\{ \frac{B(k_p + k_{\text{rad}} - 1)}{N^2 k_G k_p} \ln \frac{k_p + k_{\text{rad}}}{B[k_G + (1 - k_G)(k_p + k_{\text{rad}})]} + \frac{B + 1}{2B} \left[\frac{k_{\text{rad}}}{k_G} - B \left(1 + \frac{1 - k_G}{k_G} k_{\text{rad}} \right) \right] - \frac{B - 1}{N k_G} \right\}, \quad (3.59)$$

with

$$N = \frac{1}{k_G} \left(1 + \frac{k_{\text{rad}} - B k_G}{k_p} \right) - B \left(\frac{1}{k_G} - 1 \right) \left(1 + \frac{k_{\text{rad}}}{k_p} \right), \quad (3.60)$$

$$B = C_f \left[\frac{(1 - \varphi)}{\varphi} \right]^{\frac{10}{9}}, \quad (3.61)$$

$$k_{\text{rad}} = \frac{\lambda_{\text{rad}}}{\lambda_f} = \frac{4\sigma}{(2/\varepsilon) - 1} T^3 \frac{d}{\lambda_f}, \quad (3.62)$$

$$k_G = \frac{\lambda_G}{\lambda_f} = \left[1 + \left(\frac{l}{d} \right) \right]^{-1}, \quad (3.63)$$

$$k_p = \frac{\lambda_p}{\lambda_f}. \quad (3.64)$$

l is the modified mean free path of the gas molecules and is calculated after Equation (3.51), d is the particle diameter, ε is the particle emissivity, φ is the porosity of the bed, C_f is the form factor of the particles which has to be determined experimentally and which is 1.25 for spherical particles [149], and k_p is the relative thermal conductivity of the particles.

Equations (3.60)-(3.64) are then used in Equation (3.58) to derive the thermal conductivity of the particle bed. Equation (3.57) then gives the heat flux through the particle bed.

3.4.5 Boundary conditions

In the following, the boundary conditions for the computational domains are given.

Heat exchanger wall facing surroundings

Energy is transferred by radiation and convection from the reactor wall to the surroundings which are assumed to have a temperature of 300 K.

$$\lambda \nabla T|_{rw \rightarrow 0} = \dot{q}_{\text{rad}} + \dot{q}_{\text{conv}} \quad (3.65)$$

$$= \varepsilon_{\text{he,wall}} \sigma (T_{\text{he,wall}}^4 - T_0^4) + \alpha_{\text{conv}} (T_{\text{he,wall}} - T_0) \quad (3.66)$$

The subscripts “rw” and “0” denote the reactor wall and the surroundings, $\varepsilon_{\text{he,wall}}$ is the emissivity of the heat exchanger wall, and α_{conv} is the convective heat transfer coefficient from the reactor wall to the surroundings which is derived from the following Nusselt correlation for a vertical cylinder [150].

$$\text{Nu} = \left\{ 0.825 + 0.387 [Ra \cdot f_1(Pr)]^{1/6} \right\}^2 + 0.435 \frac{h}{D} \quad (3.67)$$

$$f_1 = \left[1 + \left(\frac{0.492}{Pr} \right)^{9/16} \right]^{-16/9} \quad (3.68)$$

Temperature of particles entering heat exchanger

The temperature of the particles entering the heat exchanger at the hot side is defined to be the reduction temperature T_H .

$$T_{\text{he,hot}} \equiv T_H \quad (3.69)$$

Analogously, the temperature of the particles entering the heat exchanger at its cold side is defined to be the oxidation temperature T_L .

$$T_{\text{he,cold}} \equiv T_L \quad (3.70)$$

Adiabatic boundary at center of heat exchanger

The heat exchanger has a three-dimensional cylindrical geometry which is represented by a two-dimensional plane in the computational model due to the geometrical symmetry. The plane reaches from the centerline of the cylinder to the outside of the heat exchanger wall facing the surroundings. At the boundary of the hot particle bed and the inert centerpiece, an adiabatic boundary condition is chosen which requires that the first derivative of the temperature be equal to zero.

$$\frac{\partial T}{\partial r} = 0 \quad (3.71)$$

3.4.6 Material properties

An overview of the material properties used for the calculations is shown in Table A.5 and Table A.6 in the Annex. The emissivity, thermal conductivity, specific heat capacity, and density of the reactor wall made from Inconel 600 are taken from [126]. Its thickness is chosen to be 3 mm. The emissivity of the Al_2O_3 insulation is from [116], its radiative extinction coefficient from [121], its thermal conductivity and density from [113], and its specific heat capacity from [131]. Effective radiative properties and parameters for the modeling of conduction in the porous insulation domain are taken from [120,121].

The emissivity of the ceria particles is taken from [116], their thermal conductivity from [115], their density from [132], and their specific heat capacity from [117].

The thermal conductivity of oxygen and the specific heat capacity of oxygen, carbon monoxide, and carbon dioxide are taken from [133].

3.4.7 Numerical solution algorithm

The numerical solution algorithm used for the particle reactor model is similar to the one used for the reactor model with internal heat diffusion in Chapter 3.3.7.

The finite volume method is used for the spatial discretization of the energy conservation Equations (3.45) and (3.56), subdividing the computational domain into a number of layers in radial and axial direction with constant properties at the cell centers. The discretization of the computational domains is shown in Figure 3.26. The system of equations is solved with the implicit Euler method, where the coefficients are estimated at the time step n instead of $n+1$ for computational performance. The solution is nearly identical with the solution after the explicit Euler method at a smaller computational cost. The energy balance is

$$\rho A \Delta x c_p \frac{T^{n+1} - T^n}{\Delta t^{\text{num}}} = \sum \dot{Q} = \dot{Q}_{\text{cond}} + \dot{Q}_{\text{rad}} + \dot{Q}_{\text{conv}}. \quad (3.72)$$

As an example, for the porous domains the discretization is written as follows.

$$\rho \pi \left(r_{i+\frac{1}{2}}^2 - r_{i-\frac{1}{2}}^2 \right) \Delta h c_p \frac{T_{i,j}^{n+1} - T_{i,j}^n}{\Delta t^{\text{num}}} = \frac{2\pi \Delta h \lambda_{\text{bed}} T_{i+1,j}^{n+1} - T_{i,j}^{n+1}}{\ln\left(\frac{r_i}{r_{i+1}}\right)} - \frac{2\pi \Delta h \lambda_{\text{bed}} T_{i,j}^{n+1} - T_{i-1,j}^{n+1}}{\ln\left(\frac{r_i}{r_{i-1}}\right)} \quad (3.73)$$

The subscripts “ i ” and “ j ” indicate the location of the volume element, where the former denotes the i -th layer in r -direction, and the latter the j -th layer in z -direction. Linear interpolation is used to find the temperatures at cell interfaces necessary for the derivation of the thermal conductivity which is a function of temperature.

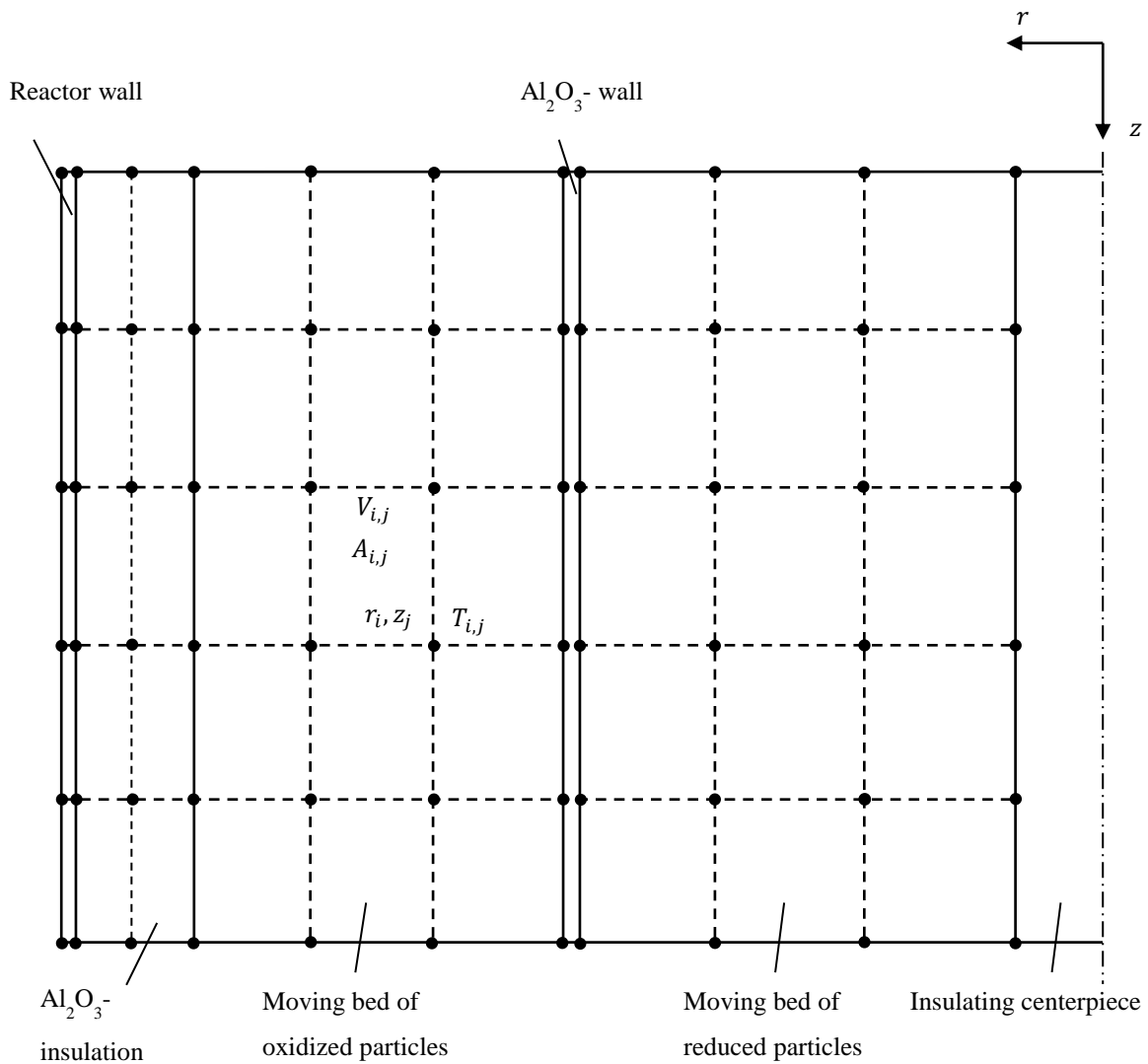


Figure 3.26 Schematic of finite volume discretization of computational domains.

The energy conservation equations are then written for the whole computational domain giving a system of coupled non-linear equations. Using the boundary conditions shown in Section 3.4.5, the system of equations is solved for each time step in Matlab. The pseudo-transient continuation method is used to approximate the steady state of the heat exchanger in operation.

A grid convergence study is performed to determine the number of computational layers in the insulation and the reactive material. Ten layers are chosen for the insulation, 100 layers in radial direction for the particle beds, and 120 layers in axial direction of the heat exchanger after the convergence study showed a deviation of less than 0.1%, 1.0 % and 0.1%, respectively, compared to the solution using at least three times the amount of layers in the

respective domains. Due to their low thickness and high thermal conductivity, a single layer is chosen for the reactor wall and the separating wall, respectively.

3.4.8 Model validation

In order to demonstrate the validity of the chosen approach of modeling the heat transfer between moving beds of particles, partial results of the model are compared to experimental results in the literature for the heat transfer coefficient α and the thermal conductivity λ_{bed} . Additionally, the modeled steady-state temperature profile in a fixed bed of particles is compared with experimental values.

3.4.8.1 Overall heat transfer coefficient α

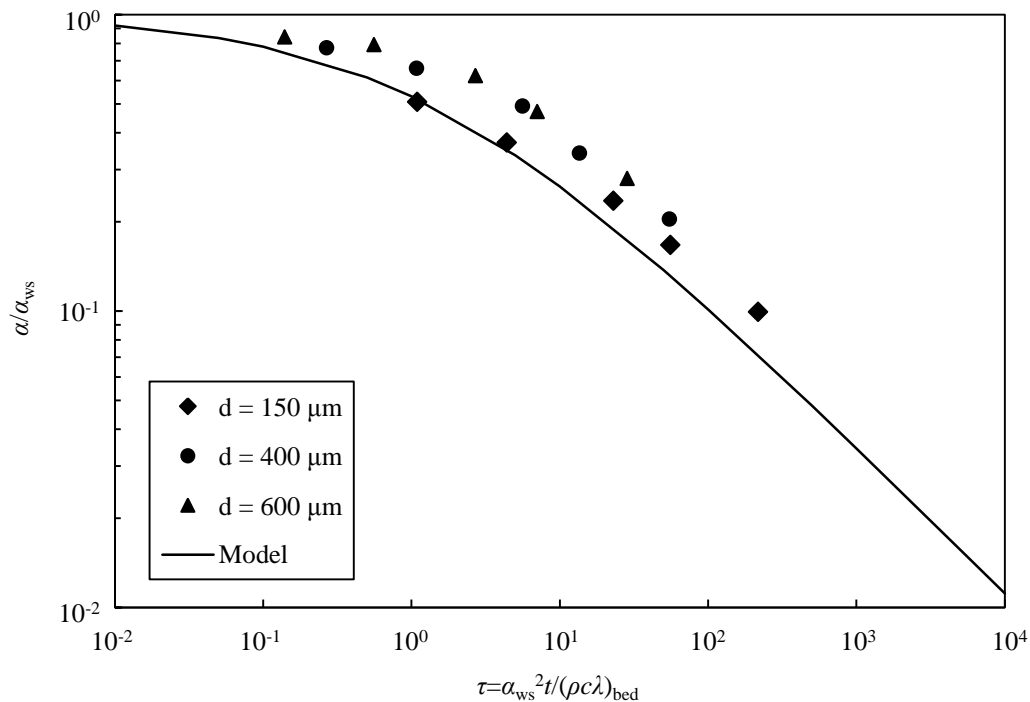


Figure 3.27 Comparison of modeled and experimental values of overall heat transfer coefficient α relative to the wall-bed heat transfer coefficient α_{ws} , for a moving bed of quartz sand particles. The experimental values are from Ernst [151].

Heat transfer between an immersed wall and a bed of particles is governed by the heat transfer at the wall, where the particles are in direct contact or separated by a small gas layer from the wall, and the heat transfer inside the bed of particles. The former is expressed with the heat

transfer coefficient α_{ws} and the latter with α_{sb} . Depending on the residence time of the bed on the wall, either the first or the second heat transfer mechanism may be dominating the overall heat transfer. The overall heat transfer coefficient α for a moving packed bed of quartz sand of particle diameters from 100 μm to 800 μm with a heated section of varying length is calculated and compared with the experiments conducted by Ernst [151]. The bed has a density of 1335 kg m^{-3} , a porosity of 0.42, a heat capacity of 730 $\text{J kg}^{-1} \text{K}^{-1}$, a plate surface coverage factor of 0.8, and a temperature of 350 K.

Thermal conductivity of the sand is 1.4 $\text{W m}^{-1} \text{K}^{-1}$, the dynamic viscosity of air is 20.7×10^{-6} Pa s, its thermal conductivity 0.030 $\text{W m}^{-1} \text{K}^{-1}$, the accommodation coefficient is 0.85, the wall and bed emissivity are both 0.8, and the pressure is 10^5 Pa. The results are shown as a function of the dimensionless time τ for a surface roughness factor of 0.5 μm in Figure 3.27. The general trend of the experimental measurements is captured well with the model, while the exact values seem to be somewhat underpredicted. In [145], the same model is seen to reproduce the experimental values even better with the deviations between the model and the experiment being within the experimental error. Schlünder concludes in [145] that his model agrees well with several experiments in the parameter ranges of $4 \mu\text{m} < d < 3100 \mu\text{m}$, $0.13 \text{ Pa} < p < 10^5 \text{ Pa}$, for various materials, and is able to predict the heat transfer coefficient satisfactorily with a relative deviation of $\pm 25\%$.

3.4.8.2 Thermal conductivity of the particle bed λ_{bed}

The calculation of the thermal conductivity of the particle bed follows the recommendations of Bauer [152], Schlünder [145], Tsoatas and Martin [104], and the VDI heat atlas [153].

Here, the model is compared with experimental measurements of heat transfer to a bed of glass beads after Ofuchi and Kunii [154] and Wakao and Kato [155]. Ofuchi and Kunii use diameters of the glass spheres in the range of 1.15 mm to 12.1 mm at bed porosities between 0.34 and 0.38 and gases used include water, air, carbon dioxide, helium and hydrogen. Wakao and Kato use diameters between 1.52 mm and 4.72 mm with air.

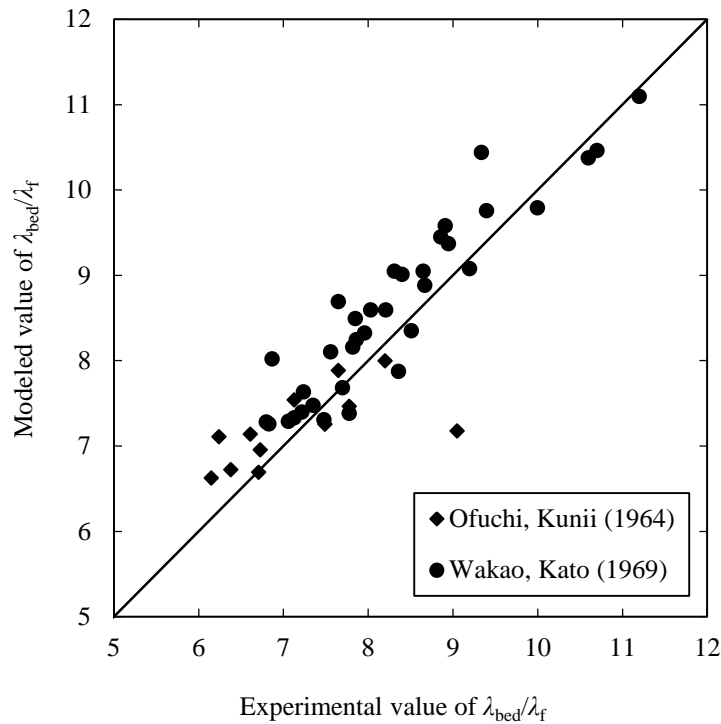
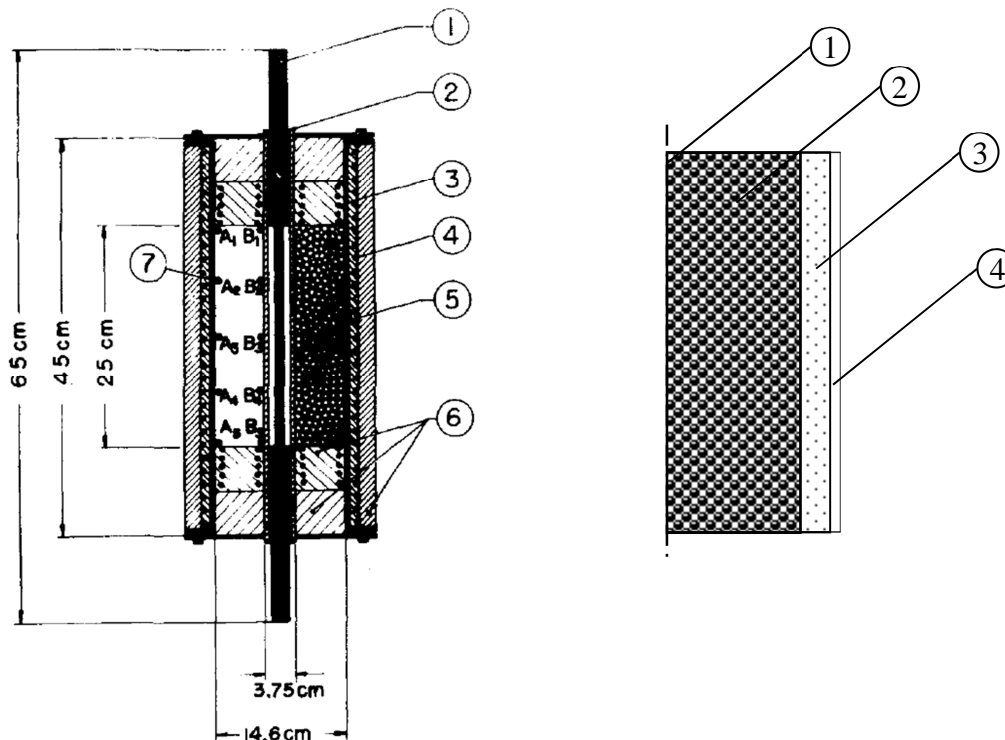


Figure 3.28 Comparison of modeled bed thermal conductivities relative to fluid thermal conductivities with experimental values of Ofuchi and Kunii [154] and Wakao and Kato [155].

Modeled bed thermal conductivities relative to fluid thermal conductivities for air are compared with experimental values in Figure 3.28. The modeled values compare rather well with the experimental values for different diameters of glass spheres in air. Tsotsas and Martin [104] have compared the model to many more experimental values from the literature and conclude that the model is suited for the calculation of the particle bed thermal conductivity in a wide range of parameters within an error of $\pm 30\%$.

3.4.8.3 Steady-state temperature profile in packed bed of particles



a) Experiment:

- 1) SiC electric heater
- 2) Silica tube
- 3) Nichrome wire for compensation of lateral heat loss
- 4) Nichrome wire for adjustment of bed temperature
- 5) Packed bed of glass beads
- 6) Insulating fire brick
- 7) Position of thermocouples

b) Model:

- 1) Boundary condition: $T=T_{\text{exp}}$.
- 2) Packed bed of glass beads
- 3) Alumina insulation
- 4) Reactor wall (Inconel 600)

Figure 3.29 Schematic representation of a) experimental setup in [156] (reprinted with permission from Wiley and sons) which has been used in a similar way in [155] and b) the computational model domains used for the calculations.

In order to allow the comparison of heat transfer coefficients and thermal conductivity of the bed at the same time, the experiment described in [155] is modeled and experimental and theoretical values are compared.

In [155], a packed bed of glass beads is used which is contained between a stainless steel tube and a Carborundum electric heater held in a coaxial silica tube.

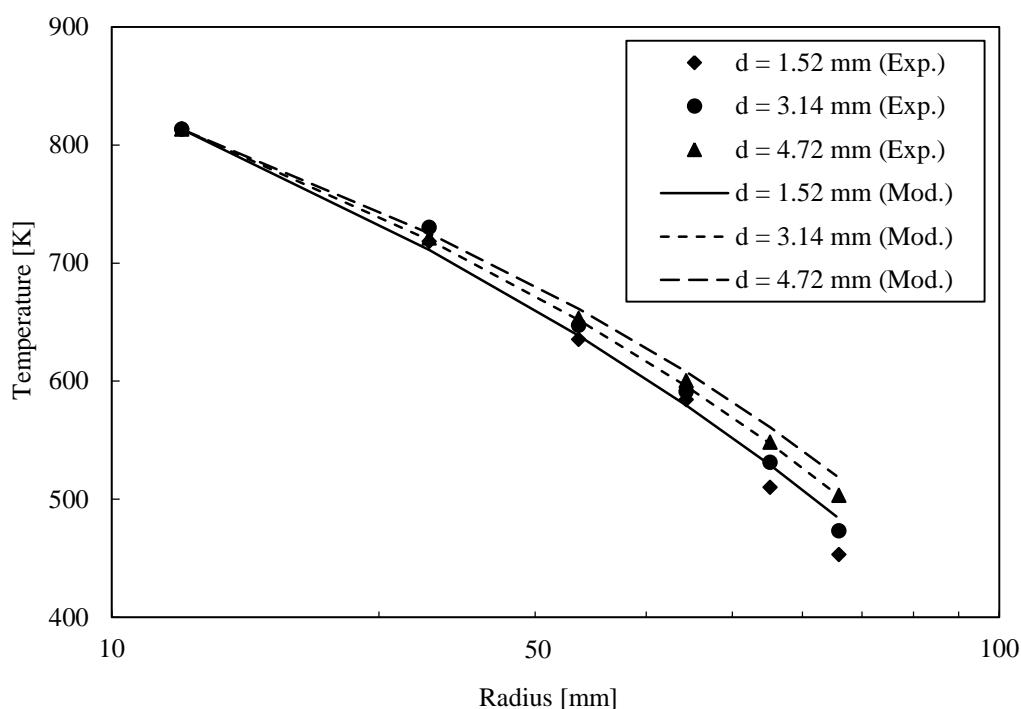


Figure 3.30 Comparison of modeled and experimental temperatures of a particle bed in a double-walled tube with a heated inner section (setup: compare Figure 3.29). Experimental values are from [155]. The difference of the computational and experimental values is partly explained by deviating material properties and unknown experimental conditions which could not fully be represented by the model.

The authors state that their experimental setup is similar to the one of [156] as shown in Figure 3.29. In Figure 3.30, the modeled temperatures are compared with the experimental data from [155]. The general temperature progression in the particle bed is predicted correctly by the model. In the experiments, the functional dependence of temperature on particle diameter is slightly stronger, however, in the model the trend of decreasing temperatures with smaller particles is captured correctly. The authors state that a steady state is reached in the experiment without giving the exact contact time, where, in the model, a contact time of 3000 s between the particle bed and the surrounding walls is found to represent the results best. An insulation thickness of 1 cm is chosen as the exact value could not be found in the description of the experiment. The density and the specific heat capacity of the fire brick insulation is taken from [157] and its thermal conductivity from [156]. The effective density of the bed is taken to be 1500 kg m^{-3} [158]. Considering that not all of the experimental conditions and material properties are known, the results from the computational model match well with the experimental data in [155].

The computational model is thus shown to be capable of correctly predicting

- i) the overall heat transfer coefficient α from a wall to a bed of particles (Figure 3.27),
- ii) the effective thermal conductivity of a bed of particles λ_{bed} of different materials (Figure 3.28), and
- iii) the temperature profile of a bed of particles in a heated double-walled tube (Figure 3.30).

The computational model is therefore considered to be well suited for the analysis of particle heat exchangers of solar reactor concepts.

3.4.9 Results

The model introduced above is used to investigate the influence of different parameters on heat exchanger efficiency (defined in Section 3.4.9.1). The following parameters are investigated: reduction and oxidation temperatures (as entry temperatures into the heat exchanger), particle diameter, heat exchanger length, residence time, and radial dimensions of the particle beds. With the exception of entry temperatures, only a single parameter is varied while the others are kept constant according to the baseline case defined in Section 3.4.9.2. Finally, the topic of gases crossing over from the oxidation to the reduction chamber due to the pressure gradient across the particle beds is discussed in Section 3.4.9.8.

3.4.9.1 Definition of heat exchanger efficiency

As discussed already for the previous reactor model, and analogously to the definition given in Equation (3.11), the efficiency of the heat exchanger is defined as the amount of energy transferred to a defined mass of particles divided by the thermal energy required to heat them from the oxidation to the reduction temperature. The heat exchanger efficiency therefore describes the recuperated fraction of the total required thermal energy for cycling between the temperature levels of the chemical reactions. The amount of energy transferred to the oxidized particles in the heat exchanger is found by integrating the (temperature dependent) heat capacity from the entry temperature to the exit temperature

$$\eta_{\text{he}} = \frac{\sum_1^{j,\text{end}} m_j \int_{T_L}^{T_{\text{he},\text{end},j}} c_p dT}{m \int_{T_L}^{T_H} c_p dT}, \quad (3.74)$$

where m_j is the mass of the j -th annular section of the cold bed, m is the mass of the top-most layer of oxidized particles in the heat exchanger, c_p is its specific heat capacity as a function of temperature, T_L and T_H are the temperatures of oxidation and reduction, respectively, and $T_{\text{he,end},j}$ is the temperature of the j -th annular section of oxidized particles coming out of the heat exchanger at the end of the heating process.

3.4.9.2 Basic configuration of heat exchanger

As a basic configuration, the parameters of the heat exchanger are chosen as shown in Table 3.4.

Table 3.4 Parameters for basic configuration of particle heat exchanger.

Parameter	Label	Value	Unit
Concentration ratio	C	3000	-
Oxidation temperature	T_L	1000	K
Reduction temperature	T_H	1800	K
Temperature of surroundings	T_0	300	K
Reduction pressure (relative to 1 atm)	p_{red}	10^{-3}	-
CO ₂ -flow (times min= δ_{red}) in oxidation chamber	f_{CO_2}	2.0	-
Efficiency of gas heat recovery	η_{gasrec}	0.5	-
Conversion efficiency of heat to electricity	$\eta_{\text{heat-to-electricity}}$	0.4	-
Total residence time in heat exchanger	t_{total}	360	s
Particle diameter	d	0.001	m
Heat exchanger height	h	0.5	m
Diameter of insulating centerpiece	$d_{\text{bed,hot,i}}$	0.04	m
Thickness of hot particle bed	$\Delta r_{\text{bed,hot}}$	0.01	m
Thickness of separation wall between particle beds	d_{sw}	0.003	m
Thickness of cold particle bed	$\Delta r_{\text{bed,cold}}$	0.007	m
Hot particle bed porosity	φ_{hot}	0.385	-
Cold particle bed porosity	φ_{cold}	0.395	-

The diameter of the cold particle bed is defined such that conservation of mass is fulfilled under the assumption of equal velocities v_{bed} of the hot and cold particle beds. The inner

radius of the cold particle bed is equal to the sum of the outer radius of the hot particle bed and the thickness of the separating wall $r_{\text{bed,cold,in}} = r_{\text{bed,hot,out}} + d_{\text{sw}}$.

$$\dot{m}_{\text{bed,cold}} = \dot{m}_{\text{bed,hot}}$$

$$\rho_{\text{bed}}\pi(r_{\text{bed,cold,out}}^2 - r_{\text{bed,cold,in}}^2)v_{\text{bed}} = \rho_{\text{bed}}\pi(r_{\text{bed,hot,out}}^2 - r_{\text{bed,hot,in}}^2)v_{\text{bed}}$$

$$r_{\text{bed,cold,out}} = \sqrt{r_{\text{bed,hot,out}}^2 - r_{\text{bed,hot,in}}^2 + (r_{\text{bed,hot,out}} + d_{\text{sw}})^2} \quad (3.75)$$

The thickness of the cold particle bed can then be derived from the inner and outer radius of the hot bed.

The porosity of fixed particle beds in cylindrical geometries was analyzed by Pushnov [159] who found a functional dependence on the diameter of the cylindrical enclosure D and the particle diameter d .

$$\varphi = \frac{A}{\left(\frac{D}{d}\right)^n} + B \quad (3.76)$$

with $A = 1$, $B = 0.375$, and $n = 2$ for spherical particles [159]. For large ratios $\frac{D}{d}$, the porosity approximates the constant B . The formula is used here with the diameter D equal to the thickness of the annular rings. In the baseline case with $\frac{\Delta r_{\text{bed,hot}}}{d} = \frac{0.01 \text{ m}}{0.001 \text{ m}}$, the porosity of the hot bed is 0.385. Due to the condition of mass conservation, the radial dimensions of the hot and cold particle beds differs which causes the porosity of the beds to deviate slightly, as well, giving a value of 0.395.

In the results shown below, the cycle efficiency as defined in Equation (3.17) in its realistic definition, i.e. with realistic assumptions of vacuum pump power and gas separation energy, is used.

3.4.9.3 Reduction and oxidation temperatures

In the definition of the boundary conditions for the heat exchanger, the entry temperatures have been chosen equal to the temperatures of the redox reactions. A change in the reduction

and oxidation temperatures thus affects both the thermodynamics of the syngas production and the thermal energy transfer in the heat exchanger: the former is affected by the trade-off between increased fuel productivity of the material and higher heat losses due to an enlarged temperature swing between reaction steps (for $\eta_{\text{he}} < 1$; as explained in Section 3.2.8.4).

The heat exchanger efficiency, on the other hand, is affected by the altered temperature difference of the particle beds driving heat exchange, and the temperature dependence of thermal conductivities and heat transfer coefficients.

In Figure 3.31, the efficiencies of the heat exchanger and the thermodynamic cycle are shown as a function of reduction and oxidation temperatures which are varied in the ranges $T_{\text{H}} = 1500\text{-}2000$ K and $T_{\text{L}} = 700\text{-}1200$ K. Heat exchanger efficiency rises from 23% at $T_{\text{H}} = 1500\text{-}1650$ K to 31% at $T_{\text{L}} = 1200$ K and $T_{\text{H}} = 2000$ K. η_{he} rises from the region of low oxidation and low reduction temperatures to the region of high oxidation and high reduction temperatures. The temperatures influence η_{he} through the temperature dependent coefficients of thermal conductivity and heat transfer, and by the temperature swing, as shall be demonstrated in the following.

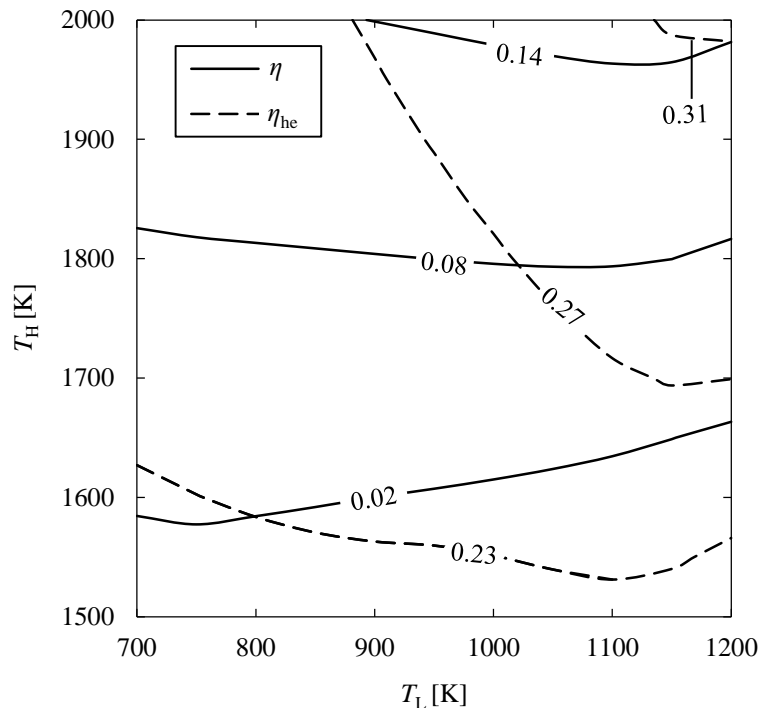


Figure 3.31 Efficiencies of the thermodynamic cycle η and of the heat exchanger η_{he} as a function of reduction and oxidation temperatures T_{H} , T_{L} .

The overall heat transfer from the hot to the cold particle bed can be considered by the following simplified thermal resistance network.

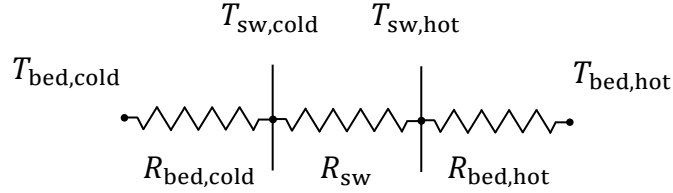


Figure 3.32 Simplified thermal resistance network of heat transfer between particle beds.

Figure 3.32 shows a network of thermal resistances that represents the heat exchange between the hot and cold particle beds including the separating wall. For the purpose of the following discussion, the heat flow is assumed to be one-dimensional. Energy conservation requires that the heat flows are equal from the hot bed to the separating wall, through the separating wall, and from the separating wall into the cold bed.

$$\dot{Q}_{\text{hot bed} \rightarrow \text{sw}} = \dot{Q}_{\text{sw}} = \dot{Q}_{\text{sw} \rightarrow \text{cold bed}} \quad (3.77)$$

$$\alpha_{\text{hot bed} \rightarrow \text{sw}} A_{\text{sw,in}} (T_{\text{hot bed}} - T_{\text{sw,in}}) = \frac{2\pi\lambda_{\text{sw}}h(T_{\text{sw,in}} - T_{\text{sw,out}})}{\ln\left(\frac{r_{\text{sw,out}}}{r_{\text{sw,in}}}\right)} \quad (3.78)$$

$$= \alpha_{\text{sw} \rightarrow \text{cold bed}} A_{\text{sw,out}} (T_{\text{sw,out}} - T_{\text{cold bed}}) \quad (3.79)$$

Introducing the thermal resistances gives

$$\dot{Q} = \frac{T_{\text{hot bed}} - T_{\text{sw,in}}}{R_1} = \frac{T_{\text{sw,in}} - T_{\text{sw,out}}}{R_2} = \frac{T_{\text{sw,out}} - T_{\text{cold bed}}}{R_3} \quad (3.80)$$

Adding numerators and denominators gives

$$\dot{Q} = \frac{T_{\text{hot bed}} - T_{\text{cold bed}}}{R_1 + R_2 + R_3} \quad (3.81)$$

with $R_1 = (\alpha_{\text{hot bed} \rightarrow \text{sw}} A_{\text{sw,in}})^{-1}$, $R_2 = \frac{\ln\left(\frac{r_{\text{sw,out}}}{r_{\text{sw,in}}}\right)}{2\pi\lambda_{\text{sw}}h}$, $R_3 = (\alpha_{\text{sw} \rightarrow \text{cold bed}} A_{\text{sw,out}})^{-1}$.

Under the conditions of the baseline case, $R_1, R_3 \gg R_2$, and the heat transfer is limited by the heat transfer between the beds and the separating wall and by the temperature difference of

the beds (see Equation (3.81)). In general, the thermal conductivity of the beds and the heat transfer coefficients from the beds to the separating wall rise with temperature at the chosen particle size. The dependency of heat exchanger efficiency on temperature in Figure 3.31 is now understood as the trade-off between an increased overall temperature difference between the beds T_H-T_L , and an enhancement of the temperature dependent thermal conductivities and heat transfer coefficients by raising the temperature of the beds T_H, T_L (Equation (3.80)). The overall heat transfer coefficients have a stronger influence on the heat exchange between the beds than the temperature difference T_H-T_L , which is why the largest heat exchanger efficiency is reached at high T_H and high T_L .

3.4.9.4 Particle diameter

For the heat exchanger in this study, the particles are assumed to be monodisperse spherical particles. A reduction of particle diameter therefore increases the total surface area of redox material which reduces the reaction time of the oxidation, a mass transfer limited process [10,11,14,15]. The porosity of the particle bed is only slightly dependent on particle diameter, as according to Equation (3.76) with the given baseline geometry, the ratio of D/d is large and the bed porosity will be close to the constant $B = 0.375$. However, reducing the diameter from the mm-range to the μm -range changes the mechanical behavior of the bed from granular to powder which could have implications on the efficiency of the transport mechanism. Importantly, a change in particle dimensions has an effect on the thermal transport properties of the particle beds. The basic concept of the heat exchanger is to exchange heat between hot and cold particle beds. This process can be described by the coupled heat transfer processes between the particle beds and the separating wall and within the wall (see model description in Section 3.3.3). According to Tsotsas [153], a critical time t_c exists such that:

- for $t < t_c$, $\alpha \approx \alpha_{ws}$, i.e. overall heat transfer between the wall and the bed is dominated by heat transfer between wall surface and bed surface,
- for $t > t_c$, $\alpha \approx \alpha_{sb}$, i.e. overall heat transfer is dominated by heat transfer from the bed surface to the bulk of the particles.

Under the conditions of the heat exchange proposed in this work, the main limitation to heat transfer between the beds is the heat transfer from the bed surface to the bulk of the particles,

where the effective thermal conductivity of the beds is the decisive parameter. The effective thermal conductivity of the particle beds is described in detail in Section 3.4.4.

Assuming a moving packed bed without fluid flow (effects on thermal heat transfer by gases crossing over from the oxidation to the reduction chamber are neglected; see discussion of pressure loss in Section 3.4.9.8), heat is transferred in the bed through conduction (in the gas phase and solid phase) and radiation. According to the temperature dependence of the radiative term, radiation dominates the overall heat transfer within the beds towards higher temperatures [149,160]. The radiative conductance term further depends on particle emissivity and diameter (Equation (3.62)), where larger particles are expected to enhance radiation and thus overall heat transfer.

This is confirmed by experiments in the literature, e.g. by Chen and Churchill [160] who measured the effect of particle size on radiative conductivity of different materials such as glass, aluminum oxide, steel, and silicon carbide.

In the following, the particle diameter is varied from a value of 10^{-6} m to 10^{-3} m to determine its influence on heat exchanger efficiency. In Figure 3.33, the efficiencies of the heat exchanger and the thermodynamic cycle, and the required solar power input (excluding the required power for vacuum pumping and gas separation, see Equation (3.9)) to the reactor are shown as a function of the particle diameter in both particle beds. As expected, the heat exchanger efficiency correlates positively with the particle diameter, rising from 3.5% at $d = 10^{-6}$ m to 26.7% at $d = 10^{-3}$ m. The relatively large increase in efficiency is due to the enhancement of the heat transfer within the particle beds through an increase of its radiation component. A requirement for this result is of course the high temperatures prevalent in the heat exchanger which lead to the dominant radiation term. At lower temperature levels, the increase of particle diameter would thus have a lower influence on the heat exchanger efficiency.

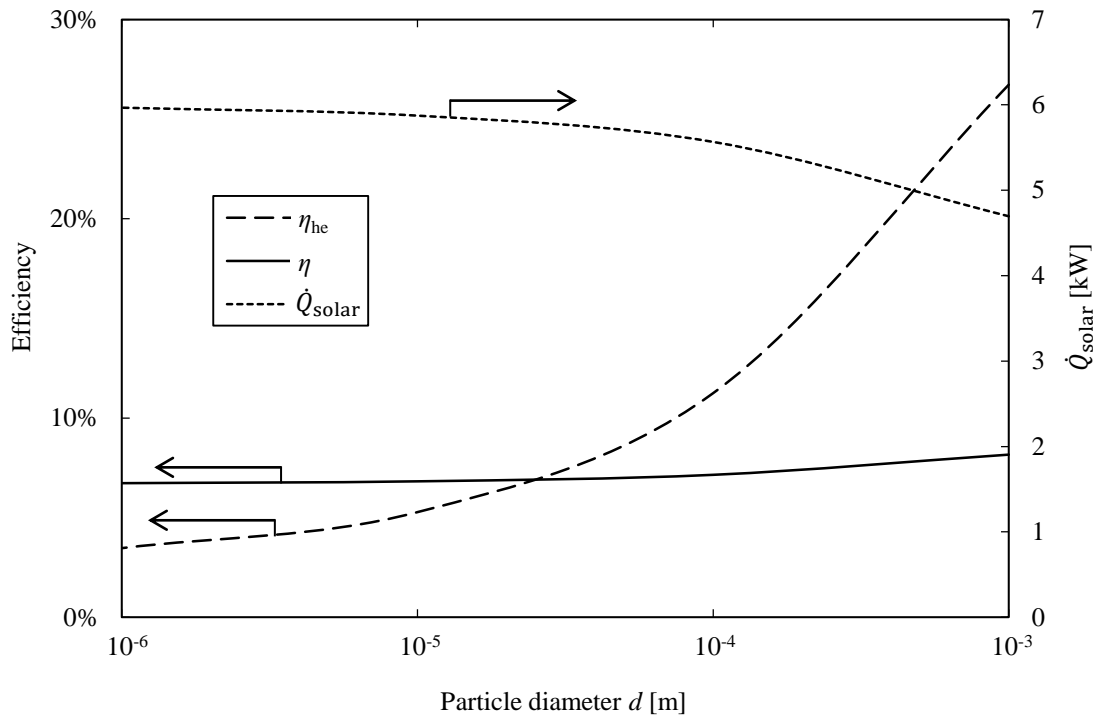


Figure 3.33 Heat exchanger efficiency η_{he} , thermodynamic cycle efficiency η and solar power input Q_{solar} as a function of particle diameter.

The amount of solar energy required for heating the redox material according to Equation (3.10) is reduced by an enhancement of the heat exchanger efficiency, leading to a total required concentrated solar energy of 6.0 kW at $d = 10^{-6}$ m and of 4.7 kW at $d = 10^{-3}$ m.

The performance of the heat exchanger is therefore enhanced with larger particles. A larger particle diameter may on the other hand also have a negative influence on the operability of the solar reactor through a larger gas cross-over from the oxidation to the reduction chamber: due to thermodynamics, oxidation is performed at atmospheric pressure and reduction at sub-atmospheric oxygen partial pressures, which causes a pressure gradient over the particle beds in case of operation with a vacuum pump.

This pressure gradient leads to a constant gas stream from the oxidation to the reduction chamber which affects negatively the vacuum pumping power and the amount of oxidant required. This effect is discussed in more detail in Section 3.4.9.8.

3.4.9.5 Heat exchanger length

Under otherwise constant conditions of the baseline case, the axial length of the heat exchanger is varied to determine its influence on heat exchanger efficiency. The mass flow rate of reactive material is kept constant which gives a constant velocity of the beds. A prolongation of the axial length thus increases the total residence time of the particles in the heat exchanger and allows for a longer heat transfer period between hot and cold particles. In case of heat transfer being limited by thermal conductivity of the reactive material, a prolongation can therefore enhance the performance of the heat exchanger. However, if the length is chosen too large, losses to the environment decrease the heat exchanger efficiency. It is therefore expected that an optimal heat exchanger length exists.

In Figure 3.34, heat exchanger efficiency, thermodynamic cycle efficiency, and required solar power input are shown as a function of heat exchanger length between 0.1 m and 5 m. Under the assumption of fixed reduction temperature and ceria mass flow rate, \dot{Q}_{solar} is then the required solar power input to the reactor to perform the thermodynamic cycle excluding the required power for vacuum pumping and gas separation (see Equation (3.9)).

The heat exchanger efficiency shows a strong increase with length from 11.5% at 0.1 m up to 36.8% at 1.5 m, while the required solar power input decreases from 5.5 kW to 4.2 kW. A further prolongation to 3 m leads to a moderate increase in heat exchanger efficiency up to 38.2% at a solar power input of 4.1 kW. Towards even longer heat exchanger lengths, efficiency decreases due to losses to the environment. At the conditions of the baseline case, a doubling of the length from 0.5 m to 1 m enhances η_{he} from 26.7% to 33.9%, at a solar power input of 4.7 kW and 4.3 kW, respectively.

The expected general behavior of the heat exchanger with respect to its length is thus confirmed. However, the optimal length and the achievable heat exchanger efficiency depend of course on other parameters of the system, e.g. the dimensions of the bed in radial direction, particle size, residence time, or inlet temperatures. The results shown in Figure 3.34 are therefore strictly valid for the chosen parameters and the assumed boundary conditions.

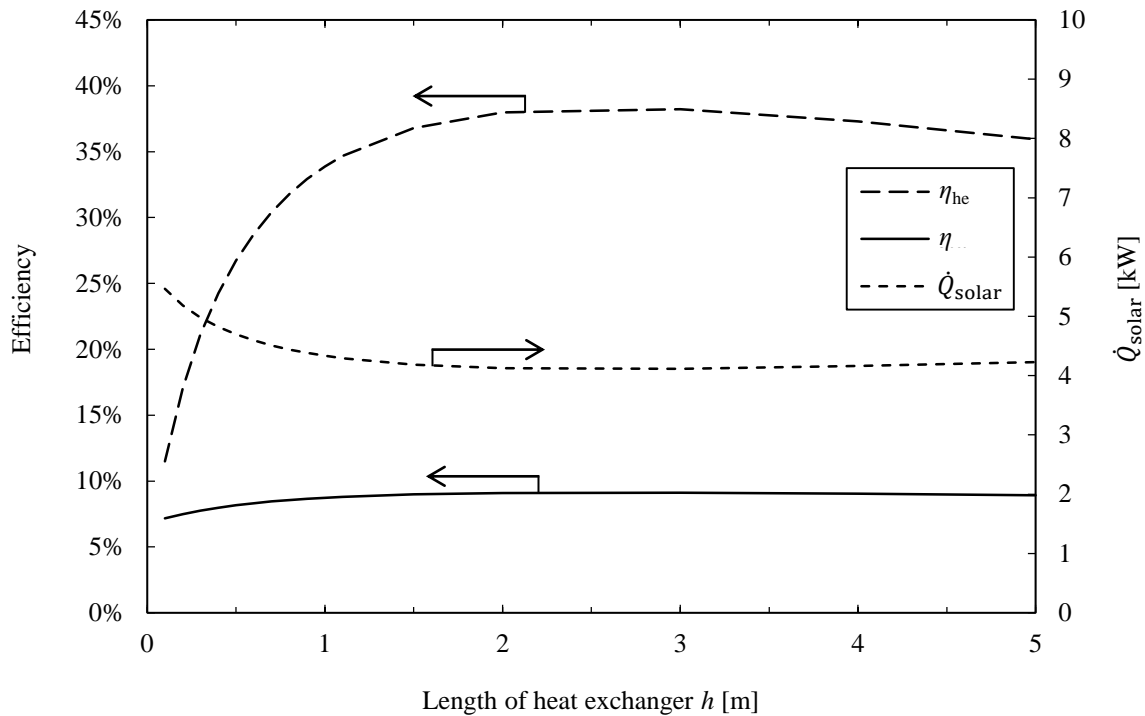


Figure 3.34 Heat exchanger efficiency η_{he} , thermodynamic cycle efficiency η and solar power input \dot{Q}_{solar} as a function of heat exchanger length.

3.4.9.6 Residence time in heat exchanger

The residence time of the particles is varied at a constant length of the heat exchanger. On the one hand, longer residence times allow a longer heat exchange period between the hot and cold material and are thus supposed to give a higher efficiency. On the other hand, losses to the environment are expected to become dominating after a certain residence time, decreasing the efficiency. The optimal residence time is then found as a trade-off between these two mechanisms.

Thermodynamic cycle efficiency, heat exchanger efficiency, and equivalent solar reactor power input (excluding power for vacuum pumping and gas separation, see Equation (3.9)) are shown as a function of residence time of the particles in the heat exchanger in Figure 3.35. The solar power input varies because the mass flow of reactive material is changed with residence time, which requires an adapted solar power input at the assumed constant conditions of the reduction reaction. Efficiencies rise up to a residence time of about 1500 s and decrease with longer residence times, where the heat exchanger efficiency reaches a maximum of 37.0% and cycle efficiency of 9.0%.

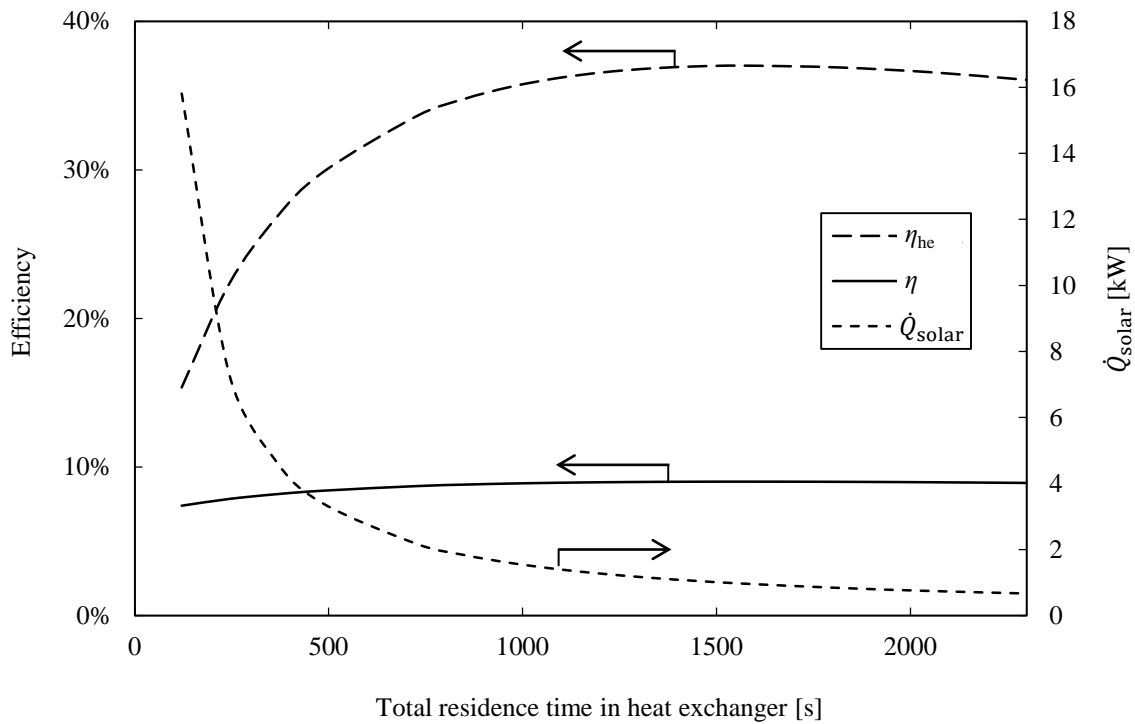


Figure 3.35 Heat exchanger efficiency η_{he} , thermodynamic cycle efficiency η and solar power input Q_{solar} as a function of the residence time of the particles in the heat exchanger.

Solar power input decreases with increasing efficiency as a larger part of the required temperature swing of the redox material is achieved in the heat exchanger and consequently a smaller amount of energy has to be supplied from the outside. The result shows the expected mechanisms of improved contact time between hot and cold material in the heat exchanger, and losses to the environment by convection and radiation from the heat exchanger surface area. The losses have a comparably small influence which can be judged from the small negative gradient of heat exchanger efficiency towards higher residence times $\Delta t_{total} > 1500$ s. Here, the subscript “total” distinguishes the total residence time in the heat exchanger from the residence time per chamber in the previous models in Chapters 3.2 and 3.3.

3.4.9.7 Radial dimension of heat exchanger

The radial thickness of the hot particle bed is varied between 0.0021 m and 0.05 m, while the cold bed thickness is adjusted accordingly to ensure mass conservation under the assumption of equal and constant bed speeds. The derivation of the radial dimensions of the cold bed is shown in Section 3.4.9.2.

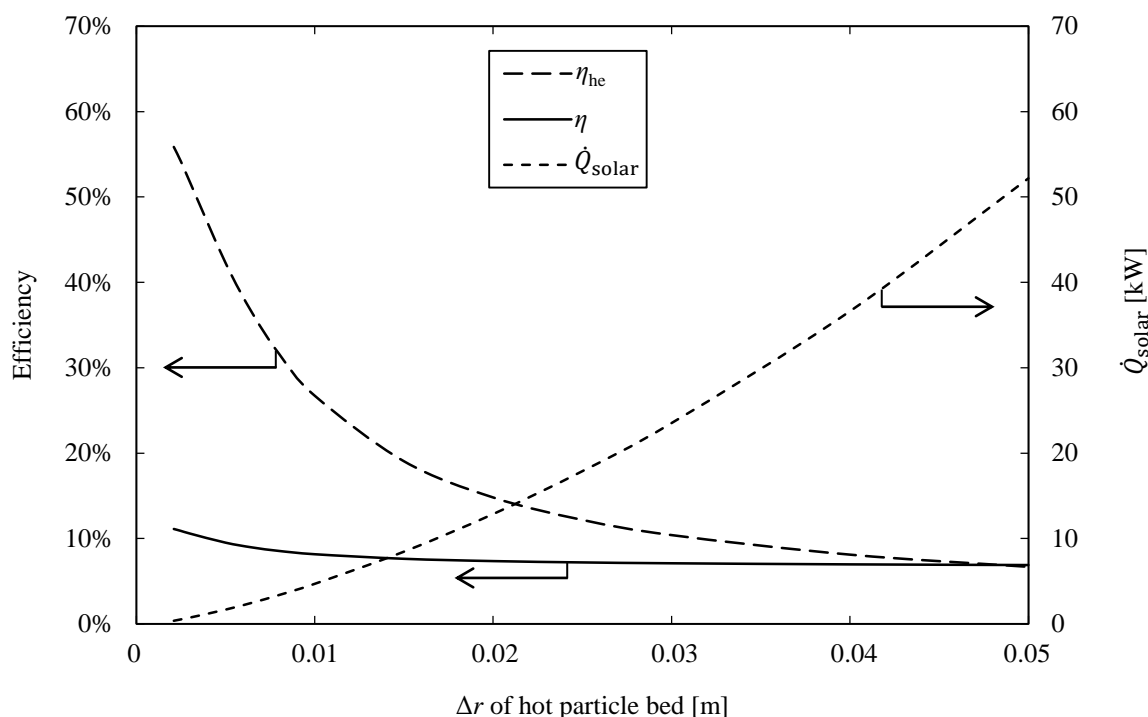


Figure 3.36 Heat exchanger efficiency η_{he} , cycle efficiency η and solar power input \dot{Q}_{solar} as a function of hot bed thickness. The radial dimensions of the cold particle bed are adjusted such as to ensure mass conservation.

The assumption of equal bed velocities is equivalent to identical residence times of a particle in the hot and cold section of the heat exchanger, respectively, which is 360 seconds in the baseline case (see Table 3.4). A change in bed diameters alters the bed volumes, which, at constant bed velocities, changes the mass flow rate of reactive material at constant residence time. At otherwise constant conditions of the reduction reaction, i.e. temperature and pressure, the mass flow rate is proportional to the solar power input. At the same heat exchanger efficiency, an increase of the diameter of the hot particle bed therefore requires a proportionally larger solar power to retain the defined nonstoichiometry.

In Figure 3.36, the heat exchanger efficiency, thermodynamic cycle efficiency and solar power input to the reactor (excluding power for vacuum pumping and gas separation, see Equation (3.9)) as a function of hot bed thickness are shown. The maximum of efficiency is reached for a reduction of the bed thickness towards the lowest values of 0.0021 m which is equivalent to two particle diameters in the baseline case. A limitation of equation (3.76) of $D/d > 2$ [159] precludes the calculation of even smaller bed geometries. It is however expected that below this bed thickness, efficiency decreases again because losses to the surroundings start dominating the energy balance of the relatively small mass of particles: as the surface-to-volume ratio of a cylinder is inversely proportional to its radius, a decrease in radial

dimensions will increase the relative weight of losses to the surroundings.

An increase of the radial dimensions of the particle beds leads to a decrease of heat exchanger efficiency from a value of over 50% at $\Delta r_{\text{hot bed}} = 0.0021$ m to about 7% at $\Delta r_{\text{hot bed}} = 0.05$ m. The reason for the decrease in efficiency is that at otherwise constant conditions of the baseline case, i.e. axial length and residence time of the heat exchanger, more mass is added which cannot be heated as efficiently.

As was already seen in Section 3.3.9.6, the heat exchange process between hot and cold material is limited by the transport of heat in the beds. For a constant residence time, the addition of material in radial direction requires a shorter time scale of heat diffusion in the material to maintain the same level of heat exchanger efficiency. As however, the thermal diffusivity remains constant, the additional material is not heated to the same degree as the material closer to the heat source which reduces the heat exchanger efficiency.

In order to reach high efficiencies in the heat exchanger, the dimensions of the particle beds in radial direction have to be chosen according to the length of the heat exchanger, the residence time of the particles, and their entry temperatures into the heat exchanger. Here, only the variable of the particle bed thickness was varied to study its influence on the heat exchange process. It is however possible to adjust the other parameters, especially residence time, accordingly to counterbalance the effect of additional mass in the heat exchanger.

3.4.9.8 Pressure loss through particle beds

In the suggested reactor concept, the particles circulate between the reduction zone and the oxidation chamber which are at different pressure levels. The separation of the two atmospheres in the reaction zones is an important property of any solar thermochemical reactor. However, its realization is not straightforward which was experimentally observed through gases undesirably crossing over from one region to the other, e.g. in the CR5 reactor [161,162]. Oxidation gases crossing over to the reduction side could prematurely reoxidize the material, lead to oxidant loss and increase the pumping power required to maintain the pressure of the reduction chamber. In case of the particle reactor concept, it was suggested that a fixed bed of reduced particles represents an effective seal between the reduction and oxidation chambers, preventing significant gas cross over [18]. In the following, the validity of this statement is analyzed.

Fluid flow through a porous medium was studied by Henry Darcy who found that the flow is proportional to the pressure difference across the medium, analogous to Ohm's law for an electric conductor. In its simple form which is valid for low fluid velocities, the Darcy law is written as follows [163],

$$\nabla p = -\frac{\mu}{K} q, \quad (3.82)$$

where ∇p is the pressure gradient in the medium, μ is the dynamic viscosity of the fluid, K is the permeability, and q is the fluid flux at average pressure. Equation (3.82) can then be written in the following form for compressible fluids [164],

$$q_{sc} = \frac{T_{sc}K(p_{ox}^2 - p_{red}^2)}{2p_{sc}TzL\mu}. \quad (3.83)$$

q_{sc} is the flow rate, T_{sc} is the standard temperature of 300 K, p_{ox} and p_{red} are the pressures of oxidation and reduction, p_{sc} is the standard pressure, T is the temperature, z is the real gas compressibility factor, L is the length of the porous medium and μ is the dynamic viscosity of the fluid.

The permeability K can be expressed as a function of material porosity and particle diameter from the Ergun equation [165]:

$$K = \frac{\varphi^3 d^2}{150(1 - \varphi)^2}, \quad (3.84)$$

where φ is the porosity of the material (here the particle bed) and d is the diameter of the particles.

The porosity φ is described by a function of the diameter of the cylindrical enclosure and the particle diameter, as described by Pushnov [159] (see Section 3.4.9.2), where here the radial thickness of the hot bed is used instead of the cylindrical diameter, owing to the deviating geometry.

Equation (3.83) then gives the fluid flux for defined values of pressure difference over the particle bed, geometry, temperature and particle diameter. This relationship is used in the following to analyze the amount of oxidant loss through the particle bed during operation of the reactor. The amount of oxidant loss through the particle bed $\dot{n}_{CO_2,loss}$ in mol s⁻¹ is derived

from Equation (3.83) by dividing the fluid flux by the specific molar volume v and multiplying with the area A of the hot bed of the heat exchanger.

$$\dot{n}_{\text{CO}_2, \text{loss}} = \frac{qA}{v_{\text{CO}_2}} \quad (3.85)$$

In Figure 3.37, the ratio of oxidant loss through the particle bed $\dot{n}_{\text{CO}_2, \text{loss}}$ and the amount of oxidant required for the oxidation reaction $\dot{n}_{\text{CO}_2, \text{Ox}}$ is shown as a function of particle diameter for three different reduction pressures (the oxidation pressure is $p_{\text{ox}}=10^5$ Pa in all cases).

For particle diameters $d \leq 10^{-4}$ m, the amount of oxidant loss through the particle bed is orders of magnitude lower than the amount used for oxidation. Only at the largest particle diameter of $d = 10^{-3}$ m the oxidant loss becomes significant. The particle bed therefore represents an effective seal against oxidant loss at particle diameters up to $d = 10^{-4}$ m.

A decreasing reduction pressure increases the pressure difference across the particle bed at a fixed oxidation pressure. Firstly, this leads to a larger gas flux through the bed according to Equation (3.83) and therefore to a larger absolute oxidant loss $\dot{n}_{\text{CO}_2, \text{loss}}$.

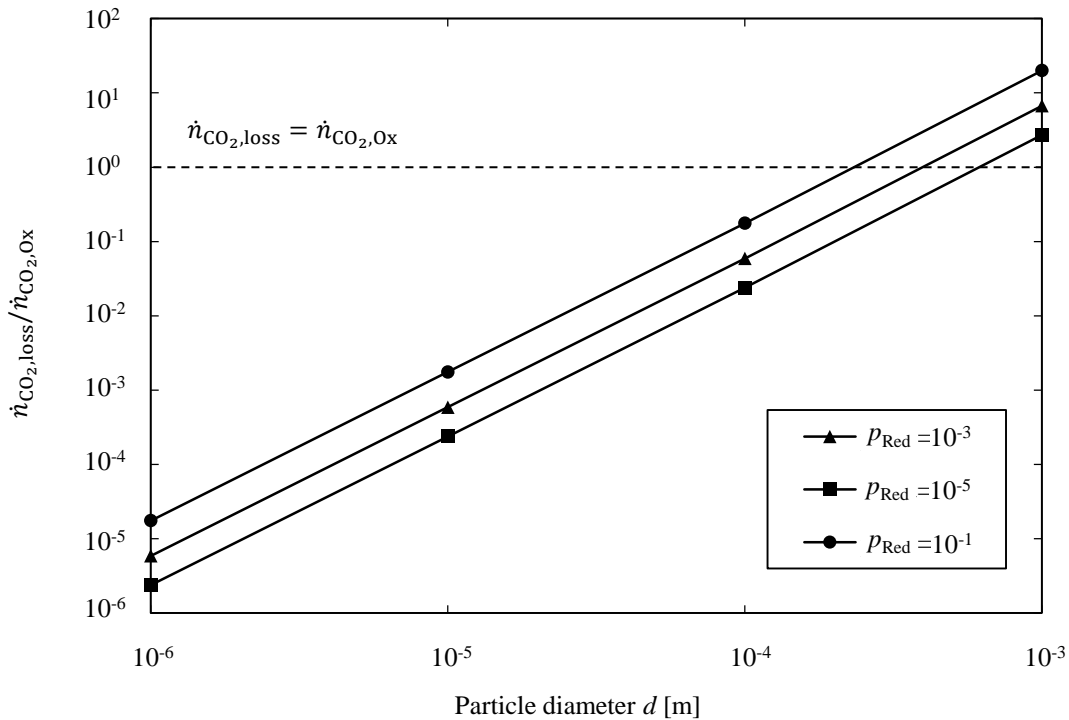


Figure 3.37 Ratio of oxidant (CO_2) loss through pressure difference over particle bed $\dot{n}_{\text{CO}_2, \text{loss}}$ to oxidant required for oxidation $\dot{n}_{\text{CO}_2, \text{Ox}}$.

Secondly, a lower reduction pressure increases the oxygen nonstoichiometry of the material and therefore the amount of oxidant required for the reaction. The relative difference of $\dot{n}_{\text{CO}_2,\text{loss}}$ between the largest and smallest pressure difference is only about 1%, while the required oxidant flow rate $\dot{n}_{\text{CO}_2,\text{Ox}}$ increases by a factor of 7-8. The relative oxidant loss $\dot{n}_{\text{CO}_2,\text{loss}}/\dot{n}_{\text{CO}_2,\text{Ox}}$ therefore diminishes with decreasing reduction pressure and particle diameter.

3.4.10 Conclusions for heat exchanger design

From the analysis shown above, recommendations for the heat exchanger design using a counter-flow of reactive redox particles are deduced:

- With the sensitivity study of unmixed beds that varied single variables starting from their values of the baseline case, heat exchanger efficiencies of close to 60% are shown to be reachable. Possibly even higher efficiencies are attainable given the right combination of parameters at a global optimum which was not analyzed here.
- The heat exchanger performance is dependent on the inlet temperatures: an increase of the bed temperatures enhances the overall heat transfer coefficient between the beds and the separating wall, while an increase of the temperature difference of the beds leads to a larger driving force for heat exchange. As heat exchange was found to be limited by heat transfer between the beds and the separating wall, the former effect is stronger and the largest heat exchanger efficiencies are found at the highest bed temperatures.
- A larger particle diameter enhances radiation heat exchange within the beds and therefore overall heat transfer. However, it also increases the gas cross-over from the oxidation to the reduction chamber in case of vacuum pumping. Below particle diameters of 10^{-4} m, the particle bed represents an effective seal.
- Heat exchanger efficiency is crucially dependent on heat diffusion in the particle beds which can be enhanced through the adjustment of heat exchanger length, residence time of the particles in the heat exchanger, and radial dimensions of the beds. For each of the parameters, an optimal value can be found which depends on the choice of the others.

3.5 Potential of thermodynamic cycle efficiency

In the previous Chapters 3.2-3.4, generic models for the determination of heat exchanger efficiencies are presented. It is shown that heat exchanger efficiency levels of 70% are achievable given an optimal design.

Table 3.5 Assumptions for baseline case and improved scenario.

Parameter	Baseline case	Improved case	Unit
Concentration ratio	3000	5000	-
Oxidation temperature	1000	1000	K
Reduction temperature	1800	2000	K
Reduction pressure (relative to 1 atm)	10^{-3}	10^{-3}	-
Efficiency of solid heat recovery	=f(...)	0.7	-
Efficiency of gas heat recovery	0.5	0.9	-
Efficiency of vacuum pumping	=f(p)	=1.5f(p)	-

In the preceding analyses, a set of assumptions was used for the determination of the thermodynamic cycle efficiency, where some of the chosen values may be improved in the future. In the following, more favorable assumptions are chosen to investigate the potential of the overall thermodynamic cycle (Table 3.5). A concentration efficiency of 5000 suns is assumed which can be reached with a solar dish concentrator. The reduction temperature is increased to 2000 K which has been shown to be a challenge in recent experiments due to sublimation of the redox material [11].

The gas heat recovery efficiency was chosen to be 50% in the baseline case, which is a conservative value with respect to values assumed in the literature [13,18,20] and is consequently increased to 90%. The efficiency of vacuum pumping, which was identified to have a limiting potential, is assumed to be increased by 50%.

The values in Table 3.5 are used to determine the efficiency of the thermodynamic cycle, assuming a heat exchanger efficiency of 70%, as was shown to be feasible with the generic heat exchanger models.

Implementing the assumed improvements one by one, an efficiency improvement from 13.0% to 23.3% is reached, when all changes are implemented at the same time. The largest influence on efficiency stems from the increase of reduction temperature by 200 K.

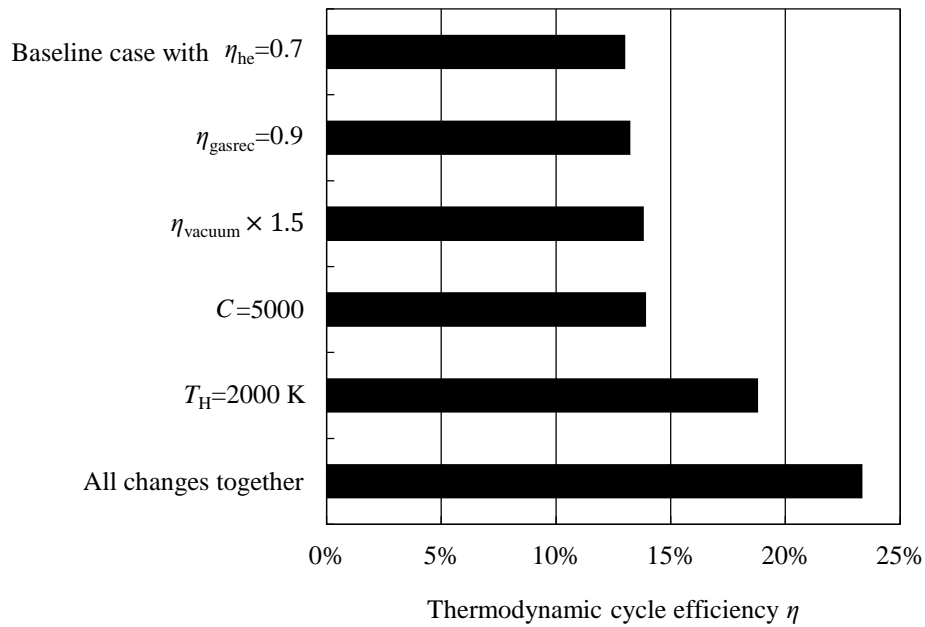


Figure 3.38 Improvements of thermodynamic cycle efficiency η for favorable changes of the baseline case assumptions. The heat exchanger efficiency is 70% in all cases and the oxygen partial pressure during reduction is 10^{-3} atm.

4 Ecological and economic analysis

4.1 Introduction

In Chapter 3, different models for the description of efficiencies of heat exchanger concepts and the associated thermodynamic cycle for the production of syngas were presented. Efficiency is an important metric for the comparison of different technical concepts because it describes the technical maturity and the ability of the system to convert primary energy into the (intermediate) product. Nevertheless, if systems are compared that use different sources of primary energy or otherwise fundamentally different assumptions, system boundaries or definitions, a comparison based on the energy conversion efficiency alone may not be sufficient to come to a meaningful conclusion. In case of the production of a liquid fuel to be used in the transportation sector, both the cost of the fuel and its environmental friendliness are important metrics to consider. The market price of the fuel is inherently difficult to determine because it not only depends on the production process itself but also on the availability of competing products such as fossil fuels, the electrification of the vehicle, or even other means of transport. In case of the environmental friendliness, an established standard tool is available, i.e. life cycle analysis, which investigates different aspects of environmental performance of a product or process. For this reason, in the following, the economic and ecological performance of solar thermochemical fuels is investigated, where the former is described by the production costs of the fuel, and the latter by a life cycle analysis of the greenhouse gas emissions, water footprint, and land requirement of the production process.

Parts of the research leading to the contents of this chapter were published in: Falter, C., Batteiger, V., and Sizmann, A., 2016, "Climate Impact and Economic Feasibility of Solar Thermochemical Jet Fuel Production," *Environmental Science and Technology*, 50(1), pp. 470–477 [25].

4.2 Prior research

The analysis of the environmental performance of processes using concentrated solar energy in the literature comprises CSP plants for the production of electricity [166–168], of zinc and syngas [169], of hydrogen [170,171], and of solar fuels based on thermochemical conversion of water and carbon dioxide mediated by redox reactions of a metal oxide [24]. A process path similar to the one suggested in this manuscript is examined with flue gas scrubbing from a fossil power plant for the provision of carbon dioxide [24]. Not including the carbon dioxide of the fossil power plant as emissions into the system boundary of fuel production, the authors show that a lower environmental burden is associated with the production and use of solar gasoline than for gasoline derived from crude oil: well-to-tank emissions of $-1.58 \text{ kg}_{\text{CO}_2\text{-equiv.}} \cdot \text{L}^{-1}$ are indicated which corresponds to well-to-wake emissions of $0.74 \text{ kg}_{\text{CO}_2\text{-equiv.}} \cdot \text{L}^{-1}$, or about 30% of the CO_2 emissions from conventional gasoline [103].

An analysis of environmental and economic viability of the solar production of methanol, using the two-step iron oxide process is presented in [23]. Assuming a quite ambitious efficiency of 20% for the conversion of unconcentrated sunlight into syngas, the authors arrive at a system efficiency of 7.1% and a break-even price of the methanol of 1.22 \$/kg. The authors claim that a significant potential exists to reduce the greenhouse gas emissions of the conventional methanol process.

Different fuel production pathways are economically investigated using solar thermochemical reactors to produce carbon monoxide, hydrogen, or a mixture thereof [5]. For their mixed pathway, where the thermochemical reactors produce syngas and a Fischer-Tropsch conversion produces liquid hydrocarbons, the authors derive a path efficiency of 11.3%. This value is based on the assumption of 20% efficiency for the production of syngas including the efficiency of solar concentration. A minimum selling price of 7.01 \$ per gallon gasoline equivalent is derived.

Hydrogen production costs from electrochemistry (using water electrolysis with electricity from a parabolic trough power plant) are compared with two solar thermochemical cycles based on metal oxide redox reactions and the hybrid-sulfur cycle [102]. The authors arrive at cost corridors of 2.1–6.8 € kg^{-1} for the electrolysis, 3.5–12.8 € kg^{-1} for the metal oxide cycle, and 3.9–5.6 € kg^{-1} for the hybrid-sulfur cycle.

Different solar thermochemical cycles for the production of hydrogen are investigated in an analysis for the Department of Energy [101]. The authors state that the best cycle under investigation is the nickel ferrite cycle based on a thin film of active material deposited on a ZrO₂-support. Assuming a high 52% cycle efficiency including 79% heat recovery efficiency, the authors derive hydrogen production costs of 4.06\$ kg⁻¹ in the year 2015 and 2.42\$ kg⁻¹ in the year 2025.

The feasibility of solar fuel production from a fundamental point of view regarding resources, scale, and economics is investigated in [3]. The authors conclude that scaling up the solar fuels technology to produce 75 million barrels of oil equivalent per day will present enormous challenges but is nevertheless not precluded by considerations of economics and resources, provided that an overall system efficiency of 10% can be reached. At such an efficiency and system costs of 200 \$ m⁻² heliostat surface area, production costs of 2 \$ kg⁻¹ gasoline equivalent are determined.

In the literature, only very few analyses appear of the production pathway to solar thermochemical fuels, as presented in this work. The present analysis has the benefit of a common set of assumptions, enabling the consistent investigation of economic and environmental performance potentials. Furthermore, different operating scenarios concerning the origin of electricity and CO₂ are discussed, widening the applicability of the analysis. Finally, the combined investigation of thermochemistry and of the whole fuel production pathway allows the analysis of efficiency targets for the thermochemical production of syngas.

4.3 Baseline plant configuration

In the following, the baseline plant configuration is defined that shall be used for the further analysis of technical, economic and ecological performance. The plant is sized for the output of 1000 barrels per day (bpd) of jet fuel. 865 bpd of naphtha are produced as a co-product from the same plant. The energy and mass balances are derived and referenced to the functional unit of one liter of jet fuel and 0.87 liters of naphtha. The plant is assumed to be located in a region with an annual direct solar irradiation of 2500 kWh m⁻² a⁻¹, which is the case in Morocco, for example.

Solar primary energy is concentrated by heliostats onto the receiver on top of a tower. As the required mirror area ($6.5 \times 10^6 \text{ m}^2$ for heat generation, see Section 4.4.5; $1.3 \times 10^6 \text{ m}^2$ for electricity generation) is relatively high, the construction of multiple towers and heliostat fields may be required. However, as the characteristic values are referenced to the area of the heliostat field, this does not change the following assessment. Water is provided by desalination of seawater and subsequent transport over 500 km distance to an altitude of 500 m, while carbon dioxide is provided by on-site capture from the atmosphere. Ceria is used as a redox material in the thermochemical conversion of water and CO_2 to syngas with an energy conversion efficiency of 20%. The syngas is stored in an above-ground pressurized storage at 30 bar and supplied to the Fischer-Tropsch conversion unit which includes a hydrocracking and distillation unit. The light hydrocarbons fraction is converted into heat and electricity with efficiencies of 40% and 28%, respectively.

4.3.1 Energy and mass balance

Solar energy is assumed to be concentrated using a tower system with a concentration efficiency of 51.6% [50] which is derived from the annual average solar concentration efficiency of the Gemasolar plant assuming a secondary concentrator with an efficiency of 92.3% [51]. Electricity is produced with an annual average energy conversion efficiency of 20% from an on-site CSP plant.

As input to the FT unit, 395.2 mol syngas are needed, which is composed of 254.4 mol of hydrogen and 127.5 mol of CO. An additional 13.3 mol of hydrogen are required for hydrocracking of the long-chained FT products. Assuming a complete conversion of water into hydrogen and oxygen, 5.1 L of water have to be supplied to the thermochemical reaction. In total, 13.4 L of water are required for the production of one functional unit, 6.5 of which are for cleaning the mirrors, 3.9 for the supply of CSP electricity, and the remaining amount is for the thermochemical conversion where the required amount of water is reduced by 2.1 L through the recycling of water produced in the FT process. For cleaning the mirrors, the value of $58.0 \text{ L m}^{-2} \text{ y}^{-1}$ derived in [172] is used as a reference. Water consumption of the Ivanpah CSP plant in the United States reaches similar values, however for the whole plant operation [173] including steam generation in a dry-cooled closed cycle. Fresh water for the process is provided through seawater desalination and subsequent transport of the water over 500 km

distance and 500 m altitude difference to the fuel plant. The desalination plant operates with reverse osmosis at an energy requirement of 3 kWh m^{-3} [34]. The energy requirements for pipeline transport of the water to the fuel plant are calculated after [174].

Carbon dioxide in the baseline plant layout is assumed to be captured from the atmosphere by adsorption [38–40] to an amine-functionalized solid sorbent with an energy requirement of 1500 kWh of heat and 200 kWh of electricity per ton of CO_2 [42]. The energy is predominantly required in the form of low-temperature heat for desorption of CO_2 from the sorbent, an energy which is oftentimes available as waste heat in industry. The capture of carbon dioxide from the atmosphere is located at the plant site, obviating long-distance CO_2 transport. 5.6 kg of CO_2 are required for the production of a functional unit which are supplied to the thermochemical reaction at ambient pressure. Alternatively, CO_2 could be provided from a fossil source such as a natural gas power plant based on chemical absorption with monoethanolamine as a sorbent. The adaption of the analysis to such a fossil-based scenario is done in a scenario analysis in Section 4.6.2 and requires the correct accounting of electricity production and CO_2 capture from the power plant, both in the environmental and the economic analysis. Due to this reason and the fact that in [175] it was found that the production of solar hydrocarbon fuels is only environmentally advantageous compared to fossil fuels if the CO_2 is captured from the atmosphere, the assumption of air capture is made here.

The thermochemical efficiency of the solar reactor is defined as the higher heating value of the produced syngas divided by the required input of concentrated solar energy and auxiliary energy. The energy conversion efficiency is defined on the basis of thermal energy, where electrical energy is converted with an efficiency of about 40% from thermal energy (resulting in an overall conversion efficiency of 20% from solar energy to electrical energy). For the thermochemical conversion of water and carbon dioxide to syngas, the input of heat is required for the temperature increase of reactive material from the lower to the higher cycle temperature, for the endothermic reaction enthalpy, for the evaporation of water and the heating of water and carbon dioxide to the lower cycle temperature. Auxiliary energy is needed for the purification of inert gases for the establishment of the low oxygen partial pressure atmosphere and for the separation of carbon monoxide and carbon dioxide. The required amount of inert gases is assumed to be ten times as large as the amount of evolved oxygen [11]. The purification of the inert gas requires the input of 16 kJ of electricity per mol of gas [176]. The gas separation of CO and CO_2 is required because an excess amount of CO_2

is supplied to the oxidation for kinetic and thermodynamic reasons. The assumed excess factor with respect to the stoichiometric amount is two and the separation energy is assumed to be 132 kJ of heat and 9 kJ of electricity, operating analogously to post-combustion processes based on the sorbent KS-1 [108]. In the baseline case, a thermochemical efficiency of 20% (including purification of inert gas and separation of gaseous products) is assumed which is well within the thermodynamic limits.

The thermochemical cycle operates under a temperature-pressure-swing [10,15], where the achieved nonstoichiometry of ceria per cycle is 0.1 and the number of cycles per day is 16. While the former represents an improvement of presently achieved values in experiments [11,14,15], a decrease of the cycle time could reduce the required nonstoichiometry per cycle. In fact, the cycle time has been reduced considerably in recent experiments [15]. Ceria has been shown to be very stable over a large number of cycles [15,86], however, a degradation process is expected that requires the remodeling of the structure to be used in the reactors. As on the other hand, ceria is not consumed in the reactions, it does not have to be replaced by new material. Under these assumptions, 7.0×10^6 kg of ceria is required in the thermochemical reactors for the production of 1000 bpd of jet fuel and 865 bpd of naphtha.

A carbon efficiency of 90% for the Fischer-Tropsch conversion from syngas to hydrocarbons and a loss of the remaining 10% CO feed as CO₂ is assumed. As the FT conversion operates at a pressure of 30 bar, the syngas coming from the solar reactor has to be pressurized to this level which requires 4.2 MJ of electricity, 2.3 MJ of which are supplied by conversion of solar primary energy and 1.9 MJ are supplied from internal conversion of intermediate products. The hydrocracking and distillation step which reduces the chain lengths of the hydrocarbons to the desired ranges and separates the products, has an energy demand of 0.3 MJ of electricity and of 1.9 MJ of heat [177], both of which are supplied from the combined heat and power unit which combusts the light hydrocarbon fraction from the FT conversion. Alternatively, the light hydrocarbon fraction could be reformed into syngas and cycled back to the FT unit. However, in the baseline case, the conversion of the light hydrocarbons in a CHP plant is assumed as this is also close to the current practice of GtL plants.

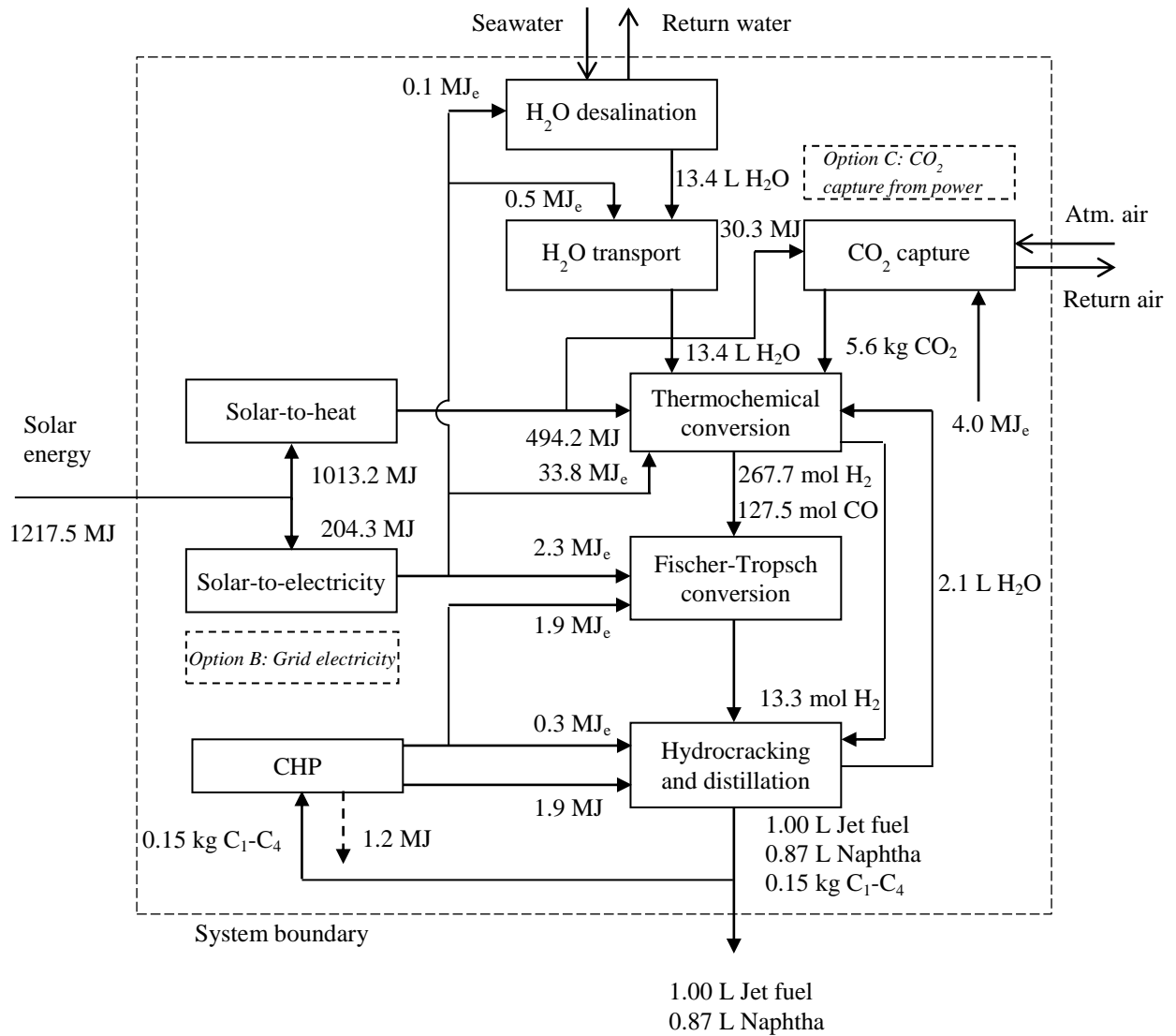


Figure 4.1 Energy and mass balance of baseline layout of solar thermochemical fuel production plant. Solar energy enters the system and is converted into heat and electricity, where the former is performed with a solar tower concentrator and the latter with a dedicated CSP plant. H₂O is supplied by pipeline transport from the seawater desalination plant and CO₂ by capture from the atmosphere. Most of the energy is required for the thermochemical conversion of H₂O and CO₂ to H₂ and CO (syngas). The syngas is converted by Fischer-Tropsch synthesis and subsequent hydrocracking and distillation into jet fuel, naphtha, and gaseous products. The latter are combusted in a combined heat and power plant (CHP) and converted into heat and electricity for the process. All energies and masses are expressed with respect to the production of one liter of jet fuel and 0.87 liters of naphtha.

In the solar stand-alone configuration (i.e. without external electricity and heat sources), the required amount of solar primary energy and the level of solar irradiation at the chosen plant location are used to calculate the size of the mirror field. In Figure 4.1, the energy and mass balance of the baseline layout of the thermochemical fuel production plant is shown.

The fuel products are assumed to be transported via pipeline over a distance of 500 km and the corresponding emissions are taken from [178].

As the FT reaction is exothermic and needs to be stabilized in temperature by cooling water, an integration with the other plant components for the use of this surplus heat could possibly be realized in the future. In fact, the energetic integration of the FT step into the whole fuel production plant is a very interesting feature which should be analyzed further with dedicated software that allows the simulation of the material and energy flows in the entire system. However, for simplicity and the fact that heat from cooling water may be difficult to use in a different process step, the heat from the FT reaction and the cooling water requirements are neglected.

4.3.2 Energy conversion efficiency

In the following, the energy conversion efficiency of the fuel production process is calculated based on the system boundary shown in Figure 4.1. The total required solar primary energy is 1217.5 MJ, of which 1013.2 MJ are converted into heat and 204.3 MJ are converted into electricity. At lower heating values of 33.4 MJ L⁻¹ for jet fuel [28] and 31.1 MJ L⁻¹ for naphtha [28], the total energy contained in the output is 1 L × 33.4 MJ L⁻¹ + 0.87 L × 31.1 MJ L⁻¹ = 60.46 MJ. The energy conversion efficiency based on the lower heating values of the products is thus $\eta = 60.46 \text{ MJ} / 1217.5 \text{ MJ} = 4.95\%$.

In the literature, the following efficiency values are found. A similar production path is analyzed in [5] and an efficiency of 11.3% excluding FT product refining is determined. In another analysis of the same production pathway [24], an energy efficiency of 8.8% is given, including energy requirements of FT refining and of additional hydrogen production for hydrocracking. In a related publication, an energy efficiency of 7.1% for the synthesis of methanol via the solar thermochemical pathway is found [23]. The higher efficiencies in the literature are explained by the assumption of higher process efficiencies for solar concentration and thermochemistry, resulting in an efficiency of 20% for the conversion of

incident sunlight into syngas. This is based on solar dish concentrators which achieve higher optical efficiencies than tower systems, exceeding 80% [56,179], and a higher thermochemical efficiency. The more conservative estimate in this study, on the other hand, is based on a thermochemical efficiency of 20% which is an ambitious but realistic target for the mid-term future, considering experimental values of about 2-5% today [10,11,14,15,110] and a potential for much higher values. Solar dish systems require a sophisticated decentralized syngas production and collection system and were therefore not considered in the baseline case.

4.4 Ecological assessment

The goal of a life cycle analysis (LCA) is the quantitative description of the environmental impact of a product or a process, based on the energy and material flows and an assessment of their effects. The background of an LCA is life cycle thinking, including all steps in the lifetime of the product or process, starting from the raw material (“well”) used for the production until the end of life (“wake”). The LCA methodology is described in different guidelines and ordinances, while the basic recommendations are clustered in the ISO standards 14040 and 14044 [180,181].

According to the ISO standards, the following steps are required for the execution of an LCA (Figure 4.2). In a first step, the goal and scope of the analysis have to be defined including the system boundaries, the analyzed products, the functional unit and the intended application of the study (Section 4.4.1). Depending on the goal of the study, the methods and tools may vary. A thorough definition of the system boundary ensures consistency in the analysis and enables the comparison of the results with other studies with identical boundaries. The functional unit (Section 4.4.2) is a measure of the main output of the process, with regard to which the results of the study are normalized.

In the next step, the life cycle inventory is analyzed (Section 4.4.3), i.e. the material and energy flows over the defined system boundary are derived. Data for each process step are collected or, when data is missing, are calculated or estimated from comparable processes.

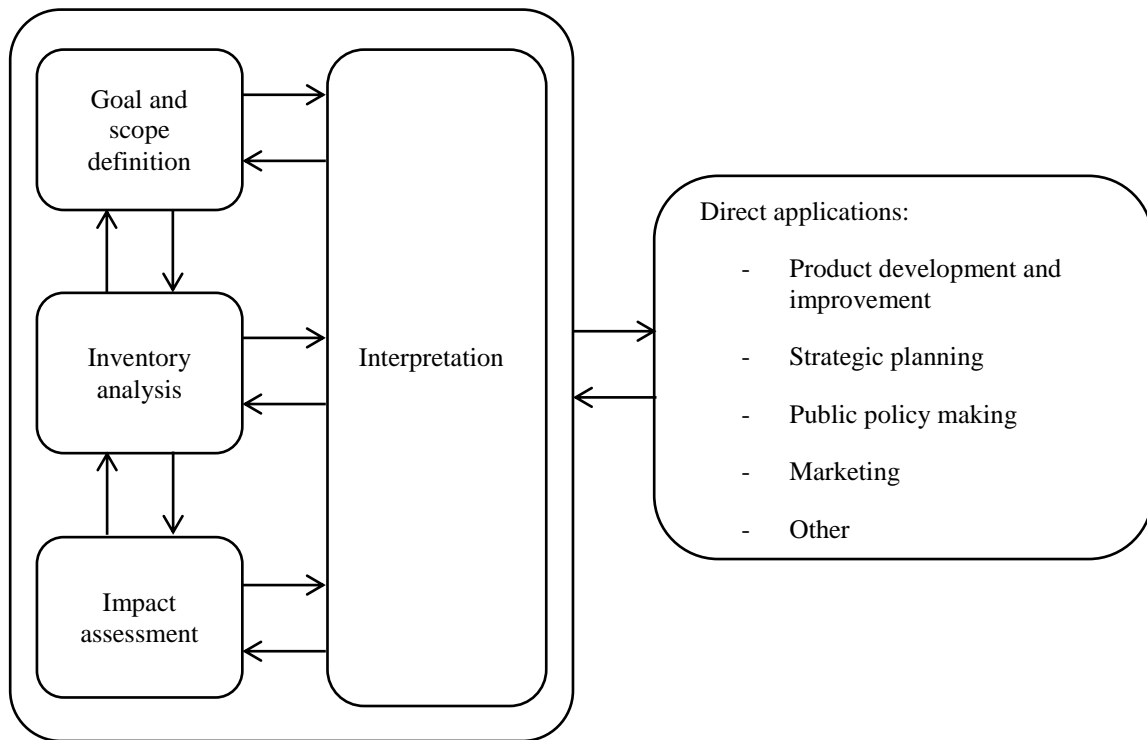


Figure 4.2 Life-cycle assessment framework including the stages of the analysis. Figure after [180].

For the co-products, adequate allocation procedures (Section 4.4.4) have to be considered which can be based on mass, energy content or economic value, for example. Data sources and further assumptions are given in Section 4.4.5.

The third step in an LCA is the environmental impact assessment (Section 4.4.6), where the impact categories are defined and the classification of the results from the inventory analysis according to the categories is performed. The environmental impact is then derived by summing the categorized flows from the life cycle inventory in common equivalence units.

In the context of the solar jet fuel production process, the primary environmental impact of interest is the global warming potential (GWP) by emissions, since the products are synthetic kerosene and naphtha. The GWP is expressed in CO₂-equivalents, summing the climate impact of all emitted gases, and referencing them to the impact of CO₂, which is a common metric for GWP.

For the calculation of life cycle emissions, the emissions from the construction, operation, and deconstruction of the plant facilities have to be taken into account. In some cases, the construction or deconstruction of the facilities will present only a minor contribution that can be neglected with respect to the larger emissions from operation.

Finally, the results from the analysis are summarized in the interpretation stage (Section 4.4.6), where a check for sensitivity, limitations and consistency is performed and conclusions are drawn.

4.4.1 Goal and scope definition

The goal of the LCA is the assessment of the ecological performance of the solar thermochemical jet fuel production facility. The product system to be analyzed is the baseline case of the facility. A location in Morocco with an irradiation of 2500 kWh/(m² y) is chosen with an assumed distance of 500 km and 500 m altitude difference to the seaside. The system boundary includes all plant components and all process steps from the provision of desalinated water and carbon dioxide captured from the air, the concentration of solar energy, thermochemical conversion, syngas conversion into hydrocarbons, conversion of the light hydrocarbon fraction into heat and power, to the transport of the final fuels. In the baseline case, the electricity requirements are satisfied within the boundaries, i.e. a CSP plant is located on-site.

Production of one liter of jet fuel is chosen as the functional unit, where at the same time 0.87 L of naphtha are produced as a by-product. It is therefore necessary to allocate between these two products which is performed on an energy basis, using the lower heating value as a reference.

The impact category is greenhouse warming potential, where the impact assessment is performed with an accounting of greenhouse gases involved in the production of the functional unit. The impact of the gases is expressed with the common metric of CO₂-equivalents. All phases from the life of the production plant are accounted for in the assessment including construction, use and decommissioning of the facility, as well as resource provision. Recycling of the materials after decommissioning is not assumed. The generation of CSP electricity requires an additional heliostat field to collect solar energy for the conversion into electrical energy. The associated environmental burden is taken into account by using a literature value for the specific GHG emissions of CSP electricity [172]. A cut-off criterion of 1% of the total GHG emissions is used and contributions below this threshold are neglected, e.g. the construction of the seawater desalination plant [182]. Due to the low technology readiness level, the infrastructure requirement for the CO₂ capture plant

could not be estimated with a high level of fidelity and is not included in the analysis. The GHG emissions associated with the construction of the FT facility were estimated based on a large-scale GtL plant in Qatar and it was found that the contribution was well below the 1% cut-off limit. Assuming that the transport of the material to the plant location and the plant deconstruction do not exceed the manufacturing, the total contribution of the FT infrastructure can be neglected.

For the derivation of life cycle emissions, both a well-to-tank and well-to-wake boundary are chosen, i.e. for the former, only the emissions associated with the production and transport of one liter of solar jet fuel are analyzed. This well-to-tank boundary thus excludes emissions from the combustion of the fuel in an airplane. In a well-to-wake analysis, these emissions are taken into account as well, however, the specific transport and combustion emissions of conventional jet fuel and alternative fuels do not differ significantly [28,178].

4.4.2 Functional unit

As functional unit, the production of one liter of jet fuel and 0.87 L of naphtha is chosen. The allocation of the system emissions to the single products is done on an energy basis, as described in the next section.

4.4.3 Inventory analysis

The energy and material balance of the baseline jet fuel production plant have been calculated in Section 4.3.1. The values are referenced to the production of the functional unit and its co-product of 0.87 L naphtha and are shown in Figure 4.1.

4.4.4 Allocation method

For the allocation of greenhouse gas emissions to the two products jet fuel and naphtha, the basis of energy content (lower heating value (LHV)) is chosen. Based on the LHVs of jet fuel

and naphtha of 33.4 MJ L^{-1} [28] and 31.1 MJ L^{-1} [28], respectively, 55.4% of the greenhouse gases are allocated to jet fuel and 44.6% to naphtha.

4.4.5 Data sources and further assumptions

In the following, the assumptions that are made for the calculation of the GHG emissions from the fuel production plant are described. For the concentration of solar radiation, a field of heliostats tracking the sun and reflecting onto a tower is assumed. As type of heliostat, a 148 m^2 glass/metal construction is chosen with elevation/azimuth tracking, as described in [172]. The emissions from the complete life cycle including construction, operation and decommission are given with 132.76 kg/m^2 . The required number of heliostats is calculated from the required heat ($5.23 \times 10^8 \text{ J}$ per functional unit) and the conversion efficiency from incident sunlight to heat (51.6%). The environmental impact of CSP electricity production is derived separately by multiplying the amount of electricity by an impact factor. This is possible because the only energetic input to the system is primary solar energy which is then converted to heat and power for the plant operations. At an efficiency of 5.95% (excluding electricity requirements) and with a solar resource of $2500 \text{ kWh}/(\text{m}^2 \text{ a})$, a reflective area of $6.53 \times 10^6 \text{ m}^2$ is required for the assigned plant size of 1000 barrels per day of jet fuel and 865 barrels of naphtha. Emissions for the tower, roads and other infrastructure concerning the plant, are 28.01 kg/m^2 of heliostat reflective area [172]. Included in this number are the phases of construction, operation and decommissioning. The tower consists mainly of concrete and steel. The thermochemical reactor is assumed to be similar to the one used for recent experiments in the literature [11,15,105] and is scaled up to the baseline plant size, assuming a constant material requirement per unit of thermal input power. In principle, as a scale-up of a reactor increases the surface-to-volume ratio, it should be expected that the specific amount of reactor housing and insulation material can be reduced. On the other hand, the larger input power may lead to a modularized reactor setup which could increase the specific amount of material. The correct values can only be found with a detailed technical reactor model which is not available at present. Therefore, the assumption of identical specific material requirements as in the experiments is made. The material used for the reactor operating in the 1000 bpd-plant is thus $6.98 \times 10^6 \text{ kg}$ of ceria, $3.49 \times 10^6 \text{ kg}$ of alumina insulation, $1.05 \times 10^7 \text{ kg}$ of steel and $2.09 \times 10^6 \text{ kg}$ of glass. The corresponding emission factors are $10.30 \text{ kg}_{\text{CO}_2\text{-eq.}}$ per kg ceria [183] (current Chinese grid mix), $16.70 \text{ kg}_{\text{CO}_2\text{-eq.}}$ per kg

alumina [24] (current US grid mix), 1.43 kg_{CO₂-eq.} per kg steel [178], 1.09 kg_{CO₂-eq.} per kg glass [178], and 0.16 kg_{CO₂-eq.} per kg concrete [178] (2030 grid mix Germany).

The required amount of water of 13.4 L per functional unit is composed of a requirement of 5.1 L for thermochemical conversion, 6.5 L for cleaning the mirrors, and 3.9 L for CSP electricity. 2.1 L are recycled internally by using the water produced in the FT conversion. The on-site life cycle water consumption of a solar tower power plant is used with 58 L/(m² a) [172]. In a different publication, the water requirement for mirror cleaning has been estimated to be drastically lower with 3 L m² y⁻¹ [52]. However, in order not to underestimate the water usage, the higher value has been assumed. The distance for the transport of water is 500 km and an altitude difference of 500 m has to be overcome. The required electricity for the desalination of seawater is 3 kWh m⁻³ [34] and the electricity for the transport of the pure water is calculated with the Darcy-Weisbach equation, where the friction coefficient is derived with a modified form of the Colebrook-White equation [174], assuming a pump efficiency of 80%, a roughness factor of 4.5×10⁻⁵ m for the pipe and a velocity of 1 m s⁻¹ of the water in the pipe. The emissions associated with the infrastructure for desalination of the water are neglected as they present below one percent of the emissions associated to the operation of the desalination plant [182]. The pipeline used for water transport is assumed to be available for the solar fuel production plant and is therefore neglected.

The required amount of 5.6 kg carbon dioxide is assumed to be captured on-site from the air by adsorption to a solid amine-functionalized sorbent [38–40]. As the air capture technology is not yet commercially available, an estimation of the emissions coming from the construction of the capture facility remains subject to large uncertainties. A comparison of emissions from the construction and operation phases of the Fischer-Tropsch conversion unit or the seawater desalination plant shows that construction does not play a decisive role as its share is well below one percent of the operational emissions. For the CO₂ capture unit, emissions are thus neglected for the construction and decommissioning phase. In the operational phase, 1500 kWh of low-temperature heat and 200 kWh_{el} are required for the capture of one ton of CO₂ [42]. Heat and electricity are provided on-site by conversion of incident sunlight, which causes additional life cycle emissions. The heat and electricity requirements for the capture of CO₂ are however small compared to the ones for operation of the thermochemical solar reactor.

The Fischer-Tropsch unit causes emissions due to the construction of its facility and due to its operation. For the construction of the FT plant, the basic material requirements were estimated from the construction of the 140000 bpd-Shell GtL plant in Qatar [184], scaled

linearly to the size of 1000 bpd. It was seen that the emissions associated with the construction of the FT facility are well below 1% of the final GHG emissions of the products and are therefore neglected according to the cut-off criterion defined in Section 4.4.1. Emissions associated with the decommissioning are also neglected, assuming that decommissioning does not cause larger emissions than the construction of the plant. In the operational phase of the FT conversion, CO₂ is emitted through vented gas, gas leakages and ancillary sources [185]. For the calculation of operational emissions, a mass and energy balance of the FT unit including all three steps of synthesis, hydrocracking and distillation is performed, where data for energy consumption is taken from Beiermann [177]. The fraction of light hydrocarbons is assumed to be combusted in a combined heat and power unit which produces electricity with 28% efficiency and heat with 40% efficiency with respect to the higher heating value of the gases, both of which are used to partly cover the energy demand of the FT unit. The produced gases (C₁-C₄) are determined by assuming an Anderson-Schulz-Flory distribution of the FT products with a growth factor of 0.9. The largest fraction on a mol-basis is thus methane, followed by ethane, propane and butane. A mass balance then gives the amount of carbon dioxide produced by gas combustion under the assumption of a complete reaction. Thus, from the combustion of light hydrocarbons, 0.45 kg CO₂ is emitted per functional unit. As also 2.3 MJ of electricity are required for the Fischer-Tropsch process step which cannot be covered by the CHP plant, the overall emissions from the FT conversion are increased by 0.01 kg per functional unit due to the emissions associated with electricity generation. Finally, as the carbon efficiency is 90%, the unconverted CO is assumed to be lost as CO₂ to the environment, emitting 0.55 kg CO₂ per functional unit. This may present a conservative estimate but takes into account possible important sources of CO₂ leakage. The total emissions from the FT conversion step are then 1.0 kg of CO₂ equivalents.

4.4.6 Impact assessment and interpretation

In the following, the results of the life cycle impact assessment are presented. Chosen impact categories are global warming potential, water use, and land use.

4.4.6.1 Global warming potential

The global warming potential of the gases emitted during the construction, the operation, and the deconstruction of the fuel production plant are derived from the inventory analysis and literature data. The impact indicator of global warming potential is then the accumulated radiative forcing of all considered gases integrated over a 100 year time horizon, relative to that of CO₂. The results are normalized to the functional unit of one liter of jet fuel by allocating the emissions on an energy basis (LHV) to the products of jet fuel and naphtha.

Provision of water

The emissions of greenhouse gases from water desalination and its transport to the fuel production plant are accounted for by the electricity requirements and the multiplication with the CSP GHG emission factor of 0.023 kg_{CO₂-eq.} kWh_{el}⁻¹ [172]. At the required amount of 13.4 L of water per functional unit, 5.12×10⁻⁴ kg_{CO₂-eq.} L⁻¹ of jet fuel are emitted for desalination and 1.83×10⁻³ kg_{CO₂-eq.} L⁻¹ of jet fuel for the transport to the plant site. These emissions are included in the following section of electricity provision but are shown here to identify the origin of the emissions.

Carbon dioxide capture

The capture of carbon dioxide is conducted on-site from the air by chemical adsorption to a solid amine-functionalized sorbent and requires the input of heat by concentration of solar energy and electricity by CSP. The emissions associated with the required concentration infrastructure for heat provision are 0.023 kg_{CO₂-eq.} L⁻¹ of jet fuel and are included in the value of solar concentration below. CSP electricity contributes 0.014 kg_{CO₂-eq.} L⁻¹ of jet fuel. These emissions are included in the following chapters of electricity provision and solar concentration.

3.11 kg_{CO₂-eq.} L⁻¹ of jet fuel are captured from the atmosphere and are counted negatively in the emissions balance. The infrastructure of the capture unit is not taken into account due to inherent uncertainties of estimating the emissions of a technology still in its demonstration stage.

Electricity provision

Solar electricity is assumed to be provided by concentrated solar power with an emission factor of $0.023 \text{ kg}_{\text{CO}_2\text{-eq. kWh}_{\text{el}}^{-1}}$ [172]. $11.4 \text{ kWh}_{\text{el}}$ are required for the production of one functional unit consisting of one liter of jet fuel and 0.87 liters of naphtha. Thus, $0.26 \text{ kg}_{\text{CO}_2\text{-eq.}}$ are emitted per functional unit, where 80.0% are used for inert gas production, 9.9% for CO_2 capture, 5.7% for FT conversion, 2.8% for CO/CO_2 separation, 1.3% for water transport, and 0.4% for water desalination.

Solar concentration

A field of heliostats with a total aperture of $6.53 \times 10^6 \text{ m}^2$ is used for the generation of heat to drive the thermochemical conversion and the capture of carbon dioxide. For the manufacture, construction, deconstruction, and disposal of the heliostats and the towers, GHG emissions of $0.42 \text{ kg}_{\text{CO}_2\text{-eq. L}^{-1}}$ of jet fuel are generated which includes mirror replacement. Of these emissions, 94% are due to thermochemical conversion and 6% due to carbon dioxide capture.

Thermochemical conversion

The materials used for the production of the thermochemical reactors, i.e. steel, glass, alumina, and the reactive material ceria cause GHG emissions of $5.63 \times 10^{-2} \text{ kg}_{\text{CO}_2\text{-eq. L}^{-1}}$ of jet fuel. The emissions caused by the heliostats used for the generation of heat for the thermochemical conversion are included in the value for solar concentration above.

Fischer-Tropsch conversion

Fugitive emissions of carbon dioxide due to the carbon efficiency being lower than unity and the combustion of the light hydrocarbon fraction in the CHP plant cause emissions of $0.56 \text{ kg}_{\text{CO}_2\text{-eq. L}^{-1}}$ of jet fuel, where the former accounts for 56% and the latter for the remaining 44%. The additionally required electricity adds $8.27 \times 10^{-3} \text{ kg}_{\text{CO}_2\text{-eq. L}^{-1}}$ of jet fuel to give a total amount of $0.57 \text{ kg}_{\text{CO}_2\text{-eq. L}^{-1}}$ of jet fuel.

Fuel transport

The produced fuels jet fuel and naphtha are assumed to be transported via pipeline over a distance of 500 km, causing emissions of $6.44 \times 10^{-2} \text{ kg}_{\text{CO}_2\text{-eq. L}^{-1}}$ of fuel, where the corresponding specific emissions are taken from the Gemis software [178].

Well-to-tank (WTT) emissions

The total amount of GHG emissions is derived by summation of the contributions for the single process steps shown above. The production of one liter of jet fuel with the baseline plant therefore causes WTT GHG emissions of $-1.87 \text{ kg}_{\text{CO}_2\text{-eq. L}^{-1}}$ of jet fuel and $-1.73 \text{ kg}_{\text{CO}_2\text{-eq. L}^{-1}}$ of naphtha. The negative value indicates that for the fuel production, a net reduction of greenhouse gases is achieved. This result is expected, as carbon dioxide is captured from the atmosphere and stored in liquid hydrocarbons.

Well-to-wake (WTW) emissions

Adding the specific emissions of combustion to the well-to-tank emissions, the well-to-wake emissions are derived which indicate the total life cycle of the production and use of the fuels. The WTW emissions are $0.49 \text{ kg}_{\text{CO}_2\text{-eq. L}^{-1}}$ of jet fuel and $0.55 \text{ kg}_{\text{CO}_2\text{-eq. L}^{-1}}$ of naphtha. An overview of the WTT and WTW GHG emissions is given in Table 4.1.

The baseline case of the fuel production plant thus already shows a very promising reduction of the greenhouse gas emissions by 84% compared to conventional jet fuel. In [28] only three out of seventeen biomass-based options are found to have a GHG emission reduction of 75% or more with respect to conventional jet fuel. The authors of the BURNfair project [186] arrive at a similar conclusion with reductions in the range of 18-76%, where only one of the analyzed biomass-based alternative fuel pathway reached a reduction of 76%.

Table 4.1 Overview of well-to-tank (WTT) and well-to-wake (WTW) greenhouse gas emissions of baseline solar fuel production plant. Results are shown for the single process steps per liter of jet fuel, per liter of naphtha, and per functional unit (1 L jet fuel + 0.87 L naphtha).

GHG emissions	Jet fuel [kgCO ₂ -eq. L ⁻¹]	Naphtha [kgCO ₂ -eq. L ⁻¹]	Functional unit [kgCO ₂ -eq. f.u. ⁻¹]
CO ₂ capture from air	-3.11	-2.89	-5.61
Electricity	0.14	0.13	0.26
Solar concentration	0.42	0.39	0.75
Thermochemical conversion	0.06	0.05	0.10
Fischer-Tropsch conversion	0.56	0.52	1.01
Fuel transport	0.06	0.06	0.12
WTT GHG emissions	-1.87	-1.73	-3.36
Fuel combustion	2.35 ¹	2.28 ¹	4.32 ²
WTW GHG emissions	0.49	0.55	0.96
WTW GHG emissions of conv. fuel	3.03 ¹	3.13 ³	5.74 ²
WTW GHG emissions relative to conventional fuel	16%	17%	16%

¹[28],²calculated from [28] and [187],³[187]

From an environmental point of view, the solar thermochemical jet fuel pathway could therefore represent an interesting option for the substitution of conventional jet fuel in the future. Process optimizations are possible to further reduce the emissions below the value of the baseline plant.

The sources of GHG emissions during fuel production and use are shown in Figure 4.3. The largest share of the WTW emissions stems from the combustion of the produced jet fuel in an airplane engine which causes 2.35 kgCO₂-eq. L⁻¹ [28]. Fugitive emissions and the combustion of light hydrocarbons during Fischer-Tropsch conversion cause 15.6% of the overall emissions. Emissions associated with the establishment of the solar concentration infrastructure and its decommissioning are responsible for 11.6% of the emissions. The other contributions of electricity generation by CSP, the construction of the thermochemical reactors and fuel transport have only a small influence of less than 5% on the overall emissions. Concerning electricity generation, the assumption of a CSP plant leads to quite low specific emissions of 0.023 kg kWh_{el}⁻¹ [172]. Were the electricity taken from the local grid which has in most cases considerably higher specific emissions or from any fossil source, both overall emissions and the share of electricity related emissions would rise significantly. This topic of grid electricity

use and its influence on environmental and economic performance of the fuel production process is discussed in Section 4.6.3.

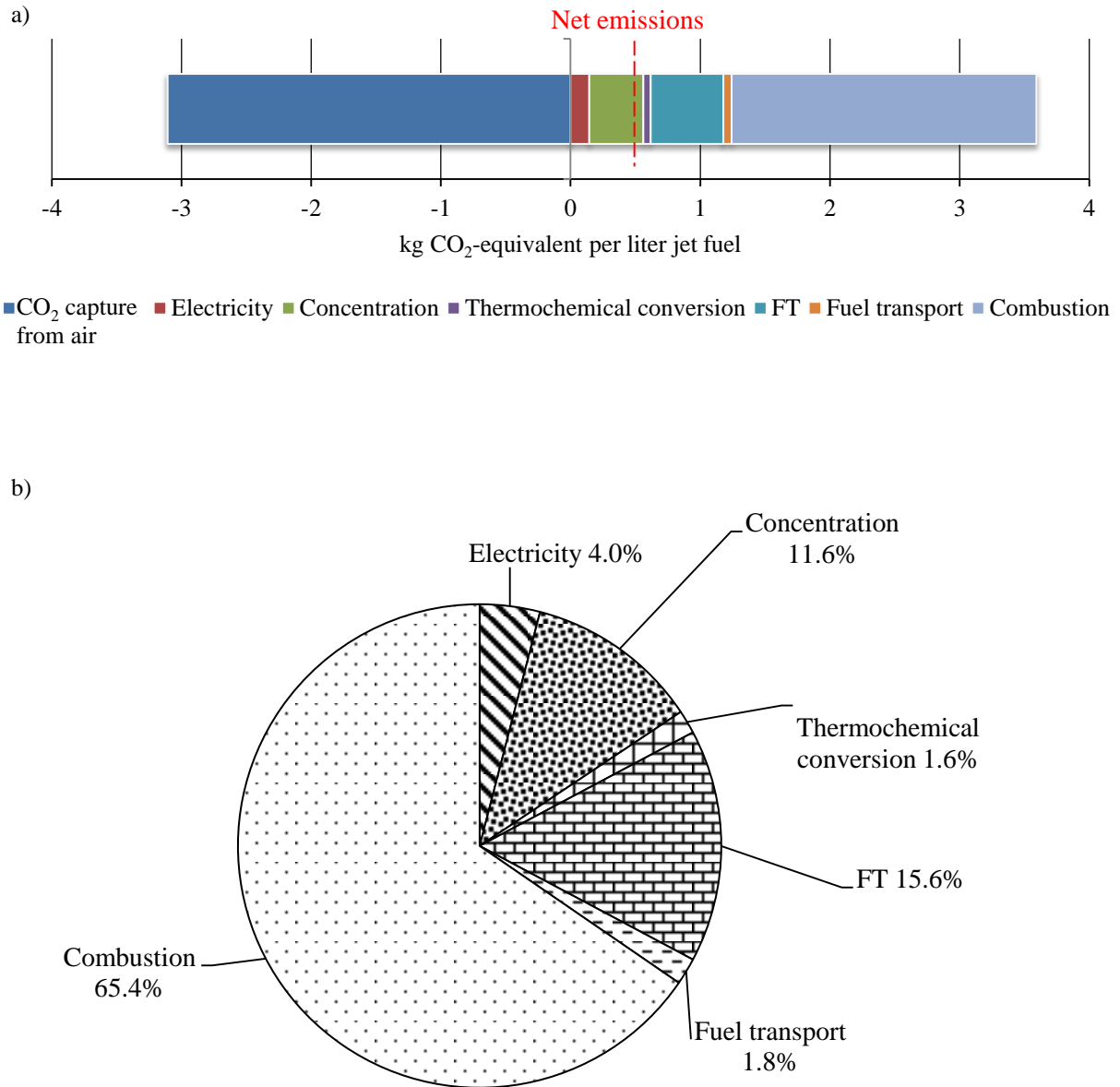


Figure 4.3 Origin of WTW life cycle greenhouse gas emissions for the production of jet fuel in the baseline case. a) Absolute values including negative emissions by CO₂ capture from the atmosphere, b) contributions to positive CO₂ emissions (without CO₂ capture) which add up to 3.59 kg_{CO₂-eq.} L⁻¹. The overall emissions of 0.49 kg_{CO₂-eq.} L⁻¹ are derived by offsetting the positive emissions by the capture of 3.11 kg_{CO₂-eq.} L⁻¹ from the atmosphere. The largest shares are due to combustion, FT conversion, and the solar concentration infrastructure.

Emission reduction possibilities

In the following, possibilities for the reduction of the GHG emissions for the contributors of FT conversion and the heliostat field are discussed. The other components have only a limited emission reduction potential with respect to the overall fuel production process due to their small share in the overall emissions.

During the combustion of the fuel, the bonds of the carbon and hydrogen atoms in the fuel break and carbon dioxide and water are produced through the reaction with oxygen, releasing heat. From an energetic point of view, all of the fuel should react with oxygen in order to liberate all of the stored chemical energy. A reduction of carbon dioxide emissions from the combustion of the (chemically identical) hydrocarbon fuel is therefore hardly possible. However, process improvements during the production of the fuel may be possible to reduce the WTT emissions. Some important possibilities are discussed in the following.

For the Fischer-Tropsch conversion, a carbon efficiency of 90% was used and the remaining 10% of the carbon monoxide were assumed to be lost as carbon dioxide emissions. This is a rather conservative estimate since the unconverted gases are emitted to the atmosphere. This is partly true since leaks and fugitive gases in the process lead to losses to the surroundings. Through process improvements such as better sealings and a recycling of the unconverted gases, this value may be reduced.

Another source of emissions is the combustion of light hydrocarbons in the combined heat and power plant to produce heat and electricity for the Fischer-Tropsch unit. Even though this is a common way to make use of the gaseous by-products, it is rather undesirable from an environmental point of view, as it leads to considerable emissions of about $0.45 \text{ kg}_{\text{CO}_2\text{-eq.}} \text{ L}^{-1}$ of jet fuel, about half of the specific emissions of the FT unit ($1.01 \text{ kg}_{\text{CO}_2\text{-eq.}} \text{ L}^{-1}$). The emissions of the overall production process could thus be considerably reduced if the light hydrocarbon fraction of the FT conversion were not combusted but reformed into syngas and fed back to the FT reactor. The required heat and power would then be provided by the conversion of solar primary energy. This could even be attractive from an economic point of view, as the main product of the process has a high value and heat and electricity may be supplied comparably cheaply at the plant location. The removal of the CHP plant from the production process is discussed in Section 4.6.7.

The solar concentration facility contributes to the overall emissions through the use of fossil primary energy mainly during its manufacturing process and during its decommissioning. As

the required reflective area of the heliostat field is large, the number of heliostats and therefore the material requirements and emissions are significant. Emissions associated with the heliostat field could be reduced through an increase of the optical efficiency, reducing the required number of heliostats, or through a reduction of the material intensity of the single heliostat. An increase of optical efficiency is possible for smaller fields and receivers [51] and through an improvement of the field layout [188,189], for example. The material intensity of the heliostats, on the other hand, could be diminished through a reduction of the required structural stability. This may be achieved by lighter mirrors [190–192], e.g. reflective polymers instead of coated glass, through a reduction of the wind loads on the field by fences or shelters [193–195], or through a higher share of renewable energy in the production.

Sensitivity study of factors influencing GHG emissions

To analyze the influence of important variables on the life cycle greenhouse gas emissions of the fuel plant, a sensitivity study is performed on the baseline case, in which selected variables are varied by $\pm 10\%$ at constant output of the plant. The chosen variables are solar irradiation level (annual direct normal irradiation), thermochemical efficiency, lifetime of the plant, and emissions from the construction, use and deconstruction of the concentration infrastructure (Figure 4.4). Results show that a variation of the plant lifetime, of thermochemical efficiency, or of solar irradiation has a similar influence on the GHG emissions: a decrease of 10% of the variables increases the GHG emissions by 10-12%, while a 10% larger value decreases the costs by 8-10%. In case of the lifetime, the reason for the change in emissions is that the environmental burdens associated with the infrastructure and operation of the plant are distributed over a varied number of years and thus the specific emissions per unit fuel produced changes. The level of solar irradiation and thermochemical efficiency directly influence the required area of mirrors and thus the emissions associated with their production and decommissioning. The large number of heliostats required for the concentration of sunlight has an important impact also through the associated emission factor per unit of mirror area. If this emission factor is varied by $\pm 10\%$, the life cycle GHG emissions change by $\pm 8.6\%$. This highlights the possible improvement through a decrease of the material intensity of the heliostats, a topic which is even more interesting for economic reasons (see Section 4.5.3).

The fact that GHG emissions vary in proportion with these variables reflects the near direct or inverse proportional scaling of the emissions with the single variables for the chosen assumptions, especially the solar stand-alone configuration. A different sensitivity with respect to the chosen variables would be observed for CO₂ capture from fossil sources, which then dominates the emissions.

The climate impact of solar jet fuel production could therefore be reduced through the choice of a highly irradiated plant location, the enhancement of the thermochemical conversion step, a prolongation of the lifetime of the plant components, and a reduction of the material intensity of the mirrors and the solar tower.

The preceding analysis permits the determination of the ecological key drivers of the baseline case of the fuel production plant under the condition of a similar change of the chosen variables.

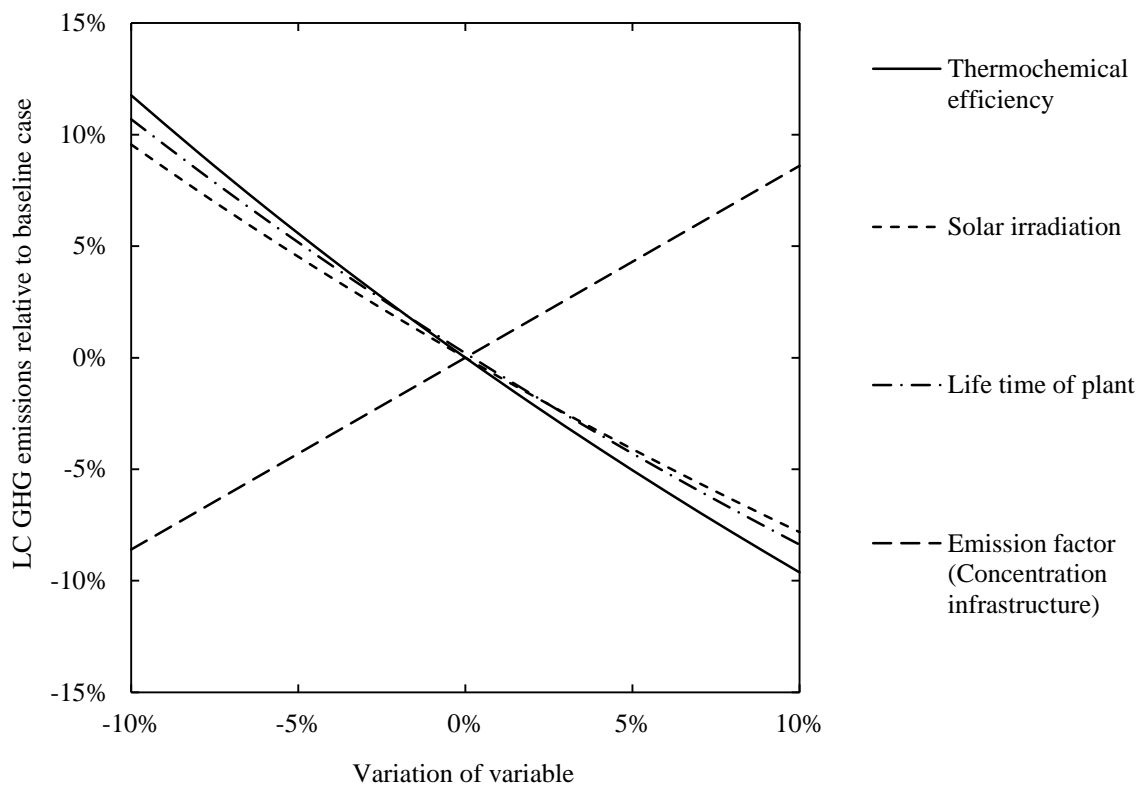


Figure 4.4 Sensitivity of life cycle GHG emissions for a variation of $\pm 10\%$ of efficiency of thermochemical syngas production, annual amount of direct normal solar irradiation, lifetime of the plant, and emission factor for the solar concentration infrastructure, assuming a constant output of 1000 bpd of jet fuel.

4.4.6.2 Water footprint

Although there is no global shortage, fresh water supplies are locally scarce which contributes to poverty and health problems. Historically, the fresh water withdrawal has risen quicker than the growth of the population in the past century [196], which will put additional pressure on the water resources in some regions of the earth, together with other factors such as climate change. According to the United Nations, by 2025, 1.8 billion people will live in regions with absolute water scarcity and two thirds of the population could live in regions of stressed water conditions [196]. Fresh water provision is likely to play a decisive role in the development of certain regions of the earth in the present century. The responsible use of fresh water resources is therefore a necessity for ecological, political, and ethical reasons.

In the baseline case, fresh water is derived by the desalination of seawater and is transported over 500 km distance and 500 m altitude difference. This requires the input of electrical energy which is produced by concentrated solar power at the plant site. However, compared to the other process steps, the energy requirement is small: 1.7% of the total electrical energy is used for desalination and water transport to the plant site, which corresponds to 0.013 € of the final production costs of 2.23 € and 0.2% of the positive on-site GHG emissions (CO₂ capture from the atmosphere is counted as a negative emission). The provision of fresh water to the plant site is therefore not an obstacle even in remote regions. Nevertheless, in general the provision of fresh water may have an influence on the problems of water scarcity in some regions. In order to estimate the impact of the fresh water consumption of the analyzed fuel production pathway, a water footprint assessment is conducted and a comparison with other fuel production pathways is performed. For the water footprint comparison, different sources of fresh water - blue, green, and grey water – are introduced, as this discrimination is an important aspect of fuels based on the irrigation of biomass. For the present solar thermochemical fuel pathway, fresh water is assumed to be supplied by seawater desalination and is therefore not taken directly from existing fresh water resources. As the desalinated water resembles a reservoir of fresh water, it corresponds to the definition of blue water which is given below. A further distinction by the source of the fresh water is not made for solar thermochemical fuels.

A water footprint assessment measures the volume of fresh water used to produce a product, evaluated over the whole supply chain. It therefore gives important information on the requirements on the local resources and on possible competition with drinking water.

However, it does not indicate the severity of the environmental impact because the latter depends on the local scarcity of fresh water and the number of local consumers and polluters [197]. The water footprint is an important indicator for the estimation of the impact on water resources even though it cannot predict local scarcity or conflicts.

In the following, the amount of fresh water used for the fuel production is derived. In order not to neglect important contributions, the water consumption for both the development of the production facilities as well as for their operation is taken into account. A distinction is therefore made between water consumption *on-site* for operation and *off-site* for the provision of the materials, comparable to O&M costs and investment costs in an economic analysis. It is important to distinguish between on-site and off-site consumption because the criticality of fresh water consumption has to be judged by both the availability of local resources and the amount of its reduction. The consumption of one liter of fresh water from the local resources is much more critical in a region with a low natural availability such as desert regions as compared to an affluent region such as the European alpine region. As different materials are required for the construction of the fuel production plant, water consumption is likely to occur in different regions of the earth. However, this level of detail is not included into the analysis due to the unavailability of the data. Nevertheless, on-site water is provided by seawater desalination which does not deplete local water resources.

Off-site water consumption includes contributions for building the heliostat field and tower, the thermochemical reactors, and the Fischer-Tropsch conversion unit. In case of the heliostat field and tower, also construction, dismantling, and disposal are taken into account. However, compared to the other life cycle phases of manufacturing of the materials and operation of the plant, these phases only have a very small influence on the result [172], and are subsequently neglected for the Fischer-Tropsch facility and the thermochemical reactors.

On-site consumption includes contributions from cleaning the mirrors, from the thermochemical splitting of water, and from the provision of CSP electricity. In the following, the contributions to on- and off-site water consumption are explained in more detail.

Heliostat field

Fresh water is consumed for heliostat manufacturing, construction, dismantling and disposal, as well as for the provision of the basic materials, i.e. steel, concrete, and glass. Data are taken

from a recent life cycle assessment of CSP power plants [172], where the authors give detailed information about the water consumption in the different phases of the power plant and for the manufacturing phase of the heliostat field and tower. Assuming that the relative shares of water consumption in the single phases (manufacturing, construction, O&M, dismantling, and disposal) of the solar concentration facility are identical to the ones of the overall CSP plant, water consumption of the CSP heliostat field and tower during their manufacture, construction, dismantling, and disposal is derived. For construction, a value of $0.22 \text{ L}_{\text{H}_2\text{O}} \text{ kWh}_{\text{el}}^{-1}$ for the heliostat field and of $0.029 \text{ L}_{\text{H}_2\text{O}} \text{ kWh}_{\text{el}}^{-1}$ for the tower is indicated. With the data given for annual output of the plant, its heliostat aperture size, and its lifetime, these values are converted to the basis of unit area of heliostat reflective area. The values are then $380 \text{ L}_{\text{H}_2\text{O}} \text{ m}^{-2}$ for the solar tower and $2850 \text{ L}_{\text{H}_2\text{O}} \text{ m}^{-2}$ for the heliostat field. For the calculation of the water consumption of the heliostat field and tower of the solar fuel production plant, these values are multiplied with the aperture area of the heliostat field of $6.53 \times 10^6 \text{ m}^2$. The water consumption is then $1.86 \times 10^{10} \text{ L}_{\text{H}_2\text{O}}$ for the overall heliostat field ($7.10 \text{ L}_{\text{H}_2\text{O}} \text{ L}^{-1}$ jet fuel) and $2.49 \times 10^9 \text{ L}_{\text{H}_2\text{O}}$ for the solar towers ($0.95 \text{ L}_{\text{H}_2\text{O}} \text{ L}^{-1}$ jet fuel).

Thermochemical reactors

The materials used for the thermochemical reactors are steel, alumina, ceria, and glass, with the respective amounts of $1.05 \times 10^7 \text{ kg}$, $3.49 \times 10^6 \text{ kg}$, $6.98 \times 10^6 \text{ kg}$, and $2.09 \times 10^6 \text{ kg}$ given in Section 4.4.5. The water consumption for the production of steel is 10.85 kg per kg and of glass 13.81 kg per kg [178]. Production of one kilogram of ceria requires 11830 kg of water [183]. For the production of alumina, the value of 2.3 kg per kg for the largest production plant in the world given by the manufacturer is used [198]. The water consumption is then derived by multiplication of the material requirements with the respective specific water consumption. In descending order and with respect to the production of one liter of jet fuel, the individual contributions are then ceria with $3.15 \times 10^1 \text{ L}_{\text{H}_2\text{O}} \text{ L}^{-1}$, steel with $4.34 \times 10^{-2} \text{ L}_{\text{H}_2\text{O}} \text{ L}^{-1}$, glass with $1.10 \times 10^{-2} \text{ L}_{\text{H}_2\text{O}} \text{ L}^{-1}$, and alumina with $3.07 \times 10^{-3} \text{ L}_{\text{H}_2\text{O}} \text{ L}^{-1}$.

Fischer-Tropsch conversion

For the construction of the Fischer-Tropsch conversion facility, the material requirements were estimated with linear scaling of the requirements of the Pearl GtL plant in Qatar. For the fuel production plant with a capacity of 1000 bpd of jet fuel and 865 bpd of naphtha, 1.07×10^6 kg of steel and 6.39×10^6 kg of concrete are required. Using the specific water consumption for the production of steel from the previous section and of 0.25 kg kg^{-1} for concrete [178], a specific water consumption for the Fischer-Tropsch conversion facility of $4.42 \times 10^{-3} \text{ L}_{\text{H}_2\text{O}} \text{ L}^{-1}$ of jet fuel for steel and $6.15 \times 10^{-4} \text{ L}_{\text{H}_2\text{O}} \text{ L}^{-1}$ of jet fuel for concrete are derived. The water consumption for the construction of the FT facility is thus negligible.

Heliostat cleaning

Water is required for the cleaning of the mirror surface in order to remove dirt and to maintain the mirror reflectivity which has an important influence on both the technical and the economic performance of the plant. In [172], a water consumption for mirror cleaning of $58.1 \text{ L}_{\text{H}_2\text{O}} \text{ m}^{-2} \text{ a}^{-1}$ is estimated. Using this value for the fuel production plant, $6.54 \text{ L}_{\text{H}_2\text{O}}$ per functional unit or $3.62 \text{ L}_{\text{H}_2\text{O}} \text{ L}^{-1}$ jet fuel are required.

Thermochemical conversion

For the production of syngas, 280.99 mol or 5.06 liters of water are required. This value is reduced to 2.99 liters when the water from the Fischer-Tropsch conversion is used. This corresponds to $1.66 \text{ L}_{\text{H}_2\text{O}} \text{ L}^{-1}$ of jet fuel produced.

Electricity

For the operation of the fuel production plant, the use of CSP electricity is assumed. In analyses of water consumption of CSP electricity, oftentimes only the contributions from the operational phase of the plant are taken into account. However, as is shown in [172], the operational on-site water consumption may take on very low values for dry-cooled plants, which is supported by values found in the literature, e.g. $0.11 \text{ L}_{\text{H}_2\text{O}} \text{ kWh}_{\text{el}}^{-1}$ for the Ivanpah plant in the United States [173]. On the other hand, water consumed for the construction of

the CSP plant including the provision of the materials may have an additional influence. Taking into account these additional factors, a value of $0.77 \text{ L}_{\text{H}_2\text{O}} \text{ kWh}_{\text{el}}^{-1}$ is assumed [172]. At an electrical energy requirement of $11.4 \text{ kWh}_{\text{el}}$ for the production of one functional unit (1 L jet fuel and 0.87 L naphtha), $2.14 \text{ L}_{\text{H}_2\text{O}} \text{ L}^{-1}$ of jet fuel are required on-site and $2.70 \text{ L}_{\text{H}_2\text{O}} \text{ L}^{-1}$ for the construction of the CSP facility.

Overall water consumption

On-site

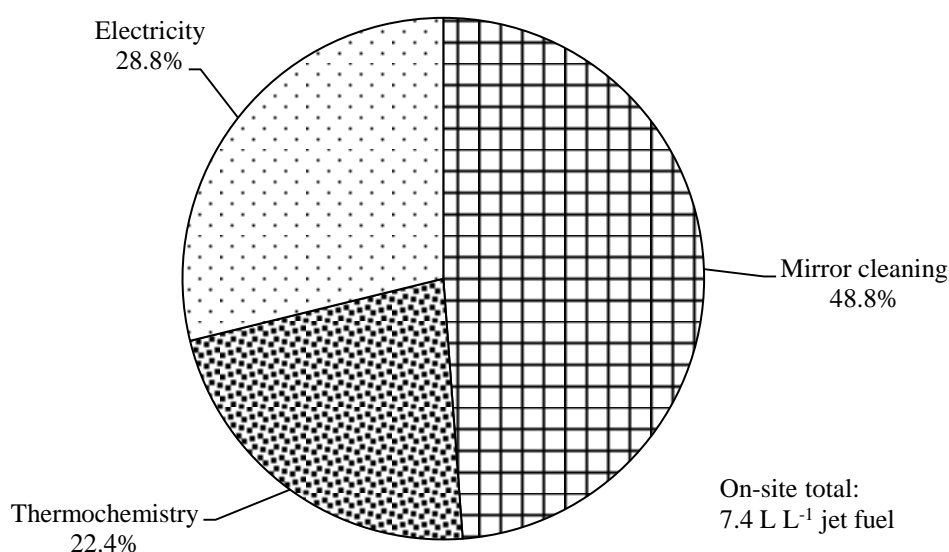
The overall on-site water requirement is 13.4 liter per functional unit (1 L of jet fuel and 0.87 L of naphtha), which corresponds to $7.4 \text{ L}_{\text{H}_2\text{O}} \text{ L}^{-1}$ of jet fuel, or $6.9 \text{ L}_{\text{H}_2\text{O}} \text{ L}^{-1}$ of naphtha.

The contributions to the overall on-site water consumption are shown in Table 4.2 and Figure 4.5. It is composed of the sum of the water requirements for thermochemistry ($2.99 \text{ L functional unit}^{-1}$), mirror cleaning ($6.54 \text{ L functional unit}^{-1}$), and electricity provision ($3.86 \text{ L functional unit}^{-1}$). The corresponding shares are 48.8% for mirror cleaning, 28.8% for CSP electricity, and 22.4% for thermochemistry.

Most of the water for on-site operation is thus required for the cleaning of the heliostat surfaces which could in theory be recycled by a cleaning process to reduce the required amount of water. The provision of CSP electricity causes about one quarter of the on-site water consumption due to water required for the collector system and heliostat washing of the CSP facility. Of the water used for CSP electricity, 44% are used for washing the mirrors of the CSP plant [172], increasing the total share of mirror cleaning from 48.8% to 61.5%. However, to clearly mark the water used for the generation of CSP electricity, the shares are separated. Thermochemistry only accounts for less than a quarter of the on-site water consumption.

Table 4.2 Overall on-site water consumption of the fuel production plant.

	L L ⁻¹ jet fuel	L L ⁻¹ Naphtha	L per functional unit
Mirror cleaning	3.62	3.37	6.54
Thermochemistry	1.66	1.54	2.99
Electricity	2.14	1.99	3.86
Total	7.41	6.90	13.39

**Figure 4.5** Contributions to overall on-site water consumption in the baseline case of the solar thermochemical fuel production plant.

Off-site

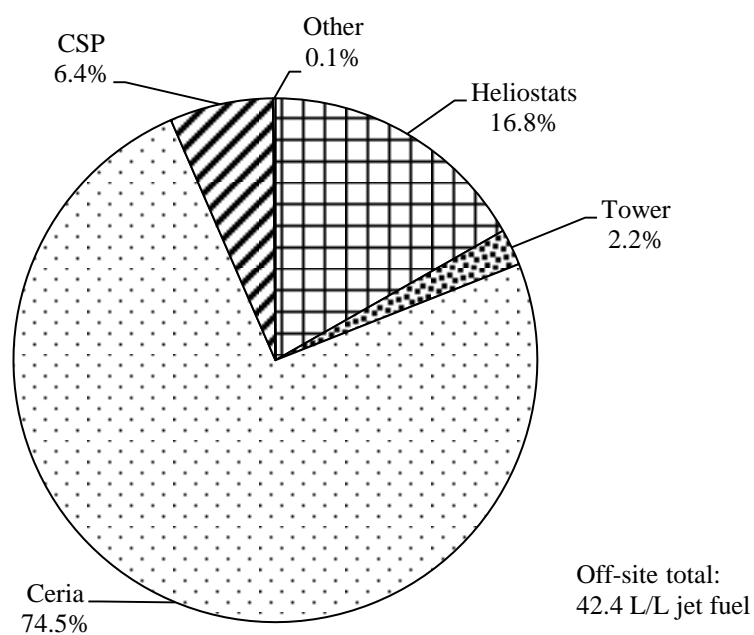
The overall off-site water consumption is 76.5 L per functional unit, 42.4 L L⁻¹ of jet fuel, or 39.4 L L⁻¹ of naphtha and is shown in Table 4.3 and Figure 4.6.

It is composed of the sum of the water requirements for construction and decommissioning of heliostats (7.10 L L⁻¹ of jet fuel) and of the tower (0.95 L L⁻¹ of jet fuel), for the provision of materials for the thermochemical reactors (31.6 L L⁻¹ of jet fuel), for the materials of the CSP facility (2.70 L L⁻¹ of jet fuel), and for the materials of the FT conversion unit (0.0050 L L⁻¹ of jet fuel).

The corresponding shares are 74.5% for the provision of ceria, 16.8% for the materials of the heliostats (steel, concrete, glass), 2.2% for the tower, 6.4% for the materials of the CSP plant, and minor contributions for the remaining materials.

Table 4.3 Overall off-site water consumption of the baseline solar fuel production plant.

Solar concentration infrastructure	L L ⁻¹ jet fuel	L L ⁻¹ Naphtha	L per functional unit
Heliostats	7.10	6.61	12.83
Tower	0.95	0.89	1.72
Thermochemistry			
Ceria	31.5	29.4	56.9
Alumina	0.0031	0.0029	0.0055
Steel	0.043	0.040	0.078
Glass	0.011	0.010	0.020
CSP infrastructure	2.70	2.52	4.88
Fischer-Tropsch infrastructure			
Steel	0.0044	0.0041	0.0080
Concrete	0.00062	0.00057	0.0011
Total	42.4	39.4	76.5

**Figure 4.6** Contributions to overall off-site water consumption of baseline solar fuel production plant.

Total water consumption

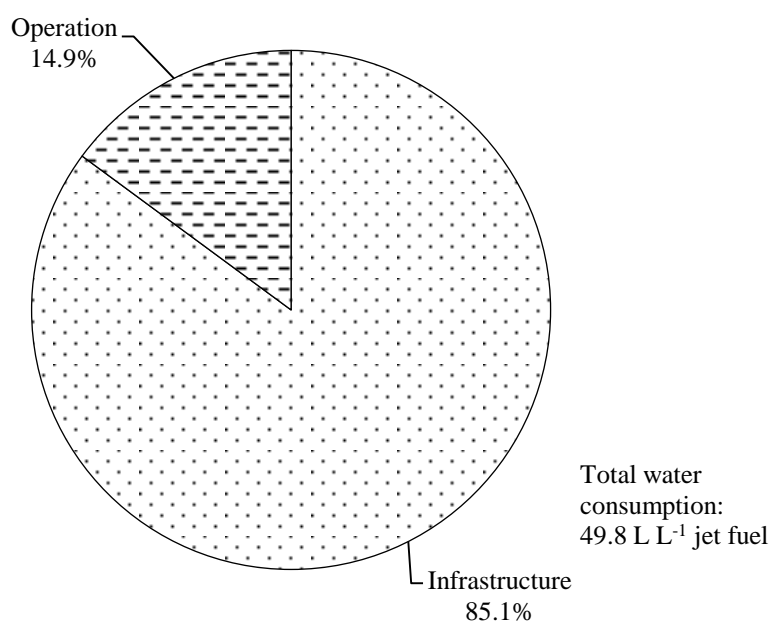


Figure 4.7 Distribution of on-site and off-site water consumption for baseline solar fuel production plant. On-site water consumption is dominated by mirror cleaning, off-site water consumption is dominated by ceria mining.

The total water consumption is then the sum of the on-site and off-site consumption and has a value of 89.9 L functional unit⁻¹, or 49.8 L L⁻¹ jet fuel or 46.3 L L⁻¹ naphtha. It is thus comprised of 85% off-site consumption and 15% on-site consumption.

Most of the water resources are used for the mining of the rare earth metal ceria which today takes place in mines mostly located in China. If a large-scale production of solar thermochemical fuels based on redox reactions of ceria were to be implemented it is conceivable that other locations for rare earth mines would be established and the production would thus be distributed over several countries. As the thermochemical technology develops, other materials may be used instead of ceria since in fact millions of material combinations are possible using e.g. perovskites.

Only 3.3% of the total water consumption (22.4% of on-site consumption) is used for the production of hydrogen in the thermochemical reactors and therefore for the production of the fuel.

Comparison with other fuel pathways

In order to assess the water footprint of the solar thermochemical fuel pathway, the results are compared with those of other fuel pathways. From the general method of water footprint assessment after [197], a distinction between blue, green, and grey water consumption is made for biofuels: *Blue water* is defined as surface and ground water which i) is lost through evapotranspiration, ii) is incorporated into the final product, iii) does not return to the same catchment area, or iv) does not return in the same period. The largest influence is expected from evapotranspiration, the combination of evaporation of water from the soil of biomass irrigation and of transpiration of water from the plants. This definition therefore includes water from ground or surface which is removed and which does not return to the same catchment area in the same period of the analysis [197].

Green water is precipitation from the atmosphere that is stored in the soil or temporarily stays on top of the soil of vegetation and that does not become blue water by running off. It can be partially taken up by plants, where a fraction is always lost through evaporation to the atmosphere. The possible pathways for green water thus include inclusion into the plant, evaporation from the plants or the soil, and transpiration from the plants. The distinction with respect to blue water is important because social and environmental impacts, as well as opportunity costs differ significantly [197].

Grey water is the volume of fresh water that is required to dilute the effluent pollutants of the production process to the naturally occurring levels, i.e. the levels that would exist without human interference into the local ecosystem.

For fuels based on biomass, a distinction between the origins of the fresh water can be made. In order to compare the overall water footprint, the blue, green, and grey water requirements are added.

In the following, the total water requirements of fuel production pathways based on conventional jet fuel production, conversion from oil sands and oil shale, coal-to-liquids, gas-to-liquids, different biofuels, and solar thermochemistry are compared. In Table 4.4 on p. 155, an overview of the water footprints of the chosen fuel pathways is shown. The lowest water footprint is achieved for the fossil-based fuel pathways. In case of conventional jet fuel production, only a small amount of water is required for the recovery of the crude oil from underground and for its refining into the final products. Enhanced oil recovery may increase

the water footprint significantly if water is pressurized to recover a higher share of the crude oil trapped underground. The processing of Canadian oil sands does not require a larger amount of water than conventional fuel production, while the gas- and coal-to-liquid processes may have a somewhat larger impact on the water resources, depending partly on the chosen technologies and in case of the coal-to-liquid process also on the water content of the coal. The biomass-based pathways have a higher water footprint by three orders of magnitude compared to the fossil-based pathways. This is due to the large amount of water which is required to irrigate the feedstock and the water lost through evaporation and transpiration from the plant, while in case of the fossil fuels the feedstock already contains carbon or even hydrocarbons and can more easily be transferred into the final product. Among the biomass-based pathways, biodiesel from biomass has a larger water footprint than ethanol, while biodiesel from micro-algae is in the same overall range as ethanol. For the solar thermochemical fuel pathway, a range of 7-40 liters of water per liter of jet fuel is derived from the calculations in this chapter, where the lower value corresponds only to the water required on-site and the higher value corresponds to the fuel life cycle water footprint including on-site and off-site consumption. For the comparison with the other fuel pathways, the lower value is chosen as commonly only the on-site operational requirements are accounted for.

The solar thermochemical pathway has a similar water footprint compared to the fossil-based options and thus a considerably lower one than the biomass-based options. Even the consideration of the higher value of the solar thermochemical fuel pathway does not change this result. The water footprint is thus slightly higher than the best fossil-based pathways but drastically lower than the biomass-based pathways.

Compared to the competing solar electrochemical pathway based on water electrolysis, reverse water gas shift, and Fischer-Tropsch synthesis, the on-site water footprint is expected to be equal. The reason for this is an efficient hydrocarbon synthesis that does not include biomass-based plant growth with the associated losses of evapotranspiration. Additionally, water is required for cleaning the mirrors or PV modules and potentially for electricity taken from the grid. A more detailed analysis for the solar electrochemical pathway is needed to clarify the water requirements associated with the materials of the electrolyzer.

Table 4.4 Overview of water footprints of different fuel production pathways in liters of water per liters of product (gasoline, jet fuel, ethanol, biodiesel, FT liquids) and converted to the common metric of liters of jet fuel, where the conversion is based on lower heating value equivalents. The calculated water footprint for the solar thermochemical fuel pathway is low compared to biofuel pathways. The lowest footprint is achieved for the fossil fuel pathways because of the low water intensity of the involved process steps.

Fuel pathway	Water footprint [L L ⁻¹]	Water footprint [L L ⁻¹ jet fuel]	Source
Conventional gasoline ^a	1-3	1-3	US DOE [199]
(US conv. crude)	3-7	3-7	Wu et al. [200]
Canadian oil sands (gasoline) ^a	3-6	3-6	Wu et al. [200]
Enhanced oil recovery	2-350	2-350	US DOE [199]
Coal-to-liquid (FT-liquid) ^b	5-7	5-7	US DOE [199]
(jet fuel) ^c	10-60	10-60	Vera-Morales et al. [201]
Gas-to-liquid (jet fuel) ^d	2-7	2-7	Vera-Morales et al. [201]
Ethanol from biomass	≥1000 ^e	≥1582	Dominguez-Faus et al. [202]
	1200-7000 ^f	1899-11075	Mekonnen et al. [203]
	420-4254 ^g	665-6731	Gerbens-Leenes et al. [204]
	1380 ^h	2183	US DOE [199]
Biodiesel	5150-18150 ^f	5274-18586	Mekonnen et al. [203]
	7521-11636 ^g	7702-11916	Gerbens-Leenes et al. [204]
	5625 ^h	5760	US DOE [199]
Biodiesel from micro-algae	591-3650 ⁱ	605-3738	Yang et al. [205]
	1000-9000	1024-9216	Vera-Morales et al. [201]
Solar thermochemical	7-50 ^j	7-50	This study

The LHVs used for the conversion to the common basis of liter of jet fuel are: jet fuel 33.4 MJ L⁻¹ [28], gasoline 32.2 MJ L⁻¹ [206], biodiesel 32.6 MJ L⁻¹ [206], and ethanol 21.1 MJ L⁻¹ [206].

^a Values include exploration, production, and refining, ^b Range of values depends on origin and water content of coal

^c Includes coal mining and washing, coal-to-liquids conversion, ^d Includes only gas-to-liquid conversion process

^e Includes irrigation and evapotranspiration for a range of different feedstock, ^f Global average value which includes green, blue, and grey water for a range of different feedstock, ^g Total-weighted global average value which includes green and blue water for a range of different feedstock, ^h Irrigation water based on a survey of the USDA, ⁱ Value depends on water recycle rate, ^j Lower value includes only on-site consumption; higher value includes also off-site consumption.

4.4.6.3 Land requirement

Land requirement is defined as the total required area of land for the production of a defined amount of jet fuel. This metric can be used to compare different fuel production pathways from unconventional fuel production, biofuels or other alternatives. A smaller land requirement is advantageous, as the environmental and social impact will be reduced. However, also the plant location is very important because a plant construction in a desert region is likely to have a much smaller impact on the environment and the regional population than a construction in areas of large population density and rich flora and fauna. In the metric of land requirement this is not reflected. Also, the quality of the land coverage is decisive: while biological plants are perceived to be a more natural environment, industrial facilities may be seen more critical.

When choosing the system boundaries for different fuel paths in such a way that primary energy, CO₂ and H₂O are utilized for jet fuel production, land requirement is directly related to the system efficiency as the latter describes how well the primary solar energy is converted into the product. For a lower efficiency, more land is required to supply the primary energy for the conversion into the same amount of product. The reference area of the solar thermochemical efficiency is the reflective area of the mirrors. In order to derive the total covered land area of the facility, a land coverage factor has to be defined. In case of concentrated solar tower plants, this factor is around 25% [207], i.e. the total covered land area is four times the reflective area of the mirrors. The area requirement for the solar tower and the fuel conversion plant is neglected since it covers a small area compared to the heliostat field.

The land requirement $A_{\text{total ground}}$ of the solar thermochemical process is thus calculated in the following way

$$A_{\text{total ground}} = \frac{N_{\text{fuel,daily}} \cdot 365 \frac{\text{d}}{\text{a}} \cdot \text{LHV}_{\text{jet fuel}}}{\text{DNI}_{\text{annual}} \cdot \eta_{\text{land coverage}} \cdot \eta_{\text{solar-to-jet fuel}}}. \quad (4.1)$$

In the equations above, $\text{DNI}_{\text{annual}}$ is the annual direct normal insolation per unit area at the plant location, $\eta_{\text{solar-to-jet fuel}}$ is the energy conversion efficiency of solar primary energy to jet fuel¹, $\eta_{\text{land coverage}}$ is the land coverage factor (assumed to be 25%), $N_{\text{fuel,daily}}$ is the daily

¹ $\eta_{\text{solar-to-jet fuel}}$ is equal to 55.4% of the overall energy conversion efficiency from sunlight to 1 L jet fuel and 0.87 L naphtha based on an energy allocation (LHV).

jet fuel production from the plant in liters and $LHV_{\text{jet fuel}}$ is the lower heating value of jet fuel (33.4 MJ L^{-1} [28]). For a facility with a total jet fuel production of 1000 bpd (and 865 bpd naphtha) located in a favorable region with a solar irradiation of $2500 \text{ kWh m}^{-2} \text{ y}^{-1}$ and an efficiency of 5.0% in Section 4.3.2, an area of 31.40 km^2 would be required, i.e. a square with a length of about 5.5 km. The corresponding annual production per hectare is 18480 L jet fuel and 15985 L naphtha, or $1.85 \text{ L of jet fuel m}^{-2} \text{ y}^{-1}$ and $1.60 \text{ L of naphtha m}^{-2} \text{ y}^{-1}$.

The land requirement of the solar thermochemical fuel pathway is compared with other pathways, i.e. the biomass-to-liquid pathway (BtL, gasification of biomass and FT conversion of the syngas), hydrogenated ester and fatty acids (HEFA, hydrogenation of native fat or oil and subsequent refining), and power-to-liquid (PtL, production of hydrogen by water electrolysis, reverse water gas shift and FT conversion). Firstly, the land requirements of several biomass-based pathways are taken from literature. In [208], the productivity of 18 different plants is derived in a rigorous analysis based on high-resolution geometric data. The maximum productivity under ideal circumstances for plant growth is found to be 5812 L of jet fuel-equivalent per hectare and year for oil palms with the HEFA pathway. The BtL pathway with plantation wood achieves a value of $4318 \text{ L ha}^{-1} \text{ y}^{-1}$, the HEFA pathway with the jatropha plant $3001 \text{ L ha}^{-1} \text{ y}^{-1}$, ethanol from corn $2992 \text{ L ha}^{-1} \text{ y}^{-1}$, and ethanol from sugar cane $3653 \text{ L ha}^{-1} \text{ y}^{-1}$. At the lower end of the scale, cotton and HEFA from soy bean achieve productivities of 91 and $699 \text{ L ha}^{-1} \text{ y}^{-1}$, respectively. In the final report of the project BurnFAIR [186], the authors indicate productivities of $510 \text{ L ha}^{-1} \text{ y}^{-1}$ for a HEFA process based on the conversion of the jatropha plant in Mexico, of $2041 \text{ L ha}^{-1} \text{ y}^{-1}$ for a FT-based conversion of woody biomass in Germany, and of $5263 \text{ L ha}^{-1} \text{ y}^{-1}$ for the FT-based conversion of eucalyptus in Brazil. The order of magnitude of these results is in good agreement with the values derived in [208].

In the PtL pathway, liquid hydrocarbon fuels are produced by Fischer-Tropsch conversion of syngas, where the hydrogen in the syngas is derived from water electrolysis and the carbon monoxide from a reverse water gas shift which converts carbon dioxide and hydrogen into carbon monoxide and water. The efficiency of this pathway using solar photovoltaic electricity and including energy penalties for carbon dioxide capture and for the mismatch between the photovoltaic and the electrolysis potential is estimated to be 7.7% in [209]. The efficiency from electrical energy to chemical energy stored in the FT fuels is determined to be 44.6% in [210]. With literature data for the specific land requirements of different electricity generation pathways [211], the area-specific productivity of the power-to-liquid fuel pathway

can be estimated. The specific values of land use are $11 \text{ m}^2 \text{ MWh}_{\text{el}}^{-1} \text{ y}^{-1}$ for a parabolic trough plant in Spain [211] and assumed $6 \text{ m}^2 \text{ MWh}_{\text{el}}^{-1} \text{ y}^{-1}$ at a higher irradiation of $2500 \text{ kWh m}^{-2} \text{ y}^{-1}$ [212], $17 \text{ m}^2 \text{ MWh}_{\text{el}}^{-1} \text{ y}^{-1}$ for a solar tower plant in Spain [211] and $8 \text{ m}^2 \text{ MWh}_{\text{el}}^{-1} \text{ y}^{-1}$ at $2500 \text{ kWh m}^{-2} \text{ y}^{-1}$ (own computations), $56 \text{ m}^2 \text{ MWh}_{\text{el}}^{-1} \text{ y}^{-1}$ for a PV plant in Germany [211], $2.9\text{--}72.1 \text{ m}^2 \text{ MWh}_{\text{el}}^{-1} \text{ y}^{-1}$ for a wind farm (lower value: cleared ground area, higher value: totally affected ground area) [213], and $60 \text{ m}^2 \text{ MWh}_{\text{el}}^{-1} \text{ y}^{-1}$ for coal mining (lignite) in Germany [211]. By multiplication with the electricity-to-fuel efficiency of the PtL pathway derived above and by referencing the result to produced liters per hectare and year, area-specific productivities are derived for comparison with the BtL and the solar thermochemical pathway. The results are shown in Figure 4.8.

The largest area-specific productivities are achieved for the various PtL pathways, with the highest value for electricity generation based on wind power, using only the actually covered land area as a reference. If the totally affected land area is used, the productivity is decreased drastically to the level of biofuels. In [213] it is stated that the directly cleared land area is only about 3-5% of the totally affected area for wind power as the habitat in between the single wind turbines is deteriorated. PtL with parabolic troughs in Spain (grey bar) and under a larger solar irradiation of $2500 \text{ kWh m}^{-2} \text{ y}^{-1}$ (black bar) achieve the second largest productivities. Due to a lower packing density, the PtL productivities using solar towers in Spain (grey bar) and at $2500 \text{ kWh m}^{-2} \text{ y}^{-1}$ (black bar) achieve lower values than the trough systems.

The reason for the high values of the PtL-pathways is the comparably large conversion efficiency of 7.7% from solar primary energy to liquid hydrocarbons, as described in [209], which surpasses the solar thermochemical efficiency of the baseline plant by 50% and the efficiency of the biomass-based processes by up to orders of magnitude. The latter are based on photosynthesis for the conversion of sunlight, water and carbon dioxide into biomass, a process which is limited to a theoretical upper-limit efficiency of about 5% [214]. However, the practical efficiency of photosynthesis is oftentimes considerably lower than this upper-limit value [15,215].

Solar thermochemical fuels in the baseline case have an area-specific productivity of $33.4 \times 10^4 \text{ L}$ of jet fuel-equivalent $\text{ha}^{-1} \text{ y}^{-1}$ and therefore achieve a higher value than some of the power-to-liquid pathways, i.e. those based on electricity from coal combustion, photovoltaics in Germany, and a solar tower in Spain.

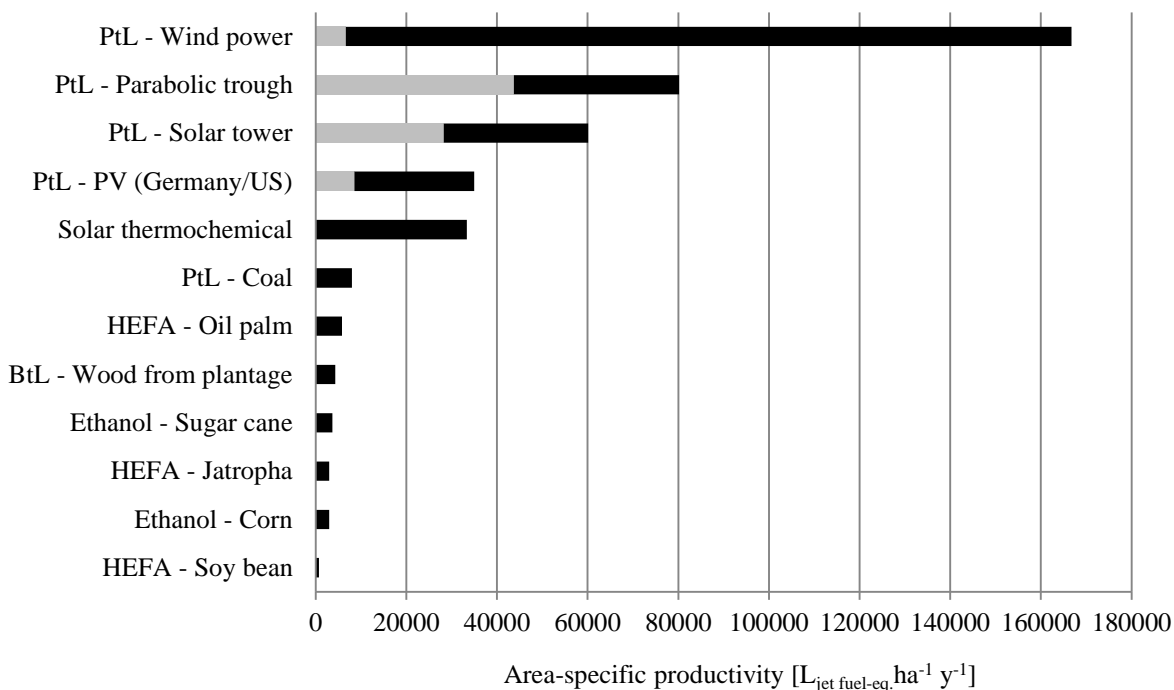


Figure 4.8 Area-specific productivities of the solar thermochemical fuel pathway in comparison with biomass-based pathways (BtL, HEFA, ethanol, sources: [186,208]) and power-to-liquid pathways (PtL, based on different sources of electricity, sources: [209,211–213,216] and own computations). The results are given in liters of jet fuel equivalent per hectare and year, where the conversion is done on an energy basis (LHV). The grey and black bars denote the actually covered land area (black) and the totally affected land area for wind power (grey), plants in Spain (grey) and under a higher solar resource of $2500 \text{ kWh m}^{-2} \text{ y}^{-1}$ (black) for solar trough and tower, and plant locations in Germany (grey) and the US (black) for solar PV. The assumptions are ideal conditions for plant growth of the biomass-based pathways and favorable developments of the thermochemical conversion efficiency and the energy penalty of carbon dioxide capture for the solar thermochemical pathway as described in Section 4.3.1.

The reason for the higher value of solar thermochemistry over the PtL pathway with a solar tower in Spain is the higher solar irradiation of the baseline case plant over the location in Spain. The PtL pathway based on coal combustion has a lower productivity than the solar thermochemical fuel pathway due to a relatively high area demand for coal mining in Germany [211]. All biomass-based fuel pathways achieve lower productivities due to lower energy conversion efficiencies and hence higher area demands.

The solar thermochemical fuel pathway therefore achieves area-specific productivities on the same order of magnitude as electrochemical pathways, where the final values depend on the specific assumptions made, e.g. primary energy source or plant location.

4.5 Assessment of economic performance

Financial planning is a crucial instrument that accompanies any investment decision in the private and public sector. An investment binds capital for possibly long periods of time and therefore limits the room to maneuver of the investor. Depending on the volume of the investment, its revenues and benefits can be important for the further development and oftentimes for the survival of a company, or in the case of a public investor, for the efficient use of taxes. For long project durations, high risks may be involved regarding the development of prices of resources or of competing products. This is the also case for the production of fuels based on the gas-to-liquid technology, where natural gas is converted into liquid hydrocarbons: as the complexity of the involved conversion processes dictates production costs which are higher than those of conventional fuels from large oil fields, a break-even crude oil price exists which represents a threshold for the economics of the gas-to-liquid conversion. Above this threshold, the production of GtL fuels will generate profits, while below, the involved costs are too high so that the production costs exceed the market price of conventional fuels. Another example is the generation of electricity in a natural gas power plant. The electricity generation costs are mainly dependent on the natural gas prices and naturally have to follow resource price fluctuations. When boundary conditions such as the price of alternative electricity generation change the economic foundation of a project can be endangered. This is the case for the natural gas power plant in Irsching in Germany which was extended with two stages of a gas-steam power station in recent years. Following an enlarged supply of renewable power, market prices dropped, making the production costs of the natural gas power plant relatively high. The owners of the plant subsequently decided to put it out of service [217]. This example shows that a large risk can be associated with investments into long-term projects in the energy sector.

Capital budgeting is a key component of the financial decision making process and comprises different instruments. A rather simple instrument is the payback period which indicates the required time until the accumulated revenues equal the investment costs, and which does not take into account the time value of money. It thus gives a rough estimate of how long it will take to regain the initial investment made [218]. Another possibility for assessing the economic viability of a project is the net present value (NPV) analysis which is a discounted cash flow technique. It subtracts the present value of the investment costs from that of the revenues and thus takes into account the time value of money which changes over the

duration of the project. If the NPV is positive, the project will create a benefit and could thus be pursued, while a negative NPV incurs losses. Another related financial assessment instrument is the internal rate of return (IRR) which indicates the interest created by a project at which the NPV is zero. If the IRR is larger than the required rate of return, the project will create a net benefit and could thus be judged positively. Also based on the concept of net present value is the annuity method which expresses the NPV as a constant annualized value over the project lifetime. It can be used for the assessment of economic efficiency and for the comparison of projects with different durations [218,219].

In this work, the annuity method is chosen to derive an estimate of the production costs for one liter of jet fuel from the baseline fuel production plant with a capacity of 1000 barrels per day (bpd) of jet fuel and 865 bpd of naphtha as outlined in Section 4.3. In the following, the method is described in more detail.

4.5.1 Annuity method for estimation of production costs

The annuity method converts a series of distributed cash flows into an equivalent annual value [220]. Firstly, the cash flows are discounted to their present value in the base year. This takes into account the time value of the money which is dependent on the interest rate and the year in which the cash flow occurs. The nominal value of money increases through inflation or through an investment with the interest rate i . 1 € in year n has thus the nominal value $\frac{1}{(1+i)^n}$ in the base year and equally a series of cash flows can be discounted to the base year with

$$PV = \sum_{j=1}^n \frac{C_j}{(1+i)^j}, \quad (4.1)$$

where PV is the present value of the accumulated cash flows over n years, C_j is the cash flow in year j and i is the interest rate. If the yearly cash flows are constant ($C_j = \text{const.}$),

$$PV = C_j \times \sum_{j=1}^n \frac{1}{(1+i)^j} = C_j \times \frac{1 - (1+i)^{-n}}{i} = C_j \times A, \quad (4.2)$$

where $A = \frac{1 - (1+i)^{-n}}{i}$ is the annuity factor.

Assuming equal annual amounts of O&M costs $C_{O\&M}$, their present value is

$$PV_{O\&M} = C_{O\&M} \times A. \quad (4.3)$$

As inflation increases the nominal amount of $C_{O\&M}$, the annuity factor has to be calculated with a nominal interest rate which also takes inflation into account. Alternatively, constant annual O&M-costs can be assumed and the annuity factor is calculated with a real interest rate.

The next step is the calculation of the total life cycle costs (TLCC) which are the accumulated costs over the lifetime of the fuel production plant discounted to their present value in the base year [220]. The TLCC are comprised of the initial investment costs I which are assumed to be due in the base year, and the present value both of the depreciation PV_{DEP} and of the O&M costs $PV_{O\&M}$. The depreciation can be subtracted from the taxable income and has thus a negative value. O&M costs are paid before taxes and are thus multiplied with $(1 - T)$, where T is the tax rate. Division by $(1 - T)$ delivers the required revenue before taxes.

$$TLCC = \frac{I - (T \times PV_{DEP}) + (1 - T)PV_{O\&M}}{1 - T} \quad (4.4)$$

Division of the TLCC by the annuity factor gives the annualized value of the total costs over the whole project lifetime [220]. The production costs per unit of fuel are then derived by further division by the annual amount of produced fuel Q .

$$PC = \frac{TLCC}{Q \times A} \quad (4.5)$$

This formula is valid for the production of a single product. If by-products are produced at the same time, their value has to be taken into account. If the selling price of the by-product is known, this can be done by subtracting the revenue of their sale from the TLCC. In the present case, however, the selling price of naphtha is likely to be subject to considerable change over the project duration. The assumption of a fixed price, even with the inclusion of inflation, may lead to erroneous results. An alternative calculation is therefore chosen here, where a fixed relation between the production costs of jet fuel and the selling price of naphtha is assumed. For products derived from crude oil, such a fixed relation exists, as can be seen in Figure 4.9. The market prices of jet fuel and naphtha are correlated with the market price of crude oil, which is expected as they are both derived from crude oil through refining processes.

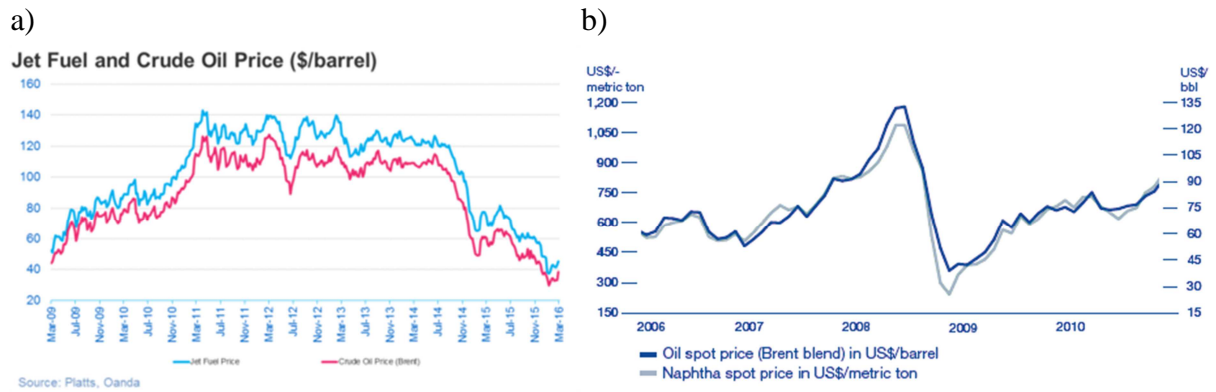


Figure 4.9 Development of market prices of crude oil and a) jet fuel [221] and b) naphtha [222] in recent years. Prices of both jet fuel and naphtha are correlated with the crude oil price, as they are derived from it through refining processes.

It is therefore assumed here that naphtha can be sold at a price that is directly linked to the calculated production costs of solar thermochemical jet fuel. As a reference, the market prices on 13 February 2015 of $621.4 \text{ \$ t}^{-1}$ of jet fuel [223] and of $500.8 \text{ \$ t}^{-1}$ [222] of naphtha are taken. Naphtha then achieves revenue based on 80.6% of the calculated jet fuel production costs. For the calculations, this is equal to an additional production of jet fuel, corresponding to 80.6% of the amount of produced naphtha. In Equation (4.5), Q is therefore comprised of the fuel production of jet fuel and naphtha.

Equation (4.4) is written including depreciation of the initial investment and taxes which are applicable for financing by a private company or a company in the utility sector. If the project is financed by the public, e.g. by the government with tax money, it can be assumed that no taxes have to be paid and Equation (4.4) is simplified to

$$\text{TLCC} = I + \text{PV}_{\text{O\&M}}. \quad (4.6)$$

For the calculation of jet fuel production costs, it is therefore required to derive investment and operation and maintenance costs, and to indicate further boundary conditions of the project such as lifetime, interest rates, tax rates, etc. In the following, first the boundary conditions of the baseline case are defined.

4.5.2 Boundary conditions for baseline case

For the calculation of the baseline case of a publicly owned fuel production plant with a capacity of 1000 bpd jet fuel and 865 bpd naphtha at a location with a solar irradiation of $2500 \text{ kWh m}^{-2} \text{ a}^{-1}$, the following boundary conditions with respect to the economic assessment

are defined. Oxygen, as another by-product from the production process, is not assumed to be sold in the baseline case but its economic value is analyzed in Section 4.6.7.

The interest rate reflects the desired rate of return of the investor and is related to the involved risks of the investment and the possibilities of earning money with competing projects. The rate can therefore either be assumed to be the cost of capital, the desired rate of return including profits, or opportunity costs. For the case of a publicly owned fuel production plant, no profit has to be created and existing risks do not have to be monetized in the same way as for a private investor. The nominal interest rate is accordingly set to 6% for the baseline case which is also assumed for solar thermochemical hydrogen production in [102] and which is higher than the value indicated for public projects in [220]. For private ownership, profits and possibly a different evaluation of the risks involved will lead to a higher cost of capital and thus to a higher interest rate. Private ownership is the topic of Section 4.6.1. In the baseline case, a publicly owned production plant is analyzed.

A plant lifetime of 25 years is assumed which is in the range of commonly assumed lifetimes for solar power plants in the concentrating solar power sector and heliostat production [23,102,172,220,224,225]. With the interest rate and the lifetime defined, the annuity factor can be derived from Equation (4.2). A higher interest rate and a shorter lifetime of the project will decrease the annuity factor, while a lower interest rate and a longer lifetime will increase the annuity factor. In general, a smaller annuity factor will lead to higher production costs at otherwise constant conditions. The annuity factor can be calculated either with a nominal or a real interest rate. Here, the nominal interest rate is chosen to indicate the final result in current currency, taking into account an annual inflation of 2% over the project lifetime.

In the baseline case, the publicly owned facility is assumed exempt from taxes and therefore depreciation and the tax rate are not discussed here but are deferred to Section 4.6.1. All costs during the plant lifetime, as well as the revenues, are assumed to be subject to an annual inflation rate of 2%.

4.5.3 Investment costs

The investment costs are associated with the construction of the fuel production facility. This comprises the heliostat field and the tower for the concentration of solar energy, the thermochemical reactors for the conversion of H₂O and CO₂ into syngas, syngas compressors, the initial stock of inert gas, the Fischer-Tropsch unit for the conversion of syngas into

hydrocarbons, and the required buildings. The costs are taken from estimates of existing facilities, where applicable, or from the literature and are indicated in the following. In general, the investment costs of a component include all costs that occur until the component is ready to use, such as transport of the material to the plant site, engineering services, and construction works. The investment costs for the water desalination plant and the carbon dioxide air capture unit are included in the assumed unit price of the feedstock, i.e. one liter of water and one kilogram of carbon dioxide. In case of water desalination, there exist accurate economic analyses of existing facilities which provides a secure data basis. In case of carbon dioxide air capture, no commercial facilities exist so far, making a reliable cost estimate based on investment costs into the infrastructure and operation and maintenance costs very difficult and quite possibly erroneous. Due to this reason, further modeling of the economics of carbon dioxide air capture is not pursued but unit costs of product are assumed.

Heliostat field and tower

With several operating CSP plants around the world, solar concentration with a field of heliostats and a central tower receiver has reached commercial maturity. However, the size of the heliostats diverges between the single plants, which indicates that the optimal size may yet to be found. There exist several analyses in the literature about the current and future cost of the solar concentration system, that estimate the current investment costs of heliostats to be in the range of 110-165 €₂₀₁₄ m⁻² [190,192,226–229] and the future costs in the range of 60-100 €₂₀₁₄ m⁻² [190,192,227–229]. The costs are converted to euros in the year 2014 [230,231]. As the commercial introduction of the proposed solar fuel production plant requires further research and development, future cost estimates of the heliostat investment costs are applicable and a value of 100 €₂₀₁₅ m⁻² is assumed for the calculations. At a total required heliostat reflective area of 6.5 million m², the investment costs for the heliostat field are 653.4 million €.

The tower investment costs are taken to be 20 € kW_{th}⁻¹ after [226], where two studies for CSP plants with tower costs of 25-27 \$₂₀₁₀ m⁻² are cited. Assuming solar irradiation with a power of 1 kW m⁻² and a solar concentration efficiency of 51.6% [50], the tower costs are 10.33 € per m² of heliostat reflective area. The relative costs between heliostat field and tower compare well with those indicated for a CSP plant in [50]. The investment costs for the solar tower of the baseline case are thus 67.5 million €.

Thermochemical reactors

As there is no commercial implementation of a redox cycle for solar thermochemical syngas production today, an economic study of solar thermochemical methanol production is used for the estimation of the investment costs of the thermochemical reactors. In [23], an array of solar dishes equipped with reactors for the thermochemical splitting of carbon dioxide and water into syngas for methanol production is investigated. The thermochemical reactors are therefore similar to the ones required for the production of solar jet fuel. The authors assume either ferrites or ceria as the reactive material in the reactors. Their estimate of 2313 \$₂₀₁₀ per unit includes the reactor walls, insulation, window, reactive material and piping for a 88 m² dish reflector. For the purpose of this investigation, the reactive material costs are subtracted from this value and added separately to study their influence on the production costs. As however, in the baseline case of the present analysis, a tower concentrator is used, the receiver size is larger than for a solar dish. It is therefore likely that the unit size of the reactors is also larger than the one assumed in [23]. Larger receivers have a more favorable volume-to-surface ratio and are thus likely to have decreased specific costs. As however, a priori, the exact size of the reactors is not known, it is assumed here that the costs remain the same as for the dish sized reactors per unit of concentrated solar power input. The cost of the reactor without the reactive material is thus 17.98 €₂₀₁₅ kW_{th}⁻¹.

For the baseline plant size of 1000 bpd of jet fuel, 3.4 GW_{th} of average solar thermal input power to the reactors are needed for the tower concentrator. The investment costs for the reactors excluding the reactive material are thus 60.7 million €.

The redox material ceria has undergone significant price fluctuations in the past years. At the end of February 2015, the price of ceria dropped below 4 € kg⁻¹ [232] and is assumed to be purchased at 5 € kg⁻¹ here. This estimate is therefore slightly above the current market price but also well below the price peak of the recent years which saw more than a tenfold increase in prices. The development of the market price is inherently difficult to predict as it has been crucially dependent on strategic decisions of the largest supplier China. The increase of the market share of other suppliers or the entry into the market of new suppliers may stabilize the market supply of ceria in the future. The risk of price fluctuations should be taken into account if a large supply of ceria is required for a commercial fuel production plant. The required amount of ceria for the baseline case is 6982 t at an average nonstoichiometry of 0.1 per cycle and 16 cycles per day. As the material is not consumed in the redox reactions, it can be used for many cycles which has already been shown in experiments [10,15,86]. Material

refurbishment due to degradation is required, however, where the associated costs are assumed not to be critical and are neglected here. The investment costs of the reactive material ceria are thus 34.9 million €.

Fischer-Tropsch conversion

The costs of the FT unit depend on the chosen reactor technology, as temperature levels, catalyst materials, and cooling systems differ significantly. For the present aim of producing long-chained hydrocarbons that can be hydrocracked to the desired length in the jet fuel and naphtha range, a low-temperature FT unit operating with a cobalt catalyst is applicable. Another crucial aspect of the FT economics is the plant capacity, where in general, a larger output reduces the specific investment costs. The plant size of 1865 bpd of liquid FT product is at the lower end of the economic scale [233,234], as traditional gas-to-liquid plants operate in the region above 30000 bpd [234]. However, there are emerging smaller-scale units for the conversion of bio-derived syngas and projects to make use of otherwise flared gas from refining processes. Here, investment costs of 23000 € bpd⁻¹ of liquid product are indicated by a manufacturer of small-scale FT units and are assumed for the analysis [233]. This cost includes only the conversion of clean syngas to liquid hydrocarbons. The provision of the syngas is covered by the other up-stream process steps. At the plant output of 1865 bpd of liquid product (1000 bpd jet fuel and 865 bpd naphtha), the investment costs for the FT unit are 42.9 million €.

Other components

Other components taken into account in the investment costs are two syngas compressors to increase the pressure of the gas stream coming from the thermochemical reactors of 1 bar to the 30 bar operating pressure of the FT unit. Each centrifugal compressor has a power of 4.10 MW and a pressure rating of 69×10^5 Pa at a unit cost of 1.54 million € [235].

The combined heat and power plant (CHP) is assumed to work with a gas turbine and to have specific investment costs of 1048.83 € kW_{el}⁻¹ [236]. For the chosen size of the fuel production plant, 0.15 kg of light hydrocarbons are combusted in the CHP plant for every functional unit (one liter of jet fuel and 0.87 liters of naphtha) produced. The composition of the light

hydrocarbon fraction is assumed to follow the Anderson-Schulz-Flory distribution with a growth factor of 0.9. The gases then have a higher heating value of 7.74 MJ and the electrical and thermal energy output of the CHP plant is 2.17 MJ and 3.10 MJ per functional unit, respectively. The investment costs of the CHP plant are 4.18 million €.

Buildings for the plant are taken into account at a price of 600 € m⁻² [102]. The required area is taken from an analysis for a solar thermochemical hydrogen production facility in [102], where 1900 m² were assigned for the plant output of 4150 t y⁻¹. For the production of 1865 bpd of liquid FT products, 32616 tons of hydrogen and 207169 tons of carbon monoxide are produced from the thermochemical reactors per year. Assuming that the required area of the buildings scales with the molar output of the thermochemical reactors, 21715 m² are required, corresponding to investment costs of 13.0 million €.

Investment costs for other components such as piping are assumed to be included in the costs listed above. Parts which are not mentioned are assumed to have only a small influence on the economics of the overall process and are neglected.

Summary of investment costs

Table 4.5 Overview of investment costs of the baseline case plant.

Investment cost item	× 10 ⁶ €	Share
Heliostats	653.4	74.3%
Thermochemical reactors	95.6	10.9%
Solar tower	67.5	7.7%
Fischer-Tropsch	42.9	4.9%
Buildings	13.0	1.5%
CHP	4.18	0.5%
Syngas compressors	3.08	0.4%
Total	879.6	100%

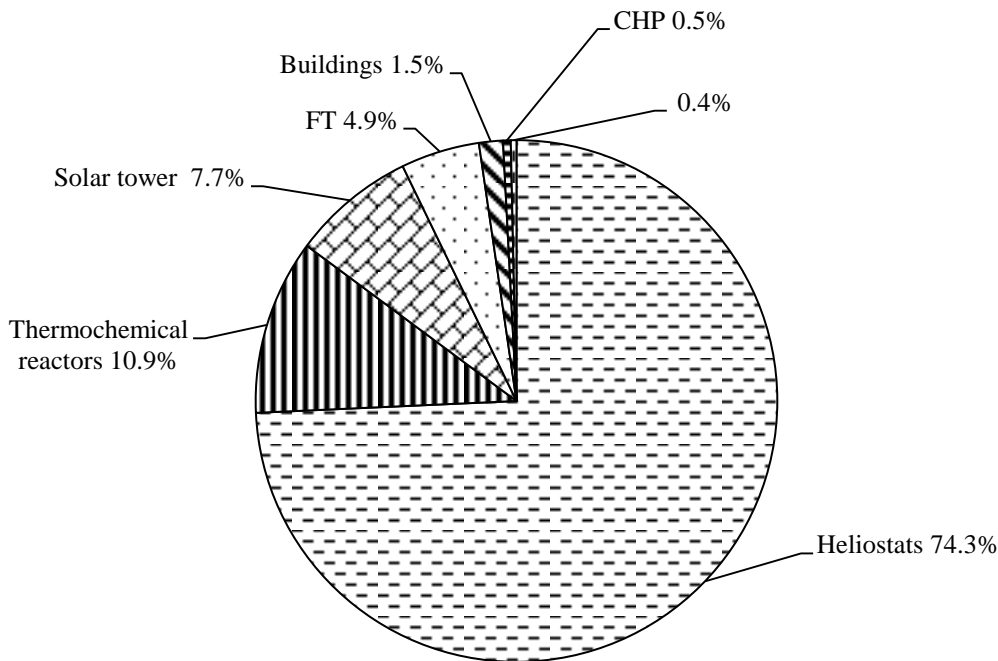


Figure 4.10 Distribution of investment costs of baseline case plant. The investment costs are strongly dominated by the solar concentration infrastructure. The thermochemical reactors including the reactive material have a share of 11%. All other components only have minor contributions. As the overall economics are strongly influenced by the investment costs, solar concentration presents a large cost driver.

The total investment costs of the baseline case are listed in Table 4.5 and have a value of 8.80×10^8 €.

Figure 4.10 shows the distribution of the investment costs. The largest share of 74.3% is due to the heliostat field, 10.9% to the thermochemical reactors including the reactive material, 7.7% to the solar tower, and 4.9% to the Fischer-Tropsch conversion unit. All other components only have minor contributions.

4.5.4 Operation and maintenance costs

In general, operation and maintenance costs can be subdivided into fixed and variable costs, where the former relates to costs that occur independently of the operation of the plant, while the latter is directly related to the amount of plant output. In the following, the operation and maintenance cost components are explained for the individual process steps. In general, the annual O&M costs are assumed to escalate over time with the inflation rate $i = 2\%$ [220].

Water provision

The plant location is chosen 500 km from the sea at an altitude of 500 m. As water is assumed to be desalinated at the sea side and transported via an existing pipeline to the fuel production site, both desalination and transport have to be accounted for. Desalination is assumed to be carried out with a reverse osmosis plant at a specific energy requirement of 3 kWh m^{-3} [34,237]. The energy requirement for the transport of the desalinated water is calculated with [174]. The electric energy needed for water desalination and transport is provided by CSP electricity at the plant site at future specific costs of $0.06 \text{ € kWh}_{\text{el}}^{-1}$ (see also section on O&M costs of electricity). A state-of-the-art unit cost of 0.5 € m^{-3} [237] is assumed, which includes both the investment costs of the plant infrastructure, and fixed and variable O&M costs. The consideration of both electrical energy and unit costs presents a conservative estimate of the costs which may overestimate the actual value. However, to include the investment costs without complex accounting of the desalination plant and to establish a coherent approach of economic and ecological performance analysis, this procedure is chosen. The annual O&M costs are $3.88 \times 10^5 \text{ €}$ for the unit costs and $6.40 \times 10^5 \text{ €}$ for the electricity for desalination and transport.

Carbon dioxide provision

In the baseline case of the fuel production plant, carbon dioxide is provided through capture from the air at the plant site. Similarly to the provision of water, a unit cost that covers investment costs, and fixed and variable O&M costs of 100 € t^{-1} is assumed. For the process of carbon dioxide air capture, heat from solar concentration is used. For the provision of solar heat, additional heliostats are required which increases the investment costs and the O&M costs of the solar field. The energy requirement of the capture process currently is 1500 kWh t^{-1} of mostly low-temperature heat below 100°C and $200 \text{ kWh}_{\text{el}} \text{ t}^{-1}$ of electricity, as shown recently in a demonstration plant [42]. The O&M costs are thus comprised of the unit costs for the capture process and the additional O&M costs of the enlarged solar field and the electricity costs, representing a possibly conservative scenario due to the accounting of unit costs, and heat and electricity costs separately. The annual O&M costs for the baseline plant are then $3.26 \times 10^7 \text{ €}$ for CO_2 unit costs, $2.60 \times 10^6 \text{ €}$ for the O&M costs of the enlarged field, $1.11 \times 10^6 \text{ €}$ for electricity, or $3.63 \times 10^7 \text{ €}$ in total.

Concentration of solar energy

As of today, no commercial implementation of the thermochemical fuel production technology exists. However, the concentration of solar energy with a field of heliostats and a central tower is already used in the concentrated solar power industry for the generation of solar electricity using a Rankine cycle. The estimation of the operation and maintenance costs of the solar concentration step is thus based on analyses of CSP technology. The annual O&M costs of CSP plants today are estimated at about 45 € kW_{el}⁻¹ [226,228] and estimates of the future costs are in the range of 25-50 € kW_{el}⁻¹ [226–228,238]. For the annual O&M costs of the heliostat field and the tower, 7 € kW⁻¹ of primary solar energy is assumed which corresponds to 35 € kW_{el}⁻¹. At a solar irradiation of 1 kW m⁻², this is equal to annual O&M costs of 7 € m⁻². At a heliostat field size of 6.5 million m², the annual O&M costs for solar concentration are 4.57×10^7 €.

Fischer-Tropsch conversion

Operation and maintenance costs of Fischer-Tropsch units have been estimated in the literature with 4-15 € per barrel of liquid product [234,239] or with a relative annual share of 3.5-4.5% of the total capital investment [240–243]. Here, O&M costs of the plant including labor costs but excluding electricity costs are assumed to be 4 € per barrel of liquid product [233], i.e. 6.3% of the total capital investment. However, as a cost factor, the FT unit does not play a major role in the overall plant economics. The annual O&M costs are 2.72×10^6 €.

Mirror renewal

Mirror degradation and failure requires a constant renewal of parts of the heliostat field. The renewal rate depends strongly on the prevailing weather conditions, i.e. the occurrence of sand storms and the size distribution of dust particles in connection with wind speeds. The plant location is chosen in Morocco but not at specified coordinates, so that a more detailed analysis of mirror degradation at the plant site is not pursued here. Instead, an average annual renewal rate of 0.2% per year is assumed [52]. At the total heliostat area of 6.5×10^6 m² and specific investment costs of 100 € m⁻², annual O&M costs for mirror renewal are 1.31×10^6 €.

Provision of electrical energy

In the baseline case, the electrical energy requirements for the plant are provided by a CSP plant on site. Electricity has a unit cost of $0.06 \text{ € kWh}_{\text{el}}^{-1}$, assuming the achievement of the SunShot economic target value for future CSP plants [228]. From the energy and mass balance of the plant, $40.9 \text{ MJ}_{\text{el}}$ are required for the production of one liter of jet fuel and 0.87 liters of naphtha. Annual electricity costs are $3.95 \times 10^7 \text{ €}$.

Fuel transport

The fuels from the production facility are transported via pipeline over a distance of 500 km. Specific transport costs of 25.1 € TJ^{-1} on a lower heating value basis are taken from [178]. For the assumed baseline plant size of 1000 bpd jet fuel, annual transport costs are $5.26 \times 10^4 \text{ €}$.

CHP

The combustion of the light hydrocarbon fraction is assumed to be performed with a combined heat and power plant based on a gas turbine. The annual operation and maintenance costs for such a type of CHP plant have been determined in [236] to be $8.2 \text{ € MWh}_{\text{el}}^{-1}$ of variable costs and $9.84 \text{ € kW}_{\text{el}}^{-1}$ of fixed costs. At the electrical power output of $4.0 \text{ MW}_{\text{el}}$ and an annual generation of $35.0 \text{ GWh}_{\text{el}}$, the annual O&M costs of the CHP plant are $3.26 \times 10^5 \text{ €}$.

Summary of operation and maintenance costs

The O&M costs for all system components are shown in Table 4.6. The relative shares for the O&M costs are shown in Figure 4.11. The operation and maintenance of the heliostat field and tower has the greatest influence, where a large part is due to the labor costs of the personnel and cleaning of the heliostat surfaces. Generation of CSP electricity contributes slightly less than the O&M costs of the solar field. Nevertheless, it is a major cost item.

The unit cost of $0.06 \text{ € kWh}_{\text{el}}^{-1}$ is close to the values for the best plants built today. A reduction of electricity costs may in some cases be possible through the use of fossil based energy, which is going to deteriorate the ecological performance of the plant, however.

Table 4.6 Overview of operation and maintenance costs of the baseline plant.

System component	$\times 10^6$ €	Share
H ₂ O	0.388	0.3%
CO ₂	32.6	26.6%
O&M solar field	45.7	37.3%
Mirror renewal	1.31	1.1%
Fischer-Tropsch	2.72	2.2%
Electricity	39.5	32.2%
Fuel transport	0.0526	<0.1%
CHP	0.326	0.3%
Total	122.6	100%

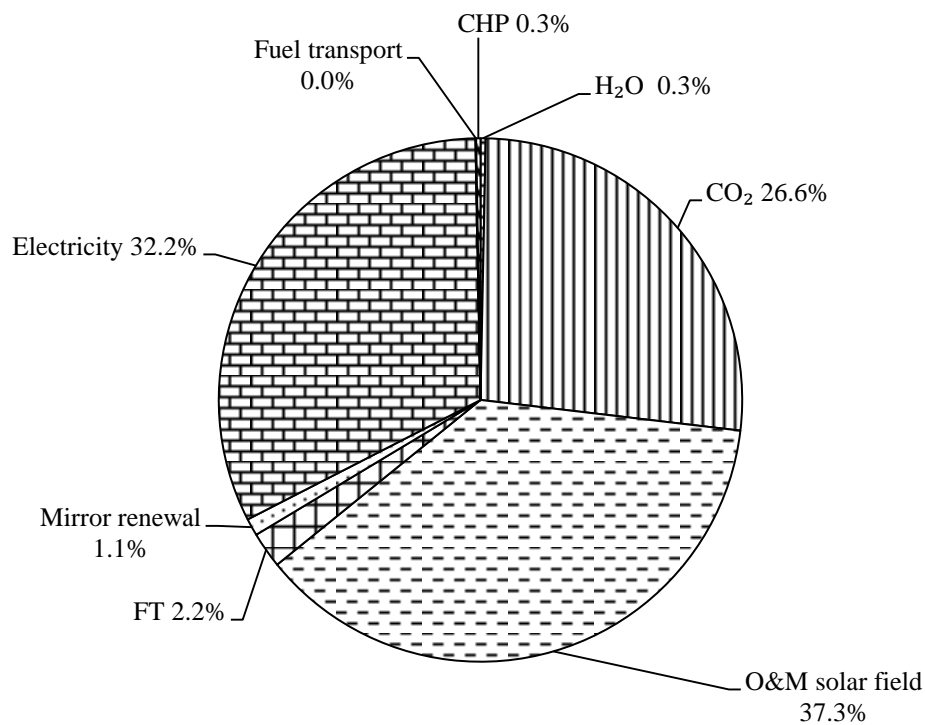


Figure 4.11 Distribution of operation and maintenance costs of baseline plant. The O&M costs are dominated by the solar field, CSP electricity provision, and CO₂ air capture. All other components together contribute less than 4%.

The provision of CO₂ has a slightly smaller share which is based on the assumption of a unit cost of 100 € t⁻¹. This is higher than estimations of unit cost from fossil sources today [35], however, to establish a sustainable process, CO₂ air capture has been assumed. All other contributions are minor.

4.5.5 Results for baseline case

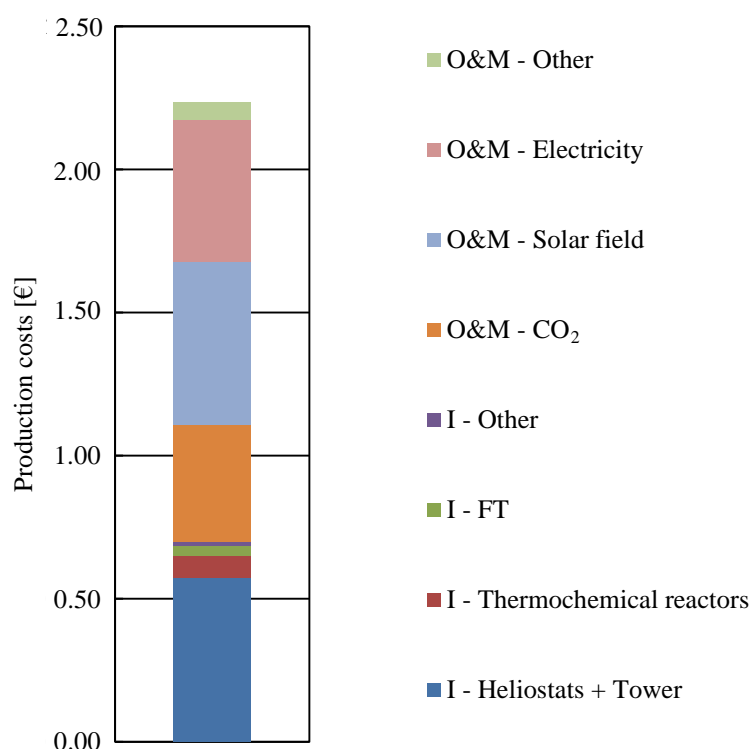


Figure 4.12 Major cost components of solar thermochemical jet fuel production. “I” denotes investment costs and “O&M” operation and maintenance costs.

Production costs for the baseline case of the publicly financed solar jet fuel production plant are derived. For this purpose, investment costs and O&M costs of the previous sections, together with the financial assumptions made, are used in the annuity method described in Section 4.5.1. The production costs are calculated to be 2.23 € L^{-1} of jet fuel. Over the course of the assumed lifetime of the plant, O&M costs contribute about two thirds to the overall production costs and the investment costs about one third. The relative magnitude of the O&M costs and the investment costs depends on the assumptions made about the single cost contributors, the plant lifetime and financing, besides others. As main cost components are identified the solar concentration infrastructure, the costs for CO₂ provision, the O&M costs of the solar field, and the provision of CSP electricity.

4.5.6 Sensitivity analysis

In the following, several parameters are varied by $\pm 10\%$ in a sensitivity analysis to investigate their influence on the production costs of jet fuel.

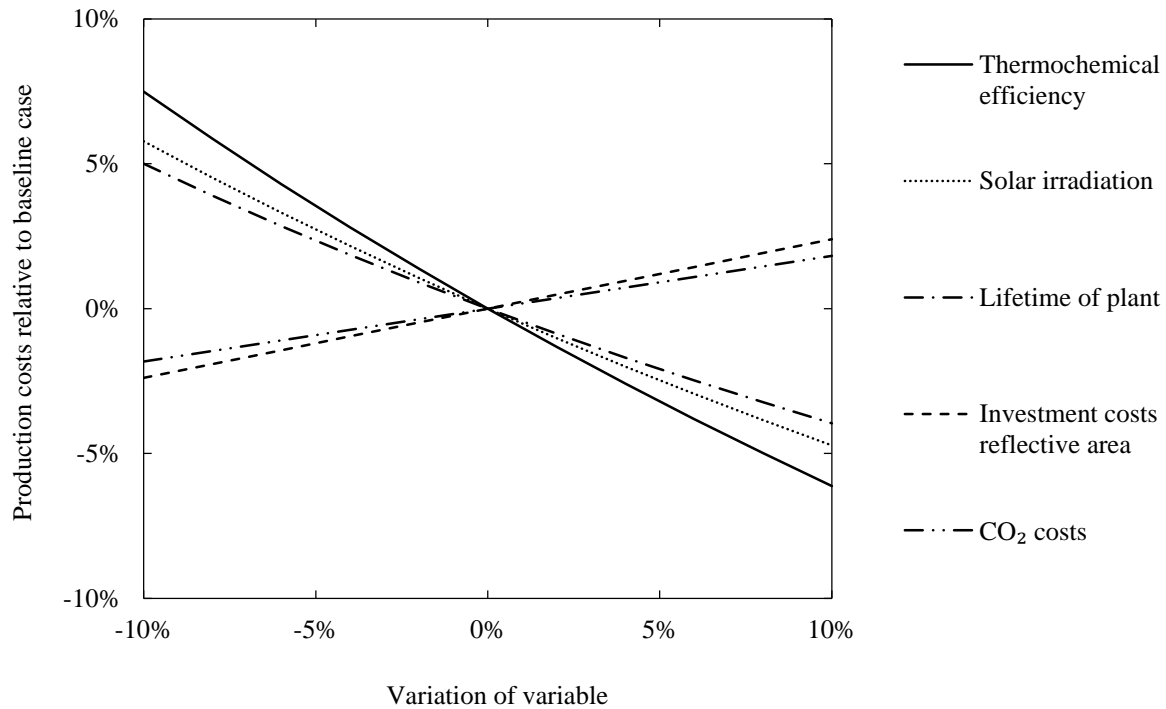


Figure 4.13 Sensitivity of production costs for a variation of $\pm 10\%$ of selected variables.

The selected variables for the economic sensitivity study are level of solar irradiation (annual sum of direct normal irradiation), thermochemical efficiency, lifetime of the plant, specific investment costs of reflective area, and costs of CO₂ provision (Figure 4.13).

An altered plant location which increases the level of solar irradiation by 10% decreases the production costs by 4.7%. Equally, a decrease in solar irradiation by 10% leads to 5.8% higher production costs. These values are not the same because the increase in solar irradiation leads to a smaller heliostat field by 9%, while its decrease requires a larger reflective surface area of 11% to collect the same amount of solar energy. A similar effect is found for the variation of thermochemical efficiency which directly influences the required size of the heliostat field: an increase of efficiency by 10% reduces the production costs by 6.1%, while a similar drop in efficiency leads to an increase of 7.5%. As the concentration of the dilute solar energy requires a large field of mirrors, investment costs for the solar concentration step play a major role. A variation by $\pm 10\%$ of the unit cost of heliostat area

shows a variation in production costs by $\pm 2.4\%$. Note that CSP electricity is not affected by this change since a fixed unit price per kWh_{el} has been assumed. A change in O&M costs for the solar concentration has a similar effect and is not shown in the graph. The 10%-reduction in lifetime of the plant leads to increased costs of 5.0%, while a 10% longer lifetime reduces the costs by 4.0%. The reason for the asymmetry here is the nonlinearity of the annuity factor (see Equation (4.2)). The CO_2 costs have a small influence of $\pm 1.8\%$ on the production costs, while the ceria price has practically no influence and is not shown in the graph. This is partly due to the assumed low price of ceria at the present time, where large price fluctuations were seen recently. These large fluctuations are not analyzed in this sensitivity study. Solar irradiation, thermochemical efficiency, and plant lifetime are found to have the largest impact on plant economics and are thus the main cost drivers of the process.

The sensitivity analysis shows the main drivers for the production costs for a similar relative change in the variables. In case of the price of ceria, large fluctuations of the market price were observed in the past years that surpass the 10% change assumed for the sensitivity analysis. It is therefore interesting to analyze the influence of a large change of ceria provision costs. Assuming a price increase from 5 € kg^{-1} in the baseline case to 50 € kg^{-1} , the production costs would rise from 2.23 € L^{-1} to 2.48 € L^{-1} , or by 11%. As far as reliable data are available on the probability of variable changes, the economic risk can be estimated in more detail.

4.6 Ecological and economic performance of further operation scenarios

In Sections 4.4 and 4.5, the ecological and economic performance of the solar thermochemical fuel pathway was estimated for the baseline case. This inherently required the definition of the plant layout and of system parameters, where a selection of the latter was varied in a sensitivity analysis. More substantial changes to the baseline case are limited to the present section, where different scenarios of the solar thermochemical production plant are analyzed from an economic and an ecological point of view. More specifically, in the first scenario, the plant is financed by a private investor instead of by the public. In the second scenario, the source of CO₂ is a natural gas-fired power plant instead of an air capture unit. In the third scenario, sunlight is concentrated with an array of dish concentrators instead of tower systems. In the fourth scenario, electricity used in the production process is supplied from the local grid instead of a CSP plant. In the fifth scenario, the baseline case is adjusted to describe the Power-to-Liquid fuel production pathway. Finally, a scenario for a substantial reduction of production costs and greenhouse gas emissions with respect to the baseline case is analyzed.

4.6.1 Private financing of production plant

In the analysis of the baseline case, the production plant is assumed to be financed with equity only, as could be the case for a publicly owned facility. In this case of public funding, the financial risk associated to a project is lower than for a private investor which reduces the required rate of return and consequently the cost of capital. On the other hand, a private investor will require a higher rate of return to generate profits which will increase the cost of capital. In the following, financing of the production facilities by a private investor is assumed to analyze the influence on the production costs.

The required investment for the fuel production plant is assumed to be composed of 30% equity with a nominal interest rate of 13.5%, and of 70% debt with a nominal interest rate of 8% [244]. Contrary to a publicly owned facility, a private owner will be subject to taxation with the possibility of deducing the depreciated share of the investment costs. Taxes are

considered with an annual rate of 35% and depreciation with a linear rate over the project lifetime of 25 years. Otherwise identical assumptions as for the publicly financed case are used. For the derivation of production costs, the same approach as in Section 4.5.1 is followed. Equation (4.6) then indicates the total life cycle costs of the privately owned fuel production plant, where the division by $1 - T$ gives the required revenue before tax. The present value $PV_{O\&M}$ of the O&M costs is derived by multiplying the annual value of the O&M costs in constant currency with the annuity factor (Equation (4.1)) based on the real average weighted cost of capital. The weighted average cost of capital (WACC) is derived from the interest rates on equity and debt [220],

$$i = \text{WACC} = \frac{E}{V} \cdot i_E + \frac{D}{V} \cdot i_D \cdot (1 - T), \quad (4.7)$$

where E is the sum of equity capital, D the sum of debt, V the total capital, i_E and i_D the interest rates for equity and debt, respectively, and T the tax rate. The share of interest for debt is reduced through the deducibility from taxes.

A distinction has to be made between real and nominal interest rates: real interest rates do not account for inflation and thus express the interest for constant currency, while the nominal interest rates denote the interest with respect to current currency, i.e. including inflation. For the O&M costs, a fixed annual amount in constant currency of the base year is assumed. Consequently, for the derivation of the present value of O&M costs, the annuity factor is calculated based on the real interest rates. This is equivalent to escalating the yearly O&M costs by the assumed inflation rate and using the nominal interest rates. For the calculation of the present value of depreciation and of the overall costs, on the other hand, the annuity factor based on the nominal interest rates is used.

Apart from the origin of the financing, identical assumptions as in the baseline calculation are used. This comprises the assumption of a fixed market price of the by-product naphtha of 80.6% of the calculated jet fuel production costs which corresponds in theory to an additional production of jet fuel. This assumption is used recognizing the fact that the prices of jet fuel and naphtha are strictly linked to the price of crude oil. The assumption of an overall fixed naphtha price would lead to results that do not take this fact into account. For a more elaborate explanation of this assumption, please refer to Section 4.5.1.

The production costs of jet fuel are calculated to be 2.57 € per liter of jet fuel for a privately owned facility using a solar tower concentrator and CO₂ capture from the air.

Compared to the baseline case value of 2.23 € per liter of jet fuel, this represents a considerable increase of more than 15% which shows that the assumptions about the cost of capital can have a strong influence on the production costs. In the baseline case, a publicly supported facility was used with a nominal average cost of capital of 6.0% compared to the privately owned facility in the current case with a value of 7.7%. As the solar thermochemical fuel production facility requires a large initial investment, the cost of capital has a decisive influence on the production costs. For comparison, in [102] an interest rate of 6% is assumed, in [23,24] a desired rate of return of 8%, and in [3] of 5%.

As this analysis shows, strategies for the reduction of capital costs could contribute significantly to the achievement of competitive jet fuel production costs. These strategies could comprise the support by the public hand through tax exemptions, a guaranteed selling price of the products, or even through direct financing of the production facility. Any of these measures may be adequate to decrease the level of risk that a private investor has to account for by demanding a corresponding rate of return.

4.6.2 CO₂ capture from NGCC plant

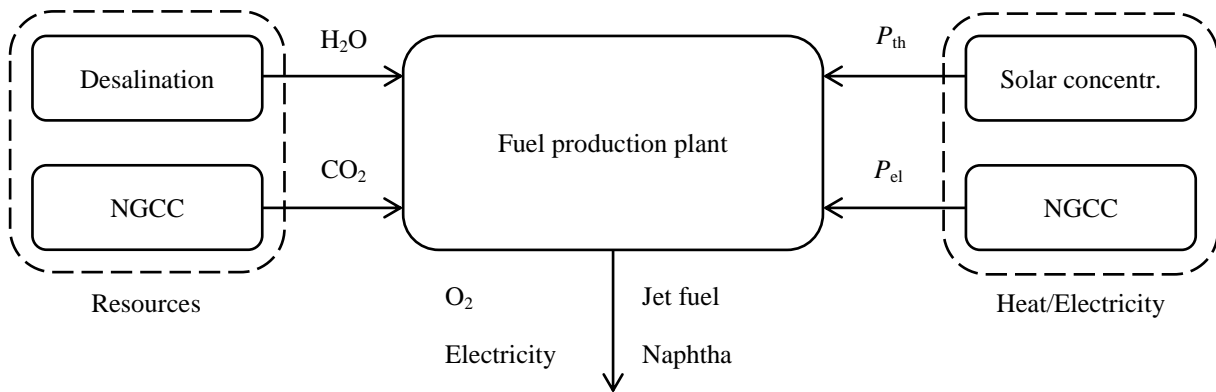


Figure 4.14 Schematic of the provision of resources, heat and electrical power in case of CO₂ capture from a NGCC power plant. CO₂ and electricity are supplied by the NGCC plant. Surplus electricity is fed into the local grid.

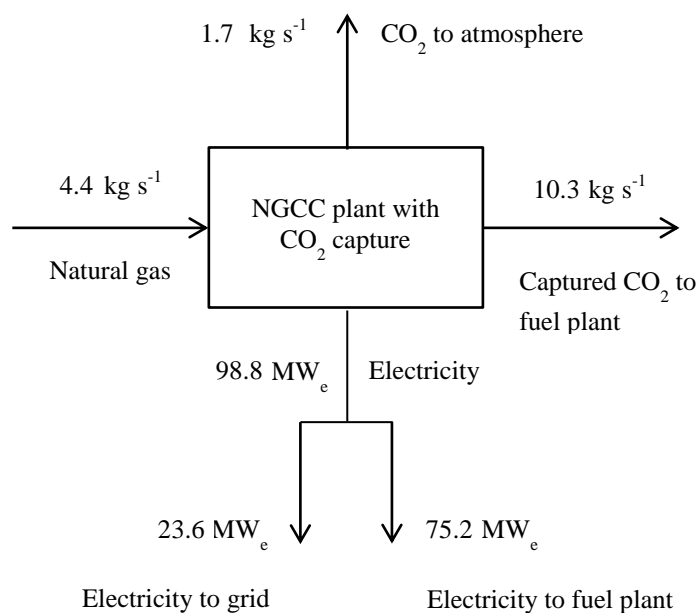


Figure 4.15 Material and energy balance of NGCC plant for the provision of CO₂ and electricity to the solar thermochemical fuel production plant. The NGCC plant is sized to provide exactly the required amount of CO₂ for the production of 1000 bpd of jet fuel and 865 bpd of naphtha. The produced electricity from the plant is used for fuel production and the surplus electricity is sold to the local market.

In the baseline case, carbon dioxide is assumed to be captured from the atmosphere. However, other sources of carbon dioxide are frequently discussed, most prominently the capture from fossil power plants. In order to include this discussion into the analysis of the fuel production plant, in this section, carbon dioxide is assumed to be captured from a natural gas combined cycle power plant (NGCC) located on the site of the fuel production plant, and the influence on the ecologic and economic performance of the fuel production is analyzed (Figure 4.14). The required technology for capture from flue gases in a gas power plant has reached the stage of large-scale technology demonstration, while on a smaller scale, air capture by chemical adsorption is shown, using an ammine-functionalized sorbent [38–40,42].

All of the required carbon dioxide for the production of 1000 bpd of jet fuel and of 865 bpd of naphtha is captured from a modern NGCC plant with a capture efficiency of 86% [245,246]. This means that 14% of the carbon dioxide generated during the combustion of natural gas is released to the atmosphere.

The NGCC plant with the capture unit further has an energy conversion efficiency based on the LHV of natural gas of 48% [245]. The LHV of natural gas is assumed with a typical value of 47.14 MJ kg^{-1} [247]. For the production of the specified amounts of jet fuel and naphtha, 4.37 kg s^{-1} or $3.78 \times 10^5 \text{ kg}$ per day of natural gas are required, 1.68 kg s^{-1} or $1.45 \times 10^5 \text{ kg}$ of

CO₂ per day are emitted from the NGCC plant while 10.3 kg s⁻¹ or 8.92 × 10⁵ kg per day of CO₂ are captured and used for the production of the fuels. The NGCC plant produces 98.8 MW_e of electricity, 75.2 MW_e of which are used for the fuel production plant to cover the electrical energy needs (otherwise satisfied by a CSP plant in the baseline case). 23.6 MW_e are thus sold to the market at a price of 0.072 € kWh_{el}⁻¹ [248] which is the grid electricity price for large consumers in Morocco in 2014. The costs for carbon dioxide storage and distribution are neglected since the capture is assumed to be performed on-site with the fuel production. The material and energy balance for the NGCC plant is shown in Figure 4.15.

For the calculation of the production costs, the costs associated to the NGCC plant are estimated with the specific electricity production cost multiplied with the amount of produced electricity, while additional revenue is created by the sale of electrical energy at the market price. Life cycle emissions are adjusted by the decreased size of the heliostat field with respect to the baseline case (where a CSP plant is used for electricity generation) and the direct emissions from the fossil plant. The total emissions are then allocated to the three products jet fuel, naphtha, and electricity on an energy basis. Under the given assumptions, the production costs are 1.91 € at life cycle emissions of 3.66 kg_{CO₂-eq.} per liter of jet fuel, 3.51 kg_{CO₂-eq.} per liter of naphtha and 0.13 kg_{CO₂-eq.} per kWh_{el} for the electricity sold to the grid. Using an allocation based on the market value of the products does not change the main result of significantly increased emissions of the produced fuels over the baseline case: GHG emissions are 3.84 kg_{CO₂-eq.} per liter of jet fuel, 3.48 kg_{CO₂-eq.} per liter of naphtha and 0.06 kg_{CO₂-eq.} per kWh_{el}.

The use of carbon dioxide and electricity from a NGCC power plant thus reduces the costs of jet fuel production from 2.23 € L⁻¹ to 1.91 € L⁻¹ as the unit cost for carbon dioxide provision is lower compared to air capture. However, it considerably increases the life cycle GHG emissions from 0.49 kg_{CO₂-eq.} L⁻¹ to 3.66 kg_{CO₂-eq.} L⁻¹, where conventional jet fuel has well-to-wake emissions of 3.03 kg_{CO₂-eq.} L⁻¹ [28]. The production of solar thermochemical fuels presents therefore a viable option over conventional fuels only if the carbon dioxide is captured from renewable sources such as the atmosphere and not from flue gases of a fossil power plant. This result is coherent with the analysis in [175] where the authors arrive at the same conclusion for the production of solar electrochemical fuels.

For the results achieved above, a specific allocation method has been used that integrates all system components into the system boundaries. Emissions from all process steps including

electricity generation from the gas power plant are counted and allocated to all products (jet fuel, naphtha, electricity). However, other practices are used as shown in [24], where the authors analyze solar thermochemical fuel production with CO₂ capture from a fossil power plant and the fossil origin of CO₂ does not appear as a burden for the produced fuels. The validity of this approach has to be seen critical from an environmental point of view.

4.6.3 Use of grid electricity

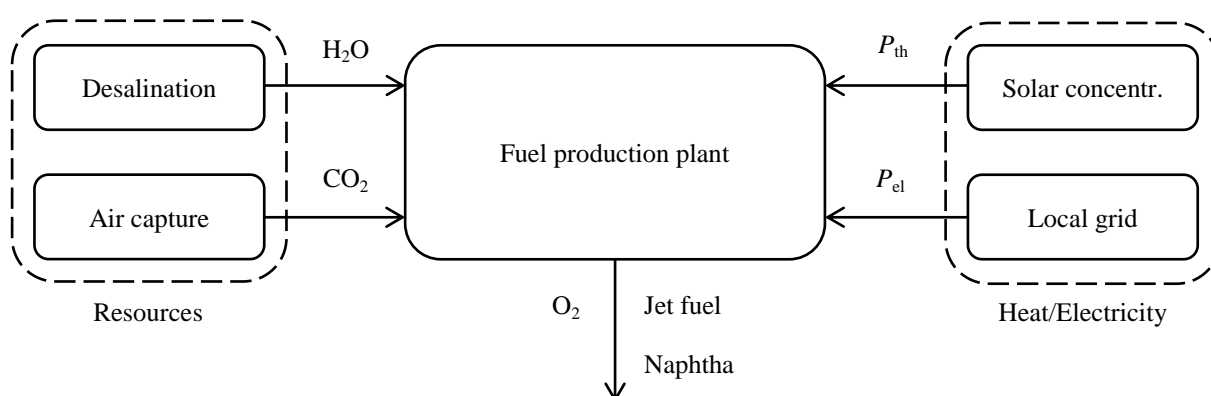


Figure 4.16 Schematic of provision of resources, heat and electricity for the solar thermochemical fuel production process in case of the use grid electricity. CO₂ is captured from the air and electricity is supplied by the grid.

Up to this point, in the baseline case, the electricity requirements were assumed to be covered by concentrated solar power produced on-site, causing generation costs of 0.06 € kWh_{el}⁻¹ [228] and specific emissions of 0.023 kg kWh_{el}⁻¹ [172]. This solar stand-alone configuration of the plant favors the environmental performance as it avoids the use of grid electricity which is likely to be at least partly based on fossil primary energy and thus the emission of greenhouse gases. When electricity is taken from the local grid, emissions are on the one hand reduced due to a smaller concentration facility, but on the other hand increased depending on the fossil contribution to the national electricity production. In the following, the use of grid electricity instead of solar electricity generation at the plant site is assumed and the consequences for the economic and environmental performance are analyzed (Figure 4.16). As a reference plant site, Morocco is chosen, as it offers the assumed level of solar irradiation and proximity to the European fuel market. The emission factor of the local grid electricity today is 0.729 kg_{CO₂-eq.} kWh_{el}⁻¹ [249] at a cost for large consumers of 7.2 € MWh_{el}⁻¹ [248] in 2014. As the solar fuel plant is assumed to operate in the mid-term future, these values may

be subject to change. For a future scenario, they are therefore adjusted to $0.480 \text{ kg}_{\text{CO}_2\text{-eq.}} \text{ kWh}_{\text{el}}^{-1}$ and $0.06 \text{ € kWh}_{\text{el}}^{-1}$, assuming 42% of the electricity production to be based on renewable energy, following the strategy of the national energy plan in 2020 [250].

If the electricity were taken at the conditions prevalent today, the production costs would rise to 2.33 € per liter of jet fuel and the life cycle GHG emissions to $4.92 \text{ kg}_{\text{CO}_2\text{-eq.}}$ per liter jet fuel and $4.68 \text{ kg}_{\text{CO}_2\text{-eq.}}$ per liter naphtha. This is only a slight increase in production costs but a dramatic increase in greenhouse gas emissions to a value higher than that of conventional jet fuel today ($3.03 \text{ kg}_{\text{CO}_2\text{-eq.}}$ per liter of jet fuel [28]). If the values for the future grid are assumed, the production costs at 2.23 € remain the same as for the baseline case and the GHG emissions rise to $3.36 \text{ kg}_{\text{CO}_2\text{-eq.}}$ per liter of jet fuel and $3.22 \text{ kg}_{\text{CO}_2\text{-eq.}}$ per liter of naphtha. This represents an increase in GHG emissions of about 10% with respect to conventional jet fuel today. Compared to the baseline case, the analysis of the use of grid electricity shows that production costs are only negligibly affected but life cycle GHG emissions are significantly increased. This is due to the fact that for the production of one liter of jet fuel and 0.87 liters naphtha, $11.4 \text{ kWh}_{\text{el}}$ of electricity are required, or about 70% of the lower heating value. Production costs rise because the assumed price for grid electricity is slightly larger than the CSP electricity costs of the baseline case. However, the carbon intensity of the grid electricity ($0.729 \text{ kg}_{\text{CO}_2\text{-eq.}} \text{ kWh}_{\text{el}}^{-1}$) is much higher than that of CSP electricity ($0.023 \text{ kg}_{\text{CO}_2\text{-eq.}} \text{ kWh}_{\text{el}}^{-1}$), which of course depends on the prevalent carbon intensity of the local grid. The largest share (80%) of the electricity is due to the inert gas purification for the thermochemical reaction. Capture of CO_2 has a smaller (10%) but also an important influence. Different reactor concepts using less electricity are thus expected to have a large impact on the environmental performance of the fuel path, in case grid electricity is used.

In the power-to-liquid path, hydrogen is produced by electrolysis, and thus even more electricity is used, as the amount of electricity has to be larger than the lower heating value. Here, nevertheless, depending on the emission intensity of the local electricity supply, the environmental performance of solar thermochemical jet fuel production may be considerably deteriorated. This underlines the importance of providing the energy inputs from renewable sources in order to produce fuels with a low level of GHG emissions.

4.6.4 Sale of oxygen

In the economic analyses so far, only the sale of naphtha as a by-product was assumed. However, also oxygen is produced during the reduction step of the thermochemical cycle which could be captured and sold to improve the plant economics. As 0.5 mol of oxygen are produced per mol of syngas and more than 400 mol of syngas are required for the production of 1 L of jet fuel and 0.87 L of naphtha, the available amount of oxygen is large. If the sale of the oxygen at a market price of 0.15 € m³ can be assumed [102], the yearly revenue amounts to 39.8 million € and the production costs of 1 L jet fuel are reduced to 1.73 €. This calculation does not include additional costs associated to the capture, storage and shipping of oxygen which reduce the revenue. Nevertheless, this analysis shows that the sale of oxygen significantly influences plant economics. However, as the plant location is likely to be remote and the market price may be influenced by the introduction of a large supply, the calculated revenue and the assumption of a constant market price of oxygen should be treated with caution. In the baseline case, oxygen sale was not considered due to these reasons.

4.6.5 Comparison of dish and tower systems for solar concentration

In the baseline case, a tower system consisting of a field of heliostats with an optical efficiency of 51.6% [50] was assumed. Tower concentrators are commonly applied in CSP facilities today and have thus reached a mature state in their development. However, also a field of dish concentrators could be used for the fuel production facility. Considerably higher optical concentration efficiencies can be achieved with dish concentrators through direct pointing at the sun which evades cosine losses, as well as the largest part of blocking and shading losses. A concentration efficiency of 85.3% is assumed for the dish concentrators [50,56,179]. As the construction of a strongly curved shape is more complex and expensive than that of a flat shape, the dish investment costs are expected to be higher and are assumed to be 216 € m⁻² [23]. The dish investment costs are thus more than twice as high compared to the tower system, however, the optical efficiency is not twice as large. The specific investment costs of a dish system are therefore higher. On the other hand, due to the higher optical efficiency, a significant reduction in overall reflective area is achieved.

Table 4.7 Investment costs and O&M costs of baseline case production facility with solar tower concentration.

Investment cost item	$\times 10^6$ €	Share	O&M cost item	$\times 10^6$ €	Share
Heliostats	653.4	74.3%	H ₂ O	0.388	0.3%
Thermochemical reactors	95.6	10.9%	CO ₂	32.6	26.6%
Solar tower	67.5	7.7%	O&M solar field	45.7	37.3%
Fischer-Tropsch	42.9	4.9%	Fischer-Tropsch	2.72	2.2%
Buildings	13.0	1.5%	Mirror renewal	1.31	1.1%
CHP	4.18	0.5%	Electricity	39.5	32.2%
Syngas compressors	3.08	0.4%	Fuel transport	0.0526	<0.1%
			CHP	0.326	0.3%
Total	879.6	100%	Total	122.6	100%

Table 4.8 Investment costs and O&M costs of 1000 bpd jet fuel production facility with solar dish concentration.

Investment cost item	$\times 10^6$ €	Share	O&M cost item	$\times 10^6$ €	Share
Dishes	854.0	84.3%	H ₂ O	0.388	0.4%
Thermochemical reactors	95.6	9.4%	CO ₂	32.6	31.0%
Fischer-Tropsch	42.9	4.2%	O&M solar field	27.7	26.4%
Buildings	13.0	1.3%	Fischer-Tropsch	2.72	2.6%
CHP	4.18	0.4%	Mirror renewal	1.71	1.6%
Syngas compressors	3.08	0.3%	Electricity	39.5	37.7%
			Fuel transport	0.0526	<0.1%
			CHP	0.326	0.3%
Total	1012.8	100%	Total	105.0	100%

As the operation and maintenance costs associated with the solar concentration are assumed to be proportional to the mirror surface area, an O&M cost reduction is achieved which does not overcompensate the increased investment costs. This result is however strictly limited to the assumptions made which include high concentration efficiency for the solar dishes and identical specific O&M costs of both concentration systems. As for an array of dishes, a larger number of solar reactors is required and other distributed equipment such as piping and compressors, the complexity is likely to increase with respect to a tower system and thus also the specific O&M costs. However, these costs are difficult to predict and uncertainty remains.

For the size of 1000 bpd jet fuel and 865 bpd naphtha production, the investment costs for the entire fuel production facility based on tower and dish concentration systems are 8.80×10^8 € and 1.01×10^9 €, respectively (see Table 4.7 and

Table 4.8). The annual O&M costs are 1.23×10^8 € and 1.05×10^8 €, respectively. Thus, under the given assumptions, the investment costs of dish concentration are higher and the O&M costs are lower. Assuming a lifetime of 25 years and CO₂ capture from the air as in the baseline case above, the production costs for one liter of jet fuel are 2.23 € (tower) and 2.12 € (dish). The higher investment costs of the dishes can therefore be compensated by the lower operation and maintenance costs.

4.6.6 Comparison to Power-to-Liquid fuel production pathway

The baseline case is adjusted to describe the Power-to-Liquid (PtL) fuel production pathway, a promising competing alternative which has gained attention lately through research projects and technical demonstrations. In the PtL pathway, electricity is used to drive water electrolysis to produce hydrogen. Parts of the hydrogen are then reacted with CO₂ in a reverse water gas shift reaction to produce carbon monoxide. The resulting syngas is then fed into a Fischer-Tropsch conversion to produce liquid hydrocarbons, similarly to the solar thermochemical pathway. The main difference is therefore the origin of the hydrogen.

For the purpose of the following comparison, the baseline case with its assumptions is used with the exception of hydrogen which is not produced by thermochemical conversion but by water electrolysis using solar electricity from a CSP plant. The plant layout is shown in Figure 4.17. The facilities for solar concentration and thermochemistry of the baseline case are replaced by an enlargement of the existing CSP facility to produce solar electricity which is partly fed into the electrolyzers to produce hydrogen from water. The energy requirement of the electrolyzers is $4.3 \text{ kWh}_{\text{el}} \text{ per m}^3$ at standard conditions [210] at investment costs of $500 \text{ € kW}_{\text{el}}^{-1}$ [251]. The capacity factor for the electrolyzers is assumed to be 50%, a value which can be easily achieved with CSP plants with thermal energy storage [224]. For the generation of 127.5 mol of CO per functional unit in the RWGS reaction, an equal amount of hydrogen is required to be produced in the electrolyzers, which adds to the 281.0 mol of the baseline case.

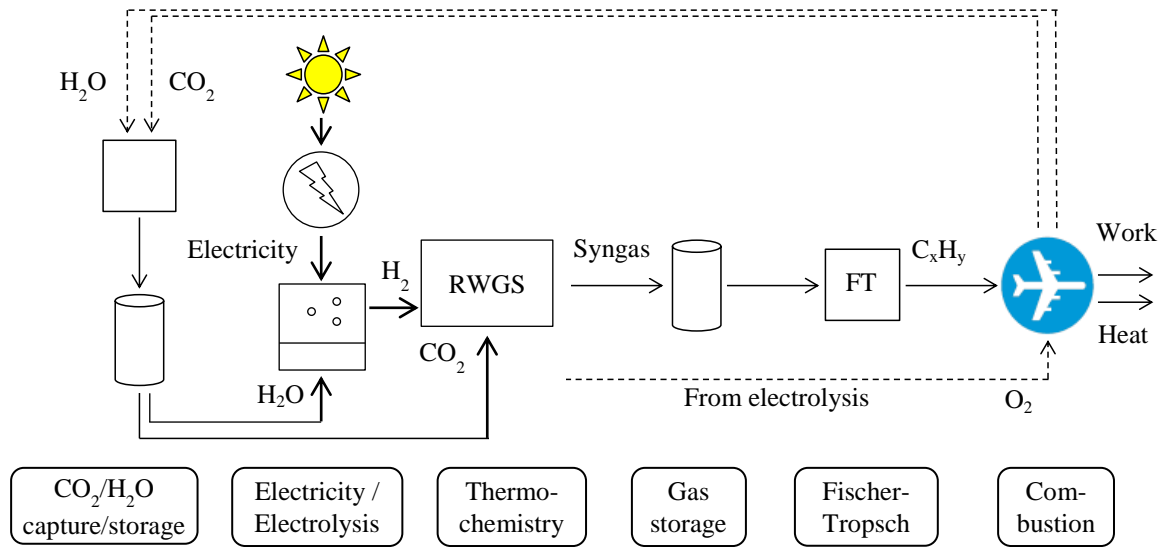


Figure 4.17 Schematic of Power-to-Liquid fuel production pathway.

The total electricity requirement is then 1.5×10^8 J, 95% of which is for electrolysis and 5% for other process steps (CO₂ capture, water desalination and transport).

The heat requirement for the RWGS reaction is 9.6 MW which may be provided by the combustion of light hydrocarbons from the FT synthesis. As however, the required amount of heat is comparably small and the light hydrocarbons are already used for other purposes in the baseline case, it is neglected in the analysis. The investment costs of the RWGS reactor are also neglected as it presents only 10% of the costs of the FT reactor [210].

Using otherwise identical assumptions as in the baseline case, production costs of 2.50 € L^{-1} jet fuel are estimated, or about 10% higher than the fuel produced with the solar thermochemical pathway. Both the investment costs and the O&M costs are dominated by the costs for the electrolyzers and for electricity, respectively. Even at an optimistic unit cost of $0.06 \text{ € kWh}_{\text{el}}^{-1}$ for CSP electricity, the O&M costs for electricity production lead to production costs which are higher than in the solar thermochemical pathway. The capacity factor of the electrolyzers has an important influence on the investment costs, however, as the O&M costs have a relative share of 90% in the total costs, its overall influence is limited. This result is in accordance with a recent study of the PtL pathway in [210], where production costs in the range of 3.4-5.9 € per liter jet fuel was estimated, however, using roughly $0.15 \text{ € kWh}_{\text{el}}^{-1}$.

The climate impact of the PtL pathway is estimated to be $0.39 \text{ kg}_{\text{CO}_2\text{-eq. L}^{-1}}$ jet fuel, using the assumptions of the baseline case after the adaptation to the new pathway layout. This value is

lower by about 20% compared to the solar thermochemical pathway. This reduction in climate impact is not straightforward and is understood by considering that for CSP electricity, unit values for economic value and specific emissions have been assumed, while for the solar concentration facility, the materials with their respective specific emissions are used. As the resulting emission factors for heliostats of the concentrating facility and of the CSP plant are not identical, a substitution of the solar concentration facility with a CSP facility, as is the case here, leads to an increase in costs and a decrease in climate impact.

4.6.7 Possibilities for cost reductions and emission reductions

Considering favorable assumptions of a publicly financed plant in a sunny region with $3000 \text{ kWh m}^{-2} \text{ a}^{-1}$ of direct normal irradiation, a thermochemical efficiency of 30% (including inert gas purification and gas separation), a reduction of the CO_2 capture costs from air to 50 € t^{-1} , and a replacement of the CHP plant by solar heat and electricity, production costs of 1.28 € L^{-1} jet fuel are estimated at life cycle GHG emissions of $0.10 \text{ kg}_{\text{CO}_2\text{-equiv}} \text{ L}^{-1}$ jet fuel. Even more favorable conditions are possible; for example, the thermochemical efficiency has a thermodynamic limit above 50% [93], the best locations for concentrated solar technologies surpass the assumed $3000 \text{ kWh m}^{-2} \text{ a}^{-1}$, and more cost-effective sources of CO_2 are available [245] (possibly at higher specific emissions). However, overly optimistic assumptions will deliver an unrealistic estimate for the ecological and economic performance which is why the baseline case has been chosen with partly ambitious but well achievable boundary conditions.

If the sale of oxygen is considered also for the scenario for the potential of cost reductions, the production cost could be further reduced to 0.79 € L^{-1} jet fuel.

5 Conclusions and outlook

Renewable fuels based on the conversion of carbon dioxide and water by sunlight are a promising solution to the challenges associated with the availability and the climate impact of future fuel supply. Solar thermochemical production of synthesis gas using redox reactions of metal oxides offers the potential of high energy conversion efficiencies, where the redox material cerium dioxide has shown encouraging experimental results and is therefore considered in this dissertation. An analysis of the integrated fuel production pathway shows that carbon dioxide capture from the atmosphere and the thermochemical conversion are the only process steps which are not yet ready to use at an industrial scale. The enhancement of thermochemical conversion efficiency is decisive for the achievement of economic targets and is thus in the center of this work. Particularly for nonstoichiometric redox cycles, as the ceria cycle, heat recuperation from the gas and solid phases is a prerequisite for high efficiencies. So far, analyses have either focused on fundamental thermodynamics without implementations or on specific reactor concepts, where the results of the latter may be difficult to transfer to other concepts. The objective of this work is to close the gap between these two approaches by introducing generic reactor models that allow the thermodynamic analysis of a wide parameter space of technically relevant reactor concepts including heat exchange.

A generic reactor model was developed, consisting of chambers for reduction and oxidation, and a defined number of intermediate chambers, where heat is recuperated by thermal radiation exchange between redox material moving in a counter-flow in the upper and lower chamber halves, respectively. In a first implementation of this model, the effect of the wall separating the chamber halves to ensure gas separation and to provide structural support is neglected, and heat diffusion within the redox material is assumed to occur infinitely fast. A potential for the heat exchanger efficiency of over 80% was derived. Nevertheless, the energy input for the thermal cycling of the redox material between the reaction temperatures was identified to be the largest input in the energy balance. Through the significant decrease of pumping efficiency towards lower pressures, a trade-off between increased fuel production and pumping energy exists, determining an optimum reduction pressure in the range of 10-100 Pa. The efficiencies of the heat exchanger and of the thermodynamic cycle are optimized towards higher reduction and oxidation temperatures because of the T^4 -dependence of

thermal radiation and the oxygen nonstoichiometry and emissivity of ceria, both of which increase with temperature. Furthermore, the total residence time of the redox material in the heat exchanger is identified to be a key design parameter, where an optimal value exists depending on the number of chambers. The potential for the chamber heat exchanger is found to be excellent with heat exchanger efficiencies of over 80%. For economic reasons, a small number of chambers can be chosen and the residence time adjusted accordingly. However, a larger number of chambers will reduce thermodynamic irreversibilities.

In a second implementation of the generic model, the effect of the separating wall and of heat diffusion within the redox material is investigated, where the separating wall is found to have only a small influence on heat exchanger efficiency. As a main difference, heat diffusion within the material is identified as a possibly limiting factor in heat exchanger design, reducing the efficiency in cases where not enough time is given for diffusion to take place. This is demonstrated by a shift of maximum efficiency towards longer residence times since the assumption of the first model was an infinitely fast diffusion process. However, by an optimal design of the heat exchanger, this limitation can be reduced, leading to efficiencies of about 70% which come close to the optimal case of the first model. Consequently, the heat exchanger has to be designed to reduce the time scale of internal heat diffusion with respect to radiation heat exchange. An increase of material thickness prolongs the time required to diffuse the thermal energy in the material, while an increase of porosity leads to faster heat diffusion: at the prevalent temperatures, the increased radiation heat exchange at higher porosities outweighs the deteriorated thermal conductivity.

Apart from porous bulk material structures, reactor concepts based on particles of redox material have been suggested, where the high surface area of the particles and their inherent resistivity against thermal shocks make them an interesting option for new reactor designs. In a third implementation, the reactor model is thus modified to allow the description of a counter-flow heat exchanger of ceria particles in a cylindrical enclosure: the hot bed of reduced particles moves downward on the inside, while the cold bed of oxidized particles moves in the opposite direction, separated by a thin wall. For the description of heat transfer both within the particle bed and between the wall and the adjacent particle bed, models described in the literature are used. Heat exchanger efficiencies close to 60% are achievable, where heat transfer within the particle beds is found to be limiting the overall heat transfer between the beds. Possibly even higher efficiencies are attainable given the right combination of parameters at a global optimum which was not analyzed here. This result is consistent with

the findings of the second model, where heat diffusion in the material was identified to be limiting the efficiency. The heat exchanger has therefore to be designed to facilitate heat diffusion in the particle beds. Reducing the bed thickness is found to increase efficiency, where heat losses to the surroundings are expected to become dominant towards very small dimensions. A larger particle diameter enhances the heat exchanger performance because of its positive influence on the radiation heat exchange in the bed. The total residence time is again found to be a crucial design parameter that has an optimum value depending on the other parameters of the system. Gases cross the particle bed due to the pressure difference between the oxidation and reduction chamber. However, the associated gas losses only become significant for particle diameters of 1 mm or larger. For smaller particles, the bed represents an effective seal. The particle reactor concept is therefore found to be an interesting option for new reactor implementations with a potential for high efficiency.

It is found that for the achievement of over 20% thermodynamic cycle efficiency with the redox material ceria, an improvement of several parameters is required, e.g. a sophisticated heat exchange with 60% efficiency, the elevation of reduction temperature to 2000 K, higher concentration efficiency of 5000 suns, and 50% more efficient vacuum pumping. All of the analyzed reactor concepts are in principle viable for this task, however, the operating conditions present a challenge from a technical point of view, especially the achievement of a reduction temperature of 2000 K due to material sublimation. A reduction of operating temperatures by doping of ceria or the use of other redox materials, e.g. perovskites, could enhance the feasibility.

For the assessment of the ecological and economic performance of solar thermochemical jet fuel production, a baseline case plant layout is defined for a location in Morocco due to the high solar resource and the proximity to a large fuel market in Europe. For the plant size of 1000 barrels per day (bpd) of jet fuel and 865 bpd of naphtha, a pathway efficiency of 5.0% is determined, assuming a solar tower concentrator with 51.6% optical efficiency, a CSP plant to provide electricity, seawater desalination, carbon dioxide capture from the atmosphere, a thermochemical conversion efficiency of 20%, and a Fischer-Tropsch conversion unit with 58% energy efficiency, where the gaseous products are combusted in a CHP plant to provide heat and power to the process. Efficiency is mainly limited by thermochemical conversion, while provision of water by desalination and transport over 500 km distance has a negligible influence on the energy balance. CO₂ capture from the atmosphere has only a small impact on the pathway efficiency.

A life cycle analysis shows greenhouse gas emissions of the baseline case plant of 0.49 kgCO₂-eq. per liter of jet fuel, which is a reduction of over 80% compared to conventional jet fuel. The main drivers of the emissions are the combustion of gaseous products, losses in the Fischer-Tropsch conversion, and the emissions associated with the solar concentrating facility. Thermodynamic efficiency and solar irradiation also have an important influence on the GHG emissions, as they determine the size of the solar concentration facility. The use of grid electricity instead of the CSP plant significantly deteriorates the jet fuel GHG emissions to a value 50% higher than conventional fuel. This is due to the fossil origin of a large share of the grid electricity in the baseline case, in combination with electricity requirements of about 70% of the lower heating value of the products jet fuel and naphtha. A similarly negative effect has the use of carbon dioxide from a natural gas power plant, increasing GHG emissions to 20% above conventional jet fuel. In general, a significant reduction of GHG emissions over conventional fuel is only possible if a renewable source of carbon dioxide and electricity is used for the production process.

An analysis of the water footprint of the fuel production plant shows a total water consumption of 47.6 liters per liter jet fuel, which is comprised of 7.4 liters on-site and 40.2 liters off-site demand. The on-site consumption is mainly driven by mirror cleaning, thermochemistry and CSP electricity, while off-site consumption is clearly dominated by ceria mining and to a much lesser degree by the construction of the solar concentration facility. Overall water consumption is about equal to that of fossil jet fuel production and orders of magnitude lower than that of biofuels due to the high water demand of plant irrigation. The water demand therefore does not represent an obstacle for large-scale implementation of the fuel production process, even in dry regions.

The area-specific productivity of solar thermochemical fuel production is determined to be 3.3×10^4 liters of jet fuel equivalent per hectare and year, which is lower than that of the best power-to-liquid pathways and about an order of magnitude higher than that of biofuels. As solar thermochemical fuels are likely to be produced in desert regions with high solar irradiation, even single countries such as Algeria have the potential to cover the global jet fuel demand.

An economic model based on the annuity method is used to determine the economic potential of solar jet fuel production, where public funding of the facility at an interest rate of 6%, a fixed relative price of jet fuel and naphtha, and a cost of 100 € per ton of carbon dioxide captured from the atmosphere, is assumed. Production costs are determined to be

2.23 € per liter of jet fuel, where the main cost drivers are the construction and operation of the solar concentration facility, the generation of CSP electricity, and supply of carbon dioxide. The annual amount of direct normal irradiation, thermochemical efficiency, and the lifetime of the plant are also drivers of economic performance. This cost is about seven times as high as the current market price of jet fuel¹ and is therefore likely to be a challenge for large-scale deployment in the near future, unless e.g. subsidies for alternative fuels are established. As conventional fuels are bound to experience a price increase due to their limited availability, this gap between production costs of solar thermochemical fuels and the price of fossil fuels is expected to decrease in the future. The sale of oxygen as a by-product from the thermochemical conversion could reduce the production costs to 1.73 € per liter and thus has a significant economic potential. However, the economic viability of oxygen sale on a large scale has to be determined for the specific location of the fuel plant.

As compared to the baseline case, the potential for reduction of production costs and GHG emissions is analyzed, assuming a direct normal irradiation of 3000 kWh per square meter and year, a thermochemical energy conversion efficiency of 30%, 50 € per ton of carbon dioxide captured from the atmosphere, investment costs of 75 € m⁻² of heliostat area, and the replacement of the CHP plant by heat and electricity from solar energy. Production costs of 1.28 € per liter of jet fuel at GHG emissions of 0.10 kg_{CO₂-eq.} per liter are determined. At this level of production costs, the production of solar thermochemical fuels could be economically interesting, assuming rising prices of conventional fuels in the future. The low GHG emissions show the large potential of this fuel pathway which could help to reduce the emissions of the transportation sector without having to change the basic fuel infrastructure.

In general, the production of a fuel with low GHG emissions is considered to be feasible through the realization of carbon dioxide capture from the atmosphere, while its economic production requires the favorable development of thermochemical conversion efficiency and of the cost of solar concentration.

As was identified in this thesis, the efficiency of thermochemical conversion is determined both by thermodynamics and heat exchanger efficiency. Further research in the modeling of solar reactors and heat exchangers could complement the work performed here by analyzing other redox materials which have an influence both on the redox reactions through their thermodynamic and kinetic behavior, as well as on the heat exchanger by their heat capacity

¹ IATA fuel price analysis, <http://www.iata.org/publications/economics/fuel-monitor/Pages/price-analysis.aspx>

and the possibly altered reaction temperatures.

Concerning the production plant, a detailed modeling of the Fischer-Tropsch conversion including hydrocracking and distillation could add more insight into the energy requirements of this process step. Also the implications of a change in product distribution and a recycling of the gaseous products for plant economics represent interesting aspects for future research. As the generation of high-temperature heat and its use in the thermochemical reactors creates heat losses, the integration of the fuel production plant with respect to utilization of waste energy streams is intriguing because it may increase overall energy conversion efficiency and thus reduce production costs.

It was shown in the present thesis that solar thermochemical fuels have the potential to drastically reduce the greenhouse gas emissions of the transportation sector by providing a drop-in alternative to conventional fuels, which obviates costly changes to the fuel distribution and powertrain architecture of existing vehicles. The presented reactor models enable the assessment of thermodynamic cycle efficiency as the crucial performance indicator for the economic and environmental balance of the overall system. Furthermore, they help to design the solar thermochemical conversion based on efficient heat exchange and the overall fuel production pathway towards an environmentally friendly and economical fuel production process.

References

- [1] International Energy Agency, 2014, “2014 Key World Energy Statistics.”
- [2] U.S. Energy Information Administration, 2014, International Energy Outlook 2014.
- [3] Stechel, E. B., and Miller, J. E., 2013, “Re-energizing CO₂ to fuels with the sun: Issues of efficiency, scale, and economics,” *J. CO₂ Util.*, **1**, pp. 28–36.
- [4] Roeb, M., Neises, M., Monnerie, N., Sattler, C., and Pitz-Paal, R., 2011, “Technologies and trends in solar power and fuels,” *Energy Environ. Sci.*, **4**(7), p. 2503.
- [5] Kim, J., Johnson, T. a., Miller, J. E., Stechel, E. B., and Maravelias, C. T., 2012, “Fuel production from CO₂ using solar-thermal energy: system level analysis,” *Energy Environ. Sci.*, **5**(9), p. 8417.
- [6] Romero, M., and Steinfeld, A., 2012, “Concentrating solar thermal power and thermochemical fuels,” *Energy Environ. Sci.*, **5**(11), p. 9234.
- [7] Steinfeld, A., and Epstein, M., 2001, “Light Years Ahead,” *Chem. Br.*, **37**(5), pp. 30–32.
- [8] Loutzenhiser, P. G., Meier, A., and Steinfeld, A., 2010, “Review of the Two-Step H₂O/CO₂-Splitting Solar Thermochemical Cycle Based on Zn/ZnO Redox Reactions,” *Materials (Basel)*, **3**(11), pp. 4922–4938.
- [9] Chueh, W. C., and Haile, S. M., 2009, “Ceria as a thermochemical reaction medium for selectively generating syngas or methane from H₂O and CO₂,” *ChemSusChem*, **2**(8), pp. 735–739.
- [10] Chueh, W. C., Falter, C., Abbott, M., Scipio, D., Furler, P., Haile, S. M., and Steinfeld, A., 2010, “High-flux solar-driven thermochemical dissociation of CO₂ and H₂O using nonstoichiometric ceria,” *Science*, **330**(6012), pp. 1797–1801.
- [11] Furler, P., Scheffe, J., Gorbar, M., Moes, L., Vogt, U., and Steinfeld, A., 2012, “Solar thermochemical CO₂ splitting utilizing a reticulated porous ceria redox system,” *Energy and Fuels*, **26**(11), pp. 7051–7059.
- [12] Hao, Y., Yang, C.-K., and Haile, S. M., 2013, “High-temperature isothermal chemical cycling for solar-driven fuel production,” *Phys. Chem. Chem. Phys.*, **15**(40), pp. 17084–92.
- [13] Bader, R., Venstrom, L. J., Davidson, J. H., and Lipiński, W., 2013, “Thermodynamic analysis of isothermal redox cycling of ceria for solar fuel production,” *Energy and Fuels*, **27**(9), pp. 5533–5544.
- [14] Furler, P., Scheffe, J., Marxer, D., Gorbar, M., Bonk, A., Vogt, U., and Steinfeld, A., 2014, “Thermochemical CO₂ splitting via redox cycling of ceria reticulated foam structures with dual-scale porosities,” *Phys. Chem. Chem. Phys.*, **16**(22), pp. 10503–11.
- [15] Marxer, D. A., Furler, P., Scheffe, J. R., Geerlings, H., Falter, C., Batteiger, V., Sizmann, A., and Steinfeld, A., 2015, “Demonstration of the entire production chain to renewable kerosene via solar-thermochemical splitting of H₂O and CO₂,” *Energy & Fuels*, **29**(5), pp. 3241–3250.
- [16] Diver, R. B., Miller, J. E., Allendorf, M. D., Siegel, N. P., and Hogan, R. E., 2008,

- “Solar Thermochemical Water-Splitting Ferrite-Cycle Heat Engines,” *J. Sol. Energy Eng.*, **130**(4), p. 041001.
- [17] Lapp, J., Davidson, J. H., and Lipiński, W., 2013, “Heat Transfer Analysis of a Solid-Solid Heat Recuperation System for Solar-Driven Nonstoichiometric Cycles,” *J. Sol. Energy Eng.*, **135**(3), p. 031004.
- [18] Ermanoski, I., Siegel, N. P., and Stechel, E. B., 2013, “A New Reactor Concept for Efficient Solar-Thermochemical Fuel Production,” *J. Sol. Energy Eng.*, **135**(3), p. 031002.
- [19] Scheffe, J. R., Welte, M., and Steinfeld, A., 2014, “Thermal Reduction of Ceria within an Aerosol Reactor for H₂O and CO₂ Splitting,” *Ind. Eng. Chem. Res.*, **53**(6), pp. 2175–2182.
- [20] Lapp, J., Davidson, J. H., and Lipiński, W., 2012, “Efficiency of two-step solar thermochemical non-stoichiometric redox cycles with heat recovery,” *Energy*, **37**(1), pp. 591–600.
- [21] Lapp, J., and Lipinski, W., 2014, “Transient Three-Dimensional Heat Transfer Model of a Solar Thermochemical Reactor for H₂O and CO₂ Splitting Via Nonstoichiometric Ceria Redox Cycling,” *J. Sol. Energy Eng.*, **136**(3), p. 031006.
- [22] Felinks, J., Brendelberger, S., Roeb, M., Sattler, C., and Pitz-paal, R., 2014, “Heat recovery concept for thermochemical processes using a solid heat transfer medium,” *Appl. Therm. Eng.*, **73**(1), pp. 1004–1011.
- [23] Kim, J., Henao, C. A., Johnson, T. A., Dedrick, D. E., Miller, J. E., Stechel, E. B., and Maravelias, C. T., 2011, “Methanol production from CO₂ using solar-thermal energy: process development and techno-economic analysis,” *Energy Environ. Sci.*, **4**(9), p. 3122.
- [24] Kim, J., Miller, J. E., Maravelias, C. T., and Stechel, E. B., 2013, “Comparative analysis of environmental impact of S2P (Sunshine to Petrol) system for transportation fuel production,” *Appl. Energy*, **111**, pp. 1089–1098.
- [25] Falter, C., Batteiger, V., and Sizmann, A., 2016, “Climate Impact and Economic Feasibility of Solar Thermochemical Jet Fuel Production,” *Environ. Sci. Technol.*, **50**(1), pp. 470–477.
- [26] Eberle, U., Felderhoff, M., and Schüth, F., 2009, “Chemical and physical solutions for hydrogen storage,” *Angew. Chemie - Int. Ed.*, **48**(36), pp. 6608–6630.
- [27] National Institute of Standards and Technology, “Thermophysical Properties of Hydrogen” [Online]. Available: http://webbook.nist.gov/cgi/fluid.cgi?Action=Load&ID=C1333740&Type=SatT&Digits=5&PLow=.5&PHigh=1.5&PInc=.1&RefState=DEF&TUnit=K&PUnit=atm&DUnit=kg/m3&HUnit=kJ/mol&WUnit=m/s&VisUnit=uPa*s&STUnit=N/m. [Accessed: 23-May-2017].
- [28] Stratton, R. W., Wong, H. M., and Hileman, J. I., 2010, Life cycle gas emissions from alternative jet fuels; PARTNER Project 28 report; Report number Partner-Coe-2010-001.
- [29] Kuhn, H., Falter, C., and Sizmann, A., 2011, “Renewable Energy Perspectives for Aviation,” *Proc. 3rd CEAS Air&sp. Conf. 21st AIDAA Congr. Venice, Italy*, pp. 1249–1259.
- [30] Van Noorden, R., 2014, “The rechargeable revolution: A better battery,” *Nature*,

- 507(7490), pp. 26–28.
- [31] Kuhn, H., Seitz, A., Lorenz, L., Isikveren, A., and Sizmann, A., 2012, “Progress and perspectives of electric air transport,” 28th Congr. Int. Counc. Aeronaut. Sci. 2012, ICAS 2012, **6**, pp. 4886–4899.
- [32] Al-Karaghoul, A., and Kazmerski, L. L., 2013, “Energy consumption and water production cost of conventional and renewable-energy-powered desalination processes,” *Renew. Sustain. Energy Rev.*, **24**, pp. 343–356.
- [33] “Desalination worldwide” [Online]. Available: <http://hbfreshwater.com/desalination-101/desalination-worldwide>. [Accessed: 15-Apr-2016].
- [34] Elimelech, M., and Phillip, W. A., 2011, “The Future of Seawater Desalination: Energy, Technology, and the Environment,” *Science* (80-.), **333**(6043), pp. 712–717.
- [35] Working Group III of the Intergovernmental Panel on Climate Change, 2005, IPCC, 2005: Special Report on Carbon Dioxide Capture and Storage.
- [36] v. Zedtwitz-Nikulshyna, V., 2009, “CO₂ capture from atmospheric air via solar driven carbonation-calcination cycles,” Dissertation, ETH Zurich.
- [37] Plasynski, S., and Chen, Z.-Y., 2000, “Review of CO₂ capture technologies and some improvement opportunities,” *Abstr. Pap. Am. Chem. Soc.*, **220**, pp. 644–649.
- [38] Wurzbacher, J. A., Gebald, C., and Steinfeld, A., 2011, “Separation of CO₂ from air by temperature-vacuum swing adsorption using diamine-functionalized silica gel,” *Energy Environ. Sci.*, **4**(9), p. 3584.
- [39] Wurzbacher, J. A., Gebald, C., Piatkowski, N., and Steinfeld, A., 2012, “Concurrent separation of CO₂ and H₂O from air by a temperature-vacuum swing adsorption/desorption cycle,” *Environ. Sci. Technol.*, **46**(16), pp. 9191–9198.
- [40] Gebald, C., Wurzbacher, J. A., Tingaut, P., Zimmermann, T., and Steinfeld, A., 2011, “Amine-based nanofibrillated cellulose as adsorbent for CO₂ capture from air,” *Environ. Sci. Technol.*, **45**(20), pp. 9101–9108.
- [41] Stephan, P., Schaber, K., Stephan, K., and Mayinger, F., 2009, *Thermodynamik*, Springer Berlin Heidelberg, Berlin, Heidelberg.
- [42] Climeworks LLC., 2015, “CO₂ air capture demonstration plant” [Online]. Available: <http://www.climeworks.com/co2-capture-plants.html>. [Accessed: 01-Jun-2014].
- [43] Zeman, F. S., and Lackner, K. S., 2004, “Capturing carbon dioxide directly from the atmosphere,” *World Resour. Rev.*, **16**(2), pp. 157–172.
- [44] Keith, D. W., Ha-Duong, M., and Stolaroff, J., 2006, “Climate strategy with CO₂ capture from the air,” *Clim. Change*, **74**, pp. 17–45.
- [45] Baciocchi, R., Storti, G., and Mazzotti, M., 2006, “Process design and energy requirements for the capture of carbon dioxide from air,” *Chem. Eng. Process. Process Intensif.*, **45**(12), pp. 1047–1058.
- [46] Socolow, R., Desmond, M., Aines, R., Blackstock, J., Bolland, O., Kaarsberg, T., Lewis, N., Mazzotti, M., Pfeffer, A., Sawyer, K., Sirola, J., Smit, B., and Wilcox, J., 2011, *Direct Air Capture of CO₂ with Chemicals*, American Physical Society.
- [47] Sterner, M., 2009, “Renewable Energies and Energy Efficiency,” Dissertation, Universität Kassel.
- [48] Stolaroff, J. K., 2006, “Capturing CO₂ from ambient air: a feasibility assessment,” Dissertation, Carnegie Mellon University.

- [49] Meier, A., and Sattler, C., 2009, Solar Fuels from Concentrated Sunlight, SOLARPACES Report.
- [50] Sargent&Lundy, 2003, Assessment of Parabolic Trough and Power Tower Solar Technology; SL-5641, Chicago, IL, USA.
- [51] Pitz-Paal, R., Botero, N. B., and Steinfeld, A., 2011, "Heliostat field layout optimization for high-temperature solar thermochemical processing," *Sol. Energy*, **85**(2), pp. 334–343.
- [52] Weinrebe, G., 2000, "Technische, ökonomische und ökologische Analyse von solarthermischen Turmkraftwerken," Dissertation, Universität Stuttgart.
- [53] Abengoa, "PS10 and PS20" [Online]. Available: http://www.abengoa.es/export/sites/abengoa_corp/resources/gestion_noticias/images/es/20091126_PS10-PS20.jpg. [Accessed: 21-Jan-2016].
- [54] National Renewable Energy Laboratory, 2011, "Concentrating solar power projects" [Online]. Available: http://www.nrel.gov/csp/solarpaces/power_tower.cfm. [Accessed: 07-Apr-2016].
- [55] CSP today, 2012, "Ripasso Energy sets new solar-to-electricity world record!" [Online]. Available: <http://social.csptoday.com/technology/ripasso-energy-sets-new-solar-electricity-world-record>. [Accessed: 22-Jan-2016].
- [56] Lovegrove, K., Zawadski, A., and Coventy, J., 2007, "Paraboloidal Dish Solar Concentrators for Multi-Megawatt Power Generation," ISES Sol. World Congr., pp. 1–4.
- [57] Kodama, T., and Gokon, N., 2007, "Thermochemical cycles for high-temperature solar hydrogen production," *Chem. Rev.*, **107**(10), pp. 4048–4077.
- [58] Baykara, S., 2004, "Experimental solar water thermolysis," *Int. J. Hydrogen Energy*, **29**(14), pp. 1459–1469.
- [59] Kogan, A., 1997, "Direct solar thermal splitting of water and on site separation of the products I. Theoretical evaluation of hydrogen yield," *Int. J. Hydrogen Energy*, **22**(5), pp. 481–486.
- [60] Nakamura, T., 1977, "Hydrogen production from water utilizing solar heat at high temperatures," *Sol. Energy*, **19**(5), pp. 467–475.
- [61] Kodama, T., 2003, "High-temperature solar chemistry for converting solar heat to chemical fuels," *Prog. Energy Combust. Sci.*, **29**(6), pp. 567–597.
- [62] Kodama, T., Nakamuro, Y., and Mizuno, T., 2006, "A Two-Step Thermochemical Water Splitting by Iron-Oxide on Stabilized Zirconia," *J. Sol. Energy Eng.*, **128**(1), p. 3.
- [63] Allendorf, M. D., Diver, R. B., Siegel, N. P., and Miller, J. E., 2008, "Two-Step Water Splitting Using Mixed-Metal Ferrites: Thermodynamic Analysis and Characterization of Synthesized Materials," *Energy & Fuels*, **22**(6), pp. 4115–4124.
- [64] Gokon, N., Hasegawa, T., Takahashi, S., and Kodama, T., 2008, "Thermochemical two-step water-splitting for hydrogen production using Fe-YSZ particles and a ceramic foam device," *Energy*, **33**(9), pp. 1407–1416.
- [65] Möller, S., Sattler, C., and Roeb, M., 2007, "Solar thermal Hydrogen Production via Reforming and Thermo - Chemical - Cycles," FVS Workshop.
- [66] Steinfeld, A., and Spiewak, I., 1998, "Economic evaluation of the solar thermalco-

- production of zinc and synthesis gas,” *Energy Convers. Manag.*, **39**(15), pp. 1513–1518.
- [67] Roeb, M., Sattler, C., Klüser, R., Monnerie, N., de Oliveira, L., Konstandopoulos, A. G., Agrafiotis, C., Zaspalis, V. T., Nalbandian, L., Steele, A., and Stobbe, P., 2006, “Solar Hydrogen Production by a Two-Step Cycle Based on Mixed Iron Oxides,” *J. Sol. Energy Eng.*, **128**(2), p. 125.
- [68] Gokon, N., Mizuno, T., Takahashi, S., and Kodama, T., 2006, “A Two-Step Water Splitting With Ferrite Particles and Its New Reactor Concept Using an Internally Circulating Fluidized-Bed,” *Solar Energy*, ASME, pp. 205–214.
- [69] Lichty, P., Liang, X., Muhich, C., Evanko, B., Bingham, C., and Weimer, A. W., 2012, “Atomic layer deposited thin film metal oxides for fuel production in a solar cavity reactor,” *Int. J. Hydrogen Energy*, **37**(22), pp. 16888–16894.
- [70] Gálvez, M. E., Loutzenhiser, P. G., Hischer, I., and Steinfeld, A., 2008, “CO₂ Splitting via Two-Step Solar Thermochemical Cycles with Zn/ZnO and FeO/Fe₃O₄ Redox Reactions: Thermodynamic Analysis,” *Energy & Fuels*, **22**(5), pp. 3544–3550.
- [71] Steinfeld, A., 2005, “Solar thermochemical production of hydrogen - A review,” *Sol. Energy*, **78**(5), pp. 603–615.
- [72] Perkins, C., Lichty, P., and Weimer, A., 2008, “Thermal ZnO dissociation in a rapid aerosol reactor as part of a solar hydrogen production cycle,” *Int. J. Hydrogen Energy*, **33**(2), pp. 499–510.
- [73] Melchior, T., Perkins, C., Weimer, A. W., and Steinfeld, A., 2008, “A cavity-receiver containing a tubular absorber for high-temperature thermochemical processing using concentrated solar energy,” *Int. J. Therm. Sci.*, **47**(11), pp. 1496–1503.
- [74] Haussener, S., Hirsch, D., Perkins, C., Weimer, A., Lewandowski, A., and Steinfeld, A., 2009, “Modeling of a Multitube High-Temperature Solar Thermochemical Reactor for Hydrogen Production,” *J. Sol. Energy Eng.*, **131**(2), p. 024503.
- [75] Palumbo, R., Léde, J., Boutin, O., Elorza Ricart, E., Steinfeld, A., Möller, S., Weidenkaff, A., Fletcher, E. A., and Bielicki, J., 1998, “The production of Zn from ZnO in a high-temperature solar decomposition quench process—I. The scientific framework for the process,” *Chem. Eng. Sci.*, **53**(14), pp. 2503–2517.
- [76] Koepf, E., Advani, S. G., Steinfeld, A., and Prasad, A. K., 2012, “A novel beam-down, gravity-fed, solar thermochemical receiver/reactor for direct solid particle decomposition: Design, modeling, and experimentation,” *Int. J. Hydrogen Energy*, **37**(22), pp. 16871–16887.
- [77] Haueter, P., Moeller, S., Palumbo, R., and Steinfeld, a, 1999, “The production of zinc by thermal dissociation of zinc oxide - Solar chemical reactor design,” *Sol. Energy*, **67**(1-3), pp. 161–167.
- [78] Schunk, L. O., Haerberling, P., Wepf, S., Wuillemin, D., Meier, A., and Steinfeld, A., 2008, “A receiver-reactor for the solar thermal dissociation of zinc oxide,” *J. Sol. Energy Eng. ASME*, **130**(2).
- [79] Schunk, L. O., Lipiński, W., and Steinfeld, A., 2009, “Heat transfer model of a solar receiver-reactor for the thermal dissociation of ZnO—Experimental validation at 10kW and scale-up to 1MW,” *Chem. Eng. J.*, **150**(2-3), pp. 502–508.
- [80] Villasmil, W., Meier, A., and Steinfeld, A., 2013, “Dynamic Modeling of a Solar Reactor for Zinc Oxide Thermal Dissociation and Experimental Validation Using IR

- Thermography,” ASME 2013 7th International Conference on Energy Sustainability, ASME, p. V001T10A002.
- [81] Abanades, S., and Flamant, G., 2006, “Thermochemical hydrogen production from a two-step solar-driven water-splitting cycle based on cerium oxides,” *Sol. Energy*, **80**(12), pp. 1611–1623.
- [82] Panlener, R. J., Blumenthal, R. N., and Garnier, J. E., 1975, “A thermodynamic study of nonstoichiometric cerium dioxide,” *J. Phys. Chem. Solids*, **36**(11), pp. 1213–1222.
- [83] Chueh, W. C., and Haile, S. M., 2010, “A thermochemical study of ceria: exploiting an old material for new modes of energy conversion and CO₂ mitigation,” *Philos Trans. A Math Phys Eng Sci*, **368**(1923), pp. 3269–3294.
- [84] Sørensen, O. T., 1976, “Thermodynamic studies of the phase relationships of nonstoichiometric cerium oxides at higher temperatures,” *J. Solid State Chem.*, **18**(3), pp. 217–233.
- [85] Abanades, S., Le Gal, A., Cordier, A., Peraudeau, G., Flamant, G., and Julbe, A., 2010, “Investigation of reactive cerium-based oxides for H₂ production by thermochemical two-step water-splitting,” *J. Mater. Sci.*, **45**(15), pp. 4163–4173.
- [86] Chueh, W. C., and Haile, S. M., 2010, “A thermochemical study of ceria: exploiting an old material for new modes of energy conversion and CO₂ mitigation,” *Philos. Trans. A. Math. Phys. Eng. Sci.*, **368**(1923), pp. 3269–3294.
- [87] Le Gal, A., Abanades, S., and Flamant, G., 2011, “CO₂ and H₂O Splitting for Thermochemical Production of Solar Fuels Using Nonstoichiometric Ceria and Ceria/Zirconia Solid Solutions,” *Energy & Fuels*, **25**(10), pp. 4836–4845.
- [88] Call, F., Roeb, M., Schmücker, M., Bru, H., Curulla-Ferre, D., Sattler, C., and Pitz-Paal, R., 2013, “Thermogravimetric Analysis of Zirconia-Doped Ceria for Thermochemical Production of Solar Fuel,” *Am. J. Anal. Chem.*, **04**(10), pp. 37–45.
- [89] Mogensen, M., 2000, “Physical, chemical and electrochemical properties of pure and doped ceria,” *Solid State Ionics*, **129**(1-4), pp. 63–94.
- [90] Singh, P., and Hegde, M. S., 2010, “Ce_{0.67}Cr_{0.33}O_{2.11}: A new low-temperature O₂ evolution material and H₂ generation catalyst by thermochemical splitting of water,” *Chem. Mater.*, **22**(3), pp. 762–768.
- [91] Kaneko, H., Miura, T., Ishihara, H., Taku, S., Yokoyama, T., Nakajima, H., and Tamaura, Y., 2007, “Reactive ceramics of CeO₂-MO_x (M=Mn, Fe, Ni, Cu) for H₂ generation by two-step water splitting using concentrated solar thermal energy,” *Energy*, **32**(5), pp. 656–663.
- [92] Bader, R., Bala Chandran, R., Venstrom, L. J., Sedler, S. J., Krenzke, P. T., De Smith, R. M., Banerjee, A., Chase, T. R., Davidson, J. H., and Lipinski, W., 2015, “Design of a Solar Reactor to Split CO₂ Via Isothermal Redox Cycling of Ceria,” *J. Sol. Energy Eng.*, **137**(3), p. 031007.
- [93] Scheffe, J. R., and Steinfeld, A., 2012, “Thermodynamic analysis of cerium-based oxides for solar thermochemical fuel production,” *Energy and Fuels*, **26**(3), pp. 1928–1936.
- [94] Apt, J., Newcomer, A., Lave, L. B., Douglas, S., and Morris Dunn, L., 2008, “An Engineering-Economic Analysis of Syngas Storage, Tepper School of Business, Paper 1120,” U.S. Dep. Energy’s Natl. Energy Technol. Lab., p. 143.
- [95] Shell Global Solutions, “Pearl GtL” [Online]. Available: <http://www.shell.com/about->

- us/major-projects/pearl-gtl.html. [Accessed: 01-Jan-2014].
- [96] Velocys, 2013, “Modular GTL – Economic Solution for Distributed Gas, 10th Natural Gas Conversion Symposium About Velocys / Oxford Catalysts Group,” Nat. Gas Convers. Symp., (March), pp. 2–7.
- [97] “CompactGTL” [Online]. Available: www.compactgtl.com. [Accessed: 20-Apr-2016].
- [98] Spath, P. L., and Dayton, D. C., 2003, “Preliminary Screening -- Technical and Economic Assessment of Synthesis Gas to Fuels and Chemicals with Emphasis on the Potential for Biomass-Derived Syngas,” Natl. Renew. Energy Lab., (December), pp. 1 – 160.
- [99] Dry, M. E., 2002, “High quality diesel via the Fischer-Tropsch process - A review,” J. Chem. Technol. Biotechnol., **77**(1), pp. 43–50.
- [100] “Gas to Liquids” [Online]. Available: [http://wiki.gekgasifier.com/w/page/6123715/Gas to Liquids](http://wiki.gekgasifier.com/w/page/6123715/Gas%20to%20Liquids). [Accessed: 23-Mar-2017].
- [101] Kromer, M., Roth, K., Takata, R., and Chin, P., 2011, Support for Cost Analyses on Solar-Driven High Temperature Thermochemical Water-Splitting Cycles; TIAX LLC; Reference D0535.
- [102] Graf, D., Monnerie, N., Roeb, M., Schmitz, M., and Sattler, C., 2008, “Economic comparison of solar hydrogen generation by means of thermochemical cycles and electrolysis,” Int. J. Hydrogen Energy, **33**, pp. 4511–4519.
- [103] Gómez, D. R., Watterson, J. D., Americanohia, B. B., Ha, C., Marland, G., Matsika, E., Namayanga, L. N., Osman-Elasha, B., Saka, J. D. K., and Treanton, K., 2006, 2006 IPCC Guidelines for National Greenhouse Gas Inventories: Chapter 2 Stationary Combustion.
- [104] Tsotsas, E., and Martin, H., 1987, “Thermal conductivity of packed beds: A review,” Chem. Eng. Process. Process Intensif., **22**(1), pp. 19–37.
- [105] Furler, P., Scheffe, J. R., and Steinfeld, A., 2012, “Syngas production by simultaneous splitting of H₂O and CO₂ via ceria redox reactions in a high-temperature solar reactor,” Energy Environ. Sci., **5**(3), p. 6098.
- [106] Pfeiffer Vacuum, 2014, “Private communication.”
- [107] Felinks, J., 2014, “Private communication.”
- [108] Zeman, F., 2007, “Energy and material balance of CO₂ capture from ambient air,” Environ. Sci. Technol., **41**(21), pp. 7558–7563.
- [109] Falter, C. P., Sizmann, A., and Pitz-Paal, R., 2015, “Modular reactor model for the solar thermochemical production of syngas incorporating counter-flow solid heat exchange,” Sol. Energy, **122**, pp. 1296–1308.
- [110] Marxer, D., Furler, P., Takacs, M., and Steinfeld, A., 2017, “Solar thermochemical splitting of CO₂ into separate streams of CO and O₂ with high selectivity, stability, conversion, and efficiency,” Energy Environ. Sci.
- [111] Howell, J. R., Siegel, R., Mengüç, M., and Pinar, R., 2011, Thermal Radiation Heat Transfer, CRC Press, Boca Raton.
- [112] Hischer, I., Hess, D., Lipiński, W., Modest, M., and Steinfeld, A., 2009, “Heat Transfer Analysis of a Novel Pressurized Air Receiver for Concentrated Solar Power via Combined Cycles,” J. Therm. Sci. Eng. Appl., **1**(4), p. 041002.
- [113] Zircar Zirconia, 2015, “Fibrous Insulation - Type Buster M35” [Online]. Available:

- <http://www.zircarzirconia.com/product-literature/buster.php>. [Accessed: 01-Jan-2015].
- [114] Engineering Toolbox, 2014, "Convective Heat Transfer" [Online]. Available: www.engineeringtoolbox.com. [Accessed: 01-Feb-2014].
- [115] Touloukian, Y. S., Powell, R. W., Ho, C. Y., and Klemens, P. G., 1971, Thermophysical Properties of Matter - The TPRC Data Series--Vol.2. Thermal Conductivity - Nonmetallic Solids, CINDAS/Purdue University.
- [116] Touloukian, Y. S., and DeWitt, D. P., 1972, Thermophysical Properties of Matter - The TPRC Data Series--Vol.8 Thermal Radiative Properties - Nonmetallic Solids, CINDAS/Purdue University.
- [117] Riess, I., Ricken, M., and Noelting, J., 1986, "Specific heat of non-stoichiometric ceria (CeO_x)," *Solid State Ionics*, **18-19**, pp. 725–726.
- [118] Siegel, N. P., Miller, J. E., Ermanoski, I., Diver, R. B., and Stechel, E. B., 2013, "Factors Affecting the Efficiency of Solar Driven Metal Oxide Thermochemical Cycles," *Ind. Eng. Chem. Res.*, **52**(9), pp. 3276–3286.
- [119] Miller, J. E., McDaniel, A. H., and Allendorf, M. D., 2014, "Considerations in the Design of Materials for Solar-Driven Fuel Production Using Metal-Oxide Thermochemical Cycles," *Adv. Energy Mater.*, **4**(2), p. 1300469.
- [120] Suter, S., Steinfeld, A., and Haussener, S., 2014, "Pore-level engineering of macroporous media for increased performance of solar-driven thermochemical fuel processing," *Int. J. Heat Mass Transf.*, **78**, pp. 688–698.
- [121] Zhang, B., Zhao, S., He, X., and Du, S., 2007, "High Temperature Thermal Physical Properties of High-alumina Fibrous Insulation," *J. Mater. Sci. Technol.*, **23**(6), pp. 860–864.
- [122] Wang, F., Shuai, Y., Tan, H., and Yu, C., 2013, "Thermal performance analysis of porous media receiver with concentrated solar irradiation," *Int. J. Heat Mass Transf.*, **62**(1), pp. 247–254.
- [123] Mey, S., Caliot, C., Flamant, G., Kribus, A., and Gray, Y., 2013, "Optimization of high temperature SiC volumetric solar absorber," *Energy Procedia*, **49**, pp. 478–487.
- [124] Petrov, V. A., 1997, "Combined radiation and conduction heat transfer in high temperature fiber thermal insulation," *Int. J. Heat Mass Transf.*, **40**(9), pp. 2241–2247.
- [125] Touloukian, Y., Saxena, S., and Hestermans, P., 1975, "Thermophysical Properties of Matter-the TPRC Data Series. Volume 11. Viscosity."
- [126] Special Metals, 2015, "Inconel Alloy 600" [Online]. Available: [www.specialmetals.com/documents/Inconel alloy 600.pdf](http://www.specialmetals.com/documents/Inconel%20alloy%20600.pdf). [Accessed: 01-Jun-2015].
- [127] Falter, C. P., and Pitz-Paal, R., 2017, "A generic solar-thermochemical reactor model with internal heat diffusion for counter-flow solid heat exchange," *Sol. Energy*, **144**, pp. 569–579.
- [128] Lapp, J., 2013, "Thermal modeling and design of a solar non-stoichiometric redox reactor with heat recovery," Dissertation, University of Minnesota.
- [129] Accuratus, 2016, "Aluminum Oxide, Al₂O₃ Ceramic Properties" [Online]. Available: <http://accuratus.com/alumox.html>. [Accessed: 25-Mar-2016].
- [130] Minter, C. C., 1963, Effect of Pressure on the Thermal Conductivity of a Gas, U. S. NAVAL RESEARCH LABORATORY, Washington. D.C.
- [131] Furler, P., 2014, "Solar thermochemical CO₂ and H₂O splitting via ceria redox

- reactions,” Dissertation, ETH Zürich.
- [132] U.S. Environmental Protection Agency, 2009, Toxicological Review Cerium Oxide and Cerium Compounds.
- [133] Kleiber, M., and Joh, R., 2013, VDI-Wärmeatlas, Kapitel D.
- [134] © The Mathworks Inc. MATLAB and Simulink are registered trademarks of The MathWorks Inc. See mathworks.com/trademarks for a list of additional trademarks. Other product or brand names may be trademarks or registered trademarks of their respective holders., 2015, “MATLAB.”
- [135] Ultramet, 2015, “Ceramic Protective Coatings” [Online]. Available: http://www.ultramet.com/ceramic_protective_coatings.html#layered. [Accessed: 15-Nov-2015].
- [136] Desmason-Brut, M., Tétard, D., Tixier, C., Faure, C., and Chabas, E., 2007, “Mechanical Properties and Oxidation Behaviour of Electroconductive Ceramic Composites,” 10th Int. Conf. Eur. Ceram. Soc., pp. 1315–1320.
- [137] Perkins, C., Lichty, P. R., and Weimer, A. W., 2008, “Thermal ZnO dissociation in a rapid aerosol reactor as part of a solar hydrogen production cycle,” *Int. J. Hydrogen Energy*, **33**(2), pp. 499–510.
- [138] Loutzenhiser, P. G., Gálvez, M. E., Hischier, I., Stamatou, A., Frei, A., and Steinfeld, A., 2009, “CO₂ Splitting via Two-Step Solar Thermochemical Cycles with Zn/ZnO and FeO/Fe₃O₄ Redox Reactions II: Kinetic Analysis,” *Energy & Fuels*, **23**(5), pp. 2832–2839.
- [139] Brendelberger, S., and Sattler, C., 2015, “Concept analysis of an indirect particle-based redox process for solar-driven H₂O/CO₂ splitting,” *Sol. Energy*, **113**, pp. 158–170.
- [140] Ho, C., Christian, J., Gill, D., Moya, a., Jeter, S., Abdel-Khalik, S., Sadowski, D., Siegel, N., Al-Ansary, H., Amsbeck, L., Gobereit, B., and Buck, R., 2013, “Technology advancements for next generation falling particle receivers,” *Energy Procedia*, **49**, pp. 398–407.
- [141] Ermanoski, I., and Orozco, A., 2015, “C2R2: Compact Compound Recirculator / Recuperator for Renewable Energy and Energy Efficient Thermochemical Processing,” SANDIA Report, SAND2015-7320, (August), pp. 1–46.
- [142] Tan, T., and Chen, Y., 2010, “Review of study on solid particle solar receivers,” *Renew. Sustain. Energy Rev.*, **14**(1), pp. 265–276.
- [143] Loutzenhiser, P. G., Elena Gálvez, M., Hischier, I., Graf, A., and Steinfeld, A., 2010, “CO₂ splitting in an aerosol flow reactor via the two-step Zn/ZnO solar thermochemical cycle,” *Chem. Eng. Sci.*, **65**(5), pp. 1855–1864.
- [144] Maag, G., Zanganeh, G., and Steinfeld, A., 2009, “Solar thermal cracking of methane in a particle-flow reactor for the co-production of hydrogen and carbon,” *Int. J. Hydrogen Energy*, **34**(18), pp. 7676–7685.
- [145] Schlünder, E., 1984, “Heat transfer to packed and stirred beds from the surface of immersed bodies,” *Chem. Eng. Process. Process Intensif.*, **18**(1), pp. 31–53.
- [146] Martin, H., Verfahrenstechnik, T., and Institut, K., 2013, VDI-Wärmeatlas, Springer Berlin Heidelberg, Berlin, Heidelberg.
- [147] Heyde, M., and Klocke, H.-J., 1979, “Wärmeübergang zwischen Wirbelschicht und Einbauten - ein Problem des Wärmeübergangs bei kurzfristigem Kontakt,” *Chemie Ing.*

- Tech., **51**(4), pp. 318–319.
- [148] Martin, H., 1980, “Wärme- und Stoffübertragung in der Wirbelschicht,” *Chemie Ing. Tech.*, **52**(3), pp. 199–209.
- [149] Ullrich, C., and Bodmer, T., 2013, *VDI-Wärmeatlas, D6 Stoffwerte von Feststoffen*, Springer Berlin Heidelberg, Berlin, Heidelberg.
- [150] Klan, H., 2013, *VDI-Wärmeatlas*, Springer Berlin Heidelberg, Berlin, Heidelberg.
- [151] Ernst, R., 1960, “Wärmeübergang an Wärmeaustauschern im Moving Bed,” *Chemie Ing. Tech. - CIT*, **32**(1), pp. 17–22.
- [152] Bauer, M., 2001, “Theoretische und experimentelle Untersuchungen zum Wärmetransport in gasdurchströmten Festbettrohrreaktoren,” Dissertation, Martin-Luther-Universität Halle-Wittenberg.
- [153] Tsotsas, E., 2013, *VDI-Wärmeatlas*, Springer Berlin Heidelberg, Berlin, Heidelberg.
- [154] Ofuchi, K., and Kunii, D., 1965, “Heat-transfer characteristics of packed beds with stagnant fluids,” *Int. J. Heat Mass Transf.*, **8**(5), pp. 749–757.
- [155] Wakao, N., and Kato, K., 1969, “Effective thermal conductivity of packed beds,” *J. Chem. Eng. Japan*, **2**(1), pp. 24–33.
- [156] Yagi, S., and Kunii, D., 1957, “Studies on effective thermal conductivities in packed beds,” *AIChE J.*, **3**(3), pp. 373–381.
- [157] Mantec Technical Ceramics, 2016, “Ultralite Insulating Firebricks - Technical Data Sheet” [Online]. Available: http://www.mantectechnicalceramics.com/sites/default/files/uifb_technical_data_sheet_june_2016_v5.pdf.
- [158] Harakas, N. K., and Beatty, K., 1963, “Moving Bed Heat Transfer: I Effect of Interstitial Gas with Fine Particles,” *Chem. Eng. Symp. Ser.*, **59**, pp. 122–128.
- [159] Pushnov, A. S., 2006, “Calculation of average bed porosity,” *Chem. Pet. Eng.*, **42**(1-2), pp. 14–17.
- [160] Chen, J. C., and Churchill, S. W., 1963, “Radiant heat transfer in packed beds,” *AIChE J.*, **9**(1), pp. 35–41.
- [161] Diver, R. B., Miller, J. E., Siegel, N. P., and Moss, T. A., 2010, “Testing of a CR5 Solar Thermochemical Heat Engine Prototype,” *Proceedings of the ASME 4th International Conference on Energy Sustainability*, pp. 97–104.
- [162] Miller, J. E., Allendorf, M. a, Ambrosini, A., Coker, E. N., Diver, R. B., Ermanoski, I., Evans, L. R., Hogan, R. E., and Mcdaniel, A. H., 2012, “Development and assessment of solar-thermal-activated fuel production: phase 1 summary,” *Sandia Rep.*, (July), pp. 1–38.
- [163] Sobieski, W., and Zhang, Q., 2014, “Sensitivity Analysis of Kozeny-Carman and Ergun Equations,” **17**(3), pp. 235–248.
- [164] Craft, B. C., and Hawkins, M., 1991, “Applied Petroleum Reservoir Engineering.”
- [165] Ergun, S., and Lu, A. P., 1952, “Fluid Flow Through Packed Columns,” *Chem. Eng. Prog.*, **48**(2), pp. 89–94.
- [166] Lechón, Y., de la Rúa, C., and Sáez, R., 2008, “Life Cycle Environmental Impacts of Electricity Production by Solarthermal Power Plants in Spain,” *J. Sol. Energy Eng.*, **130**(2), p. 021012.

- [167] Burkhardt, J. J., Heath, G., and Cohen, E., 2012, "Life Cycle Greenhouse Gas Emissions of Trough and Tower Concentrating Solar Power Electricity Generation: Systematic Review and Harmonization," *J. Ind. Ecol.*, **16**(SUPPL.1).
- [168] Piemonte, V., De Falco, M., Tarquini, P., and Giaconia, A., 2011, "Life cycle assessment of a high temperature molten salt concentrated solar power plant," *Sol. Energy*, **85**(5), pp. 1101–1108.
- [169] Werder, M., and Steinfeld, A., 2000, "Life cycle assessment of the conventional and solar thermal production of zinc and synthesis gas," *Energy*, **25**(5), pp. 395–409.
- [170] Felder, R., and Meier, A., 2008, "Well-To-Wheel Analysis of Solar Hydrogen Production and Utilization for Passenger Car Transportation," *J. Sol. Energy Eng.*, **130**(1), p. 011017.
- [171] Koroneos, C., Dompros, a., Roubas, G., and Moussiopoulos, N., 2004, "Life cycle assessment of hydrogen fuel production processes," *Int. J. Hydrogen Energy*, **29**(14), pp. 1443–1450.
- [172] Whitaker, M. B., Heath, G. a, Burkhardt, J. J., and Turchi, C. S., 2013, "Life Cycle Assessment of a Power Tower Concentrating Solar Plant and the Impacts of Key Design Alternatives," *Environ. Sci. Technol.*, **47**(11), pp. 5896–5903.
- [173] Brightsource Energy, 2010, "Ivanpah Project Facts" [Online]. Available: http://www.brightsourceenergy.com/stuff/contentmgr/files/0/8a69e55a233e0b7edfe14b9f77f5eb8d/folder/ivanpah_fact_sheet_3_26_14.pdf.
- [174] Milnes, M., "The mathematics of pumping water," *R. Acad. Eng.* [Online]. Available: http://www.raeng.org.uk/education/diploma/maths/pdf/exemplars_advanced/17_pumping_water.pdf. [Accessed: 01-Jan-2013].
- [175] Van Der Giesen, C., Kleijn, R., and Kramer, G. J., 2014, "Energy and climate impacts of producing synthetic hydrocarbon fuels from CO₂," *Environ. Sci. Technol.*, **48**(12), pp. 7111–7121.
- [176] Häring, H. W., and Ahner, C., 2008, *Industrial Gases Processing*, Wiley - VCH Verlag GmbH & Co. KgaA, Weinheim, Germany.
- [177] Beiermann, D., 2007, "Development of an Upgrading Model and Application to XtL Processes Integration of the upgrading unit into the BtL process chain," *DGMK/SCI-Conference*, pp. 199–206.
- [178] Institute for Applied Ecology, 2008, "Gemis."
- [179] Stine, W. B., and Diver, R. B., 1994, *A compendium of solar dish/Stirling technology*, SAND93-7026 UC-236.
- [180] Technisches Komitee ISO/TC "Environmental management" in Zusammenarbeit mit dem CEN-Management-Zentrum (CMC), 2009, "ISO 14040: Umweltmanagement - Ökobilanz - Grundsätze und Rahmenbedingungen," pp. 1–44.
- [181] Technisches Komitee ISO/TC "Environmental management" in Zusammenarbeit mit dem CEN-Management-Zentrum (CMC), 2006, "ISO 14044: Umweltmanagement - Ökobilanz - Anforderungen und Anleitungen," pp. 1–84.
- [182] Raluy, G., Serra, L., and Uche, J., 2006, "Life cycle assessment of MSF, MED and RO desalination technologies," *Energy*, **31**(13), pp. 2025–2036.
- [183] Koltun, P., and Tharumarajah, A., 2014, "Life Cycle Impact of Rare Earth Elements," *ISRN Metall.*, **2014**, pp. 1–10.

- [184] Hoek, A., 2005, "The Shell GTL Process: Towards a World Scale Project in Qatar," *Chemie Ing. Tech.*, **77**(8), pp. 1172–1172.
- [185] Marano, J., and Ciferno, J., 2001, "Life-cycle greenhouse-gas emissions inventory for Fischer-Tropsch fuels," Energy and Environmental Solutions, LLC.
- [186] Gröngröft, A., Meisel, K., Hauschild, S., Grasemann, E., Peetz, D., Meier, K., Roth, A., Riegel, F., and Endres, C., 2014, Abschlussbericht Projekt BurnFAIR.
- [187] Mandil, C., 2005, "Energy Statistics–Manual," Int. Energy Agency, Paris, Fr., pp. 1–196.
- [188] Noone, C. J., Torrillon, M., and Mitsos, A., 2012, "Heliostat field optimization: A new computationally efficient model and biomimetic layout," *Sol. Energy*, **86**(2), pp. 792–803.
- [189] Schmitz, M., Schwarzbözl, P., Buck, R., and Pitz-Paal, R., 2006, "Assessment of the potential improvement due to multiple apertures in central receiver systems with secondary concentrators," *Sol. Energy*, **80**(1), pp. 111–120.
- [190] Coventry, J., and Pye, J., 2013, "Heliostat cost reduction - Where to now?," *Energy Procedia*, **49**, pp. 60–70.
- [191] Pfahl, A., 2013, "Survey of Heliostat Concepts for Cost Reduction," *J. Sol. Energy Eng.*, **136**(1), p. 014501.
- [192] Kolb, G. J., Jones, S. A., Donnelly, M. W., Gorman, D., Thomas, R. C., Davenport, R., and Lumia, R., 2007, Heliostat cost reduction study., Albuquerque, NM, and Livermore, CA.
- [193] Google, 2014, RE < C : Heliostat Project Overview.
- [194] Pfahl, A., Brucks, A., and Holze, C., 2014, "Wind Load Reduction for Light-weight Heliostats," *Energy Procedia*, **49**, pp. 193–200.
- [195] Bierman, B., O'Donnell, J., Burke, R., McCormick, M., and Lindsay, W., 2013, "Construction of an Enclosed Trough EOR system in South Oman," *Energy Procedia*, **49**, pp. 1756–1765.
- [196] United Nations, 2013, UN water scarcity fact sheet.
- [197] Hoekstra, A. Y., Chapagain, A. K., Aldaya, M. M., and Mekonnen, M. M., 2011, *The Water Footprint Assessment Manual*, Earthscan Ltd., London, Washington, D.C.
- [198] Norsk Hydro ASA, "How alumina is extracted from bauxite" [Online]. Available: <http://www.hydro.com/en/About-aluminium/Aluminium-life-cycle/Alumina-refining/>. [Accessed: 08-May-2015].
- [199] US Department of Energy, 2006, "Energy Demands on Water Resources," Report to Congress on the Interdependency of Energy and Water, U.S. DoE.
- [200] Wu, M., Mintz, M., Wang, M., and Arora, S., 2009, "Water consumption in the production of ethanol and petroleum gasoline," *Environ. Manage.*, **44**(5), pp. 981–997.
- [201] Vera-Morales, M., and Schäfer, A., 2009, "Final Report: Fuel-Cycle Assessment of Alternative Aviation Fuels," University of Cambridge Institute for Aviation and the Environment.
- [202] Dominguez-Faus, R., Powers, S. E., Burken, J. G., and Alvarez, P. J., 2009, "The water footprint of biofuels: A drink or drive issue?," *Environ. Sci. Technol.*, **43**(9), pp. 3005–3010.

- [203] Mekonnen, M., and Hoekstra, A., 2010, “The green, blue and grey water footprint of crops and derived crop products, Vol. 1 - Main Report, Value of Water Research Report Series No. 47,” **2**(47), pp. 1–1196.
- [204] Gerbens-Leenes, W., Hoekstra, A. Y., and van der Meer, T. H., 2009, “The water footprint of bioenergy,” *Proc. Natl. Acad. Sci. U. S. A.*, **106**(25), pp. 10219–10223.
- [205] Yang, J., Xu, M., Zhang, X., Hu, Q., Sommerfeld, M., and Chen, Y., 2011, “Life-cycle analysis on biodiesel production from microalgae: Water footprint and nutrients balance,” *Bioresour. Technol.*, **102**(1), pp. 159–165.
- [206] Don Hofstrand, 2008, “Liquid Fuel Measurements and Conversions,” (October), pp. 1–4 [Online]. Available: <http://www.extension.iastate.edu/agdm/>. [Accessed: 01-Jan-2015].
- [207] Trieb, F., Schillings, C., O’Sullivan, M., Pregger, T., and Hoyer-Klick, C., 2009, “Global potential of concentrating solar power,” *SolarPACES 2009*.
- [208] Riegel, F., 2014, “Das nachhaltige Potenzial von Flüssigkraftstoffen aus Biomasse: Eine globale Abschätzung auf der Basis von hochaufgelösten Geodaten,” Dissertation, submitted, Ludwig-Maximilians-Universität München.
- [209] Haije, W., and Geerlings, H., 2011, “Efficient Production of Solar Fuel Using Existing Large Scale Production Technologies,” *Environ. Sci. Technol.*, **45**(20), pp. 8609–8610.
- [210] König, D. H., Freiberg, M., Dietrich, R.-U., and Wörner, A., 2015, “Techno-economic study of the storage of fluctuating renewable energy in liquid hydrocarbons,” *Fuel*, **159**, pp. 289–297.
- [211] European Academies Science Advisory Council, 2011, *Concentrating solar power: its potential contribution to a sustainable energy future*.
- [212] Eberle, M. K., 2010, “Sonnenkraft aus der Steckdose - Concentrating Solar Power (CSP) – eine Renaissance,” *ETH Zürich, Treffpunkt Science City 9. Mai 2010*.
- [213] McDonald, R. I., Fargione, J., Kiesecker, J., Miller, W. M., and Powell, J., 2009, “Energy sprawl or energy efficiency: Climate policy impacts on natural habitat for the United States of America,” *PLoS One*, **4**(8).
- [214] Hall, D. O., and Rao, K. K., 1999, *Photosynthesis*, Cambridge University Press.
- [215] Blankenship, R. E., Tiede, D. M., Barber, J., Brudvig, G. W., Fleming, G., Ghirardi, M., Gunner, M. R., Junge, W., Kramer, D. M., Melis, A., Moore, T. a, Moser, C. C., Nocera, D. G., Nozik, A. J., Ort, D. R., Parson, W. W., Prince, R. C., and Sayre, R. T., 2011, “Comparing photosynthetic and photovoltaic efficiencies and recognizing the potential for improvement,” *Science*, **332**(6031), pp. 805–809.
- [216] Brown, P., and Whitney, G., 2011, “U.S. Renewable Electricity Generation : Resources and Challenges,” *Congressional Research Service*.
- [217] 2015, “Gaskraftwerk Irsching” [Online]. Available: <http://www.tagesschau.de/wirtschaft/gaskraftwerk-irsching-103~nimex.html>. [Accessed: 21-Apr-2015].
- [218] CliffsNotes, “Capital Budgeting Techniques” [Online]. Available: <http://www.cliffsnotes.com/more-subjects/accounting/accounting-principles-ii/capital-budgeting/capital-budgeting-techniques>. [Accessed: 21-Apr-2015].
- [219] Energypedia, “Annuity Method” [Online]. Available: https://energypedia.info/wiki/Annuity_Method. [Accessed: 21-Apr-2015].

- [220] Short, W., Packey, D. J., and Holt, T., 1995, "A Manual for the Economic Evaluation of Energy Efficiency and Renewable Energy Technologies," NREL/TP-462-5173.
- [221] International Air Transport Association, "Jet Fuel Price Development" [Online]. Available: <http://www.iata.org/publications/economics/fuel-monitor/Pages/price-development.aspx>. [Accessed: 30-Mar-2016].
- [222] "Historic Naphtha Prices" [Online]. Available: <http://www.finanzen.net/rohstoffe/naphtha/historisch>. [Accessed: 17-Feb-2015].
- [223] International Air Transport Association, "Fuel Price Analysis" [Online]. Available: <http://www.iata.org/publications/economics/fuel-monitor/Pages/price-analysis.aspx>. [Accessed: 01-Jan-2015].
- [224] International Renewable Energy Agency, 2012, "Volume 1: Power Sector, Concentrating Solar Power," IRENA working paper.
- [225] Heath, G. A., Burkhardt, J. J., and Turchi, C. S., 2012, "Life Cycle Environmental Impacts Resulting from the Manufacture of the Heliostat Field for a Reference Power Tower Design in the United States," SolarPACES 2012, Marrakech, Morocco, pp. 6–12.
- [226] Mancini, T. R., Gary, J. A., Kolb, G. J., and Ho, C. K., 2011, Power Tower Technology Roadmap and Cost Reduction Plan., Albuquerque, NM, and Livermore, CA (United States).
- [227] Turchi, C., Mehos, M., Ho, C. K., and Kolb, G. J., 2010, "Current and Future Costs for Parabolic Trough and Power Tower Systems in the US Market," SolarPACES 2010, Perpignan, France.
- [228] SunShot U.S. Department of Energy, 2012, "SunShot Vision Study," U.S. Dep. Energy, pp. 69–96.
- [229] Monreal, A., Burisch, M., Sanchez, M., Pérez, D., Villasante, C., Olabarrieta, E., Olasolo, D., and Olarra, A., 2014, "EASY: An Innovative Design for Cost Effective Heliostats/Solar Fields," Energy Procedia, **49**, pp. 174–183.
- [230] Williamson, S. H., 2015, "Seven Ways to Compute the Relative Value of a U.S. Dollar Amount, 1774 to present" [Online]. Available: <http://www.measuringworth.com/uscompare/relativevalue.php>. [Accessed: 22-Apr-2015].
- [231] "Ozforex, foreign exchange services - Yearly average rates" [Online]. Available: <http://www.ozforex.com.au/forex-tools/historical-rate-tools/yearly-average-rates>. [Accessed: 22-Apr-2015].
- [232] "Metal prices of cerium" [Online]. Available: <http://www.metal-pages.com/metalprices/cerium/>. [Accessed: 26-Feb-2015].
- [233] Velocys, 2013, "Private Communication."
- [234] Goellner, J. F., Shah, V., Turner, M. J., Kuehn, N. J., Littlefield, J., Cooney, G., and Marriott, J., 2013, "Analysis of Natural Gas-to Liquid Transportation Fuels via Fischer-Tropsch," NETL-Report 2013/1597.
- [235] www.Match.com, "Equipment cost" [Online]. Available: <http://match.com/equipcost/Compressor.html>. [Accessed: 21-May-2015].
- [236] Rutgers Edward J. Bloustein School of Planning and Public Policy, 2010, "CHP Database" [Online]. Available: <http://ceep.rutgers.edu/combined-heat-and-power->

- cost-benefit-analysis-materials/. [Accessed: 23-Apr-2015].
- [237] Fritzmann, C., Lowenberg, J., Wintgens, T., and Melin, T., 2007, "State-of-the-art of reverse osmosis desalination," *Desalination*, **216**(1-3), pp. 1–76.
- [238] Diver, R., Kolb, G., and Price, H., 1997, "Solar power tower," *Renewable Energy Technology Characterizations*, Chapter 5: Solar Thermal, United States Department of Energy.
- [239] Velocys Inc., 2012, "Workshop presentation," Pemex – World Bank GGFR Gas Utilization and Flare Reduction Workshop, Veracruz, Mexico.
- [240] van Vliet, O. P. R., Faaij, A. P. C., and Turkenburg, W. C., 2009, "Fischer-Tropsch diesel production in a well-to-wheel perspective: A carbon, energy flow and cost analysis," *Energy Convers. Manag.*, **50**(4), pp. 855–876.
- [241] Edwards, R., Larivé, J.-F., and Beziat, J.-C., 2004, "Well-to-wheels analysis of alternative fuels and powertrains in the European context," Joint Research Centre.
- [242] Larson, E. D., Jin, H., and Celik, F. E., 2005, "Gasification-Based Fuels and Electricity Production from Biomass, without and with Carbon Capture and Storage," Princeton University, Environmental Institute.
- [243] Hamelinck, C. N., and Faaij, a. P. C., 2002, "Future prospects for production of methanol and hydrogen from biomass," *J. Power Sources*, **111**(1), pp. 1–22.
- [244] Kost, C., Mayer, J. N., Thomsen, J., Hartmann, N., Senkpiel, C., Philipps, S., Nold, S., Lude, S., and Schlegl, T., 2013, "Studie Stromgestehungskosten Erneuerbare Energien," Fraunhofer-Institut für solare Energiesysteme ISE, (November), p. 45.
- [245] Rubin, E., Meyer, L., and de Coninck, H., 2005, "Technical Summary," IPCC Special Report on Carbon dioxide Capture and Storage, B. Metz, O. Davidson, H. de Coninck, M. Loos, and M. Meyer, eds., Cambridge University Press, Geneva, Switzerland.
- [246] Ramezan, M., Skone, T. J., Nsakala, N., and Liljedahl, G., 2007, "Carbon Dioxide Capture from Existing Coal-Fired Power Plants," US Department of Energy, DOE/NETL-401/110907.
- [247] U.S. Department of Energy, 2011, Biomass Energy Data Book.
- [248] Pérez, D., Fondo, C., and Gutierrez, L., 2014, "PV Grid Parity Monitor, Utility Scale, 1st Issue" [Online]. Available: http://www.leonardo-energy.org/sites/leonardo-energy/files/documents-and-links/pv_gpm_4_utility_2014.pdf. [Accessed: 15-Mar-2015].
- [249] International Energy Agency, 2013, CO₂ Emissions from Fuel Combustion Highlights.
- [250] International Energy Agency, "MTMR" [Online]. Available: <http://www.iea.org/publications/mtmr/countries/morocco/>. [Accessed: 01-Feb-2015].
- [251] Langas, H., 2015, "Large scale hydrogen production," NEL Hydrogen, Renewable Energy and Hydrogen Export, presentation.
- [252] Heath, G. A., and J. J. Burkhardt III, 2011, "Meta-Analysis of Estimates of Life Cycle Greenhouse Gas Emissions from Concentrating Solar Power," SolarPACES 2011, Granada, Spain.
- [253] Tidball, R., Bluestein, J., Rodriguez, N., and Knoke, S., 2010, Cost and performance assumptions for modeling electricity generation technologies; NREL; NREL/SR-6A20-48595.
- [254] Engineering Toolbox, 2015, "Specific Heat Capacity of Gases" [Online]. Available:

www.engineeringtoolbox.com. [Accessed: 30-Oct-2015].

List of Figures

Figure 2.1 Schematic of solar thermochemical jet fuel production pathway.....	6
Figure 2.2 Theoretical separation work for a mixture of two gases and experimental values from the literature (Zeman et al. [43], Keith et al. [44], Baciocchi et al. [45], APS [46], Sterner [47], Stolaroff [48], Climeworks [42], Nikulshyna [36]). For comparison, the higher heating value of one mol of CO is $283.4 \text{ kJ mol}^{-1}$	9
Figure 2.3 Two CSP tower plants in Spain (PS10 and PS20) [53]......	11
Figure 2.4 The Big Dish prototype at the campus of the Australian National University [56].	13
Figure 2.5 Oxygen nonstoichiometry of pure CeO_2 as a function of temperature and oxygen partial pressure (reprinted from [82] with permission from Elsevier).	18
Figure 2.6 Schematic of two Fischer-Tropsch reactors: (a) Tubular fixed bed reactor, b) slurry bed reactor for the production of long-chained hydrocarbons such as jet fuel (figure taken from [100])......	21
Figure 3.1 Schematic of generic reactor model including n chambers, one each for reduction ($i=1$) and oxidation ($i = n$), and $n-2$ physical heat exchange chambers ($i = 2 \dots n-1$), each containing the mass m of reactive material. Each heat exchanger chamber is subdivided in an upper and a lower half-chamber by a gas-tight separating wall.....	36
Figure 3.2 Schematic of upper and lower heat exchanger control volumes in the k -th chamber between two chamber openings, i.e. for $t \in [n\Delta t; (n+1)\Delta t]$. Heat is transferred by radiation from the upper chamber at $T_{k,u}$ to the lower chamber at $T_{k,l}$ and energy is lost to the surroundings by radiation and convection.	38
Figure 3.3 Comparison of results of the generic model and of the model by Ermanoski et al. in [18]. Shown are values of thermodynamic cycle efficiency η as a function of reduction pressure p_{red} and heat exchanger efficiency η_{he}	41
Figure 3.4 Comparison of results of the generic model and of the model by Chueh and Haile in [86]. Shown are values of thermodynamic cycle efficiency η as a function of reduction temperature T_H and oxidation temperature T_L . Heat recuperation efficiency from the gaseous and solid phase is zero.....	41
Figure 3.5 Temperature profile for generic reactor model with $n = 80$ chambers and a residence time Δt of 10 s and other parameters from Table 3.1.....	44

Figure 3.6 Energy balance of generic vacuum reactor with $n = 80$ chambers and a residence time Δt of 10 s. The two values shown for gas separation and pump power are based on the minimum thermodynamic work (black bars) and realistic efficiencies (grey bars). The oxidation temperature T_L is 1000 K and the reduction temperature T_H is 1800 K. Energy from gas heat recuperation is negative.....	45
Figure 3.7 Idealized (thermodynamic work for vacuum pump and gas separation assumed) and realistic (realistic efficiencies for vacuum pump and gas separation assumed) efficiency of generic vacuum reactor with $n = 80$ chambers and a residence time $\Delta t = 10$ s as a function of reduction temperature T_H for different values of reduction oxygen partial pressure p_{O_2} (relative to standard state of 1 atm). Realistic pump efficiencies are 1.3%, 6.7% and 84.4% for the pressures of $p_{O_2}=10^{-5}, 10^{-3}$ and 1, respectively. The oxidation temperature is chosen such as to maximize efficiency with values of T_L in the range 750-1250 K, depending on T_H and p_{O_2}	47
Figure 3.8 Contour plot of heat exchanger efficiency of generic vacuum reactor with $n = 80$ chambers and a residence time $\Delta t = 10$ s as a function of oxidation temperature T_L and reduction temperature T_H	48
Figure 3.9 Contour plot of idealized (thermodynamic work for vacuum pump and gas separation assumed) and realistic (realistic efficiencies for vacuum pump and gas separation assumed) cycle efficiency of generic vacuum reactor with $n = 80$ chambers and a residence time $\Delta t = 10$ s as a function of oxidation temperature T_L and reduction temperature T_H for a reduction oxygen partial pressure of 10^{-3} atm.	50
Figure 3.10 Efficiency of the thermodynamic cycle η and of the heat exchanger η_{he} as a function of the number of heat exchanger chambers n_{he} and the residence time per chamber Δt	51
Figure 3.11 Efficiency of the thermodynamic cycle η and of the heat exchanger η_{he} as a function of the total residence time of the reactive material in the heat exchanger $n_{he} \times \Delta t$	51
Figure 3.12 Comparison of temperature profiles in upper and lower chambers for idealized internal heat transfer within the reactive medium and modeled internal heat transfer using the Rosseland diffusion approximation and the three resistor model. See Section 3.3.4 for equations and Figure 3.13 for an illustration of the approach for the calculations. The heat exchanger has eight chambers with a residence time of 10 s each. This example shows that internal heat transfer may have a significant influence on the performance of the heat exchanger.	54

Figure 3.13 Schematic of one representative heat exchanger chamber for the modeling of radiation heat exchange between chamber halves and internal heat transfer in the reactive medium and adjacent insulation. Indicated are also the boundary conditions and the movement of the reactive material.	59
Figure 3.14 Schematic of representative porous media volume elements in finite volume discretization. Shown are the upper chamber halves of three adjacent chambers.	67
Figure 3.15 Schematic of test case used for validation of the Rosseland diffusion model with the Monte Carlo model. At the beginning of the simulation, two RPCs, separated by two layers of SiC/HfC and Al ₂ O ₃ (1 mm thickness each) are at temperatures of 1600 K and 1200 K, respectively, with adiabatic boundary conditions towards the environment. In the transient simulation, the temperature profiles of the RPCs and the separating walls are calculated after 40 s with both models and compared.	69
Figure 3.16 Temperature profiles obtained with the Monte Carlo model (MC) and the Rosseland diffusion approximation (RDA) for two RPCs separated by two layers of SiC/HfC and Al ₂ O ₃ (1 mm thickness each), after 40 s of heat exchange. The starting temperatures are 1600 K for the first RPC ($0 \leq x \leq 50$ mm) and the walls ($50 < x \leq 52$ mm), and 1200 K for the second RPC ($53 \leq x \leq 103$ mm).	69
Figure 3.17 Comparison of computational domains for calculations a) with separating walls and b) without separating walls. Shown is one generic heat exchanger chamber.	72
Figure 3.18 Cycle efficiency η and heat exchanger efficiency η_{he} as a function of the number of heat exchanger chambers $n_{he}=(n-2)$ and residence time per chamber Δt . Parameter values are defined according to Table 3.3.	74
Figure 3.19 Cycle and heat exchanger efficiency as a function of the total residence time of the elements in the heat exchanger $n_{he} \times \Delta t$. At a given value of total residence time, a larger number of chambers reduces the irreversibilities of the heat exchange process by introduction of more intermediate temperature levels. Parameter values are defined according to Table 3.3.	75
Figure 3.20 Cycle efficiency and heat exchanger efficiency as a function of reduction and oxidation temperatures for a heat exchanger with $n = 10$ chambers at a residence time of 40 s and a material thickness of 0.05 m. All other parameter values are defined according to Table 3.3.	76
Figure 3.21 Heat exchanger efficiency η_{he} and cycle efficiency η as a function of RPC thickness for a heat exchanger with $n = 10$ chambers at a residence time of 40 s. All other parameter values are defined according to Table 3.3.	78

Figure 3.22 Comparison of heat exchanger temperature profiles for an RPC thickness of a) 0.02 m and b) 0.10 m. The heat exchanger has 8 chambers ($2 \leq i \leq 9$). Shown is the temperature profile of the heat exchanger including insulation and walls. The thinner material is heated more evenly to a higher temperature and thus allows for a higher heat exchanger efficiency (compare temperature profile in lower chamber half at $i = 2$). Parameter values are defined according to Table 3.3.	79
Figure 3.23 Heat exchanger efficiency η_{he} and cycle efficiency η as a function of porosity of the reactive elements for a heat exchanger with $n = 10$ chambers at a residence time of 40 s, and a material thickness of 0.05 m. All other parameter values are defined according to Table 3.3.	81
Figure 3.24 Heat exchanger efficiency and cycle efficiency as a function of oxygen partial pressure for a heat exchanger with $n = 10$ chambers at a residence time of 40 s. All other parameter values are defined according to Table 3.3.	82
Figure 3.25 Schematic of particle heat exchanger model including computational domains. .	89
Figure 3.26 Schematic of finite volume discretization of computational domains.	98
Figure 3.27 Comparison of modeled and experimental values of overall heat transfer coefficient α relative to the wall-bed heat transfer coefficient α_{ws} , for a moving bed of quartz sand particles. The experimental values are from Ernst [151].	99
Figure 3.28 Comparison of modeled bed thermal conductivities relative to fluid thermal conductivities with experimental values of Ofuchi and Kunii [154] and Wakao and Kato [155].	101
Figure 3.29 Schematic representation of a) experimental setup in [156] (reprinted with permission from Wiley and sons) which has been used in a similar way in [155] and b) the computational model domains used for the calculations.	102
Figure 3.30 Comparison of modeled and experimental temperatures of a particle bed in a double-walled tube with a heated inner section (setup: compare Figure 3.29). Experimental values are from [155]. The difference of the computational and experimental values is partly explained by deviating material properties and unknown experimental conditions which could not fully be represented by the model.	103
Figure 3.31 Efficiencies of the thermodynamic cycle η and of the heat exchanger η_{he} as a function of reduction and oxidation temperatures T_{H} , T_{L}	107
Figure 3.32 Simplified thermal resistance network of heat transfer between particle beds. ...	108
Figure 3.33 Heat exchanger efficiency η_{he} , thermodynamic cycle efficiency η and solar power input Q_{solar} as a function of particle diameter.	111

Figure 3.34 Heat exchanger efficiency η_{he} , thermodynamic cycle efficiency η and solar power input Q_{solar} as a function of heat exchanger length.....	113
Figure 3.35 Heat exchanger efficiency η_{he} , thermodynamic cycle efficiency η and solar power input Q_{solar} as a function of the residence time of the particles in the heat exchanger.	114
Figure 3.36 Heat exchanger efficiency η_{he} , cycle efficiency η and solar power input Q_{solar} as a function of hot bed thickness. The radial dimensions of the cold particle bed are adjusted such as to ensure mass conservation.....	115
Figure 3.37 Ratio of oxidant (CO_2) loss through pressure difference over particle bed $n_{CO_2,loss}$ to oxidant required for oxidation $n_{CO_2,Ox}$	118
Figure 3.38 Improvements of thermodynamic cycle efficiency η for favorable changes of the baseline case assumptions. The heat exchanger efficiency is 70% in all cases and the oxygen partial pressure during reduction is 10^{-3} atm.	121
Figure 4.1 Energy and mass balance of baseline layout of solar thermochemical fuel production plant. Solar energy enters the system and is converted into heat and electricity, where the former is performed with a solar tower concentrator and the latter with a dedicated CSP plant. H_2O is supplied by pipeline transport from the seawater desalination plant and CO_2 by capture from the atmosphere. Most of the energy is required for the thermochemical conversion of H_2O and CO_2 to H_2 and CO (syngas). The syngas is converted by Fischer-Tropsch synthesis and subsequent hydrocracking and distillation into jet fuel, naphtha, and gaseous products. The latter are combusted in a combined heat and power plant (CHP) and converted into heat and electricity for the process. All energies and masses are expressed with respect to the production of one liter of jet fuel and 0.87 liters of naphtha.	129
Figure 4.2 Life-cycle assessment framework including the stages of the analysis. Figure after [180].	132
Figure 4.3 Origin of WTW life cycle greenhouse gas emissions for the production of jet fuel in the baseline case. a) Absolute values including negative emissions by CO_2 capture from the atmosphere, b) contributions to positive CO_2 emissions (without CO_2 capture) which add up to $3.59 \text{ kg}_{CO_2\text{-eq.}} \text{ L}^{-1}$. The overall emissions of $0.49 \text{ kg}_{CO_2\text{-eq.}} \text{ L}^{-1}$ are derived by offsetting the positive emissions by the capture of $3.11 \text{ kg}_{CO_2\text{-eq.}} \text{ L}^{-1}$ from the atmosphere. The largest shares are due to combustion, FT conversion, and the solar concentration infrastructure.	142
Figure 4.4 Sensitivity of life cycle GHG emissions for a variation of $\pm 10\%$ of efficiency of thermochemical syngas production, annual amount of direct normal solar irradiation, lifetime of the plant, and emission factor for the solar concentration infrastructure, assuming a constant output of 1000 bpd of jet fuel.	145

Figure 4.5 Contributions to overall on-site water consumption in the baseline case of the solar thermochemical fuel production plant.....	151
Figure 4.6 Contributions to overall off-site water consumption of baseline solar fuel production plant.....	152
Figure 4.7 Distribution of on-site and off-site water consumption for baseline solar fuel production plant. On-site water consumption is dominated by mirror cleaning, off-site water consumption is dominated by ceria mining.....	153
Figure 4.8 Area-specific productivities of the solar thermochemical fuel pathway in comparison with biomass-based pathways (BtL, HEFA, ethanol, sources: [186,208]) and power-to-liquid pathways (PtL, based on different sources of electricity, sources: [209,211–213,216] and own computations). The results are given in liters of jet fuel equivalent per hectare and year, where the conversion is done on an energy basis (LHV). The grey and black bars denote the actually covered land area (black) and the totally affected land area for wind power (grey), plants in Spain (grey) and under a higher solar resource of $2500 \text{ kWh m}^{-2} \text{ y}^{-1}$ (black) for solar trough and tower, and plant locations in Germany (grey) and the US (black) for solar PV. The assumptions are ideal conditions for plant growth of the biomass-based pathways and favorable developments of the thermochemical conversion efficiency and the energy penalty of carbon dioxide capture for the solar thermochemical pathway as described in Section 4.3.1.....	160
Figure 4.9 Development of market prices of crude oil and a) jet fuel [221] and b) naphtha [222] in recent years. Prices of both jet fuel and naphtha are correlated with the crude oil price, as they are derived from it through refining processes.	164
Figure 4.10 Distribution of investment costs of baseline case plant. The investment costs are strongly dominated by the solar concentration infrastructure. The thermochemical reactors including the reactive material have a share of 11%. All other components only have minor contributions. As the overall economics are strongly influenced by the investment costs, solar concentration presents a large cost driver.	170
Figure 4.11 Distribution of operation and maintenance costs of baseline plant. The O&M costs are dominated by the solar field, CSP electricity provision, and CO ₂ air capture. All other components together contribute less than 4%.....	174
Figure 4.12 Major cost components of solar thermochemical jet fuel production. “I” denotes investment costs and “O&M” operation and maintenance costs.	175
Figure 4.13 Sensitivity of production costs for a variation of $\pm 10\%$ of selected variables. ..	176

Figure 4.14 Schematic of the provision of resources, heat and electrical power in case of CO ₂ capture from a NGCC power plant. CO ₂ and electricity are supplied by the NGCC plant. Surplus electricity is fed into the local grid.....	180
Figure 4.15 Material and energy balance of NGCC plant for the provision of CO ₂ and electricity to the solar thermochemical fuel production plant. The NGCC plant is sized to provide exactly the required amount of CO ₂ for the production of 1000 bpd of jet fuel and 865 bpd of naphtha. The produced electricity from the plant is used for fuel production and the surplus electricity is sold to the local market.	181
Figure 4.16 Schematic of provision of resources, heat and electricity for the solar thermochemical fuel production process in case of the use grid electricity. CO ₂ is captured from the air and electricity is supplied by the grid.....	183
Figure 4.17 Schematic of Power-to-Liquid fuel production pathway.....	188
Figure A.1 Actual pump efficiency data as provided by Pfeiffer Vacuum [106,107] and a function to fit the data including its mathematical description.	222
Figure A.2 Extinction coefficient of a porous medium as a function of material porosity after [120].	223
Figure A.3 Thermal conductivity of RPC as a function of porosity φ and temperature T	224
Figure A.4 Overall thermal conductivity in $\text{W m}^{-1} \text{K}^{-1}$ including conduction and radiation as a function of temperature T and porosity φ	225

List of Tables

Table 2.1 Annual average efficiency of solar tower concentration at the Gemasolar CSP plant [50]. Field optical efficiency includes cosine losses, and losses due to blocking and shading, heliostat tracking, and focal length and shape deviations.	11
Table 2.2 Annual average efficiency of solar dish concentration [56]. Intercept includes losses due to slope errors and misalignment of mirror and receiver.	12
Table 3.1 Parameter values for example system.	43
Table 3.2 Numerical energy requirements corresponding to Figure 3.6.	45
Table 3.3 Chosen parameter values for the baseline case.	73
Table 3.4 Parameters for basic configuration of particle heat exchanger.	105
Table 3.5 Assumptions for baseline case and improved scenario.	120
Table 4.1 Overview of well-to-tank (WTT) and well-to-wake (WTW) greenhouse gas emissions of baseline solar fuel production plant. Results are shown for the single process steps per liter of jet fuel, per liter of naphtha, and per functional unit (1 L jet fuel + 0.87 L naphtha).	141
Table 4.2 Overall on-site water consumption of the fuel production plant.	151
Table 4.3 Overall off-site water consumption of the baseline solar fuel production plant. ...	152
Table 4.4 Overview of water footprints of different fuel production pathways in liters of water per liters of product (gasoline, jet fuel, ethanol, biodiesel, FT liquids) and converted to the common metric of liters of jet fuel, where the conversion is based on lower heating value equivalents. The calculated water footprint for the solar thermochemical fuel pathway is low compared to biofuel pathways. The lowest footprint is achieved for the fossil fuel pathways because of the low water intensity of the involved process steps.	156
Table 4.5 Overview of investment costs of the baseline case plant.	169
Table 4.6 Overview of operation and maintenance costs of the baseline plant.	174
Table 4.7 Investment costs and O&M costs of baseline case production facility with solar tower concentration.	186
Table 4.8 Investment costs and O&M costs of 1000 bpd jet fuel production facility with solar dish concentration.	186
Table A.1 Assumptions for baseline case of fuel production plant.	226
Table A.2 Assumptions for ecological analysis.	227

Table A.3 Fuel properties.....	228
Table A.4 Assumptions for economic model.....	228
Table A.5 Material properties and assumptions used in the calculations.	230
Table A.6 Specifications of material properties as functions of temperature from Table A.5.	233

A Annex

A.1 Derivation of realistic pump efficiency

Data of actual vacuum pumps for different operating points was provided by Pfeiffer Vacuum [106,107] and a function fitted to describe the efficiency as a function of operating pressure (Figure A.1).

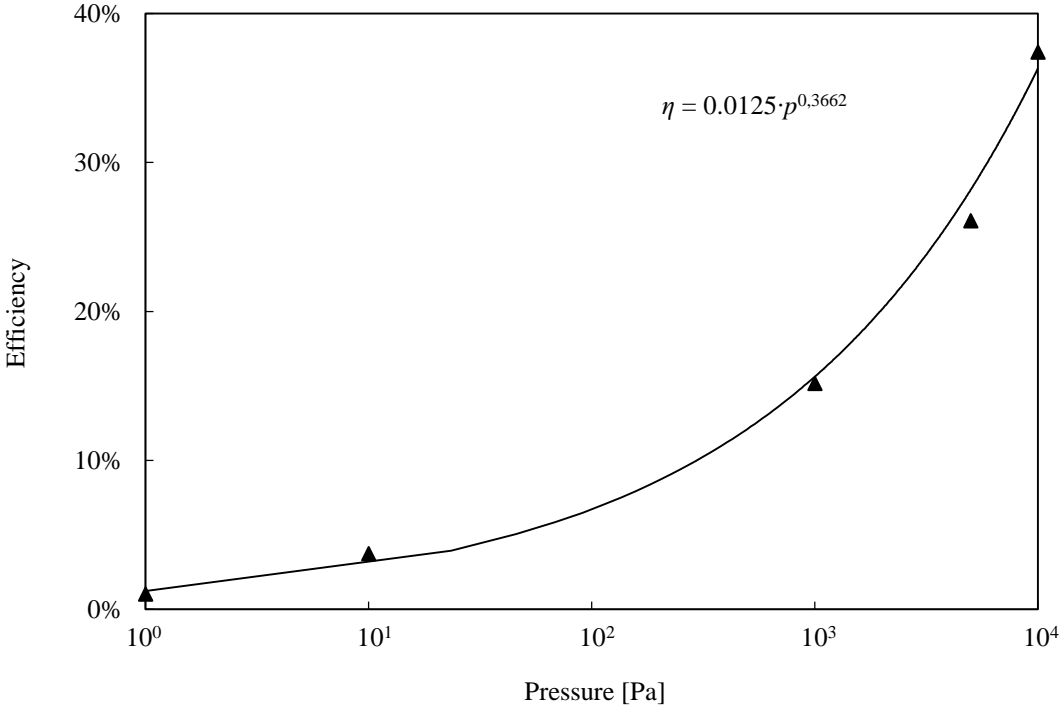


Figure A.1 Actual pump efficiency data as provided by Pfeiffer Vacuum [106,107] and a function to fit the data including its mathematical description.

A.2 Rosseland extinction coefficient as a function of porosity

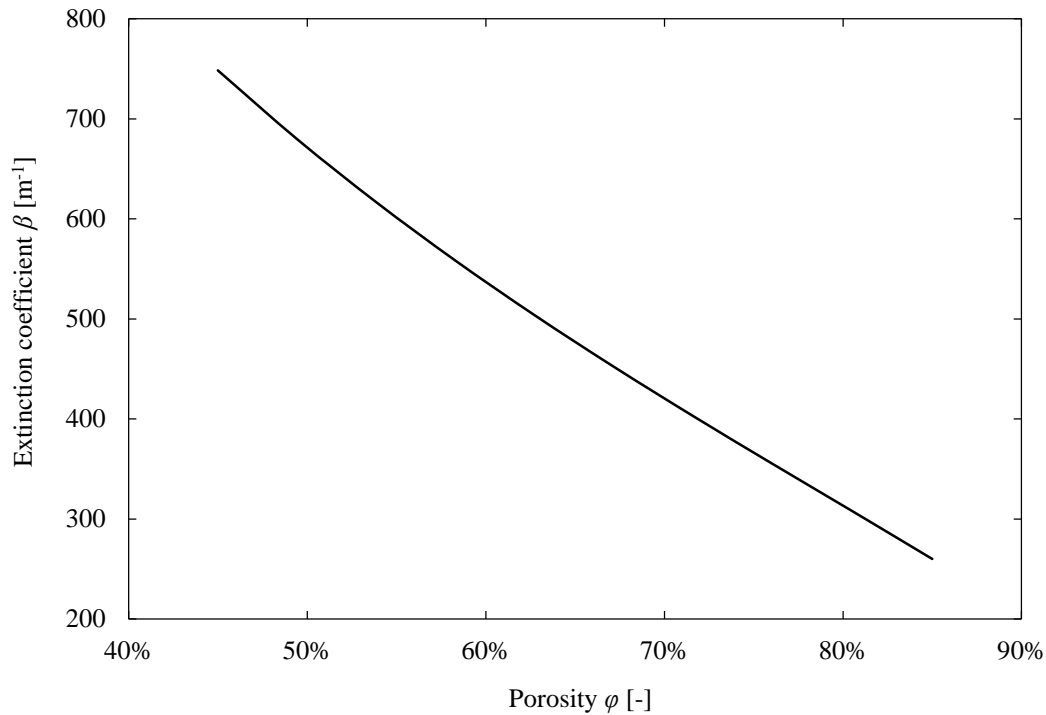


Figure A.2 Extinction coefficient of a porous medium as a function of material porosity after [120].

The extinction coefficient β used in the Rosseland diffusion approximation for the calculation of heat transfer by radiation in Section 3.3 is shown in Figure A.2 as a function of material porosity, where Equations (3.31) and (3.32) are used for its derivation [120].

$$\beta(\varphi) = \frac{1.765\sqrt{1-\varphi}}{2.2 \times 10^{-3}\varphi + 7.59 \times 10^{-4}} \quad (\text{A.1})$$

A larger porosity decreases the extinction coefficient and thus increases the heat transfer due to radiation according to Equation (3.30).

A.3 Thermal conductivity of RPC

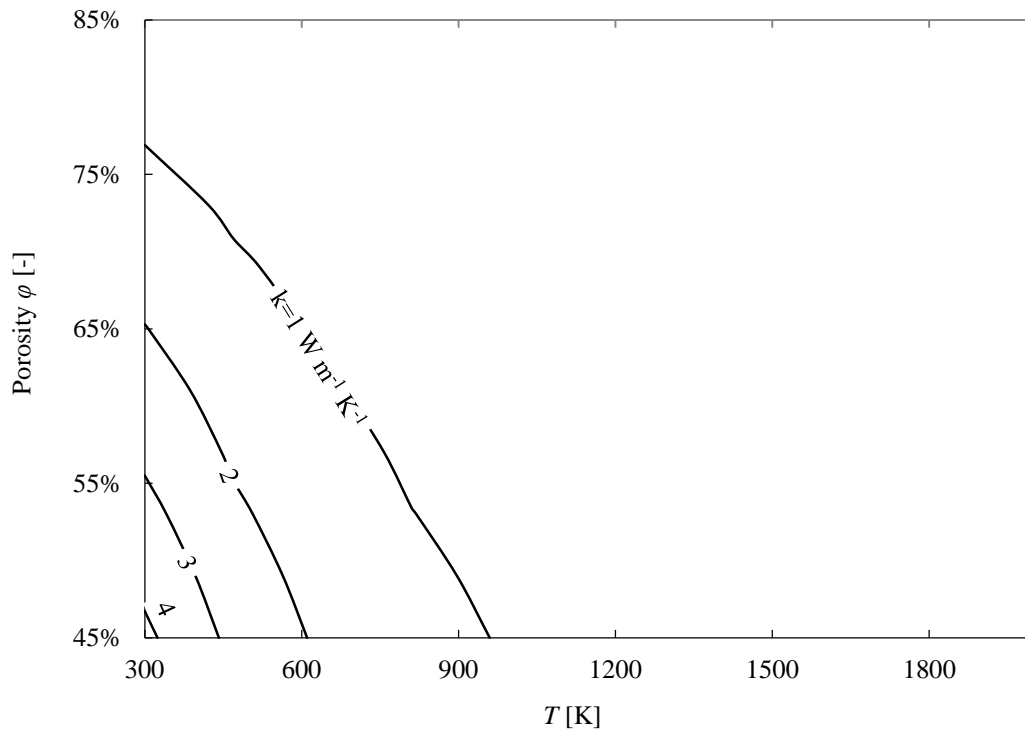


Figure A.3 Thermal conductivity of RPC as a function of porosity φ and temperature T .

Figure A.3 shows the effective thermal conductivity of the RPC derived with the three resistor model (excluding radiation) as a function of porosity and temperature. This model expresses the conductivity of a porous medium as a function of the serial and parallel thermal resistances of the solid and fluid domain, respectively. Suter et al. have analyzed an RPC sample with tomographic scans and determined the free parameter of the three resistor model to describe accurately its thermal conductivity [120].

Thermal conductivity of the RPC varies roughly between 0 and 4 W m⁻¹ K⁻¹, where an increase of porosity and temperature deteriorate the ability of the material to conduct heat (Equation (3.33)). A rise in porosity increases the void volume of the RPC and thus the relative weight of the domain with the smaller thermal conductivity (relative thermal conductivities of fluid and solid domains between 1000 K and 1800 K: $k_f / k_s \cong 0.03-0.16$). A rise in temperature increases the thermal conductivity of the fluid but diminishes that of the solid, which leads to an overall decrease of thermal conductivity.

A.4 Overall thermal conductivity of RPC including radiation term

Implementing the Rosseland diffusion approximation, the overall thermal conductivity of the porous ceria sample is expressed as the sum of thermal conductivity and the radiation term (Equation (3.23)). The overall thermal conductivity as a function of temperature and porosity is shown in Figure A.4.

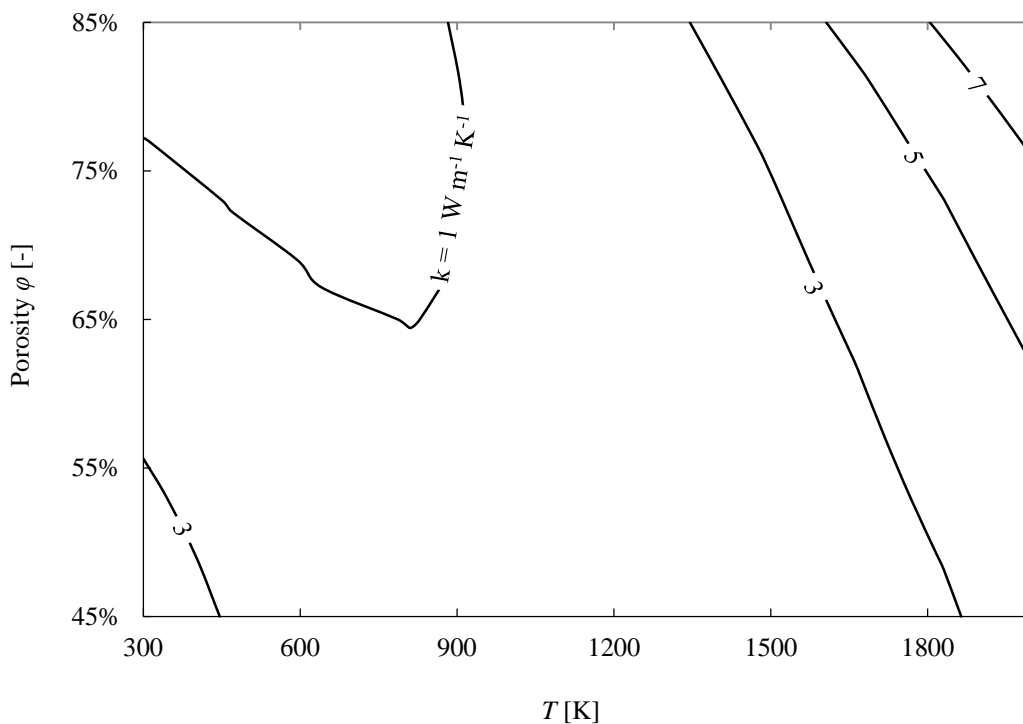


Figure A.4 Overall thermal conductivity in $\text{W m}^{-1} \text{K}^{-1}$ including conduction and radiation as a function of temperature T and porosity φ .

The overall thermal conductivity is a superposition of the conductivity due to conduction and radiation heat transfer:

- A larger porosity decreases the extinction coefficient (see Figure A.2) and thus increases the radiative conductivity, while it decreases the thermal conductivity of the material (see Figure A.3).
- With temperature, the radiative conductivity increases due to the T^4 -dependence of the radiative source term, while the thermal conductivity of the material decreases.

The overall thermal conductivity depends therefore on the temperature regime:

- $T \lesssim 1000$ K: $k \cong k_c$

The overall thermal conductivity decreases with temperature and porosity since conduction is the dominating heat transfer mechanism.

- $T \gtrsim 1000$ K: $k \cong k_{\text{rad}}$

The overall thermal conductivity increases with porosity and temperature since radiation is the dominating heat transfer mechanism.

A.5 Technical assumptions for baseline case of fuel production plant

Table A.1 Assumptions for baseline case of fuel production plant.

Item	Value	Reference
Solar resource [$\text{kWh m}^{-2} \text{y}^{-1}$]	2500	
Plant jet fuel output [bpd]	1000	
Plant naphtha output [bpd]	865	
Solar concentration efficiency [%]	51.7	[50]
Overall efficiency [%]	5.0	
Mirror reflective area [m^2]	6.5×10^6	
Annual renewal rate reflectors [%]	0.2	[52]
Redox cycles per day [-]	16	
Ceria nonstoichiometry per cycle [-]	0.1	
Amount of ceria in thermochemical reactors [kg]	7.0×10^6	
Efficiency of CHP of heat production [-]	0.40	
Efficiency of CHP of electricity production [-]	0.28	
Heat requirement for CO/CO ₂ separation [kJ mol^{-1}]	132.0	[108]

Electricity requirement for CO/CO ₂ separation [kJ mol ⁻¹]	9.0	[108]
Electricity requirement for inert gas purification [kJ mol ⁻¹]	16.0	[176]
Energy requirement for CO ₂ capture [kJ mol ⁻¹]	237.6	[42]
Amount of CO ₂ supplied to oxidation rel. to minimum [-]	2	[83]
Amount of inert gas rel. to amount of oxygen during reduction [-]	10	
HHV CO [kJ mol ⁻¹]	283.4	
HHV H ₂ [kJ mol ⁻¹]	286.0	
Electricity requirement water desalination [kWh _{el} m ⁻³]	3.0	[34]
Required amount of water for mirror cleaning [L m ² y ⁻¹]	58.1	[172]
Required amount of water for CSP electricity [L kWh _{el} ⁻¹]	1.4	[172]
Pressure in FT-reactor [Pa]	3×10 ⁶	
Efficiency of gas compressor [-]	0.8	

A.6 Assumptions for derivation of greenhouse gas emissions

Table A.2 Assumptions for ecological analysis.

Item	Value	Reference
Emission factor heliostats [kg _{CO2-eq.} m ⁻²]	132.8	[172]
Emission factor tower, buildings, streets [kg _{CO2-eq.} m ⁻²]	28.0	[172]
Emission factor CSP electricity [kg _{CO2-eq.} kWh _{el} ⁻¹]	0.023	[252]
Emission factor ceria production [kg _{CO2-eq.} kg ⁻¹]	10.3	[183]
Emission factor alumina [kg _{CO2-eq.} kg ⁻¹]	16.7	[178]
Emission factor steel [kg _{CO2-eq.} kg ⁻¹]	1.43	[178]

Emission factor glass [$\text{kg}_{\text{CO}_2\text{-eq.}} \text{kg}^{-1}$]	1.09	[178]
Emission factor concrete [$\text{kg}_{\text{CO}_2\text{-eq.}} \text{kg}^{-1}$]	0.016	[178]
Emissions of fuel pipeline transport [$\text{kg}_{\text{CO}_2\text{-eq.}} \text{TJ}^{-1}$]	1780.8	[178]
Emissions from jet fuel combustion [$\text{kg}_{\text{CO}_2\text{-eq.}} \text{L}^{-1}$]	2.4	[28]
Emissions from naphtha combustion [$\text{kg}_{\text{CO}_2\text{-eq.}} \text{L}^{-1}$]	2.3	[103]

A.7 Fuel properties

Table A.3 Fuel properties.

Item	Value	Reference
Density of jet fuel [kg m^{-3}]	0.76	[28]
Density of naphtha [kg m^{-3}]	0.70	[28]
LHV of jet fuel [MJ L^{-1}]	33.4	[28]
LHV of naphtha [MJ L^{-1}]	31.1	[28]

A.8 Assumptions for calculation of economic performance

Table A.4 Assumptions for economic model.

Item	Value	Reference
Life time of plant [years]	25	
Publicly supported:		
Nominal interest rate per year [%]	6	
Privately owned:		
Share of equity/debt [%]	30/70	
Nominal interest rate equity/debt [%]	15/8	

Tax rate [%]	35	
Annual inflation rate [%]	2	
Cost of solar reactor per kW _{th} [€]	18.0	[23]
Cost per m ² of reflective area [€ m ²]	100	[228]
Cost of solar tower [€ kW _{th} ⁻¹]	20	[226]
Solar concentration O&M costs [€ m ² y ⁻¹]	7	[226–228,253]
FT investment costs [€ bpd ⁻¹]	23000	[233]
FT O&M costs [€ bbl ⁻¹]	4	[233]
Cost of water provision [€ t _{H2O} ⁻¹]	0.5	[34]
Cost of CO ₂ from air capture [€ t _{CO2} ⁻¹]	100	
Cost of ceria [€ kg ⁻¹]	5	[183]
Market price of oxygen [€ m ³]	0.15	[102]
Cost of solar electricity [€ kWh _{el} ⁻¹]	0.06	[228]
Selling price of naphtha [€ kg ⁻¹]	0.806×Jet fuel production cost	[223]
Specific costs for syngas compressors [€ kW ⁻¹]	7.5×10 ²	[235]
Cost of inert gas [€ m ³]	2	
Cost of buildings [€ m ²]	600	[102]
Depreciation period [years]	25	
CHP investment costs [€ kW _{el} ⁻¹]	1048.8	[236]
CHP O&M costs [€ kWh _{el} ⁻¹]	0.008	[236]
CHP O&M costs [€ kW ⁻¹ y ⁻¹]	9.84	[236]

A.9 Assumptions for generic reactor models

Table A.5 Material properties and assumptions used in the calculations.

Property	Symbol	Value	Unit	Ref.
Convective heat transfer coefficient	α_{conv}	15	$\text{W m}^{-1} \text{K}^{-1}$	[112]
Temperature of surroundings	T_0	300	K	
Reactor wall				
Emissivity (Inconel 600)	$\varepsilon_{\text{wall}}$	0.69	-	[126]
Thickness	d_{wall}	0.003	m	
Thermal conductivity	λ_{wall}	15.9	$\text{W m}^{-1} \text{K}^{-1}$	[126]
Specific heat capacity	$c_{p,\text{wall}}$	465	$\text{J kg}^{-1} \text{K}^{-1}$	[126]
Density	ρ_{wall}	8470	kg m^{-3}	[126]
Insulation ($\text{Al}_2\text{O}_3\text{-SiO}_2$)				
Emissivity	ε_{Ins}	=f(T)	-	[116]
Thickness	d_{Ins}	0.05/0.1	m	
Radiative extinction coefficient	β_{Ins}	=f(T)	m^{-1}	[121]
Thermal conductivity	λ_{Ins}	=f(T)	$\text{W m}^{-1} \text{K}^{-1}$	[113]
Density	ρ_{wall}	560.6	kg m^{-3}	[113]
Specific heat capacity	$c_{p,\text{Ins}}$	=f(T)	$\text{J kg}^{-1} \text{K}^{-1}$	[131]
RPC (CeO_2)				
Emissivity	ε_{RPC}	=f(T)	-	[116]
Effective thermal conductivity RPC	λ_{RPC}	=f(T)	$\text{W m}^{-1} \text{K}^{-1}$	[120]

Radiative extinction coefficient	β_{RPC}	=f(T)	m^{-1}	[120]
----------------------------------	---------------	-------	----------	-------

Ceria (CeO₂)

Thermal conductivity ceria	λ_{CeO2}	=f(T)	$W m^{-1} K^{-1}$	[115]
----------------------------	------------------	-------	-------------------	-------

Density ceria	ρ_{CeO2}	7650	$kg m^{-3}$	[132]
---------------	---------------	------	-------------	-------

Specific heat capacity ceria	$c_{p,CeO2}$	=f(T)	$J kg^{-1} K^{-1}$	[117]
------------------------------	--------------	-------	--------------------	-------

Separating wall 1 (Al₂O₃)

Specific heat capacity	$c_{p,sw,1}$	880	$J kg^{-1} K^{-1}$	[129]
------------------------	--------------	-----	--------------------	-------

Thermal conductivity	$\lambda_{sw,1}$	35	$W m^{-1} K^{-1}$	[129]
----------------------	------------------	----	-------------------	-------

Density	$\rho_{sw,1}$	3890	$kg m^{-3}$	[129]
---------	---------------	------	-------------	-------

Thickness	$d_{sw,1}$	0.001	m	
-----------	------------	-------	---	--

Separating wall 2 (SiC 0.75/HfC 0.25)

Specific heat capacity	$c_{p,sw,2}$	552.5	$J kg^{-1} K^{-1}$	[135]
------------------------	--------------	-------	--------------------	-------

Thermal conductivity	$\lambda_{sw,2}$	80	$W m^{-1} K^{-1}$	[135]
----------------------	------------------	----	-------------------	-------

Density	$\rho_{sw,2}$	5582.5	$kg m^{-3}$	[135]
---------	---------------	--------	-------------	-------

Thickness	$d_{sw,2}$	0.001	m	
-----------	------------	-------	---	--

Emissivity	$\varepsilon_{sw,2}$	0.85	-	[135]
------------	----------------------	------	---	-------

Gases CO, CO₂, H₂

Specific heat capacity	$c_{p, gas}$	=f(T)	$J kg^{-1} K^{-1}$	[254]
------------------------	--------------	-------	--------------------	-------

Gas O₂

Thermal conductivity	λ_{O_2}	=f(T)	W m ⁻¹ K ⁻¹	[133]
----------------------	------------------------	-------	-----------------------------------	-------

Gas air

Thermal conductivity	λ_{air}	=f(T)	W m ⁻¹ K ⁻¹	[133]
----------------------	------------------------	-------	-----------------------------------	-------

Kinematic viscosity	ν_{air}	=f(T)	m ² s ⁻¹	[133]
---------------------	--------------------	-------	--------------------------------	-------

Specific heat capacity	$c_{p,\text{air}}$	=f(T)	J kg ⁻¹ K ⁻¹	[133]
------------------------	--------------------	-------	------------------------------------	-------

The functions of temperature are shown in Table A.6. Outside of the specified temperature regimes, the function value at the closest regime boundary is chosen as a constant.

Table A.6 Specifications of material properties as functions of temperature from Table A.5.

Property	Value	Temperature regime
ε_{Ins}	$= -0.6531 \cdot \left(\frac{T}{1000}\right)^4 + 2.9156 \cdot \left(\frac{T}{1000}\right)^3 - 4.3378 \cdot \left(\frac{T}{1000}\right)^2 + 2.1094 \cdot \left(\frac{T}{1000}\right) + 0.4484$	$362 < T < 1500 \text{ K}$
β_{Ins}	$= 1.73267 \times 10^{-8} \cdot T^4 - 4.98842 \times 10^{-5} \cdot T^3 + 6.13294 \times 10^{-2} \cdot T^2 - 3.15279 \times 10 \cdot T + 1.08081 \times 10^4$	$T < 973 \text{ K}$
$c_{p,\text{Ins}}$	$= 4 \times 10^{-7} \cdot T^3 - 1.3797 \times 10^{-3} \cdot T^2 + 1.5987289 \cdot T + 477.6995948$	$T < 1480 \text{ K}$
$c_{p,\text{Ins}}$	$= 1118.44$	$T \geq 1480 \text{ K}$
ε_{RPC}	$= 0.5 + (T - 1100)/(1300 - 1100)(0.9 - 0.5)$	$1100 \text{ K} < T < 1500 \text{ K}$
c_{p,CeO_2}	$= (67.95 - 9.9 \times 10^5 \cdot T^{-2} + 0.0125 \cdot T)/M_{\text{CeO}_2}$	
$c_{p,\text{CO}}$	$= -30.1 \cdot \left(\frac{T}{1000}\right)^5 + 250.8 \cdot \left(\frac{T}{1000}\right)^4 - 770.9 \cdot \left(\frac{T}{1000}\right)^3 + 1008.9 \cdot \left(\frac{T}{1000}\right)^2 - 349.2 \cdot \left(\frac{T}{1000}\right) + 1072.8$	
c_{p,CO_2}	$= 14.2 \cdot \left(\frac{T}{1000}\right)^5 - 146.6 \cdot \left(\frac{T}{1000}\right)^4 + 615.6 \cdot \left(\frac{T}{1000}\right)^3 - 1353.5 \cdot \left(\frac{T}{1000}\right)^2 + 1646.2 \cdot \left(\frac{T}{1000}\right) + 458.5$	
c_{p,O_2}	$= -8.9518 \cdot \left(\frac{T}{1000}\right)^5 + 59.2966 \cdot \left(\frac{T}{1000}\right)^4 - 106.8374 \cdot \left(\frac{T}{1000}\right)^3 - 54.7090 \cdot \left(\frac{T}{1000}\right)^2 + 491.4936 \cdot \left(\frac{T}{1000}\right) + 807.8693$	
$c_{p,\text{air}}$	$= 3.5248 + (-0.6366 - 3.5248) \cdot \left(\frac{T}{2548.932 + T}\right)^2 \left(1 - \frac{2548.932}{2548.932 + T}\right) \cdot \dots$ $\left(-3.4281 + 49.8238 \cdot \frac{T}{2548.932 + T} - 120.3466 \cdot \left(\frac{T}{2548.932 + T}\right)^2 + 98.8658 \cdot \left(\frac{T}{2548.932 + T}\right)^3\right)$	
λ_{Ins}	$= 6 \times 10^{-8} \cdot T^2 - 2 \times 10^{-5} \cdot T + 0.0805 + 16\sigma T^3/(3 \cdot \beta_{\text{Ins}})$	

$$\lambda_{\text{CeO}_2} = 4.6133 \cdot \left(\frac{T}{1000}\right)^4 - 26.6438 \cdot \left(\frac{T}{1000}\right)^3 + 58.2986 \cdot \left(\frac{T}{1000}\right)^2 - 59.2786 \cdot \left(\frac{T}{1000}\right) + 25.5218$$

$$\beta_{\text{RPC}} = 1.765 \cdot \sqrt{1 - \varphi} / (2.2 \times 10^{-3} \cdot \varphi + 7.59 \times 10^{-4})$$

$$\lambda_{\text{RPC}} = (1 - f) \cdot \lambda_{\text{O}_2} / ((\varphi + \lambda_{\text{O}_2} / \lambda_{\text{CeO}_2} \cdot (1 - \varphi))) + f \cdot (\lambda_{\text{O}_2} \cdot \varphi + \lambda_{\text{O}_2} \cdot (1 - \varphi))$$

$$\lambda_{\text{O}_2} = -1.285 \times 10^{-3} + 0.10655 \times 10^{-3} \cdot T - 0.052630 \times 10^{-6} \cdot T^2 + 0.025680 \times 10^{-9} \cdot T^3 - 0.005040 \times 10^{-12} \cdot T^4$$

173 K < T < 773 K, extrapolated
to higher temperatures

$$\lambda_{\text{air}} = -0.908 \cdot 10^{-3} + 0.111161 \cdot 10^{-3} T - 0.08433310 \cdot 10^{-6} T^2 + 0.05696410 \cdot 10^{-9} T^3 - 0.01563110 \cdot 10^{-12} T^4$$

173 K < T < 773 K

$$v_{\text{air}} = (-0.01702 \cdot 10^{-5} + 0.7996510 \cdot 10^{-7} T - 0.72183 \cdot 10^{-10} T^2 + 0.0496 \cdot 10^{-12} T^3 - 0.01388 \cdot 10^{-15} T^4) / p / (R_{\text{air}} T)$$
